Observation of Dijet Production by Double Pomeron Exchange in 1.8-TeV Proton-Antiproton Collisions

Koji TERASHI

A dissertation submitted to the Doctoral Program
in Physics, the University of Tsukuba
in partial fulfillment of the requirements for the
degree of Doctor of Philosophy (Science)

January, 2000

Abstract

We report the first observation of dijet production by Double Pomeron Exchange (DPE) in $\bar{p}p$ collisions at $\sqrt{s} = 1.8\,\mathrm{TeV}$ using the Collider Detector at Fermilab (CDF).

In DPE events, large *rapidity gaps*, defined as a region of rapidity or pseudorapidity devoid of particles, are left in both forward directions. In a sample of events containing a leading antiproton in diffractive $\bar{p}p$ interactions at $\sqrt{s} = 1.8\,\mathrm{TeV}$, we select events with at least 2 jets with transverse energy $E_T > 7\,\mathrm{GeV}$ in the kinematical region $0.035 < \xi_{\bar{p}} < 0.095$ and $|t_{\bar{p}}| < 1.0\,\mathrm{GeV}^2$ where $\xi_{\bar{p}}$ is the fractional momentum loss of the $\bar{p}$ and $t_{\bar{p}}$ is the four momentum transfer squared at the $\bar{p}$ vertex.

In this sample of single diffractive (SD) dijet events, we observe DPE dijet events as an excess of events with a rapidity gap in the forward pseudorapidity region $2.4 < \eta < 5.9$ on the outgoing p direction. Using the information on particles detected with the CDF detector, we estimate the fractional momentum loss of the p to be $0.01 < \xi_p < 0.03$. We measure the cross sections for non-diffractive (ND), single diffractive, and DPE dijet productions.

In comparison of DPE dijets with SD and ND dijets, we find that the DPE dijet is characterized by the E_T spectrum being similar to that of SD dijet and being slightly softer than that of ND dijet. Also, the DPE dijet is kinematically produced toward the outgoing $\bar{p}$ direction, and is more back-to-back than SD and ND dijets.

The cross section ratio $R_{\frac{DPE}{SD}}$ of DPE to SD dijet production is compared between the data and the predictions of the Monte Carlo simulations based on the Ingelman-Schlein model with the Donnachie-Landshoff pomeron flux factor. We find the presence of a disagreement of $R_{\frac{DPE}{SD}}$ ratio between the data and the simulations.

The dijet mass fraction, defined as the mass of dijets divided by the total mass of the central system, is evaluated based on the measurements of ξ for the p and $\bar{p}$. From the observed data distribution, we find that the contribution of *non-factorizable DPE* events, in which only the two jets are produced in the central system, is small in our kinematical range.

Acknowledgments

I would like to thank my thesis advisor, Professor Koji Takikawa, for his guidance and encouragement throughout my graduate years. He guided me to the right direction and his suggestions and instructions were very crucial in progress of understanding the particle physics. I am also thankful to Professor Kunitaka Kondo and Professor Shinghong Kim for their support. They and Professor Koji Takikawa gave me the opportunity to join the University of Tsukuba group, and continue to work on diffractive physics.

I am deeply grateful to Professor Emeritus Shunichi Hasegawa, who gave me fun of high energy physics and the opportunity to join the CDF experiment. His advice always directed me to the right answer. Also, I would like to thank Professor Emeritus Youichi Fujimoto for his guidance and support. I remember that the discussions with him were always instructive for me. During the time which I spent with them, I learned a lot of things about high energy physics.

Many thanks go to Professor Michael Albrow, Professor Konstantin Goulianos and Dr. Kerstin Borras. They provided me with a lot of advice throughout my study, and lead me to the right direction. I would like to thank Dr. Philip Melese, Dr. Suren Bagdasarov, Dr. Alexander Akopian and Mr. Kenichi Hatakeyama of Rockefeller University, and Mr. Housai Nakada, Dr. Hirofumi Ikeda of University of Tsukuba. My study in this thesis relies on their studies and experiences in many phase. I could not have finished this work without them. Also, I am deeply thankful to Professor Junsuke Iwai. When I was staying at Fermilab, he always helped me so much not only in studies but also in life. I believe that the installation and operation of Roman Pots could not be done without him.

I wish to thank Dr. Tetsuo Arisawa, Mr. Toshihiro Kodaka, Mr. Shin Uesaka, Mr. Yasuhiro Yoda, Mr. Junji Yamamuro, Ms. Masayo Moriya, Mr. Kimihiko Ono, Mr. Norihisa Usui and other members of Waseda University group for their help. I had a good time with them at Waseda University.

Many people in University of Tsukuba group helped me not only in Japan but also in Fermilab. I want to thank them, Professor Fumihiko Ukegawa, Dr. Yoshihiro Seiya, Dr. Kiyoshi Yasuoka, Dr. Kazuhiko Hara, Dr. Makoto Shimojima, Dr. Takashi Asakawa, Dr. Ryuutaro Oishi, Dr. Junichi Suzuki, Mr. Toshiharu Uchida, Dr. Takeshi Takano, Dr. Shin Aota, Dr. Hiroyuki Minato, Dr. Toshiaki Kikuchi, and other colleagues. Also, I wish to thank Dr. Takanobu Handa, Mr. Hirotoshi Toyoda, Mr. Kouichi Kurino for having a good time at Fermilab.

I thank the Fermilab staffs and the technical staffs of the participating institutions for their vital contributions. I am grateful also to many CDF collaborators who have participated in the CDF experiment. I wish to express many thanks to Ms. Dee Hahn, Ms. Carol Picciolo, Ms. Barbara Perington, and Ms. Kyoko Kunori, Ms. Mutsumi Uenishi and Ms. Kazuko Kumashiro for their secretarial works.

Finally I thank my parents and a brother for their constant help and support. Especially I want to express my special appreciation to my wife. I could not do this work without her understanding, help and encouragement.

This work was supported by the U.S. Department of Energy and National Science Foundation; the Italian Instituto Nazionale di Fisica Nucleare; the Ministry of Education, Science and Culture of Japan; the Natural Sciences and Engineering Research Council of Canada; the National Science Council of the Republic of China; the A. P. Sloan Foundation; and the Max Kade Foundation; and the German Landes-Ministry.

Contents

List of Figures

List of Tables

The CDF Collaboration

F. Abe,[17] H. Akimoto,[39] A. Akopian,[31] M. G. Albrow,[7] A. Amadon,[5] S. R. Amendolia,[27] D. Amidei,[20] J. Antos,[33] S. Aota,[37] G. Apollinari,[31] T. Arisawa,[39] T. Asakawa,[37] W. Ashmanskas,[5] M. Atac,[7] P. Azzi-Bacchetta,[25] N. Bacchetta,[25] S. Bagdasarov,[31] M. W. Bailey,[22] P. de Barbaro,[30] A. Barbaro-Galtieri,[18] V. E. Barnes,[29] B. A. Barnett,[15] M. Barone,[9] G. Bauer,[19] T. Baumann,[11] F. Bedeschi,[27] S. Behrends,[3] S. Belforte,[7] G. Bellettini,[27] J. Bellinger,[40] D. Benjamin,[35] J. Bensinger,[3] A. Beretvas,[7] J. P. Berge,[7] J. Berryhill,[5] S. Bertolucci,[9] S. Bettelli,[27] B. Bevensee,[26] A. Bhatti,[31] K. Biery,[7] C. Bigongiari,[27] M. Binkley,[7] D. Bisello,[25] R. E. Blair,[1] C. Blocker,[3] K. Bloom,[20] S. Blusk,[30] A. Bodek,[30] W. Bokhari,[26] G. Bolla,[29] Y. Bonushkin,[4] K. Borras,[31] D. Bortoletto,[29] J. Boudreau,[28] L. Breccia,[2] C. Bromberg,[21] N. Bruner,[22] R. Brunetti,[2] E. Buckley-Geer,[7] H. S. Budd,[30] K. Burkett,[11] G. Busetto,[25] A. Byon-Wagner,[7] K. L. Byrum,[1] M. Campbell,[20] A. Caner,[27] W. Carithers,[18] D. Carlsmith,[40] J. Cassada,[30] A. Castro,[25] D. Cauz,[36] A. Cerri,[27] P. S. Chang,[33] P. T. Chang,[33] H. Y. Chao,[33] J. Chapman,[20] M. -T. Cheng,[33] M. Chertok,[34] G. Chiarelli,[27] C. N. Chiou,[33] F. Chlebana,[7] L. Christofek,[13] R. Cropp,[14] M. L. Chu,[33] S. Cihangir,[7] A. G. Clark,[10] M. Cobal,[27] E. Cocca,[27] M. Contreras,[5] J. Conway,[32] J. Cooper,[7] M. Cordelli,[9] D. Costanzo,[27] C. Couyoumtzelis,[10] D. Cronin-Hennessy,[6] R. Culbertson,[5] D. Dagenhart,[38] T. Daniels,[19] F. DeJongh,[7] S. Dell'Agnello,[9] M. Dell'Orso,[27] R. Demina,[7] L. Demortier,[31] M. Deninno,[2] P. F. Derwent,[7] T. Devlin,[32] J. R. Dittmann,[6] S. Donati,[27] J. Done,[34] T. Dorigo,[25] N. Eddy,[13] K. Einsweiler,[18] J. E. Elias,[7] R. Ely,[18] E. Engels, Jr.,[28] W. Erdmann,[7] D. Errede,[13] S. Errede,[13] Q. Fan,[30] R. G. Feild,[41] Z. Feng,[15] C. Ferretti,[27] I. Fiori,[2] B. Flaugher,[7] G. W. Foster,[7] M. Franklin,[11] J. Freeman,[7] J. Friedman,[19] H. Frisch,[5] Y. Fukui,[17] S. Gadomski,[14] S. Galeotti,[27] M. Gallinaro,[26] O. Ganel,[35] M. Garcia-Sciveres,[18] A. F. Garfinkel,[29] C. Gay,[41] S. Geer,[7] D. W. Gardes,[20] P. Giannetti,[27] N. Giokaris,[31] P. Giromini,[9] G. Giusti,[27] M. Gold,[22] A. Gordon,[11] A. T. Goshaw,[6] Y. Gotra,[28] K. Goulianos,[31] H. Grassmann,[36] C. Green,[29] L. Groer,[32] C. Grosso-Pilcher,[5] G. Guillian,[20] J. Guimaraes da Costa,[15] R. S. Guo,[33] C. Haber,[18] E. Hafen,[19] S. R. Hahn,[7] R. Hamilton,[11] T. Handa,[12] R. Handler,[40] W. Hao,[35] F. Happacher,[9] K. Hara[37], A. D. Hardman,[29] R. M. Harris,[7] F. Hartmann,[16] J. Hauser,[4] E. Hayashi,[37] J. Heinrich,[26] A. Heiss,[16] B. Hinrichsen,[14] K. D. Hoffman,[29] C. Holck,[26] R. Hollebeek,[26] L. Holloway,[13] Z. Huang,[20] B. T. Huffman,[28] R. Hughes,[23] J. Huston,[21] J. Huth,[11] H. Ikeda,[37] M. Incagli,[27] J. Incandela,[7] G. Introzzi,[27] J. Iwai,[39] Y. Iwata,[12] E. James,[20] H. Jensen,[7] U. Joshi,[7] E. Kajfasz,[25] H. Kambara,[10] T. Kamon,[34] T. Kaneko,[37] K.

Karr,[38] H. Kasha,[41] Y. Kato,[24] T. A. Keaffaber,[29] K. Kelley,[19] R. D. Kennedy,[7] R. Kephart,[7] D. Kestenbaum,[11] D. Khazins,[6] T. Kikuchi,[37] M. Kirk,[3] B. J. Kim,[27] H. S. Kim,[14] S. H. Kim,[37] Y. K. Kim,[18] L. Kirsch,[3] S. Klimenko,[8] D. Knoblauch,[16] P. Koehn,[23] A. Köngeter,[16] H. Kondo,[37] J. Konigsberg,[8] K. Kordas,[14] A. Korytov,[8] E. Kovacs,[1] W. Kowald,[6] J. Kroll,[26] M. Kruse,[30] S. E. Kuhlmann,[1] E. Kuns,[32] K. Kurino,[12] T. Kuwabara,[37] A. T. Laasanen,[29] S. Lami,[27] S. Lammel,[7] J. I. Lamoureux,[3] M. Lancaster,[18] M. Lanzoni,[27] G. Latino,[27] T. LeCompte,[1] S. Leone,[27] J. D. Lewis,[7] M. Lindgren,[4] T. M. Liss,[13] J. B. Liu,[30] Y. C. Liu,[33] N. Lockyer,[26] O. Long,[26] M. Loreti,[25] D. Lucchesi,[27] P. Lukens,[7] S. Lusin,[40] J. Lys,[18] K. Maeshima,[7] P. Maksimovic,[11] N. Mangano,[27] M. Mariotti,[25] J. P. Marriner,[7] G. Martignon,[25] A. Martin,[41] J. A. J. Matthews,[22] P. Mazzanti,[2] K. McFarland,[30] P. McIntyre,[34] P. Melese,[31] M. Menguzzato,[25] A. Menzione,[27] E. Meschi,[27] S. Metzler,[26] C. Miao,[20] T. Miao,[7] G. Michail,[11] R. Miller,[21] H. Minato,[37] S. Miscetti,[9] M. Mishina,[17] S. Miyashita,[37] N. Moggi,[27] E. Moore,[22] Y. Morita,[17] A. Mukherjee,[7] T. Muller,[16] A. Munar,[27] P. Murat,[27] S. Murgia,[21] M. Musy,[36] H. Nakada,[37] T. Nakaya,[5] I. Nakano,[12] C. Nelson,[7] D. Neuberger,[16] C. Newman-Holmes,[7] C.- Y. P. Ngan,[19] H. Niu,[3] L. Nodulman,[1] A. Nomerotski,[8] S. H. Oh,[6] T. Ohmoto,[12] T. Ohsugi,[12] R. Oishi,[37] M. Okabe,[37] T. Okusawa,[24] J. Olsen,[40] C. Pagliarone,[27] R. Paoletti,[27] V. Papadimitriou,[35] S. P. Pappas,[41] N. Parashar,[27] A. Parri,[9] D. Partos,[3] J. Patrick,[7] G. Pauletta,[36] M. Paulini,[18] A. Perazzo,[27] L. Pescara,[25] M. D. Peters,[18] T. J. Phillips,[6] G. Piacentino,[27] M. Pillai,[30] K. T. Pitts,[7] R. Plunkett,[7] A. Pompos,[29] L. Pondrom,[40] J. Proudfoot,[1] F. Ptohos,[11] G. Punzi,[27] K. Ragan,[14] D. Reher,[18] M. Reischl,[16] A. Ribon,[25] F. Rimondi,[2] L. Ristori,[27] W. J. Robertson,[6] A. Robinson,[14] T. Rodrigo,[27] S. Rolli,[38] L. Rosenson,[19] R. Roser,[13] T. Saab,[14] W. H. Sakumoto,[30] D. Saltzberg,[4] A. Sansoni,[9] L. Santi,[36] H. Sato,[37] P. Schlabach,[7] E. E. Schmidt,[7] M. P. Schmidt,[41] A. Scott,[4] A. Scribano,[27] S. Segler,[7] S. Seidel,[22] Y. Seiya,[37] F. Semeria,[2] T. Shah,[19] M. D. Shapiro,[18] N. M. Shaw,[29] P. F. Shepard,[28] T. Shibayama,[37] M. Shimojima,[37] M. Shochet,[5] J. Siegrist,[18] A. Sill,[35] P. Sinervo,[14] P. Singh,[13] K. Sliwa,[38] C. Smith,[15] F. D. Snider,[15] J. Spalding,[7] T. Speer,[10] P. Sphicas,[19] F. Spinella,[27] M. Spiropulu,[11] L. Spiegel,[7] L. Stanco,[25] J. Steele,[40] A. Stefanini,[27] R. Ströhmer,[7*] J. Strologas,[13] F. Strumia,[10] D. Stuart,[7] K. Sumorok,[19] J. Suzuki,[37] T. Suzuki,[37] T. Takahashi,[24] T. Takano,[24] R. Takashima,[12] K. Takikawa,[37] M. Tanaka,[37] B. Tannenbaum,[4] F. Tartarelli,[27] W. Taylor,[14] M. Tecchio,[20] P. K. Teng,[33] Y. Teramoto,[24] K. Terashi,[37] S. Tether,[19] D. Theriot,[7] T. L. Thomas,[22] R. Thurman-Keup,[1] M. Timko,[38] P. Tipton,[30] A, Titov,[31] S. Tkaczyk,[7] D. Toback,[5] K. Tollefson,[30] A. Tollestrup,[7] H. Toyoda,[24] W. Trischuk,[14] J. F. de Troconiz,[11] S. Truitt,[20] J. Tseng,[19] N. Turini,[27] T. Uchida,[37] F. Ukagawa,[26] J. Valls,[32] S. C. van den Brink,[15] S. Vejcik, III,[20] G. Velev,[27] I. Volobouev,[18] R. Vidal,[7] R. Vilar,[7*] D. Vucinic,[19] R. G. Wagner,[1] R. L. Wagner,[7]

J. Wahl,[5] N. B. Wallace,[27] A. M. Walsh,[32] C. Wang,[6] C. H. Wang,[33] M. J. Wang,[33] A. Warburton,[14] T. Watanabe,[37] T. Watts,[32] R. Webb,[34] C. Wei,[6] H. Wenzel,[16] W. C. Wester, III,[7] A. B. Wicklund,[1] E. Wicklund,[7] R. Wilkinson,[26] H. H. Williams,[26] P. Wilson,[7] B. L. Winer,[23] D. Winn,[20] D. Wolinski,[20] J. Wolinski,[21] S. Worm,[22] X. Wu,[10] J. Wyss,[27] A. Yagil,[7] W. Yao,[18] K. Yasuoka,[37] G. P. Yeh,[7] P. Yeh,[33] J. Yeh,[7] C. Yosef,[21] T. Yoshida,[24] I. Yu,[7] A. Zanetti,[36] F. Zetti,[27] and S. Zucchelli [2]

(CDF Collaboration)

[1] *Argonne National Labaratory, Argonne, Illinois, 60439*

[2] *Istituto Nazionale di Fisica Nucleare, University of Bologna, I-40127, Bologna, Italy*

[3] *Brandeis University, Waltham, Massachusetts 02254*

[4] *University of California at Los Angels, Los Angels, California 90024*

[5] *University of Chicago, Chicago, Illinois 60637*

[6] *Duke University, Durham, North Caroline 27708*

[7] *Fermi National Accelerator Laboratory, Batavia, Illinois 60510*

[8] *University of Florida, Gainesville, Florida 32611*

[9] *Laboratori Nazionali di Frascati, Istituto Nazionale di Fisica Nucleare, I-00044 Frascati, Italy*

[10] *University of Geneva, CH-1211 Geneva 4, Switzerland*

[11] *Harvard University, Cambridge, Massachusetts 02138*

[12] *Hiroshima University, Higashi-Hiroshima 724, Japan*

[13] *University of Illinois, Urbana, Illinois 61801*

[14] *Institute of Particle Physics, McGill University, Montreal H3A 2T8, and University of Toronto, Toronto M5S 1A7, Canada*

[15] *The Johns Hopkins University, Baltimore, Maryland 21218*

[16] *Institut für Experimentelle Kernphysik, Universität Karlsruhe, 76128 Karlsruhe, Germany*

[17] *National Laboratory for High Energy Physics (KEK), Tsukuba, Ibaraki 305, Japan*

[18] *Ernest Orlando Lawrence Berkeley National Laboratory, Berkeley, California 94720*

[19] *Massachusetts Institute of Technology, Cambridge, Massachusetts 02139*

[20] *University of Michigan, Ann Arbor, Michigan 48109*

[21] *Michigan State University, East Lansing, Michigan 48824*

[22] *University of New Mexico, Albuquerque, New Mexico 87131*

[23] *The Ohio State University, Columbus, Ohio 43210*

[24] *Osaka City University, Osaka 588, Japan*

[25] *Universita di Padova, Istituto Nazionale di Fisica Nucleare, Sezione di Padova, I-35131 Padova, Italy*

[26] *University of Pennsylvania, Philadelphia, Pennsylvania 19104*

[27] *Istituto Nazionale di Fisica Nucleare, University and Scuola Normale Superiore of Pisa, I-56100 Pisa, Italy*

[28] *University of Pittsburgh, Pittsburgh, Pennsylvania 15260*

[29] *Purdue University, West Lafayette, Indiana 47907*

[30] *University of Rochester, Rochester, New York 14627*

[31] *Rockefeller University, New York, New York 10021*

[32] *Rutgers University, Piscataway, New Jersey 08855*

[33] *Academia Sinica, Taipei, Taiwan 11530, Republic of China*

[34] *Texas A&M University, College Station, Texas 77843*

[35] *Texas Yech University, Lubbock, Texas 79409*

[36] *Istituto Nazionale di Fisica Nucleare, University of Trieste/ Udine, Italy*

[37] *University of Tsukuba, Tsukuba, Ibaraki 305, Japan*

[38] *Tufts University, Medford, Massachusetts 02155*

[39] *Waseda University, Tokyo 169, Japan*

[40] *University of Wisconsin, Madison, Wisconsin 53706*

[41] *Yale University, New Haven, Connecticut 06520*

Chapter 1

Introduction

Since the theory of strong interactions, Quantum Chromo Dynamics (QCD), was established many years ago, theoretical predictions based on perturbative QCD have provided good agreement with experimental data in large transverse momentum process. The QCD framework successfully describes such a short range interaction with small coupling constant $\alpha_s(Q^2)$ where Q^2 is the square of the momentum transfer in the process, but it has less predictive power for the processes with small Q^2 and hence large $\alpha_s(Q^2)$. On the contrary, it is well known that in *Regge Phenomenology* [1] several processes such as elastic or diffractive scattering are described by the exchange of a Regge trajectory called the "pomeron" that carries the quantum numbers of the vacuum. One of the processes related to pomeron exchange, single diffractive dissociation (simply single diffraction or SD) [2], occupies a large fraction ($10 \sim 15\,\%$) of inelastic hadron interactions. In the single diffractive dissociation process:

$$h_1 + h_2 \rightarrow h_1 + X, \tag{1.1}$$

the incident hadron h_1 (p or $\bar{p}$) goes through quasi-elastically with the final momentum smaller by $10\,\%$ or less than the initial momentum, and the other hadron h_2 is excited into high mass state, then breaks up into multi-hadronic particle state X. Due to colorless nature of the pomeron, the pomeron exchange between h_1 and h_2 leaves a *rapidity gap*, defined as a region of rapidity or pseudorapidity where there is no particle,

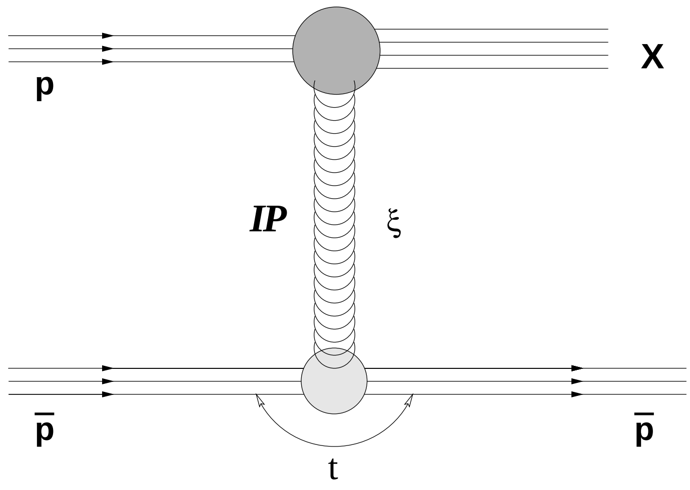

Figure 1.1: A diagram of single diffractive dissociation in $\bar{p}p$ collisions. $I\!P$ denotes the pomeron in Regge theory.

between the scattered h_1 and the particle state X. Figure 1.1 shows a diagram of single diffractive dissociation with a leading antiproton in $\bar{p}p$ collisions. The diffractively excited mass M is given by the formula:

$$M^2 = s\,(1 - x_F), \tag{1.2}$$

where s is the square of the center of mass energy in $\bar{p}p$ collisions and x_F is the Feynman variable of $\bar{p}$ defined as momentum fraction of the quasi-elastically scattered $\bar{p}$ to the incident $\bar{p}$ beam in the center of mass system, $x_F \equiv P^L_{out}/P^L_{in}$ where $P^L_{in(out)}$ is the longitudinal momentum of the incident (scattered) antiproton. In Eq. (1.2), the two approximations that the mass of the $\bar{p}$ can be neglected in comparison with M and $\sqrt{s}$, and the transverse momentum of the scattered $\bar{p}$ is negligibly small, are used. It is worth noting that the variable ξ, defined as

$$\xi \equiv \frac{M^2}{s}, \tag{1.3}$$

is also frequently used. The ξ and x_F are related by $\xi = 1 - x_F$, so that the ξ represents the fractional momentum loss of the antiproton. The t in the figure represents the four

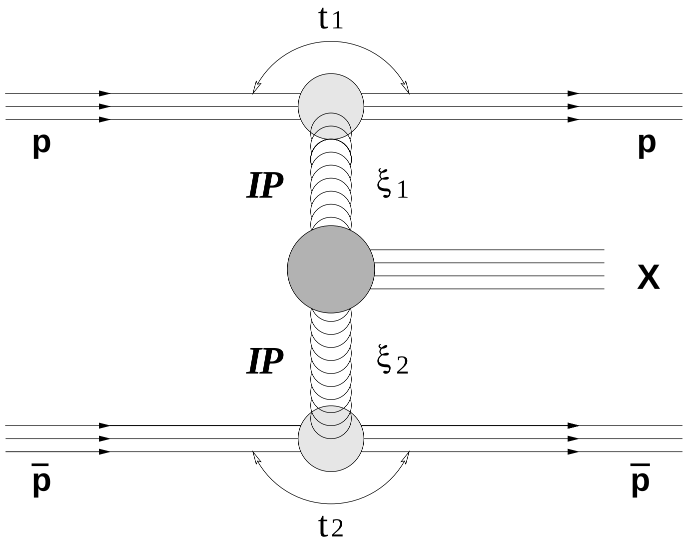

Figure 1.2: A diagram of Double Pomeron Exchange (DPE) process in $\bar{p}p$ collisions. $I\!P$ denotes the pomeron in Regge theory.

momentum transfer squared, defined as

$$t \equiv (P_{out} - P_{in})^2, \tag{1.4}$$

where $P_{in(out)}$ is the four momentum of the incident (scattered) antiproton. At the Tevatron energy of $\sqrt{s} = 1.8\,\mathrm{TeV}$, the diffractive cluster mass reaches about $400\,\mathrm{GeV}$ at the range of $x_F > 0.95$ in which the Regge theory predicts that the pomeron exchange is dominant over other reggeon exchanges such as ρ, ω, ϕ. In this high mass diffraction, we expect the presence of diffractive processes involving a large momentum transfer subprocess, called *hard diffraction*, in addition to usual *soft diffraction*. Hard diffraction is characterized by a hard scattering process such as productions of high transverse momentum (p_T) jets, W/Z bosons and heavy quarks, so it would be a possible probe to the "parton structure of the pomeron".

The process called Double Pomeron Exchange (DPE) is defined as the reaction:

$$h_1 + h_2 \to h_1 + h_2 + X, \tag{1.5}$$

where a system X of produced particles in the central region is separated by large rapidity gaps in both forward directions from outgoing hadrons. A diagram of Double Pomeron Exchange in $\bar{p}p$ collisions is shown in Figure 1.2.

In this thesis we report the study of Double Pomeron Exchange events in $\bar{p}p$ collisions at $\sqrt{s} = 1.8\,\mathrm{TeV}$ using the Collider Detector at Fermilab (CDF). This is the first observation of the DPE event at the Tevatron. In the data analysis we do not rely on any hypothetical models in standard Regge theory and stick to what the experimental data shows. Especially what we focus our concentration is an observation of the jets in DPE events. The production of DPE jets would provide another probe to the exchanged objects regardless of what they are, i.e., pomerons, reggeons or something else, and hence confirm the validity of the constituent picture of these objects.

Another motivation of focusing jets in DPE events is that this result is, if we observe, the first direct measurement of DPE jets using an unbiased sample by the gap requirements. As discussed later, jet production by DPE was studied using the UA1 detector [3]. They reported a measurement of DPE jets in $\bar{p}p$ collisions at $\sqrt{s} = 630\,\mathrm{GeV}$. However, their data sample clearly has the bias arising from requiring the rapidity gaps on both the forward directions. Moreover, they required that there was an energy deposition above threshold in the central region, which would bias the accepted events towards higher mass, so that they did not conclusively demonstrate that their observed jets were really produced in DPE process.

The outline of the thesis is as follows. I start the thesis with an introduction for high energy diffraction including the descriptions about the standard Regge theory and the models for hard diffraction, and their experimental tests. The recent activities of CDF for hard diffraction are mainly reviewed. We see there that the standard Regge approach and hard diffraction models which the pioneers proposed do not describe the data. Then, the Tevatron and the CDF detector are described in Chapter 3. New detectors for CDF hard diffraction experiment are also described there. Chapter 4 presents the data and trigger used in the analysis. Next the analysis procedure of data containing the jets is described in Chapter 5. We obtain a sample of events containing the dijets that are produced in single diffractive interactions. In Chapter 6 the analysis results of DPE dijets, the main topic of the thesis, are presented. It contains the measurement of dijet cross sections, studies of diffractive structure functions of the proton and antiproton, and mass fraction of the dijet and so forth. The Monte Carlo programs used for the comparison with the data are described in Chapter 7. Finally, I summarize the results and present the conclusions.

Chapter 2

High Energy Diffraction

2.1 Standard Regge Picture

It is well known that the behavior of high energy elastic, diffractive and total cross sections is described in the framework of Regge Pole Phenomenology [1]. In the Regge pole picture of high energy proton and antiproton interactions (see Figure 2.1), the total cross section $\sigma_T^{\bar{p}p}$ is expressed as follows,

$$\sigma_T^{\bar{p}p} \;=\; \beta_{I\!P}^{\bar{p}}(0)\,\beta_{I\!P}^{p}(0)\left(\frac{s}{s_0}\right)^{\alpha_{I\!P}(0)-1} \;=\; \sigma_0^{\bar{p}p}\left(\frac{s}{s_0}\right)^{\varepsilon}, \tag{2.1}$$

where $\beta_{I\!P}^{p(\bar{p})}$ is the coupling of the pomeron $I\!P$ to the proton p (antiproton $\bar{p}$), s is the square of the center of mass energy in $\bar{p}p$ collisions, s_0 is the energy scale constant. The pomeron trajectory $\alpha_{I\!P}(t)$ is given as $\alpha_{I\!P}(t) = 1 + \varepsilon + \alpha' t$ ($\varepsilon > 0$). The total cross section $\sigma_T^{\bar{p}p}$ is thus *factorized* into the pomeron-hadron couplings and the universal contribution from the pomeron exchange.

Single diffractive cross section $\sigma_{SD}^{\bar{p}p}$ (single diffraction with a diffracted proton) is given in the standard Regge formalism as

$$\frac{d^2\sigma_{SD}^{\bar{p}p}}{d\xi\, dt} \;=\; \frac{1}{16\pi}\,\beta_{I\!P}^{p}(t)^2\,\xi^{1-2\alpha_{I\!P}(t)}\left[\beta_{I\!P}^{\bar{p}}(0)\,g(t)\left(\frac{s'}{s'_0}\right)^{\alpha_{I\!P}(0)-1}\right] \tag{2.2}$$

$$\;=\; f_{I\!P/p}(\xi,\, t)\;\sigma_T^{I\!P\bar{p}}(s',\, t), \tag{2.3}$$

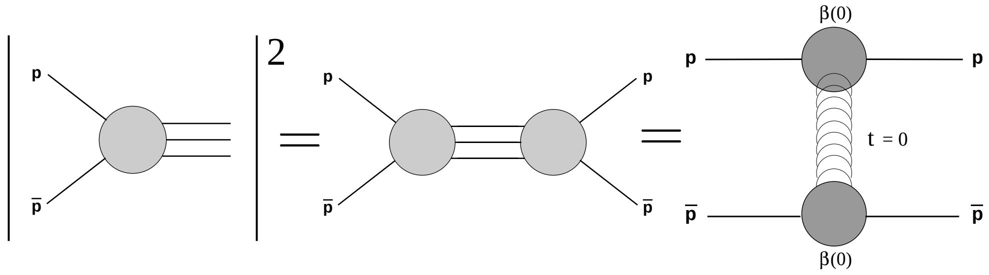

Figure 2.1: Diagrams for total cross section in $\bar{p}p$ collisions.

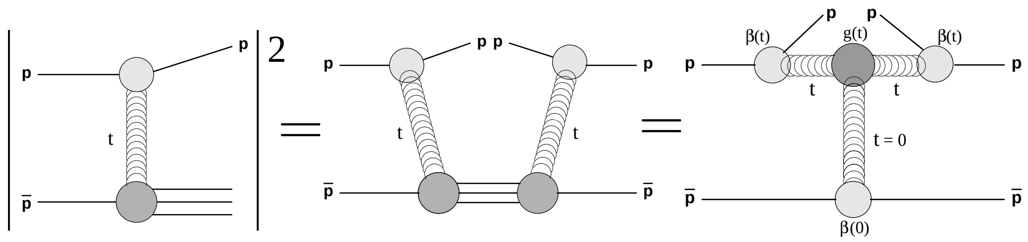

Figure 2.2: Diagrams for single diffractive cross section in $\bar{p}p$ collisions.

where $g(t)$ is the triple-pomeron coupling, $s' = M^2 = s\,\xi$ is the square of the center of mass energy of the pomeron-antiproton system, s'_0 is the energy scale constant. The term in the brackets of Eq. (2.2) represents the pomeron-antiproton total cross section $\sigma_T^{I\!P\bar{p}}(s',\,t)$ and it is written as

$$\sigma_T^{I\!P\bar{p}}(s',\,t) \;=\; \sigma_0^{I\!P\bar{p}}\left(\frac{s'}{s'_0}\right)^{\alpha_{I\!P}(0)-1} \;=\; \sigma_0^{I\!P\bar{p}}\left(\frac{s'}{s'_0}\right)^{\varepsilon}, \tag{2.4}$$

by assuming that the triple-pomeron coupling $g(t)$ is independent of t [2] and writing $\beta_{I\!P}^{\bar{p}}(0)\,g(t) = \beta_{I\!P}^{\bar{p}}(0)\,g(0) = \sigma_0^{I\!P\bar{p}}$. Diagrams related to the single diffractive cross section are shown in Figure 2.2.

As in Eq. (2.3), single diffractive cross section divided by the pomeron-antiproton total cross section defines the *pomeron flux factor*:

$$\begin{aligned} f_{I\!P/p}(\xi,\,t) \;&\equiv\; \frac{d^2\sigma_{SD}^{\bar{p}p}/d\xi\,dt}{\sigma_T^{I\!P\bar{p}}(s',\,t)} = \frac{1}{16\pi}\,\beta_{I\!P}^{p}(t)^2\,\xi^{1-2\alpha_{I\!P}(t)} \\ &=\; \frac{1}{16\pi}\,\beta_{I\!P}^{p}(0)^2\,F(t)^2\,\xi^{1-2\alpha_{I\!P}(t)} \end{aligned}$$

$$= \frac{1}{16\pi}\,\sigma_0^{pp}\,F(t)^2\,\xi^{1-2\alpha_{I\!P}(t)}, \tag{2.5}$$

where the proton form factor $F(t) \equiv \beta^p_{I\!P}(t)/\beta^p_{I\!P}(0)$ provides a t dependence of pomeron-proton coupling $\beta^p_{I\!P}$, and the relation $\beta^p_{I\!P}(0)^2 = \sigma_0^{pp}$ is used in analogy to $\beta^{\bar{p}}_{I\!P}(0)\,\beta^p_{I\!P}(0) = \sigma_0^{\bar{p}p}$.

An apparent problem of the standard Regge approach is that it shows a unitarity violation due to the incorrect s dependence of single diffractive cross section. The single diffractive cross section integrated over ξ and t is given by

$$\begin{aligned}
\sigma_{SD}^{\bar{p}p} &= \sigma_0^{I\!P\bar{p}}\left(\frac{s'}{s'_0}\right)^{\varepsilon}\int_{\xi_{min}}^{\xi_{max}}\int_{-\infty}^{0} f_{I\!P/p}(\xi,\,t)\,d\xi\,dt \\
&= \frac{\sigma_0^{I\!P\bar{p}}\sigma_0^{pp}}{16\pi}\left(\frac{s}{s'_0}\right)^{\varepsilon}\int_{\xi_{min}}^{\xi_{max}}\int_{-\infty}^{0}\xi^{\varepsilon}\,\xi^{1-2\alpha_{I\!P}(t)}\,F(t)^2\,d\xi\,dt \\
&\sim s^{\varepsilon}\cdot\int_{\xi_{min}}^{\xi_{max}}\xi^{-(1+\varepsilon)}\,d\xi \\
&\sim s^{2\varepsilon},
\end{aligned} \tag{2.6}$$

where $s' = s\xi$ and the integral is carried over the entire diffraction region between $\xi_{min} = M_0^2/s$ with $M_0 = 1.5\,\mathrm{GeV}^2$ (effective threshold) and $\xi_{max} = 0.1$ (coherence limit) [4]. The single diffractive cross section $\sigma_{SD}^{\bar{p}p}$ behaves like $\sim s^{2\varepsilon}$, while the total cross section $\sigma_T^{\bar{p}p}$ behaves like $\sim s^{\varepsilon}$, as shown in Eq. (2.1). Since $\sigma_{SD}^{\bar{p}p}$ grows faster than $\sigma_T^{\bar{p}p}$, the unitarity violates at some s.

A possible solution of this problem is given by a hypothesis of *pomeron flux renormalization* [4]. Based on the hypothesis that the pomeron flux factor integrated over all phase space cannot exceed unity, the pomeron flux factor is normalized as follows,

$$f^N_{I\!P/p}(\xi,\,t) = \begin{cases} f_{I\!P/p}(\xi,\,t) & \text{if } N(s) \le 1, \\ \dfrac{f_{I\!P/p}(\xi,\,t)}{N(s)} & \text{if } N(s) > 1, \end{cases} \tag{2.7}$$

$$\text{where}\quad N(s) = \int_{\xi_{min}}^{\xi_{max}}\int_{-\infty}^{0} f_{I\!P/p}(\xi,\,t)\,d\xi\,dt, \tag{2.8}$$

where usually $\xi_{min} = M_0^2/s$ with $M_0 = 1.5\,\mathrm{GeV}^2$ (effective threshold) and $\xi_{max} = 0.1$ (coherence limit) [4]. With this renormalization, the single diffractive cross section is kept below the total cross section at all energies. The normalization factor $N(s)$ depends on s since $\xi_{min} = M_0^2/s$. Also, the renormalized pomeron flux prediction is in good agreement with soft diffraction cross section data [4, 5].

2.2 Hard Diffraction

About 15 years ago, G. Ingelman and P.E. Schlein proposed a possibility of exploring the nature of the pomeron based on the production of high transverse momentum (p_T) jets in high mass diffraction [6]. In the diffractive process $\bar{p} + p \to \bar{p} + X$, they suggested that the exchanged pomeron could be probed by a process in which a hard scattering occurs between e.g., a gluon in the pomeron and a parton in the proton, and this type of event would give rise to high p_T jets produced opposite in rapidity the quasi-elastically scattered antiproton. Thus, such a diffractive process involving a large momentum transfer (Q^2) subprocess is regarded as *hard diffraction* [7]. It is worth noting that the *hard diffraction* and *diffractive hard scattering* are different processes [8]. The former is a process in which a momentum transfer across the rapidity gap due to an exchange of color singlet object (normally the pomeron) is small, but a high Q^2 subprocess occurs between the exchanged object and the other hadron. On the other hand, in the latter the color singlet object is exchanged with large momentum transfer across the rapidity gap.

In this section, we briefly describe about the original hard diffraction model proposed by Ingelman and Schlein. Since their proposal some important theoretical progress (e.g., Donnachie-Landshoff approach) has been made. After presenting them, we then describe experimental studies, in particular the recent results which are closely related to the motivation of this thesis.

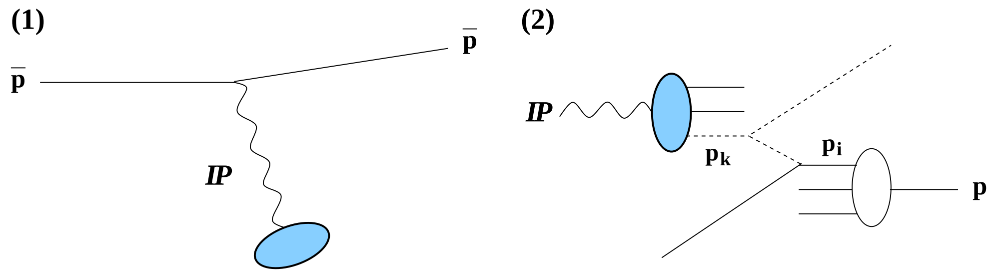

Figure 2.3: Diagrams of Ingelman-Schlein model for hard diffraction in single diffractive scattering: $\bar{p}+p \to \bar{p}+X$. (1) A pomeron ($I\!P$) is emitted from the $\bar{p}$. (2) A hard scattering occurs between a parton p_i in the proton and the other parton p_k (e.g., gluon) in the pomeron. The scattered two partons become jets, and the remaining partons form the spectator (beam) jets along the pomeron or proton directions.

2.2.1 Ingelman–Schlein Model

The basic idea which Ingelman and Schlein proposed [6] is that the exchange mechanism of the pomeron is the same for hard diffraction and traditional (soft) diffractive dissociation, and the pomeron consists of the constituent partons. Accordingly, the factorization property, which may be justified by the success of pomeron phenomenology in elastic and diffractive scattering, is assumed to be valid even in hard diffraction. For the process $\bar{p}+p \to \bar{p}+X$, this factorization based picture would naturally lead to the following two step reactions: 1) a pomeron is emitted from the antiproton with a small momentum transfer t, (Figure 2.3, left), then 2) the pomeron interacts with the proton between the partons at a large momentum transfer scale (Figure 2.3, right). Due to the assumed factorization property, they suggested that the hard diffraction cross section (e.g., σ_{SD}^{jj} for two jet production) could be expressed in terms of single diffractive cross section, σ_{SD}, as follows,

$$\frac{d^4\sigma_{SD}^{jj}}{dx_{I\!P}\,dt\,dx_1\,dx_2} = \left[\frac{1}{\sigma(pI\!P \to X)} \cdot \frac{d^2\sigma_{SD}}{dx_{I\!P}\,dt}\right] \cdot \frac{d^2\sigma(pI\!P \to jj+X)}{dx_1\,dx_2}, \tag{2.9}$$

where $x_{I\!P}$ is the momentum fraction of the pomeron to the antiproton, and t is the four momentum transfer squared, $\sigma(pI\!P \to X)$ is the proton-pomeron total cross section and $\sigma(pI\!P \to jj+X)$ is the proton-pomeron hard scattering cross section. The term in brackets stands for the pomeron flux factor $f_{I\!P/\bar{p}}(x_{I\!P},\, t)$, and it only depends on $x_{I\!P}$ and t. The remaining term $d^2\sigma(pI\!P \to jj + X)/dx_1\, dx_2$ is interpreted as the proton-pomeron hard scattering differential cross section depending on x_1 and x_2 that are the momentum fractions of the interacting partons p_i and p_k in the proton and pomeron respectively. The hard scattering cross section is therefore given as

$$\frac{d^3\sigma(pI\!P \to jj + X)}{dx_1\, dx_2\, d\hat{t}} = \sum_{i,k} f_{p_i/p}(x_1,\, Q^2) \cdot f_{p_k/I\!P}(x_2,\, Q^2) \cdot \frac{d\hat{\sigma}(ik \to jj)}{d\hat{t}}, \qquad (2.10)$$

in terms of the parton density functions of the proton $f_{p_i/p}(x_1,\, Q^2)$, and the pomeron $f_{p_k/I\!P}(x_2,\, Q^2)$, and the cross section for the parton subprocesses $d\hat{\sigma}(ik \to jj)/d\hat{t}$. In the original evaluations of Eq. (2.10), they assumed for the simplicity of calculation that the pomeron was a pure gluonic object and the momentum sum was kept unity by the gluons. Furthermore, the pomeron parton density function $f_{g/I\!P}$ was assumed to be independent of not only Q^2 but also t. They used the two functional forms for $f_{g/I\!P}$:

$$x\, f_{g/I\!P}(x) = 6x\,(1-x), \qquad (2.11)$$

$$x\, f_{g/I\!P}(x) = 6\,(1-x)^5. \qquad (2.12)$$

They were referred to as *hard gluon* (Eq. (2.11)) and *soft gluon* (Eq. (2.12)) structure functions respectively.

The pomeron flux factor which they assumed is a simple t-dependent form [6, 9] such as $(1/x_{I\!P}) \cdot (e^{5.6t} + 0.04e^{2t})$ in [6], obtained from the fit to single diffractive cross section data. The model with the above assumptions which they proposed is called the *Ingelman-Schlein model* or *IS model*. The parton distribution functions and exponential t dependence of the pomeron flux factor of original IS model are rather primitive and hence this model is unlikely to describe the recent data at Tevatron and HERA.

2.2.2 Donnachie–Landshoff Model

After the original IS model was proposed, A. Donnachie and P.V. Landshoff suggested another hard diffraction model [10] (called *Donnachie-Landshoff model* or *DL model*). The most significant differences between the DL model and the above IS model are the following two. First, the DL model is based on the assumption that the pomeron is dominantly made of quarks and antiquarks, in contrast to the IS model assuming the gluonic pomeron. Second, the momentum sum rule is not assumed in the DL model. The first assumption could be justified, at the time when they suggested, by the results of soft diffraction showing the similarity of the pomeron to the photon. However, we now know that the pomeron is presumably a *mixture* of the quarks and gluons as discussed later, so that the pomeron structures which the pioneers assumed are the extreme cases.

The DL model is characterized by the pomeron flux factor defined as

$$f_{I\!P/p}(x_{I\!P},\, t) \;=\; \frac{9\beta_0^2}{4\pi^2} \cdot \Big[F_1(t)\Big]^2 \cdot \left(\frac{1}{x_{I\!P}}\right)^{2\,\alpha_{I\!P}(t)-1}, \tag{2.13}$$

where $F_1(t)$ is the proton form factor, β_0 is the pomeron-quark coupling, and $\alpha_{I\!P}(t)$ is the pomeron Regge trajectory. The $F_1(t)$ is given by

$$F_1(t) \;=\; \frac{4m_p^2 - 2.8t}{4m_p^2 - t} \cdot \left(\frac{1}{1 - t/0.7}\right), \tag{2.14}$$

where m_p is the proton mass. From the fitting of soft diffraction data, they used the pomeron trajectory $\alpha_{I\!P}(t)$ given by

$$\alpha(t) = 1 + \varepsilon + \alpha' t, \quad \varepsilon \approx 0.085, \quad \alpha' = 0.25\,\mathrm{GeV}^{-2}. \tag{2.15}$$

As discussed later in experimental results, we find that the experimental diffractive rate at the Tevatron is about a factor 5 lower than the DL model prediction, so it is found that the original DL model does not completely work.

2.2.3 Renormalized Pomeron Flux Model

Recently, K. Goulianos proposed a possible model which describes experimental data, called *Renormalized Pomeron Flux model* or *RPF model* [4], which alters a pomeron flux normalization. As described in Section 2.1, it is based on a hypothesis that the pomeron flux factor integral cannot exceed unity and the renormalized pomeron flux factor given in Eq. (2.7) is introduced. The normalization factor $N(s)$ given in Eq. (2.8) is dependent of s because $N(s)$ is a function of ξ_{min}, so the flux factor normalization is process dependent. This means that the conventional Regge factorization breaks down.

In comparison with all available experimental data, the RPF model predictions are in good agreement with both soft and hard diffraction data in $\bar{p}p$ collisions at the Tevatron, and Deep Inelastic Scattering (DIS) in ep collisions at HERA [4, 11, 12, 13].

2.2.4 Hard Diffraction Experiments

The first experimental evidence for hard diffractive (jet) production was obtained by the UA8 experiment at the CERN $Sp\bar{p}S$ collider [14, 15]. They reported the observation of localized clusters with transverse energy $E_T > 8\,\mathrm{GeV}$ in $\bar{p}p$ collisions at $\sqrt{s} = 630\,\mathrm{GeV}$, and showed that their properties were in agreement with those of typical jets. From the information of two jet system which they observed, they estimated the structure of the pomeron being consistent with a hard parton density function like $x(1-x)$, with an additional 30 % "super-hard" components showing the δ-function like distribution at $x = 1$ (x is the momentum fraction of the pomeron carried by the interacting parton).

Recently the experiments at the Tevatron $\bar{p}p$ collider and the HERA ep collider reported a number of results on hard diffraction and the structure of the pomeron. The Tevatron has a clear advantage for achieving a high mass diffraction from its high center of mass energy collisions of the protons and antiprotons. The HERA with ep collisions can precisely measure the diffractive structure function of the proton over a wide kinematic range of Q^2 or $x_{I\!P}$ in electron-proton deep inelastic scattering (DIS) ‡. These new results will provide us the deep insight into the property of hard diffraction. In the analysis of this thesis, we often quote the results of hard diffraction at Tevatron, and so, to review recent results at the Tevatron should be instructive. After that, we discuss the status of Double Pomeron Exchange studies.

Fermilab Tevatron

Two Tevatron collider experiments at Fermilab, CDF and DØ, reported a number of results of hard diffraction in $\bar{p}p$ collisions at $\sqrt{s} = 1800\,\mathrm{GeV}$ and $630\,\mathrm{GeV}$. In particular, CDF experiment has done so far more detailed studies for the production of W boson, high transverse energy jets and bottom quark in diffractive events, and gave an estimate for the gluon content of the pomeron. One of the most striking features that CDF found is a breakdown of factorization at the Tevatron, compared with HERA results. In the following, the CDF results are reviewed.

Diffractive W Boson Production

One of the most important results at the Tevatron is a measurement of the diffractive W and dijet production at CDF. Particularly the observation of diffractive W boson is the first one at the Tevatron [16]. CDF measured the production rate of diffractive W decaying into an electron or positron: $p+\bar{p} \to p$ or $\bar{p}+W^{\pm}+X$ followed by $W^{\pm} \to e^{\pm}+\nu$. For events with a central e^- (e^+) with $|\eta^e| < 1.1$ and missing E_T greater than $20\,\mathrm{GeV}$, the ratio of diffractive to non-diffractive W production was measured to be

$$R_W = [1.15 \pm 0.51(stat.) \pm 0.20(syst.)]\,\%,$$

for $\xi < 0.1$.

Diffractive Dijet Production

CDF made a search for diffractively produced dijets at $\sqrt{s} = 1800\,\mathrm{GeV}$: $p + \bar{p} \to p$

‡This measurement contains not only the hard but also soft kinematic regime. So it should be referred to as *inclusive* diffraction.

or $\bar{p} + jet1 + jet2 + X$ [17]. For events with forward dijets with $E_T^{jet} > 20\,\mathrm{GeV}$ and $1.8 < |\eta| < 3.5$, the ratio of diffractive to non-diffractive dijet production was obtained to be

$$R_{JJ} = [0.75 \pm 0.05(stat.) \pm 0.09(syst.)]\,\%,$$

for $\xi < 0.1$.

Diffractive Beauty Quark Production

CDF extended the study of hard single diffraction to the beauty (b) quark production. The process in which the diffractively produced b quark decays into a high p_T electron: $p + \bar{p} \to p$ or $\bar{p} + b + X$ followed by $b \to e + X'$, was measured [18, 19]. For a sample of high E_T central electron events with an electron $9.5 < E_T^e < 20\,\mathrm{GeV}$ and $|\eta^e| < 1.1$, the ratio of diffractive to total beauty quark production was measured to be

$$R_b = [0.62 \pm 0.19(stat.) \pm 0.14(syst.)]\,\%,$$

for $\xi < 0.1$.

In general, diffractive W and dijet production are primarily sensitive to the quark and quark/gluon contents of the pomeron ,respectively. This indicates that we can estimate the fraction of the gluon (or quark) component in the pomeron by combining the rates of diffractive W and dijet. Beauty quark production predominantly occurs through $gg \to Q\bar{Q}$ so it is also a probe to the gluon content of the pomeron. We define the discrepancy factor D by the ratio of measured to predicted diffractive rates as a function of the gluon fraction of the pomeron f_g. Figure 2.4 shows D for diffractive W, dijets and beauty quark productions. The predicted rates were obtained using the POMPYT Monte Carlo [56] with the Donnachie-Landshoff pomeron flux and a hard structure of the pomeron. $D = 1$ means that the factorization holds good for the pomeron flux. The bands for each measurement, CDF-W, CDF-DIJET and CDF-b, correspond to $\pm 1\sigma$ values of the measurements. The results of ZEUS measurements for diffractive DIS and photoproduction rates [20] are also shown. Using the CDF three measurements, we obtained the gluon fraction $f_g^{CDF} = 0.54^{+0.16}_{-0.14}$ and $D_{CDF} =$

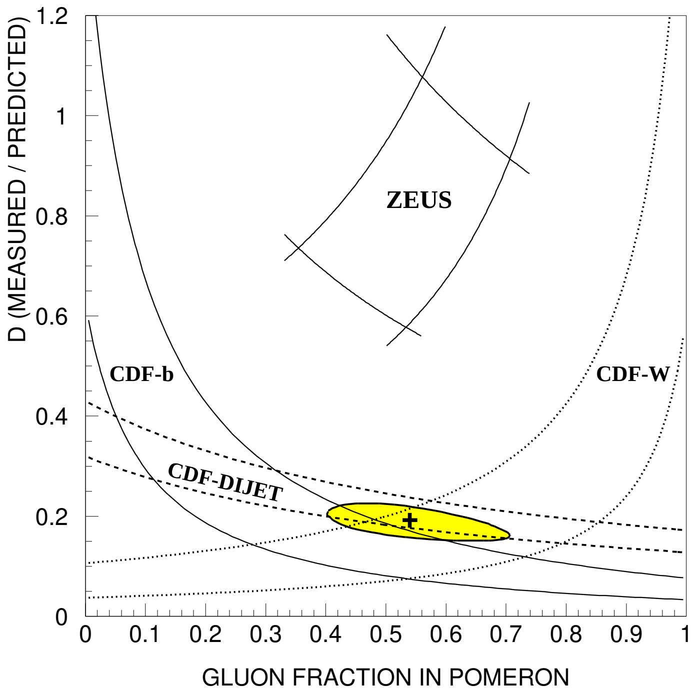

Figure 2.4: The ratio of measured to predicted diffractive rates, D, versus the gluon fraction of the pomeron, f_g. The predicted rates were obtained using the POMPYT with the Donnachie-Landshoff pomeron flux and a hard structure of the pomeron. The CDF-W curves were calculated assuming three flavor quarks for the pomeron. A least square two-parameter fit result to the three CDF measurements is shown as the black cross of the best fit and shaded ellipse of 1σ contour.

0.19 ± 0.04 [18]. In the estimation of f_g^{CDF} and D_{CDF}, a least square two-parameter fit was done for the three CDF results, and the best fit and 1σ contour is shown as the black cross and shaded ellipse in the figure. The range of f_g^{CDF} is in agreement with the ZEUS measurement $0.3 < f_g < 0.8$, but the value of D_{CDF} is much smaller than the ZEUS result. This significant discrepancy between the CDF and ZEUS measurements indicates that the factorization is not valid at the Tevatron.

The Renormalized Pomeron Flux model successfully describes this rate discrepancy between the HERA and the Tevatron. Assuming that the rapidity gap probability (equivalent to the flux ξ distribution) scales to the total gap probability (equivalent to the flux ξ distribution integrated over all available phase space), the ratio of scaling factors (corresponding to $N(s)$ in Eq. (2.8)) at HERA to the Tevatron is obtained to be 0.19 [11]. This is in excellent agreement with the measured rate discrepancy $D_{CDF} = 0.19 \pm 0.04$ [18]. This scaling of the rapidity gap probability is equivalent to the renormalization of the pomeron flux factor [11, 12, 13].

Diffractive Dijet Production with a Tagged Leading Antiproton

New CDF results on hard diffractive dijets were obtained using a technique of tagging a forward antiproton scattered in diffractive interactions at $\sqrt{s} = 1800\,\mathrm{GeV}$ and $630\,\mathrm{GeV}$ [64, 65]. In diffractive events with a leading antiproton with $0.035 < \xi < 0.095$ and $|t| < 1.0\,\mathrm{GeV}^2$, the production of dijets with $E_T > 7\,\mathrm{GeV}$ was observed.

One of the most interesting results from the above measurements is a measurement of the diffractive structure function of the antiproton. In the hard diffraction model proposed by Ingelman and Schlein [6], the diffractive dijet production cross section is given by Eqs. (2.9) and (2.10). The term in brackets of Eq. (2.9) represents the pomeron flux factor $f_{I\!P/\bar{p}}(x_{I\!P}, t)$. We denote the momentum fractions of the interacting partons p_i and p_k in the proton and pomeron by x and β, and the diffractive dijet production cross section is then written as

$$\frac{d^5\sigma_{SD}^{jj}}{d\xi\, dt\, dx\, d\beta\, d\hat{t}} = f_{I\!P/\bar{p}}(\xi, t) \cdot \sum_{i,k} f_{p_i/p}(x, Q^2)\, f_{p_k/I\!P}(\beta, Q^2)\, \frac{d\hat{\sigma}(ik \to jj)}{d\hat{t}}, \qquad (2.16)$$

where the momentum fraction of the pomeron to the antiproton is denoted by ξ instead of $x_{I\!P}$. By defining the diffractive structure function $F^D_{p_k/\bar{p}}(\xi, t, \beta, Q^2)$ of the antiproton as

$$F^D_{p_k/\bar{p}}(\xi, t, \beta, Q^2) \equiv f_{I\!P/\bar{p}}(\xi, t) \cdot f_{p_k/I\!P}(\beta, Q^2), \qquad (2.17)$$

Eq. (2.16) is written as

$$\frac{d^5\sigma_{SD}^{jj}}{d\xi\, dt\, dx\, d\beta\, d\hat{t}} = \sum_{i,k} f_{p_i/p}(x, Q^2) \cdot F^D_{p_k/\bar{p}}(\xi, t, \beta, Q^2) \cdot \frac{d\hat{\sigma}(ik \to jj)}{d\hat{t}}. \qquad (2.18)$$

In Eq. (2.17) the diffractive structure function is written as the product of $f_{I\!P/\bar{p}}(\xi, t)$ and $f_{p_k/I\!P}(\beta, Q^2)$. This property is called the factorization in the diffractive structure

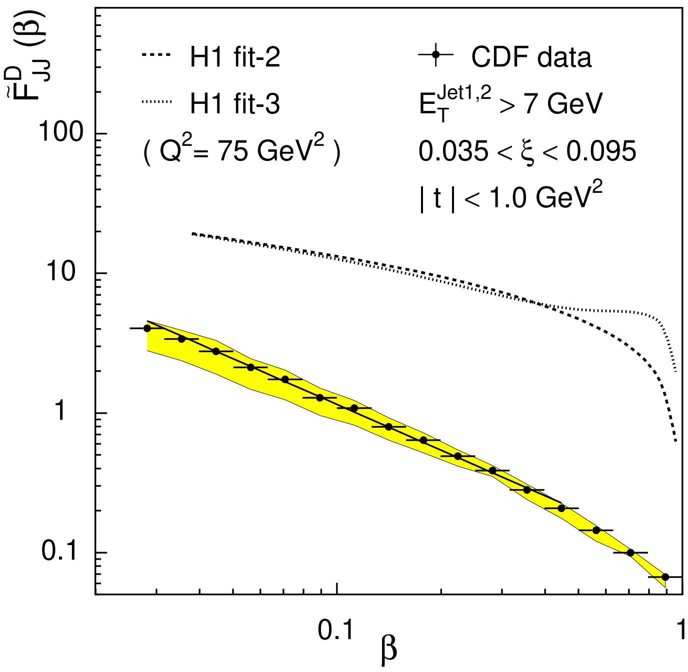

Figure 2.5: The integrated diffractive structure function $\tilde{F}^D_{jj}(\beta)$ $(= \tilde{F}^D_{p_k/\bar{p}}(\beta))$ of the antiproton as a function of β, compared with expectations (dashed and dotted lines) from the parton densities of the proton measured in diffractive deep inelastic scattering by H1 Collaboration. The solid line represents a fit to the data of the form β^{-n} in the range $(10^{-3}/\xi) < \beta < 0.5$. The shaded band surrounding the data points shows the systematic uncertainties of $\tilde{F}^D_{jj}(\beta)$ obtained from different number of jets included in β evaluation.

function. In the experiment of [64], the diffractive structure function of the antiproton integrated over the ξ, t and Q^2:

$$\tilde{F}^D_{p_k/\bar{p}}(\beta) \equiv \int d\xi \int dt \int dQ^2 \, f_{I\!P/\bar{p}}(\xi, t) \cdot f_{p_k/I\!P}(\beta, Q^2), \qquad (2.19)$$

was measured for the kinematical range $0.035 < \xi < 0.095$, $|t| < 1.0\,\mathrm{GeV}^2$ and $E_T^{jet} > 7\,\mathrm{GeV}$. The measured $\tilde{F}^D_{p_k/\bar{p}}(\beta)$ distribution is shown in Figure 2.5. The fit to the data of the form $B(\beta/0.1)^{-n}$ in the range $(10^{-3}/\xi_{min}) < \beta < 0.5$ gives $B = 1.15 \pm 0.01$ and $n = 1.09 \pm 0.01$ with $\chi^2/\mathrm{d.o.f.} = 2.2$ (the systematic uncertainty in B is ± 0.29). The measured $\tilde{F}^D_{p_k/\bar{p}}(\beta)$ differs in both shape and normalization from expectations of parton densities based on H1 measurements [21] of diffractive deep inelastic scattering. This discrepancy is interpreted as a breakdown of factorization.

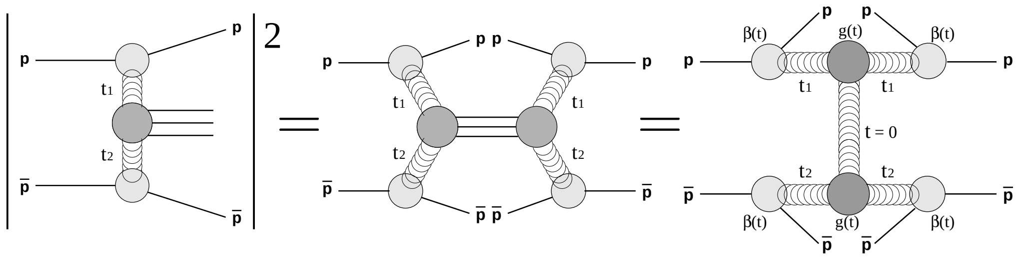

Figure 2.6: Diagrams for DPE cross section in $\bar{p}p$ collisions.

2.3 Double Pomeron Exchange

The DPE process in $\bar{p}p$ collisions is formulated as "doubly occurring single diffraction for both the p and $\bar{p}$ sides" based on factorization, so the DPE diagram is expressed as shown in Figure 2.6. The DPE cross section is therefore obtained in terms of the total and single diffraction cross sections as follows,

$$\frac{d^4\sigma_{DPE}^{\bar{p}p}}{d\xi_1\, d\xi_2\, dt_1\, dt_2} = \frac{1}{\sigma_T^{\bar{p}p}} \frac{d^2\sigma_{SD}^1}{d\xi_1\, dt_1} \frac{d^2\sigma_{SD}^2}{d\xi_2\, dt_2} \tag{2.20}$$

$$= \frac{1}{\sigma_T^{\bar{p}p}} f_{I\!P/p}(\xi_1,\, t_1)\, f_{I\!P/\bar{p}}(\xi_1,\, t_1)\, \sigma_T^{I\!Pp}(s_1',\, t_1)\, \sigma_T^{I\!P\bar{p}}(s_2',\, t_2) \tag{2.21}$$

$$= \frac{(\sigma_0^{I\!Pp})^2}{\sigma_0^{\bar{p}p}} f_{I\!P/p}(\xi_1,\, t_1)\, f_{I\!P/\bar{p}}(\xi_2,\, t_2) \left(\frac{s_1'\, s_2'}{s\, s_0'}\right)^{\varepsilon}. \tag{2.22}$$

In this derivation we use $\sigma_0^{I\!Pp} = \sigma_0^{I\!P\bar{p}}$ and assume $s_0 = s_0'$ because the energy scale should be process independent for a universal pomeron. What is of importance in this expression is the flux factor dependence of DPE cross section. From the form of Eq. (2.22), we expect that the DPE cross section at the Tevatron will be a factor D_{CDF}^2 lower than the standard Donnachie-Landshoff flux predictions because the flux factor dependence of DPE event is doubly increased, compared to (single) hard diffraction where the discrepancy of D_{CDF} is observed.

The first experimental evidence for Double Pomeron Exchange was obtained in proton-proton interactions at the CERN Intersecting Storage Rings (ISR) [23]. The process $p + p \to p + p + X$ was studied in the kinematical range where the reaction mechanism is expected to be dominated by DPE. In particular, the exclusive reaction

$p + p \to p + p + \pi^+ + \pi^-$ with $0.01 \le |t| \le 0.06\,\mathrm{GeV}^2$ and $x_F \ge 0.95$ at $\sqrt{s} = 63\,\mathrm{GeV}$ was investigated in detail [24], and used for a glueball search, because glueballs may be produced by this reaction if the pomeron has a dominant gluonic structure at low Q^2.

However, from the point of view of multi-particle production and high p_T processes, it is of interest to study this reaction at higher $\sqrt{s}$ energies. The mass M of a system X is given by

$$M^2 = s\,(1 - x_{F1})(1 - x_{F2}), \tag{2.23}$$

so that the cluster mass at the ISR is only around $3\,\mathrm{GeV}$ even at the maximum c.m. energy of $\sqrt{s} = 63\,\mathrm{GeV}$ for $x_F > 0.95$ where the pomeron exchange is dominant.

At the CERN $p\bar{p}$ collider with $\sqrt{s} = 630\,\mathrm{GeV}$ where the cluster mass reaches about $30\,\mathrm{GeV}$ for $x_F > 0.95$, Double Pomeron Exchange process was studied using the UA1 detector [3]. In this experiment, a calorimeter trigger was used to select events in which a central cluster was separated from the outgoing proton and antiproton by large rapidity gaps. The requirement that an energy deposition in the forward region $3 < |\eta| < 6$ is consistent with zero was used to select events with rapidity gaps on both sides. In addition, an energy deposition above a low threshold in the central calorimeter was required. In a sample of obtained 33,000 events after event reconstruction and background removal, they observed events with jets with $E_T > 10\,\mathrm{GeV}$. However, it was not conclusively demonstrated that the observed events were real DPE events, despite of requiring the rapidity gaps for both sides in the trigger. The mass M of a central cluster which they observed covers the range $10 < M < 70\,\mathrm{GeV}$, so that the high mass data would have large non-DPE background. Furthermore, their calorimeter triggers would bias the accepted events towards higher mass and higher central activity than unbiased and pure DPE events.

The UA8 collaboration also reported a measurement of Double Pomeron Exchange at the CERN $p\bar{p}$ collider with the same c.m. energy [25]. Using the UA2 detector and the forward spectrometers which measured the recoil p and $\bar{p}$ in the region $1 < |t| <$

$2\,\text{GeV}^2$, they obtained the events being consistent with the Double Pomeron Exchange process. In their analysis, the presence of jets was not explicitly required. The average mass of the clusters in triggered events was about $3\,\text{GeV}$, and they gave a preliminary estimate of a cross section for this process to be 30–150 μb.

In the CDF experiment described in this thesis, we tagged a diffractively scattered antiproton with the forward spectrometer, and required the presence of 2 or more jets with $E_T > 7\,\text{GeV}$. We then required a rapidity gap on the outgoing proton side to select DPE dijet production events.

Chapter 3

Experimental Setup

The Tevatron of Fermi National Accelerator Laboratory (FNAL or Fermilab), which is the most powerful accelerator in the world, can accelerate the protons and antiprotons up to 900 GeV. The resulting center of mass energy in proton-antiproton collisions is 1.8 TeV. The accelerator complex of the Tevatron is described in Section 3.1. In addition to the accelerator, the detector which measures the particles from the interaction region is also essential for particle physics. The main experimental facility of this study is the detector named "the Collider Detector at Fermilab (CDF)". The CDF detector has been described in detail elsewhere [26, 27]. In Section 3.2 the CDF detector components that play important roles in diffractive physics are described. In addition, the new detectors installed and used in this experiment are also explained.

3.1 The Tevatron Accelerator Complex

The Tevatron is the superconducting synchrotron which has the ability of accelerating the protons and antiprotons up to the energy of 900 GeV. The 1.8 TeV center of mass energy in $\bar{p}p$ collisions is the highest energy for all the accelerators in the world.

The collision at the CDF occurs after a sequence of accelerations for the protons and antiprotons [28]. Figure 3.1 shows the flow of the acceleration processes for the protons and antiprotons in the Tevatron accelerator complex at Fermilab. Creation of

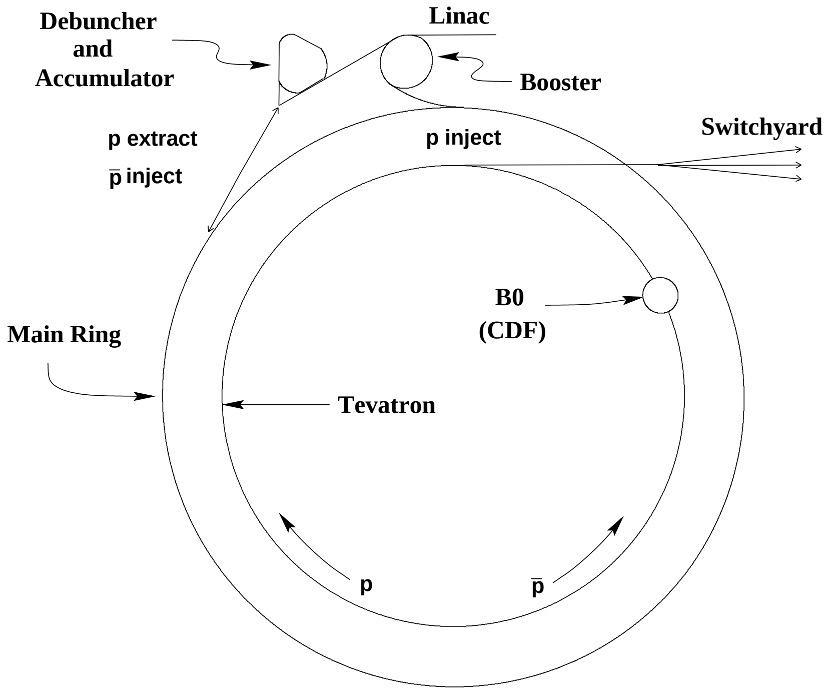

Figure 3.1: Accelerator complex in Fermilab.

the proton beam starts from the hydrogen gas. Passing the gas through the Magnetron which consists of an oval-shaped cathode surrounded by an anode, the negatively charged hydrogen ions are produced. Produced hydrogen ions are extracted through an anode, then accelerated in the Cockcroft-Walton pre-accelerator up to the energy of 750 KeV and passed through a linear accelerator called the Linac.

The Linac is a linear accelerator in which the negative hydrogen ions are accelerated up to 400 MeV. The Linac system includes a 116 MeV drift-tube (Alvarez) linac operating at 201.25 MHz for RF frequency, and a 400 MeV side-coupled cavity linac operating at 805 MHz. The hydrogen ions are then transferred to the Booster from the Linac. The Booster is a rapid cycling proton synchrotron, which raises the energy of protons up to 8 GeV. The transferred ions into the Booster are merged with any protons already in the Booster, then are passed through a carbon foil which removes the two electrons. The protons after stripped off the electrons are stored and accelerated in the Booster.

The Main Ring is a proton synchrotron with the circumference of about 6 km. During the operation with colliding beams, the Main Ring functions: 1) as a 150 GeV accelerator of the protons and antiprotons and an injector to the Tevatron, and 2) as a 120 GeV proton source used to produce the antiprotons. The protons injected from the Booster and the antiprotons from the Accumulator (described below) at 8 GeV energy are accelerated to 150 GeV, and the several bunches are combined into one to maximize the number of protons ($\sim 10 \times 10^{10}$) or antiprotons ($\sim 5 \times 10^{10}$) in a beam bunch. The antiprotons are produced in a system of fixed target, the Debuncher and the Accumulator. Extracting 120 GeV protons from the Main Ring, then colliding them with a fixed target (Nickel plate), a lot of secondary particles with positive or negative charge are produced over a wide range of the momentum. From the secondaries, negatively charged particles with about 8 GeV momentum are collected in the Debuncher. Then, the collected antiprotons are cooled down so as to store in the Accumulator for later use in the Tevatron. About one antiproton is produced for every striking of 10^5 protons to the target. This process continues until sufficient antiprotons are stored for later injection into the Main Ring. About 5×10^{10} antiprotons are made per hour. As mentioned above, the antiprotons injected into the Main Ring from the Accumulator are accelerated to 150 GeV.

The Tevatron is a proton-antiproton superconducting synchrotron which accelerates the protons and antiprotons to 900 GeV energy. For Run 1, the Tevatron was operated with counter-circulating six bunches of the protons and six bunches of the antiprotons. The bunch crossing frequency during six bunch operation was about 286 kHz. The number of possible collision points at the Tevatron is six at the maximum, and they are called A0, B0, ..., F0. The CDF detector is at B0, and the other collider detector is at D0 (The D0 detector). These two detectors are multi-purpose collider detectors designed to study the high energy proton-antiproton interactions at the Tevatron.

3.2 The CDF Detector

A schematic drawing of the major detector components is shown in Figure 3.2. As seen in the figure, the CDF detector is a forward-backward and azimuthally symmetrical detector surrounding the interaction point of the protons and antiprotons [27].

3.2.1 CDF Coordinate System

Before describing the overview of the CDF detector, it is worth showing the coordinate system used in CDF. CDF uses basically the right-handed Cartesian coordinate system given by (x, y, z). The origin is at the center of the detector and it is also nominally the interaction point in $\bar{p}p$ collisions. The beam axis is taken as the z axis, and the proton direction is regarded as positive z direction. The x (y) axis is defined as the direction pointing horizontally outwards (vertically upward). Also, note that a positive z direction (proton direction) is called "East" which is frequently used in the thesis. Accordingly the negative z direction is called "West". In addition to this coordinate system, the cylindrical coordinate system (r, θ, ϕ) is often used to describe the detectors and the characteristics of the particles nominally produced from the origin. The distance, r, is measured from the z axis. The polar angle, θ, is defined as the angle measured from the positive z axis, and the azimuthal angle, ϕ, is measured anti-clockwise from the positive x axis. The coordinate system used in CDF is shown in the inset of Figure 3.3.

3.2.2 Physical Quantities in Collider Physics

Rapidity y and Pseudorapidity η

In a collider physics, the quantity called *rapidity*, y, is frequently used instead of the polar angle. The rapidity of the particle is defined as

$$y \equiv \frac{1}{2} \ln \left(\frac{E + p_z}{E - p_z} \right). \tag{3.1}$$

The particle density in rapidity space, dN/dy, is invariant under the Lorenz boost along the z axis because the rapidity transforms as $y \to y + \tanh^{-1}\beta$ where $\beta = p/E$ and p and E are the momentum and energy of the particle. For relativistic particles (i.e., $p \gg mc$), the rapidity is well approximated by the *pseudorapidity*, η, given by

$$\eta \;=\; -\,\ln\tan\left(\frac{\theta}{2}\right). \tag{3.2}$$

The pseudorapidity is also approximately invariant under the Lorentz boost in the case $p \gg mc$. An obvious advantage of using a pseudorapidity rather than a rapidity is that it can be defined to the particle whose mass is unknown, and it allows us to measure the direction of the particle using the detector.

In the analysis of experimental data, we often use the two forms of pseudorapidity: 1) the detector η and 2) the event η. The former is measured from the center of the detector (nominal $\bar{p}p$ interaction point), and the latter is measured from the actual $\bar{p}p$ interaction point along the z axis for every event. The z position of $\bar{p}p$ collisions (called Z_{vertex}) does not exactly match with $z = 0$, but it is well approximated by the Gaussian distribution with $\sigma_z \sim 30\,\mathrm{cm}$ because the beam bunches have a similar Gaussian longitudinal profile of 30 cm.

Transverse Energy E_T

The *transverse energy*, E_T, with respect to the incident beam direction is important because it is not only a Lorentz invariant quantity but also a measure for the hardness of the interaction. It is defined as

$$E_T \;\equiv\; E\,\sin\theta, \tag{3.3}$$

where E is the energy of the cluster or the particle, and θ is the polar angle of the energy center of the cluster (particle). The *transverse momentum*, p_T, is also defined as the similar form : $p_T \equiv p\sin\theta$. Both quantities can be defined for the tracks or the jets (energy clusters), but the E_T for the clusters is usually measured by the calorimeter while the p_T for the charged tracks is measured by the tracking detector surrounded by the calorimeter in CDF.

Missing Transverse Energy $\not\!\!E_T$

In $\bar{p}p$ collisions we expect that a large fraction of the longitudinal momentum escapes outside the detector coverage towards the forward regions. This would lead to an imbalance of the longitudinal momentum when summing up all the momenta of the particles observed in the detector. However, the transverse momentum and energy should balance if we observe all the particles by the detector. An imbalance of the transverse energy indicates that a portion of the particles escapes out of the detector through the uninstrumented area ("cracks"). Several particles such as neutrinos or muons, hardly leave the trace in the calorimeter, therefore they could also become the source of the imbalance. The missing transverse energy which is a measure of the imbalance is defined as the transverse counter-vector for the sum of all visible transverse energy measured within the calorimeter:

$$\vec{\not\!\!E_T} \equiv -\sum_i \vec{E}_{Ti}. \tag{3.4}$$

In the analysis, we require that the $\not\!\!E_T$ is not significantly large for every event in order to ensure that the imbalance coming from the detector cracks or the noises is small.

3.2.3 CDF Detector Overview

The CDF detector is shown in Figure 3.2 for three dimensional view, and in Figure 3.3 for the cross section view of a quarter section. The basic design goal for the CDF detector is to measure the energy and momentum of the particles, and identify (where possible) them produced in $\bar{p}p$ collisions at the Tevatron, for as a wide solid angle as possible around the interaction region. For this purpose, the detector was designed to surround the interaction region by the detector layers and the subsystems each of which has a particular task (A detector with 4π coverage, called Full Acceptance Detector, is an ideal detector).

From the most inner region, close to the $\bar{p}p$ collisions, a beam pipe made up of

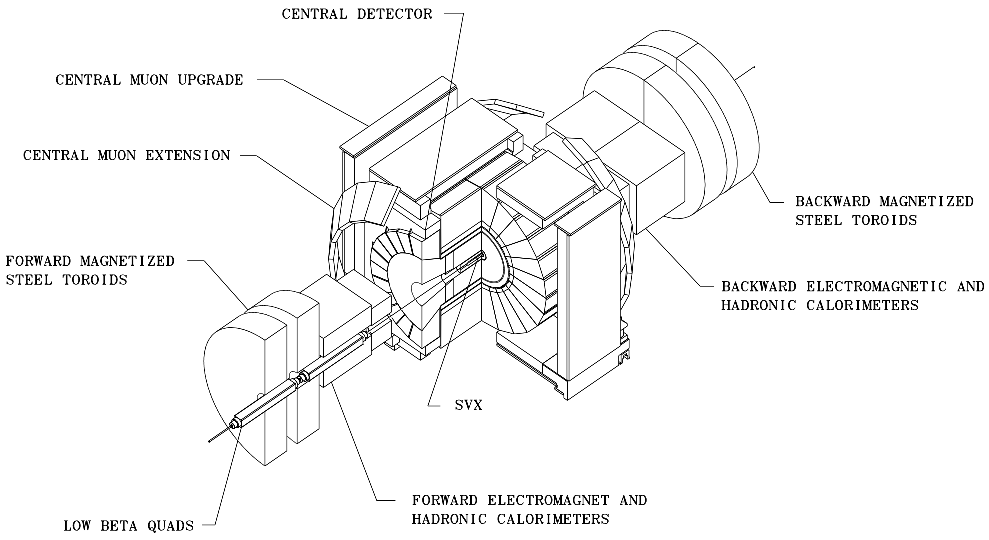

Figure 3.2: An isometric view of the main CDF detector components.

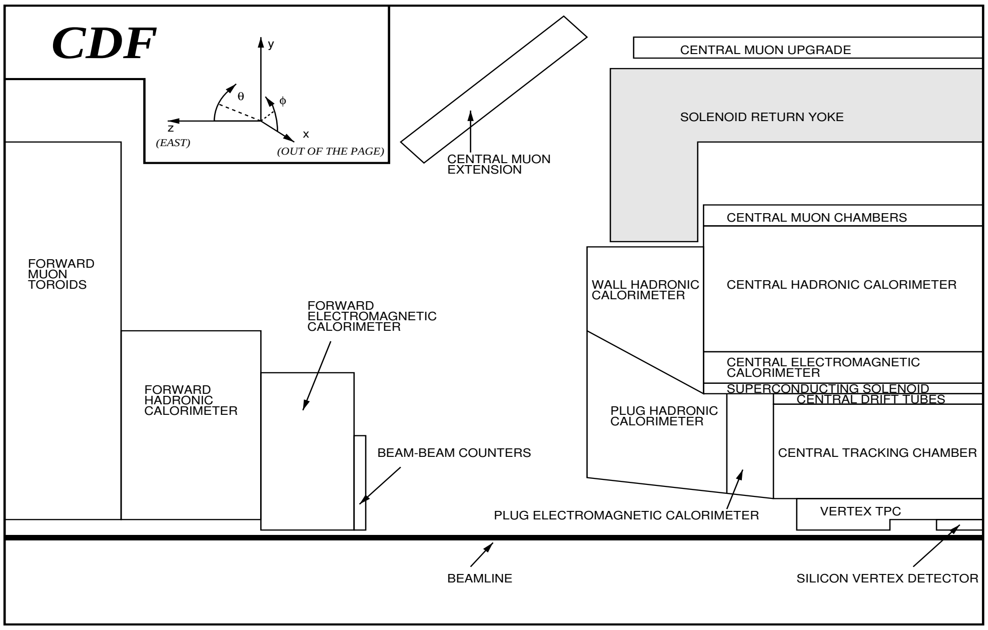

Figure 3.3: A quarter view of the cross section of the CDF detector.

Be, tracking chambers, magnet, calorimetries, muon detectors are equipped. The tracking chambers for charged particles should be minimized in volume of the material to reduce the multiple interaction which becomes possible background source for the detectors behind them. A superconducting magnet surrounding the tracking detectors gives a magnetic field, which enables us to measure the charge and momentum of the particles. The calorimeters which are behind the tracking chambers are used to measure the energy of both charged and neutral particles which make the showers in a large mass volume of the calorimeter and deposit their energies. A "jet" (a bulk of the particles traveling to the same direction) is measured using the calorimeter by making an energy cluster from the energies deposited in the calorimeter towers. So as to measure the energy flow in uniform pseudorapidity and azimuthal angle bins, the calorimeter tower has a projective geometry pointing the nominal interaction point. The muon chambers outside the calorimeters detect the muons which can easily pass the calorimeters without leaving any trace.

In the analysis, the calorimeter plays an important role. It is essential for the search for the rapidity gap signal in events, jet reconstruction and the measurement of the total system produced in Double Pomeron Exchange event. One of the tracking chambers, vertex detector (VTX), is also used to get the vertex from the $\bar{p}p$ collisions. Another important detector to search for a forward rapidity gap is a Beam-Beam Counter. It is a scintillator hodoscope placed in front of the forward calorimeter. Descriptions of these detectors which are relevant in the analysis are given below.

3.2.4 Vertex Detector

The Vertex Detector (VTX) [29] is a gas drift chamber surrounding the Silicon Vertex Detector (SVX) along the beam axis. The VTX has an outer radius of 22 cm and the pseudorapidity coverage of the VTX is $|\eta| < 3.5$. A longitudinal view of the VTX is shown in an event display of Figure 3.4. As seen in the figure, the VTX consists of 28 modules attached end-to-end along the z axis. Each module is divided into two

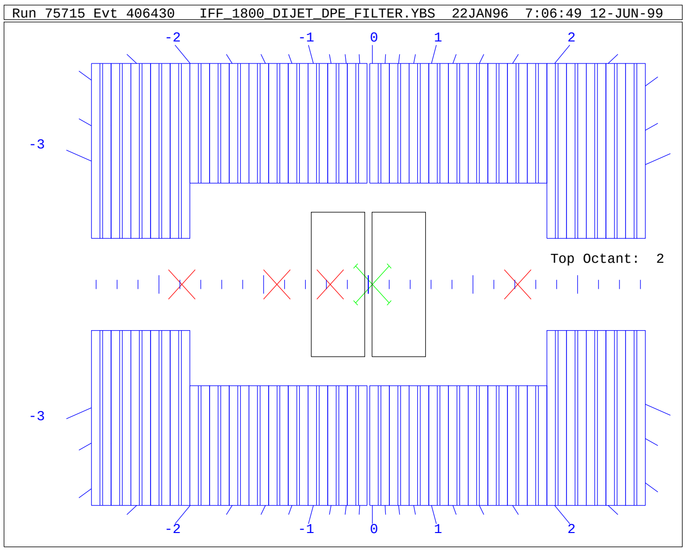

Figure 3.4: A longitudinal view of the VTX on an event display. The beam line passes horizontally through the center of the picture. The crosses along the center line represent the vertices found by the VTX. The cross with the bars at the ends shows a primary vertex with the highest multiplicity of the track. Numbers on top and bottom of the VTX (-3:3) are the event pseudorapidities measured to the position of a primary vertex.

drift regions by a central high voltage grid. In azimuth a module is segmented into 8 wedges, each of which has the coverage of 45°. For each wedge, 24 pairs of sense wires are arranged azimuthally for the 10 end modules (bigger ones), and 16 pairs are arranged azimuthally for the 18 inner modules (smaller ones). Main functions of the VTX are to provide precise tracking information for charged particles in the r-z plane, and to measure the vertex position along the z axis. It is also used to find the seed for the three dimensional reconstruction of the track in the Central Tracking Chamber (CTC). The VTX has been designed for the amount of a material to be minimized to reduce secondary interactions causing the background, such as the photon conversion electrons ($\gamma \to e^+e^-$).

3.2.5 Calorimetry

The CDF calorimetry is split into electromagnetic (EM) and hadronic (HAD) components, and furthermore it is partitioned into four detector regions defined by the pseudorapidity coverage : the central EM and HAD ($|\eta| <\sim 1.0$), the End-Wall HAD ($0.7 < |\eta| < 1.3$), the Plug EM and HAD ($\sim 1.2 < |\eta| < 2.4$), and the Forward EM and HAD ($\sim 2.2 < |\eta| < 4.2$) calorimeters [27]. They are often abbreviated to CEM, CHA for the central, WHA for the End-Wall, PEM, PHA for the plug, and FEM, FHA for the forward calorimeters. The CEM contains a central strip chamber (CES) which measures the transverse shower profile at the depth where the longitudinal shower development becomes maximum on average. These calorimeter components except the CES are summarized in Table 3.1 for the pseudorapidity coverage, energy and position resolutions, and the thickness.

All the CDF calorimeters are sampling calorimeters with the absorber (lead or steel) interleaved with the layers of active media. The central and plug/forward calorimeters use the different active media (described later). All the calorimeters use a "tower" geometry with the approximately constant segmentation for the pseudorapidity and azimuthal angle. The tower structure is projective, i.e., each tower points back to the center of the detector. Each tower has an electromagnetic shower counter in front of a corresponding hadronic calorimeter, so that the comparison between EM and hadronic energy depositions on a tower-by-tower basis enables us to identify the electrons, photons and hadrons. In addition, the electromagnetic shower counters have a precise spatial resolution of about 2 mm over the entire solid angle coverage.

The tower segmentation and the coverage of the calorimeters in one of eight identical $\eta - \phi$ quadrants ($\eta > 0$, $0° < \phi < 90°$) is shown in Figure 3.5. The size ($\eta \times \phi$) of each tower is $0.1(\eta) \times 15°(\phi)$ in the central/wall calorimeters, and $0.1(\eta) \times 5°(\phi)$ in the plug/forward calorimeters. Therefore, the physical size of a tower ranges from about $24\,\mathrm{cm}\,(\eta) \times 46\,\mathrm{cm}\,(\phi)$ in the central region to $1.8\,\mathrm{cm}\,(\eta) \times 1.8\,\mathrm{cm}\,(\phi)$ in the forward region.

Table 3.1: A summary of the CDF calorimeter information. The symbol $\oplus$ means that the energy dependent term and the constant systematic term are added in quadrature. E_T is in units of GeV. Thickness of each calorimeter component is given in units of X_0 (*radiation length*) for the EM calorimeters, and λ_0 (*interaction length*) for the Hadron calorimeters.

	$\|\eta\|$ coverage	Energy Resol. σ/E	Position Resol. [cm^2]	Thickness
Central				
EM	0 – 1.1	$13.5\,\%/\sqrt{E_T} \oplus 1.7\,\%$	0.2×0.2	$18\,X_0$
HAD	0 – 0.9	$75\,\%/\sqrt{E_T} \oplus 3\,\%$	10×5	$4.5\,\lambda_0$
End-Wall				
HAD	0.7 – 1.3	$75\,\%/\sqrt{E_T} \oplus 3\,\%$	10×5	$4.5\,\lambda_0$
Plug				
EM	1.1 – 2.4	$28\,\%/\sqrt{E_T} \oplus 2\,\%$	0.2×0.2	$18 - 23\,X_0$
HAD	1.3 – 2.4	$130\,\%/\sqrt{E_T} \oplus 4\,\%$	2×2	$5.7\,\lambda_0$
Forward				
EM	2.2 – 4.2	$25\,\%/\sqrt{E_T} \oplus 2\,\%$	0.2×0.2	$25\,X_0$
HAD	2.3 – 4.2	$130\,\%/\sqrt{E_T} \oplus 4\,\%$	3×3	$7.7\,\lambda_0$

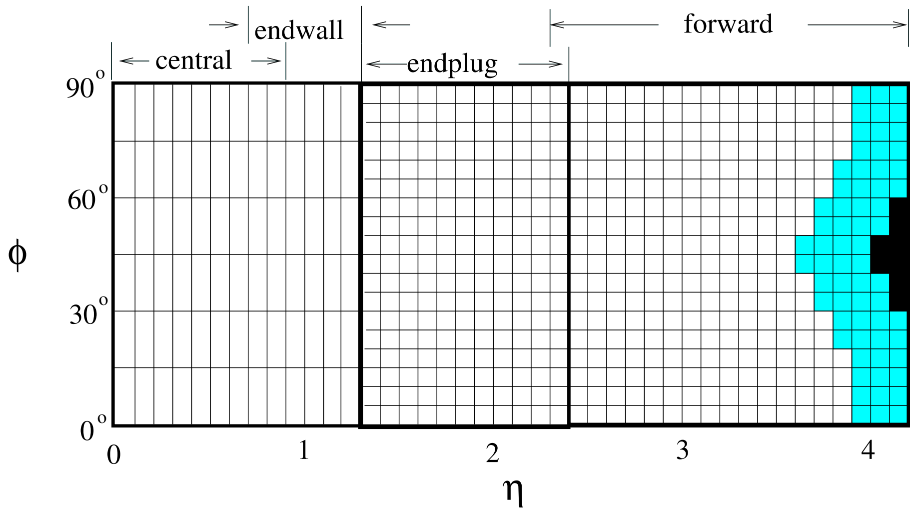

Figure 3.5: Projective tower structure of the calorimeter. Gray towers have only partial depth coverage due to overlapped low beta quadrapoles. Black towers around $\phi = 45°$ have no coverage.

Central Electromagnetic Calorimeter (CEM)

The electromagnetic part of the central calorimeter, Central Electromagnetic Calorimeter (CEM) [30], has the coverage of $|\eta| < 1.1$ in pseudorapidity and full 2π coverage in azimuth (all the calorimeters basically have full coverage in ϕ, so only the η coverage is given for the following calorimeters). The size of a tower is $0.1(\eta)\times 15°(\phi)$. The geometrical inner (outer) radius of the CEM is 173 cm (208 cm), and the thickness is 18 radiation lengths. The CEM consists of 31 layers each of which has 3.2 mm thick lead absorber interleaved with 5 mm thick polystyrene scintillator plate. Through the two wavelength shifters per tower, the scintillation light is directed to the photomultiplier tubes.

The energy resolution of the CEM was obtained using the test beams of electrons. By changing the electron energy from 10 to 100 GeV, it was estimated to be

$$\frac{\sigma(E)}{E} = \frac{13.5\,\%}{\sqrt{E_T}} \oplus 2\,\%,$$

where E_T is in units of GeV and the symbol $\oplus$ means that the two terms are added in quadrature. Initially the towers of the CEM were calibrated with 50 GeV electrons.

Central and End-Wall Hadron Calorimeter (CHA)

The Central Hadron Calorimeter (CHA) and End-Wall Hadron Calorimeter (WHA) [31] are the calorimeters for the hadronic particles such as charged pions, kaons. The pseudorapidity coverage is $|\eta| < 0.9$ for the CHA and $0.7 < |\eta| < 1.3$ for the WHA. The size of a CHA or WHA tower is the same as the CEM tower, $0.1(\eta)\times 15°(\phi)$, so that the first 9 towers are in the CHA, the intermediate 3 towers are shared with the CHA and WHA, and the last 3 towers are completely in the WHA. The CHA has 32 layers of 2.5 cm think steel absorber interleaved with 1.0 cm thick plastic scintillator. The WHA also has the similar structure: 15 layers of 5.0 cm thick steel absorber alternating with 1.0 cm thick plastic scintillator. The depth is 4.5 interaction lengths for both calorimeters.

Energy responses of the CHA and WHA were investigated with the beam of charged pions. For the energy range 10 – 150 GeV of the pion beams, the energy resolution of the CHA was obtained to be

$$\frac{\sigma(E)}{E} = \frac{75\,\%}{\sqrt{E_T}} \oplus 3\,\%.$$

It was found that the WHA also has the similar energy resolutions to the CHA.

Plug Electromagnetic Calorimeter (PEM)

The calorimeters which fit into the 30° holes like end caps, are called the plug calorimeters. As the central calorimeter, the plug calorimeter consists of the Plug Electromagnetic Calorimeter (PEM) [32] and the Plug Hadron Calorimeter (PHA) [33]. The coverage of the PEM is $1.1 < |\eta| < 2.4$ in pseudorapidity, corresponding to $36^\circ > \theta > 10^\circ$ in polar angle measured from the detector center. The PEM uses the gas proportional tubes (50 %-50 % mixture of argon-ethane with a small addition of the alcohol) as the active medium, interleaved with lead absorber. A quadrant with the azimuthal angle of 90° contains 34 layers of proportional tube arrays alternating with 2.7 mm think lead absorber layers. The PEM is segmented into 16 projective towers in η and the size in η is approximately 0.1 (although a few towers have small segmentation like 0.05). The full azimuth is segmented into 72 towers each of which has 5° in ϕ. Each tower has 3 segmentations in depth: the first 5 layers for the first, intermediate 20 layers for the second, and the last 5 layers for the third segments. The geometrical size of the PEM is 2.5 m in diameter and 50 cm in longitudinal depth. The path length from the center of the detector is about 18 – 23 radiation lengths depending on the polar angle.

The energy resolution was estimated with 20 – 200 GeV electron beams to be

$$\frac{\sigma(E)}{E} = \frac{28\,\%}{\sqrt{E_T}} \oplus 2\,\%.$$

All the towers of the PEM were calibrated with 100 GeV electrons.

Plug Hadron Calorimeter (PHA)

The PHA [33] has the coverage of $1.3 < |\eta| < 2.4$ in pseudorapidity. The PHA is also a gas calorimeter that consists of a sandwich of the gas tubes (active media) and the steel (absorber). We should note that the PHA is not continuously connected with the WHA, i.e., there is a "crack" at the interface of the PHA and WHA. The PHA consists of 20 layers of proportional gas tube arrays interleaved with 5.0 cm thick steel absorber. Each tower has the same segmentation, $0.1(\eta)\times 5^\circ(\phi)$, as the PEM.

The charged pions were used in the calibration of the PHA. By changing the energy from 20 to 230 GeV, the energy resolution was measured to be

$$\frac{\sigma(E)}{E} = \frac{130\,\%}{\sqrt{E_T}} \oplus 4\,\%.$$

The energy response was found to be linear within the above range.

Forward Electromagnetic Calorimeter (FEM)

The forward and backward regions with the small polar angle are covered by the Forward Electromagnetic Calorimeter (FEM) [34] followed by the Forward Hadron Calorimeter (FHA) [35]. The FEM has the coverage $2.2 < |\eta| < 4.2$ in pseudorapidity, or $12^\circ > \theta > 2^\circ$ in polar angle. Note that there is a crack between the plug and forward calorimeters in pseudorapidity, but the azimuthal direction is basically fully covered. The FEM is a sampling calorimeter with 30 layers of gas proportional tubes interleaved with 4.8 mm thick absorber made up of 96 % lead and 6 % antimony (Sb). The projective tower has two segmentations in depth, each of which has the thickness of 15 layers. The η segmentation of the FEM is 20 and each tower has the size of 0.1 in η except for the first tower with 0.03. The azimuthal segmentation is the same as the Plug calorimeters, 5° in ϕ. The FEM is located about 6.5 m from the nominal interaction point along the z axis and has the longitudinal depth of 1 m which approximately corresponds to 25 radiation lengths.

Calibrating the individual towers in the FEM with 20 – 200 GeV electron beams, the energy resolution was estimated to be

$$\frac{\sigma(E)}{E} = \frac{25\,\%}{\sqrt{E_T}} \oplus 2\,\%.$$

The linearity of the response to the incident energy was also obtained for the range 20 – 160 GeV.

Forward Hadron Calorimeter (FHA)

The FHA [35] is a calorimeter which measures the hadronic energy, placed behind the FEM in the small angle region. The coverage is $2.3 < |\eta| < 4.2$ in pseudorapidity, which corresponds to $11° > \theta > 2°$ in polar angle. The FHA on one side is segmented into four 90° sections around the beam pipe as the FEM. A quarter section consists of 27 steel absorber and alternating 27 ionization chambers with cathode pad readout. The projective tower structure is same as the FEM, $0.1(\eta)\times 5°(\phi)$, so a quadrant is segmented into 19 η bins, each of which has 18 ϕ bins.

The FHA was also calibrated with the pion beams. By varying the energy from 20 to 200 GeV, the energy resolution was measured to be

$$\frac{\sigma(E)}{E} = \frac{130\,\%}{\sqrt{E_T}} \oplus 4\,\%.$$

Good linearity was also observed up to 200 GeV.

We must search for a signal of Double Pomeron Exchange without any tagging devices for the recoil proton. The recoil antiproton is measured by the Roman Pots, so in this case the tagging of a rapidity gap on the proton side is essential. The forward calorimeters are used for this purpose, together with the Beam-Beam Counters described below.

3.2.6 Beam-Beam Counter

The Beam-Beam Counter (BBC) is a plane of 16 scintillation counters in both the east and west directions (32 scintillators in total). They provide the "minimum-bias" trigger and are also used as the primary luminosity monitor [27]. These scintillators are arranged in a rectangle around the beam pipe as shown in Figure 3.6. They cover the angular region from 0.32° to 4.47° measured along the beam direction, corresponding to the range of pseudo-rapidity of $5.90 > \eta > 3.24$. Excellent timing properties ($\sigma <$

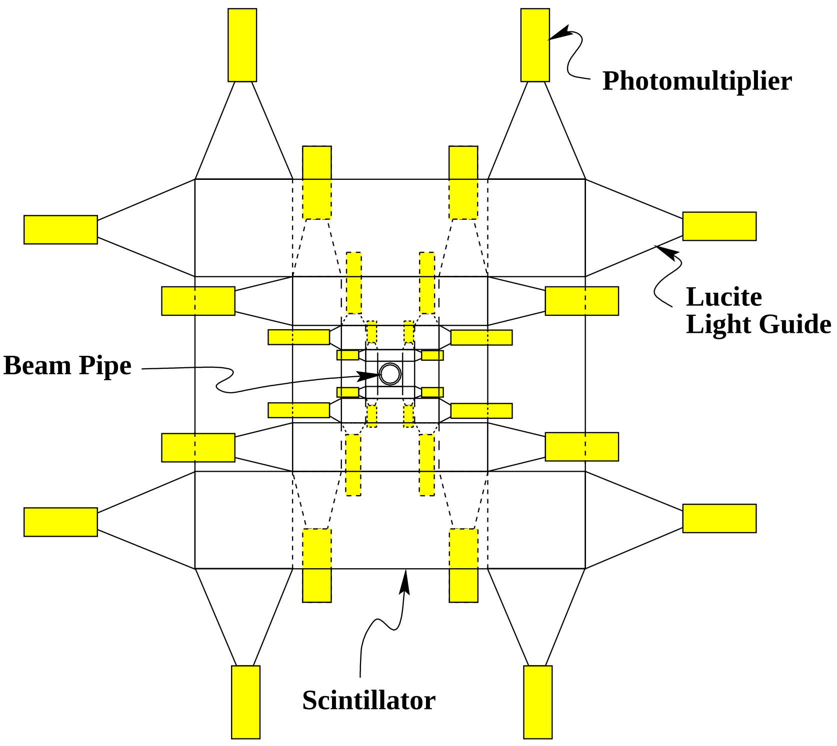

Figure 3.6: A front view of one of the Beam-Beam Counters (BBC). The beam pipe passes the center of the BBC. The shaded parts show the photomultiplier tubes for read out.

200 ps) of these counters provide the best measurement of the time of the interaction. As shown in Figure 3.6, two photomultiplier tubes (PMTs) are used to read out each scintillation counter. Note that the counters overlap in some regions so that a single particle can give one or two hits and these counters are not ideal multiplicity counters. In the "minimum-bias" trigger, one BBC hit corresponds to both tubes greater than threshold within a ± 15 nsec timing window of the beam crossing. A coincidence of both east and west counters with at least one BBC hit defines a minimum-bias event. Note that diffractive events will not be efficiently accepted by the minimum-bias trigger.

As the luminosity monitor, the BBC can provide the instantaneous (integrated) luminosity by measuring the rate (number) of the coincidences in the counters, divided by the effective BBC cross section. From the CDF measurement of the total, elastic and single diffractive cross sections at $\sqrt{s} = 1.8\,\text{TeV}$ [36, 37, 38], and CDF Run 1A data analysis, we obtain the following effective BBC cross section [39, 40, 41]:

$$\sigma_{BBC} \;=\; 51.15 \,\pm\, 1.60\,\mathrm{mb}. \qquad (3.5)$$

In the study of hard diffraction, the BBC is an important tool as well as the forward calorimeters which cover the forward regions. We use the BBC and forward calorimeters as "Gap Detectors" in a search for Double Pomeron Exchange events.

3.3 New CDF Detectors for Hard Diffraction

After the collider operation of Run 1, the CDF detector was instrumented with two new detectors [42]. One of them is a pair of two small calorimeters covering the 2° holes of the forward calorimeters and it is called the Microplug calorimeter. This device was developed to increase the pseudorapidity coverage ($|\eta| < 4.2$) of the calorimeters by a unit of pseudorapidity (up to about 5.0). The other is a set of three forward antiproton spectrometers installed in the chambers with the Roman Pot structure (simply often called the Roman Pot in the following). We can observe a recoil antiproton in the diffractive scattering using the Roman Pots since they were attached along the beam on the antiproton direction (west). This is because an opening space for setting up the Roman Pots is restricted by the Tevatron lattice and it was found only for the west side, about 56 m away from the interaction point.

The Roman Pot was intended to give the trigger for the diffractive data. A tagging of the recoil antiproton by the Roman Pot would give a trigger for inclusive diffractive scattering events in $\bar{p}p$ collisions. We can measure the forward energy flow at $\eta > 4.2$ using the Microplugs, but it is also possible to use them as the trigger devices. If we require the Microplug calorimeter response to be low below threshold ("veto"), diffractive events with the rapidity gaps over the Microplug coverage can be obtained. In the analysis, the former (called diffractive trigger) is used. A special trigger, an application of the latter, was used during a certain period of Run 1C. This trigger required both the east and west Microplugs in veto, so it was called DPE trigger.

3.3.1 Microplug Calorimeter

The Microplug calorimeter has been constructed to extend the rapidity coverage of the forward calorimeters in the CDF, and it was installed in an open space between the forward EM calorimeter and the beam pipe [42]. The coverage of the Microplug is $4.5 < |\eta| < 5.5$, and this is completely overlapped by the BBC. So, "a veto on the Microplug" would be similar to "a veto on the BBC", but the former is better for claiming the real rapidity gap on typical energy scale of hadrons (∼a few GeV) because the BBC counts even low energy particles which come not only from the primary interaction, but also from the secondary or higher interactions in the CDF detector.

The Microplug calorimeter is a sampling calorimeter with the octagonal cylinder structure with 56 cm in longitudinal length, 5.7 cm (13.8 cm) in inner (outer) radius. A schematic view of the Microplug is shown in Figure 3.7. The structure of the Microplug is similar to the plug upgrade electromagnetic calorimeter for Run II [43] : 12 layers of 1 cm thick lead absorber interleaved with scintillating tiles with wavelength shifting fibers. The Microplug has eight ϕ segments which are read out by the photomultiplier tubes. The longitudinal depth is about $22\,X_0$ in radiation length and $0.7\,\lambda_0$ in attenuation length.

The test module with four ϕ segments was calibrated with the test beam [44]. The energy resolution for the electron was estimated to be

$$\frac{\sigma(E)}{E} = \frac{22.5\,\%}{\sqrt{E}} \oplus 0.2\,\%,$$

which is almost comparable with that of the PEM or FEM. The calorimeter response was linear at the level of 1 % for the electrons from 30 to 150 GeV. Muons were detected with close to 100 % efficiency, as for the energetic electrons and photons.

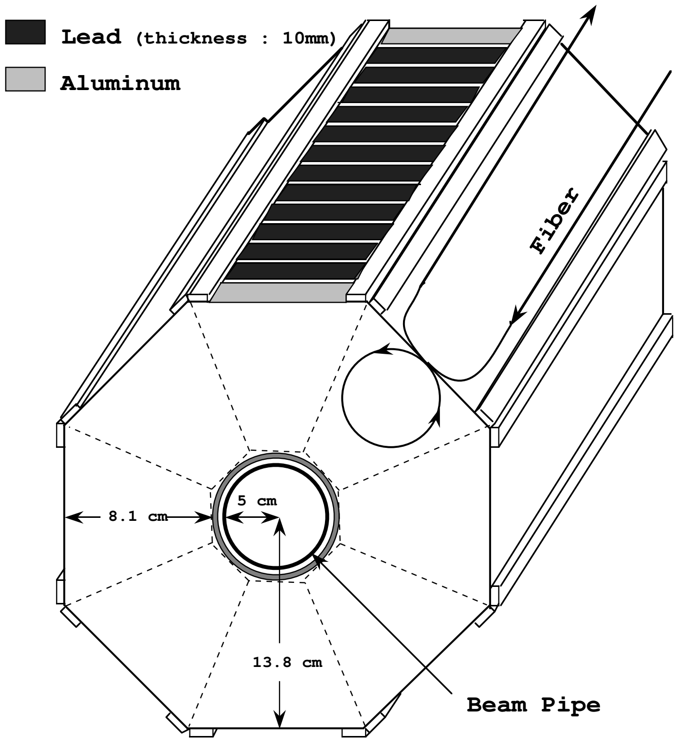

Figure 3.7: A schematic drawing of the Microplug calorimeter.

3.3.2 Forward Antiproton Spectrometer

Diffractive scattering in proton-antiproton collisions is characterized by a recoil antiproton (or proton) with momentum greater than 90 % to 95 % of the incident antiproton (proton) beam. This recoil antiproton with slightly lower momentum gets bent into the accelerator ring when passing through the magnetic field of the accelerator dipole magnets, but stays inside the beam pipe. (Here the case that the antiproton remains intact and the proton dissociates is discussed because this is the case for our study.) Therefore, by inserting a tracking detector inside the beam pipe at a suitable position, we can detect a recoil antiproton and measure its position and angle. This measurement allows us to estimate the momentum of the recoil antiproton, hence the Feynman variable $x_F \equiv P^L_{out}/P^L_{in}$ where $P^L_{in(out)}$ is the longitudinal momentum of the initial (recoil) antiproton. Also, we obtain the variable ξ from the relation $\xi = 1 - x_F$.

We can measure the momentum transfer squared t at the antiproton vertex, defined as $t \equiv (P^{\bar{p}}_{out} - P^{\bar{p}}_{in})^2$ where $P^{\bar{p}}_{in(out)}$ is the four momentum of the initial (final) antiproton. These measurements using the forward tracking detectors have some clear advantages against the rapidity gap technique in which the t is unknown and only the ξ can be measured with some ambiguity.

The insertion of the tracking detectors close to the beam can be done by using the "Roman Pots" [42]. The spectrometers are placed close or away the beam according to the beam condition by using the bellows. In addition, it is motivated by the diffractive regime of interest: e.g., high (low) ξ data can be obtained by positioning the spectrometers far (close) the beam.

Overview of the Roman Pot and Forward Spectrometer

The Roman Pots were mounted on the "spool piece", 56.54 m away from the interaction point (B0) to the west side. The structures of the Roman Pots and inside spectrometer hodoscopes are shown in Figure 3.8. The total length of the Roman Pots including the beam pipe is 266.54 cm, and the distance between the two pots is 98.5 cm. The arrangement of the Roman Pots for the CDF hard diffraction experiment is shown schematically in Figure 3.9, together with the Microplug calorimeter, the detectors with the forward coverage such as the Beam-Beam Counters ($3.2 < |\eta| < 5.9$) and forward calorimeters ($2.4 < |\eta| < 4.2$). One should note that the size of each detector is not scaled. As described below, the actual detection area of the spectrometer is about 2 cm$\times$2 cm.

One of the spectrometer hodoscopes installed inside the Roman Pots is shown in Figure 3.10. The hodoscope is placed inside the vessel with 14.8 cm diameter and the top of the hodoscope is covered by 0.4 mm thick steel. Normal air occupies the vessel. The vessel is attached to the vacuum chamber with 19.7 cm diameter through the bellows. A recoil antiproton traveling towards the left hits the tracking detector positioned at the top of the vessel. The tracking detector consists of the scintillator

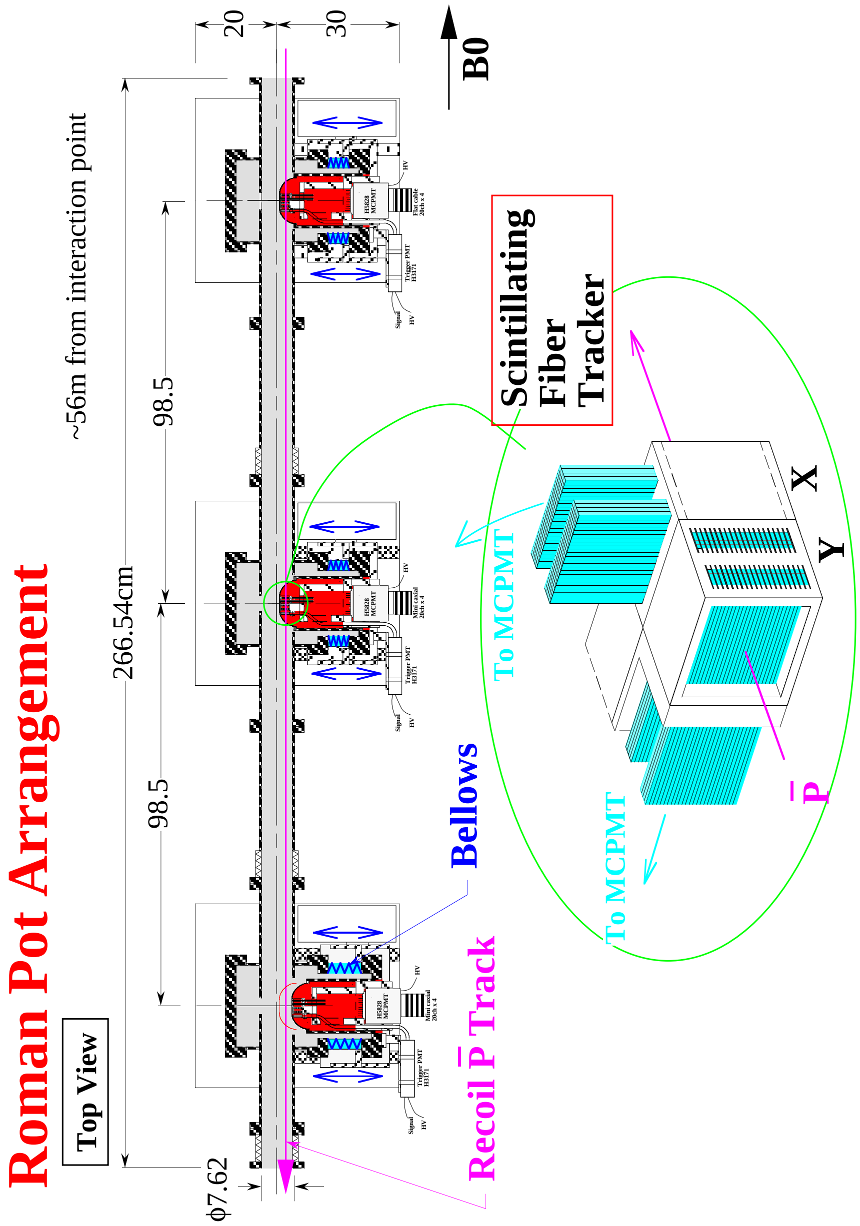

Figure 3.8: A top view drawing of the Roman Pots. The B0 interaction point is to the right about 56 m away so that recoil $\bar{p}$ in the diffractive scattering travels from right to left. In this arrangement the right pot is called Pot1, middle one is Pot2 and left is Pot3. The fiber tracker structure of the hodoscope is also shown.

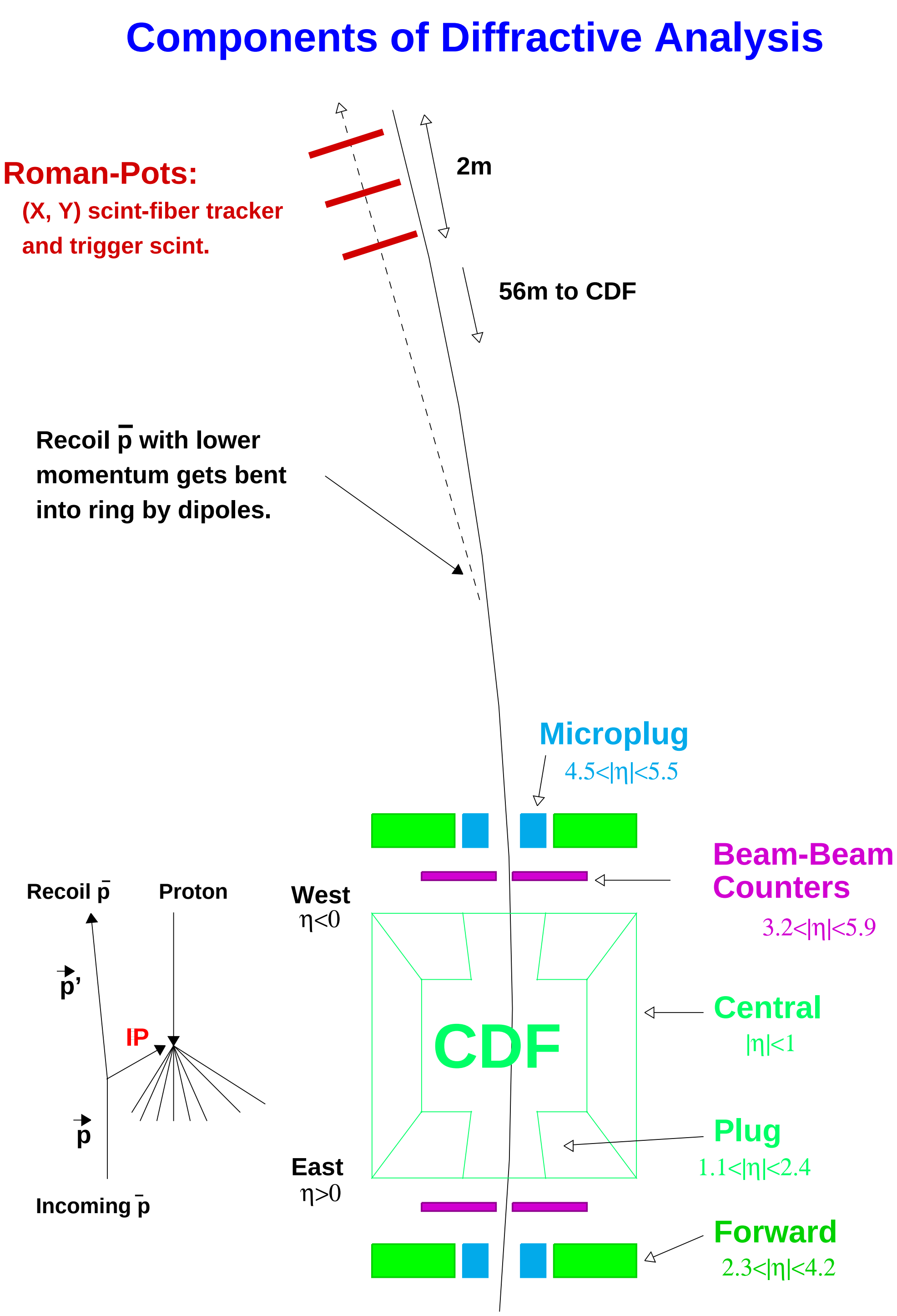

Figure 3.9: The arrangement of the Roman Pots, and the forward gap detectors in the hard diffraction experiment at CDF.

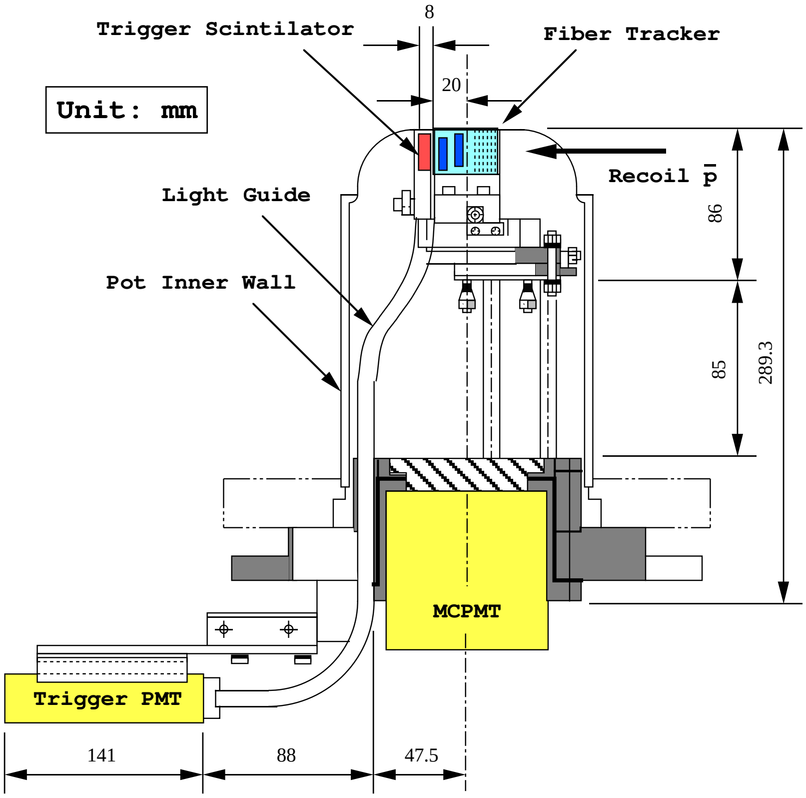

Figure 3.10: The fiber spectrometer hodoscope in the Roman Pot.

fiber arrays. Scintillation light from the hit fibers is passed to the MCPMT (multi-channel photo multiplier), 80-channel HAMAMATSU H5828, placed at the bottom. The scintillator (Bicron BC404) behind the tracking detector is 2.1 cm square and 8 mm thick and provides a timing coincidence used in the diffractive trigger. Its scintillation light is passed through the light guide to the trigger PMT, HAMAMATSU H3171-03, placed at the bottom-left of the vessel.

Scintillating Fiber Tracker

The detecting part of the spectrometer is a fiber tracker which consists of 80 scintillating fiber ribbons. As shown in Figure 3.8, the fiber array is split into two X and Y detection layers. Each X or Y detector is made of two sub-layers and each sub-layer contains 20 fiber ribbons.

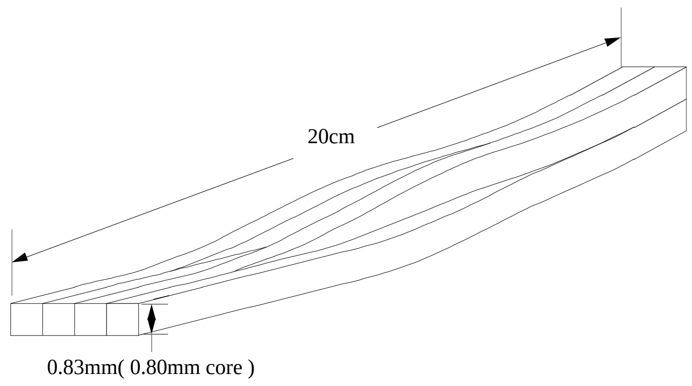

Figure 3.11: One ribbon of four scintillating fibers.

The structure of the fiber ribbon is shown in Figure 3.11. The fiber material is KURARAY SCSF81 with single cladding, and one fiber is 20 cm long and 0.833 mm×0.833 mm square. A scintillating core is 0.800 mm×0.800 mm square. One ribbon is made of four such fibers. On the detecting side, the fibers are arranged in line along the beam direction to increase the path length of the particle, while on the MCPMT side the fibers are rearranged into a square to fit the anode shape of the MCPMT.

The arrangement of the fiber ribbons is shown in Figure 3.12. 20 fiber ribbons make one sub-layer, and the two sub-layers are placed parallel to each other with a spacing of 0.267 mm corresponding to one third of the scintillating fiber core width. The spaces between the ribbons are filled up with the aluminized mylar. The distance between the centers of the two sub-layers is 8.5 mm. By using this fiber arrangement with one third shifting, we expect three types of fiber hits: (a) a track hits the fibers of both sub-layers, (b) a track hits a fiber of sub-layer named 1 and passes the space between the ribbons of the other layer named 2, (c) the opposite case of (b). The combination of the fiber hit information on the three fiber trackers enables us to reconstruct the pass of the track as shown in Figure 3.13. This figure shows the array of only the X (or Y) detection layers (the size and distance are not scaled).

The geometry of the hodoscope fiber arrays at the operation mode is shown in

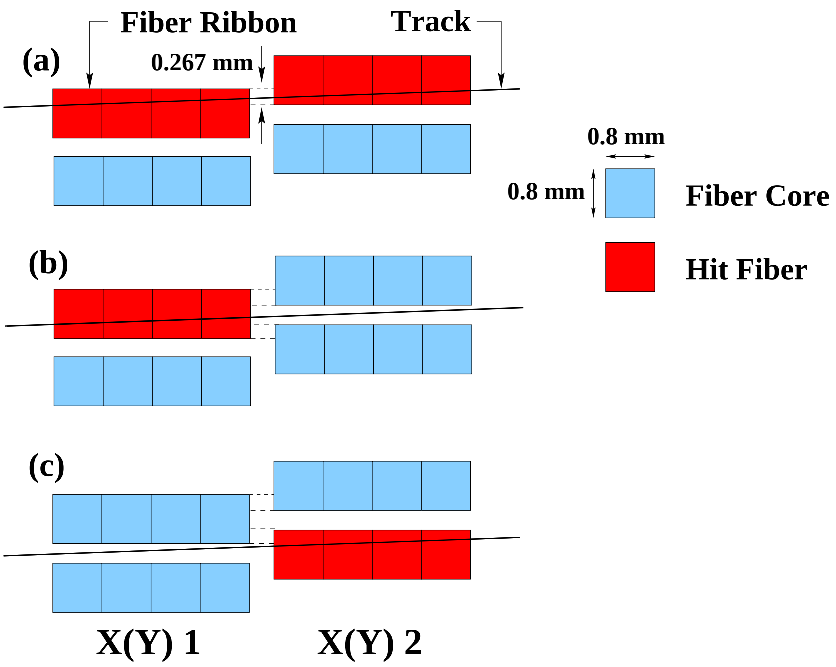

Figure 3.12: The arrangement of the fiber ribbons for the X (or Y) detection layer. (a) A track hits both the sub-layers. (b) A track hits a sub-layer 1 but not sub-layer 2. (c) the opposite case of (b).

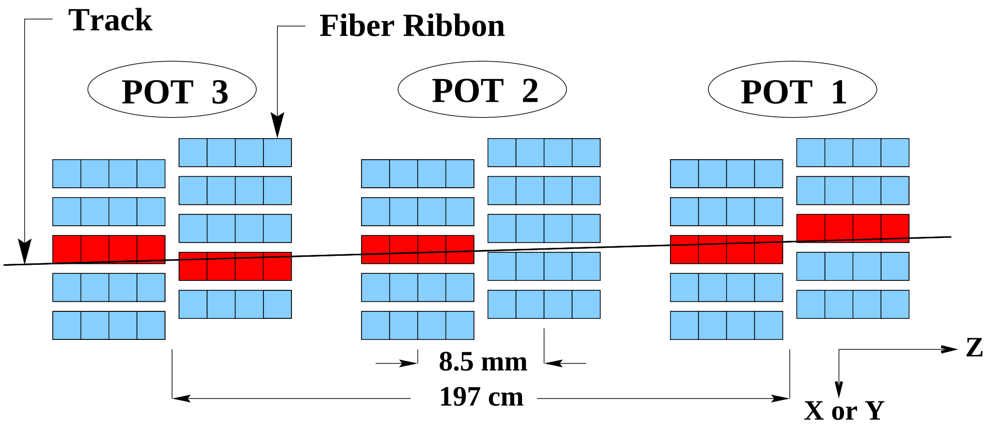

Figure 3.13: The track reconstructed from the hits of the fibers. Only the X (or Y) detection layers are shown.

Figure 3.14. Normally the p ($\bar{p}$) beam bunches pass the location of the Roman Pot at the outer (inner) position along the x direction with respect to the beam pipe center. That is, the $\bar{p}$ beam is closer to the spectrometer than the p beam. Based on this, the typical distance between the $\bar{p}$ beam orbit and the top of the spectrometer was designed to be 1.0 cm. However, it turned out that the p and $\bar{p}$ beam were flip-flopped with each other and the $\bar{p}$ was by 2.2 mm distant from the beam pipe center during this experiment. From this, we set the detector closer to the beam line by twice this distance than the original position to keep the distance between the $\bar{p}$ beam and the top of the detector designed.

In order from the detector top to the fiber, the following materials exist: the Roman Pot wall (0.4 mm thick steel), air gap (0.3 mm), detector wall (0.7 mm thick aluminum), the aluminized mylar (0.077 mm) and the acrylic clad (0.0167 mm). Therefore, the distance between the $\bar{p}$ beam and the edge of the first fiber was about 1.15 cm. As shown in the figure, the fiber ribbons were numbered as 1 to 40 along the directions of the axes for both X and Y detectors (i.e., the fiber #40 of Y detector is at $y = 0$). From 40 fiber ribbons and above one third shifting, the total number of bins is 79. Consequently the total number of effective bins which can be used for the track reconstruction is 77 except the two edge bins, #1 and #79. This means that the detection area of the spectrometer hodoscope is 2.05 cm×2.05 cm on X–Y plane. Also, the effective range of the measurements of the x and y positions (i.e., the distances between the nominal $\bar{p}$ orbit and the center of the first and last effective bins) is about $1.22 \leq x(\mathrm{cm}) \leq 3.24$ and $-1.01 \leq y(\mathrm{cm}) \leq 1.01$, respectively.

3.4 Data Acquisition and Trigger System

In normal Tevatron operation with six beam bunches of the proton and antiproton, the beam crossings occur every 3.5 μs around the center of the CDF detector, that corresponds to a rate of minimum bias events with about 285 kHz. The maximum

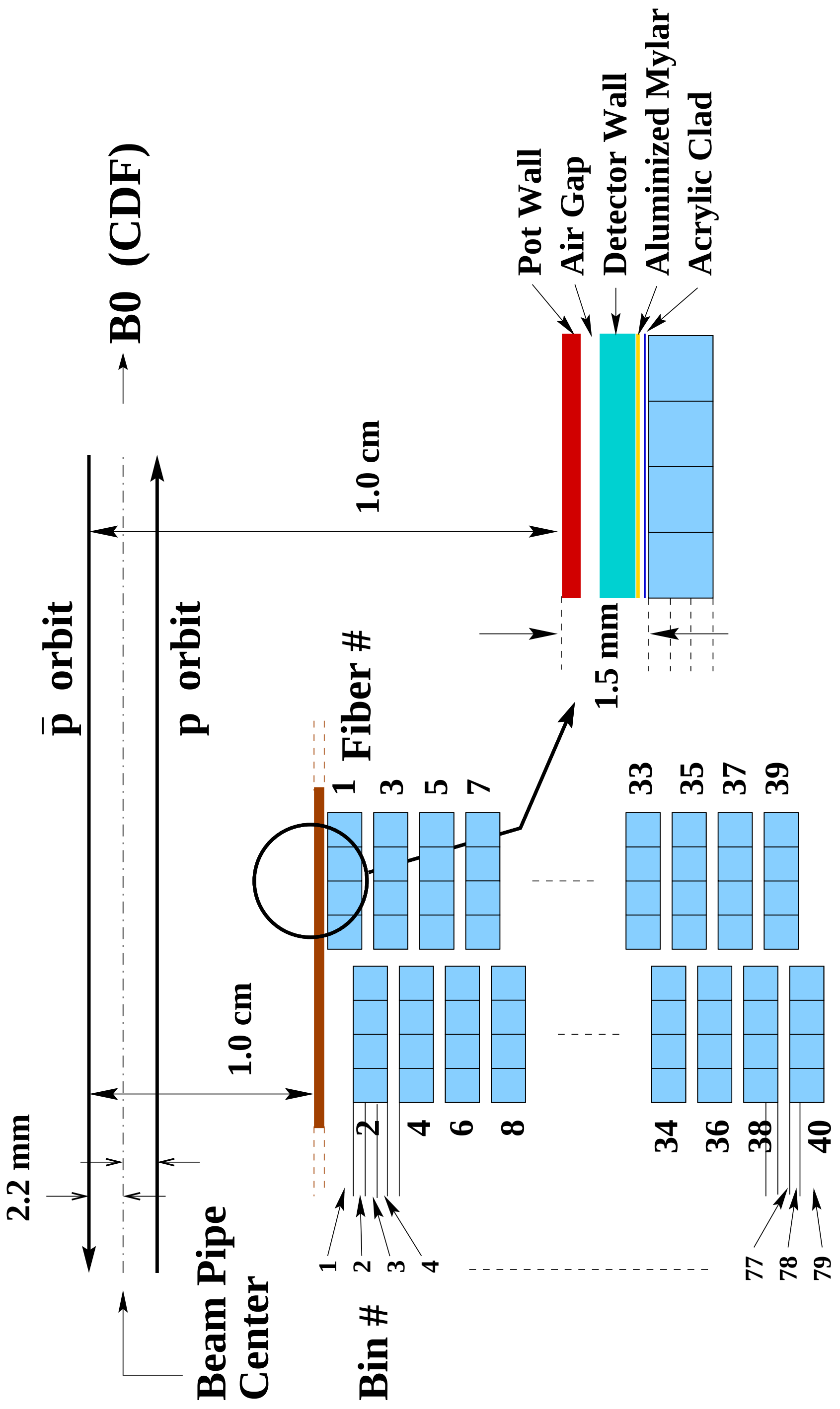

Figure 3.14: The geometry of the spectrometer hodoscope in the Roman Pot. The B0 interaction point is on the right side. The numbering scheme for the fibers (1–40) and the bins (1–79) shown in the figure is adopted only to the X detector. The Y detector uses the opposite order for numbering of the fibers (40–1) and the bins (79–1). The two edge bins (1 and 79) are not used in the track reconstruction.

rate of data storage media (8 mm tape for Run 1A or disk staged to tape for Run 1B and 1C) allowed in CDF is an order of a few events per second. It therefore requires the data taking system to select a few interesting events out of events with a few hundred kHz.

Another important factor of the data acquisition (DAQ) system is to minimize the *deadtime* where the event information is read out of the detector electronics. During the deadtime, the trigger system can not make an access to a next new beam crossing. Incorporating these requirements in the DAQ system, the CDF trigger has been constructed with the three levels in each of which a sophisticated online trigger system is employed [45]. Examining the events and then sending the interesting events out of them to the following level, more time can be used in the later level to investigate the events in more detail. The Level 1 and Level 2 triggers are implemented with specially designed hardware, and the Level 3 trigger consists of the commercial computers running software for event selection.

Level 1 Trigger

The Level 1 trigger decides to select or reject the event for every beam crossing with $3.5\,\mu$s, so it gives rise to no deadtime. The Level 1 reduces an event rate from a few hundred kHz to a few kHz. In CDF the Level 1 is implemented on custom designed hardware. The decision of Level 1 is based on calorimeter responses of electromagnetic, hadronic and total transverse energy, the transverse energy imbalance, stiff tracks in the central tracking chamber, etc. A coincidence of hits in both the BBCs is also used in Level 1. In comparison of the calorimeter and muon detector readouts with trigger thresholds, the analog *fast-outs* are used. In Level 1 (and Level 2) calorimeter trigger, a *trigger* tower with the size of 0.2 in η and 15° in ϕ is formed from adjacent *physical* towers. A physical tower has typically a segmentation of 0.1 in η, and 15° (5°) in the central (plug and forward) calorimeter, as described previously. A single trigger tower is required to have E_T above programmable thresholds.

Level 2 Trigger

The Level 2 trigger needs about 25–35 μs to process the event delivered from the Level 1. This causes 10–20 % deadtime, and during this time the next 7–10 bunch crossings are lost in the DAQ. The Level 2 trigger rate is limited to a peak of about 22 Hz for Run 1A and 40–55 Hz for Run 1B and 1C. The Level 2 trigger also consists of specially designed hardware and uses the fast-outs from readout electronics, as in Level 1. In this level, used in the trigger decision are various quantities more closely related to physical objects, such as energy clusters in the calorimeter, total transverse energy and the missing transverse energy, the presence and position of muon stubs in the muon chamber that are associated with high p_T tracks in the CTC. The energy clusters of Level 2 are produced from trigger towers with a seed threshold of $E_T > 3$ GeV by adding adjacent trigger towers with E_T above 1 GeV to the cluster.

Level 3 Trigger

After the events pass the Level 2, the data is sent to the front-end electronics on the detector to digitize the event and then to the scanners to read out the full event. These processes need about 3 ms, and so they give rise to another few percent deadtime. Once the event is read out by the scanners, the DAQ system revives and triggers on a new bunch crossing. The fully digitized event is sent to the Level 3 software trigger. The Level 3 trigger runs event reconstruction software on the computers to determine if the event should be accepted or rejected. The software used in Level 3 is the subset of offline analysis programs with the modifications that enable the process to be done faster. Various physics quantities such as energy clusters and tracks are reconstructed. The Level 3 output rate is about 5–7 Hz for Run 1A and about 10 Hz for Run 1B and 1C. There is a storage in a queue of processing (*buffer*) and the buffering and processing are done in parallel, so the Level 3 usually incurs no deadtime.

Chapter 4

Data and Event Selection

The data used in the event selection and the analysis is described in this chapter. Before starting the short run of the Tevatron (Run 1C), the trigger system dedicated for the diffractive physics was prepared based on the recoil antiproton tagging using the Roman Pot. First of all, this trigger system is described. Next, this short Tevatron run is described in the following section. Major upgrade for the CDF detector before the run was the addition of the Microplug calorimeter and the Roman Pots, so the diffraction experiment in CDF was one of the main topics for this short Tevatron operation. After that, we present the data set for the analysis. In addition to diffractive data, we are also using the non-diffractive data in inelastic $\bar{p}p$ collisions because a comparison of diffractive and non-diffractive data is essential for understanding the pomeron. In particular, a jet production in non-diffractive $\bar{p}p$ interaction is due to the hard scattering between the partons in the incident (anti)protons in the framework of QCD. Therefore the jets produced in single diffractively excited system indicate, if we observe, that there is a parton-like constituent in the pomeron. Comparison of those jet systems can tell us details about the constituents: momentum distribution in the pomeron, quark-like or gluon-like nature of the constituent.

4.1 Diffractive Trigger

The trigger system for diffractive data in the hard diffraction experiment is described [46].

Level 1

The Level 1 trigger is a 3 fold coincidence of the trigger scintillators installed in the forward spectrometers. The timing is adjusted for the outgoing $\bar{p}$, and then there is no background in the trigger from the (370 ns earlier) incoming p bunch. Triggered data is prescaled to 50–200 Hz during the normal Tevatron run in the high luminosity condition ($\sim 10^{30-31}\,\mathrm{cm}^{-2}\mathrm{s}^{-1}$), and then sent into the Level 2 trigger.

Level 2

At Level 2, the diffractive trigger is split into two paths. In one trigger path, data trigger rate is simply prescaled to about 1 Hz so that this trigger is called "diffractive inclusive" trigger. The prescale factor was varied dynamically, on an event-by-event basis, with the beam luminosity within the region of 250–1,000. The other path requires at least two Level 2 clusters with $E_T > 3\,\mathrm{GeV}$ in the calorimeter, and therefore, this trigger path is called "diffractive dijet". Diffractive dijet trigger does not require prescaling because data rate should be kept as high as possible.

Level 3

At the Level 3 trigger, two selection cuts for the primary vertex and for a reconstructed track in the Roman Pots are required. In order to select events with produced particles in the CDF detector, that is, to avoid empty events, at least one vertex with class ≥ 5 is required. At the same time, events with zero or one class 12 vertex are selected to reject multiple interaction background. For the pot track, if the number of X or Y planes in which there are ≥ 6 hits is greater than 4, this event is rejected as a Roman Pot multi-hit background. Here a plane corresponds to a superlayer that is a unit to measure X or Y position of the track, shown in Figure 3.12. In addition, at least two jets in JETS bank with $E_T > 5\,\text{GeV}$ are required in the diffractive dijet trigger.

A sample of events that passed the above 3 Levels of trigger selection is used as a diffractive trigger data sample in this analysis. Figure 4.1 shows the flow chart of the diffractive trigger.

4.2 1995–96 Tevatron Run

The short Tevatron run named "Run 1C" which followed the 1994–95 run (Run 1B) was carried out from late November 1995 to February 1996. During the shutdown of the Tevatron in summer 1995, the Roman Pots and Microplug calorimeter were installed by the CDF hard diffraction group. Following the test run for a month and half, we collected the large amount of data in the physics runs with the proton and antiproton beams at the center of mass energy of $\sqrt{s} = 630\,\text{GeV}$ and $\sqrt{s} = 1800\,\text{GeV}$. In particular, a sample of about 3 million events was obtained in low luminosity runs around $\mathcal{L}_{inst} \sim 10^{29}\,\text{cm}^{-2}\text{s}^{-1}$ at $\sqrt{s} = 1800\,\text{GeV}$. This sample was collected during the special runs in only four days (January 18–22, 1996), scheduled by request of Experiment E811 (elastic $\bar{p}p$ scattering experiment at the E0 of the Tevatron.) The data obtained during the low luminosity run is good for the diffraction study because the rate of multiple interaction in beam-beam or beam-gas collisions is very small, and the detector condition should not change for such a short period.

The run numbers corresponding to $\sqrt{s} = 630\,\text{GeV}$ or $\sqrt{s} = 1800\,\text{GeV}$ runs in Run 1C are listed in Table 4.1. The 630 GeV data taking was done before the New-Year shutdown and had several pot-fiber channels with connection problems that were fixed during the shutdown. As seen in the table, there are no good runs during $76123 \leq \text{RUN} \leq 76339$ at $\sqrt{s} = 1800$ GeV. This is due to 1) that the sense wires of the CTC were broken just after RUN 76123, and number 4 to 6 of the superlayers in north half of the chamber became useless, and 2) some problems in LUMMON system up to RUN 76338. This means that only south half of the CTC was usable during

Diffractive Trigger

Trigger Name : `DFFB_DIFFRACTIVE_INCL*, DFFB_DIFFRACTIVE_DIJET*`
`DDFB_DIFFRACTIVE_INCL*, DDFB_DIFFRACTIVE_DIJET*`

Level 1 3 fold coincidence of trigger counters.
Reject circulating p beam with trigger timing.

$\Downarrow$

Prescaled to 50-200 Hz

$\Downarrow$

Level 2 Split into 2 paths.

$\Downarrow$	$\Downarrow$
Dynamic Prescale	$\geq$ 2 Clusters with $E_T > 3\,GeV$
	(No Prescaling)
"Diffractive Inclusive"	**"Diffractive Dijet"**

$\downarrow$ Trigger Rate : $\sim$ 1 Hz $\downarrow$

Level 3

- $\geq$ 1 Vertices with Class $\geq$ 5; $\leq$ 1 Vertex with Class 12 $\cdots$ Primary Vertex
- Reject events with $\geq$ 4X or Y planes which have $\geq$ 6 hits. $\cdots$ Roman Pot

$\Downarrow$	$\Downarrow$
"Diffractive Inclusive"	**"Diffractive Dijet"**
	$\Downarrow$
	$\geq$ 2 Jets with $E_T > 5\,GeV$

Figure 4.1: Diffractive trigger flow.

Table 4.1: A summary of good physics runs in Run1C.

$\sqrt{s}$ (c.m.s)	Runs
630 GeV	74608 ≤ RUN ≤ 75109
1800 GeV	74208 ≤ RUN ≤ 74521
	75250 ≤ RUN ≤ 76123
	76339 ≤ RUN ≤ 76574
(Low Lum.	75632 ≤ RUN ≤ 75738)

good runs after RUN 76339, but it is not a serious problem for diffractive data because the CTC was not used in diffractive trigger.

4.3 Data Sets

4.3.1 Diffractive Data

As a sample of diffractive data used in the analysis, we selected the diffractive trigger data collected within the low luminosity runs 75644 ≤ RUN ≤ 76738 at $\sqrt{s} =$ 1800 GeV. This is just because multiple interaction background is expected to be very small in low luminosity condition, as mentioned above. It would be worth noting the other runs although they are not used in the analysis. During the runs 75808 ≤ RUN ≤ 76146, both the east and west Microplugs were put in veto to get a DPE-rich event sample (called DPE trigger). This sample is very interesting because diffractive dijet trigger of this sample would enhance the DPE events with high E_T jets. However, this sample should be used only when DPE jets are observed in inclusive diffractive sample that is not biased by a gap requirement. Therefore, it is left for the later analysis.

We note that the runs 76165 ≤ RUN ≤ 76403 should be used carefully because for this period the positions of the Roman Pot fiber trackers were changed from the usual position. For most physics runs, the distance between the $\bar{p}$ beam and the top of the trackers was kept to be 1.0 cm. For some runs during $76165 \leq \text{RUN} \leq 76403$ the tracker position was changed to be about -8.8 mm away from the usual position to get high $|t|$ diffractive events. These events are useful for the study of t dependence of the cross section, correlation of ξ versus t in high t region, dijet to inclusive ratio as a function of t up to high t range, etc. For the rest of runs the trackers stayed at the garage position to collect the minimum-bias events. Therefore, to get the sample obtained at the constant tracker position, we should remove the data with this period.

A typical luminosity of the data set used is around $1.0 \times 10^{29}\,\text{cm}^{-2}\text{s}^{-1}$. Table 4.2 gives a summary of data sets used in the analysis for run number and number of events, number of events collected with diffractive inclusive and dijet triggers, and the instantaneous luminosity. Finally **3,119,137** trigger events that consisted of **3,114,497** inclusive triggers, and **4,638** dijet triggers were obtained. A fraction of events passed both the inclusive and dijet trigger requirements, so they were included into inclusive trigger data. In the following analysis we use only the inclusive data of 3,114,497 events.

4.3.2 Non-Diffractive Data

Comparison of diffractive data with non-diffractive data in inelastic $\bar{p}p$ interactions is essential for understanding of the pomeron in terms of QCD. Most of all the CDF trigger data is actually non-diffractive sample, e.g., high E_T jets, inclusive lepton or photon, etc. These samples are non-diffractive, but in a comparison of inclusive diffractive events much less biased sample (i.e., inclusive non-diffractive sample) should be used. Of course, for a certain specific event such as diffractive W production, inclusive W trigger sample can be used for the comparison. As a minimal biased data, we used the data collected with so called "minimum-bias" trigger which requires the BBC hits for both the east and west in coincidence with the beam crossing. The true minimal biased trigger is a "beam crossing" trigger which only requires the beam

Table 4.2: A summary of diffractive trigger data at $\sqrt{s} = 1800\,\text{GeV}$, used in the analysis. An event collected by both the inclusive and dijet triggers was included into inclusive data. $\mathcal{L}_{inst}$ is the average instantaneous luminosity in units of $10^{29}\,\text{cm}^{-2}\text{s}^{-1}$.

Run	**Events**	**Diff. Trigger**		$\mathcal{L}_{inst}$
		Inclusive	*Dijet*	
75644	9,631	9,505	126	2.05
75645	36,642	36,433	209	1.88
75646	128	86	42	1.75
75647	361,278	360,888	390	1.49
75648	250,770	250,598	171	1.13
75650	17,502	17,486	16	1.15
75674	369,769	368,926	843	1.75
75675	57,179	57,116	63	1.35
75676	48,462	48,443	19	1.26
75677	264,550	264,542	8	1.18
75678	150,262	150,217	45	1.07
75713	349,615	349,474	140	1.07
75714	380,359	380,270	89	0.82
75715	277,906	277,875	31	0.75
75733	4,904	4,846	58	9.10
75734	76,733	76,239	494	6.85
75736	33,169	33,063	106	5.44
75737	194,217	193,278	939	4.61
75738	236,061	235,212	849	3.56
	3,119,137	**3,114,497**	**4,638**	**1.65**

crossing, but for Run 1C this trigger was not used. Run 1A data contains some runs collected with this trigger, and it will be described later.

In the analysis we used the data obtained by the minimum-bias trigger with a slightly different condition from a normal one, for the period of Run 1C low luminosity runs $75671 \leq \mathrm{RUN} \leq 75673$ and $75711 \leq \mathrm{RUN} \leq 75712$ ($\mathcal{L}_{inst} \sim 0.5 \times 10^{30}\,\mathrm{cm}^{-2}\mathrm{s}^{-1}$). This data set was collected with the following set of the triggers:

- Level 1 `MINIMUM_BIAS`,
- Level 2 `AUTOMATIC_L2_ACCEPT`,
- Level 3 `VALB_L3_AUTO_ACCEPT`,

which is different only in scaling from the normal minimum-bias trigger set below,

- Level 1 `YMON_*`,
- Level 2 `YMON_L2_*`,
- Level 3 `OTHB_YMON_*`, `OTHB_MIN_BIAS_*`.

Starting from a sample of 342,150 events, we applied the BADRUN filter module to select good runs for the analysis. Then, offline we explicitly required the event to pass the above minimum-bias triggers, and applied the COSFLT filter module to reject background from cosmic rays, beam-gas background interaction events, etc. At this stage we obtained **340,698** good minimum-bias events in this sample. It is worth noting again that true ZERO-bias data with the beam crossing would have been useful. This should be a lesson for Run II.

4.4 Data Pre-Selection

4.4.1 Diffractive Data

At the first stage, we required that the data should be collected in the inclusive trigger path because of the simple comparison between the data and Monte Carlo predictions,

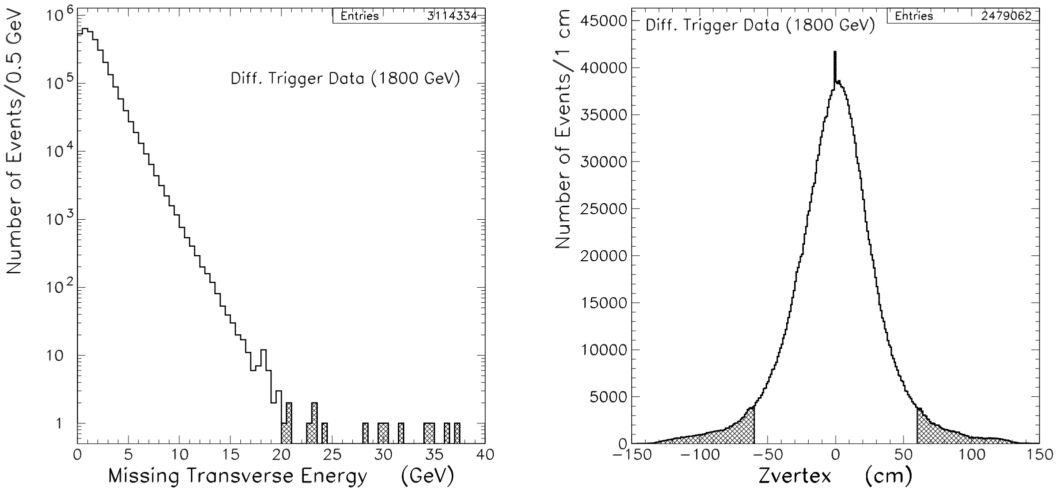

(a) Missing E_T

(b) Z_{vertex}

Figure 4.2: (a) Missing E_T and (b) Z_{vertex} distributions of diffractive trigger data. The data is required to have $\not{E}_T \leq 20\,\text{GeV}$ and single vertex in (b). The shaded region shows the events rejected by the $\not{E}_T$ and Z_{vertex} cuts.

and also between the diffractive and non-diffractive dijets in the following dijet studies. As discussed above in Section 4.3.1, there are **3,114,497** inclusive trigger events in our total data sample. Then we apply the COSFLT filter as for non-diffractive minimum-bias data. In the following, we start the data selection from a sample of inclusive trigger events after the COSFLT was applied. The number of events in this sample is **3,114,334**.

Missing E_T and Event Vertex

In Figure 4.2(a) we present the missing transverse energy ($\not{E}_T$) distribution for initial data sample. The figure shows that the data contains a fraction of events with large $\not{E}_T$ such as cosmic ray background. Therefore,we require the $\not{E}_T$ to be less than $20\,\text{GeV}$ to reject a few tail events, which left **3,114,318** events.

The number of event vertices measured by the VTX is used in the diffractive trigger as the requirement for rejecting multiple interaction background. The event vertex is classified from class 5 to 12 by the VTX hit status [47]. In general, the larger the value of the class, the better the vertex quality. In the classification algorithm the best vertex in an event is identified as a primary regardless of the value of class, so this means a low quality vertex such as class 5, 7, 8 could be identified as the primary vertex in the soft interaction. Therefore, in order to select events with a single interaction in the VTX acceptance region, we require that there is only one vertex with class greater than or equal to 5 in an event. By requiring the single vertex cut, **2,479,062** events are selected.

Figure 4.2(b) shows the event vertex position along the Z axis (Z_{vertex}) in a sample of events with $\not{E}_T \leq 20\,\mathrm{GeV}$ and a single vertex. In order to select a good vertex reconstructed in the VTX region, the cut $|Z_{vertex}| \leq 60\,\mathrm{cm}$ is applied, which brings the number of events from 2,479,062 to **2,290,541**.

Roman Pot Track

Diffractive data was collected with an in-time coincidence of Roman Pot trigger scintillator hits (Section 4.1). Then, hit information on the fiber of the detector is converted to the position of the track with respect to the beam axis. Figure 4.3(a) shows ADC pulse height distributions of 3 Roman Pot trigger counters in a sample of diffractive inclusive events with the vertex and $\not{E}_T \leq 20\,\mathrm{GeV}$ cuts. We could see clear peaks around $350 \sim 400$ ADC counts that correspond to the signal of 1 M.I.P. (Minimum Ionizing Particle), and the long tail coming from multi-M.I.P. events. So, in order to select events with ≥ 1 M.I.P. signal, ADC counts of the 3 trigger counters are each required to be greater than 250. Then, events containing ≥ 2 M.I.P.s are removed by requiring that total ADC counts of 3 trigger counters should be less than 1,800, as shown in Figure 4.3(b).

In this figure a small bump is seen around $\Sigma\mathrm{ADC}_i \simeq 2,700$ (left arrow). Selecting events within $2,600 < \Sigma\mathrm{ADC}_i < 2,900$ and looking at each ADC distribution of 3

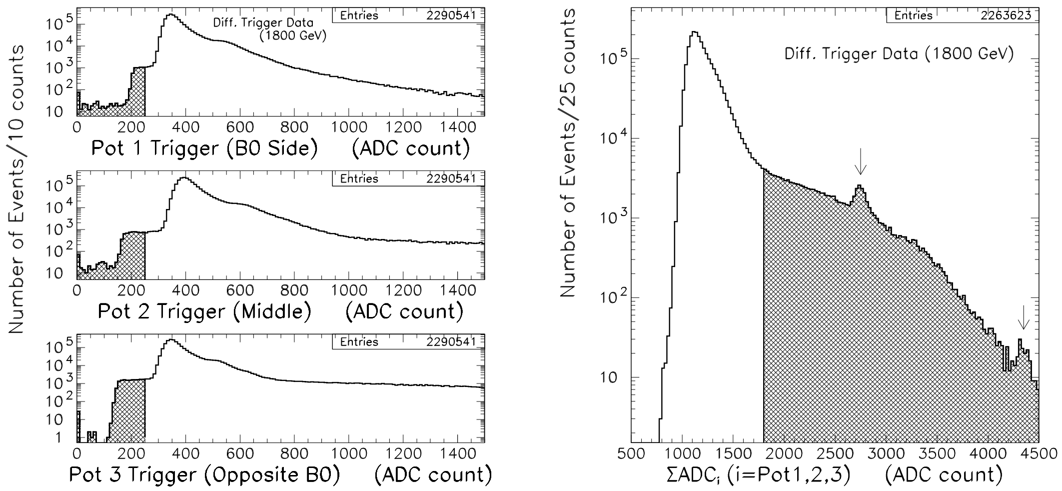

(a) Trigger ADC counts for 3 Pots

(b) Total ADC count of 3 Pots

Figure 4.3: (a) ADC pulse height distributions for 3 Roman Pot trigger counters. The top plot is for Pot 1 (B0 side), the middle for Pot 2 (middle pot) and the bottom for Pot 3 (opposite of B0). See the Roman Pot arrangement in Figure 3.8. (b) Total ADC count of 3 Roman Pot trigger counters. The shaded regions of events in left (right) plots are rejected with ≥ 1 M.I.P. selection cut (≥ 2 M.I.P.s rejection cut).

trigger counters, we see that this bump is due to overflow of a trigger counter from multi-particle hits. The same effect from overflow of two counters also appears as the second bump around $\Sigma\text{ADC}_i \simeq 4,300$ (right arrow). Anyway, as a result of the 1 M.I.P. selection cuts, 6 % of the data is removed, and the number of events becomes **2,144,022** (called 1MIP sample).

Figure 4.4 shows the multiplicity distribution of the reconstructed Roman Pot tracks in 1MIP data sample. Most 1MIP data has only one reconstructed track (68 %), but a sizeable fraction of the data (17 %) contains two tracks in the Roman Pots. As discussed in Appendix A, one of the two reconstructed tracks in an event could be attributed to an accidental mis-reconstruction that produces an extra fake track. Therefore, we select **1,819,549** events with one or two reconstructed tracks as a sample

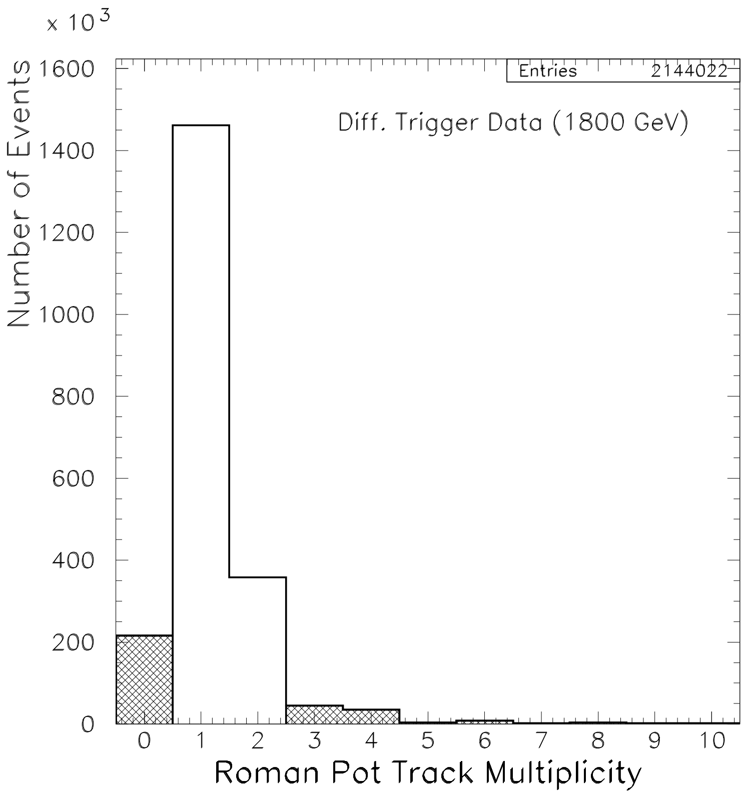

Figure 4.4: Multiplicity distribution of reconstructed tracks in the Roman Pot.

of good track events. The fiber hit quality is classified into 4 hit classes from 0 to 3 according to the number of observed hits in X and Y detectors of three Roman Pots. The hit class is defined such that the smaller the class number, the better the hit quality. In the following analysis, a sample of **1,758,877** events with the best hit class "0", defined as hits on all the three X and three Y detectors, is used. This sample is called the 1TRK sample below.

Figure 4.5 shows the distributions of horizontal (X) and vertical (Y) positions, and angles in $X-Z$ (ϑ_X) and $Y-Z$ (ϑ_Y) planes for the reconstructed tracks in the 1TRK sample. Here the $\bar{p}$ beam is nominally at $X = Y = 0$. The X distribution shows a fall-off with distance from the beam within $-2.8\,\text{cm} < X < -1.2\,\text{cm}$ that corresponds to the Roman Pot acceptance convoluted with the $\xi = 1 - x_F$ and $|t|$ distributions

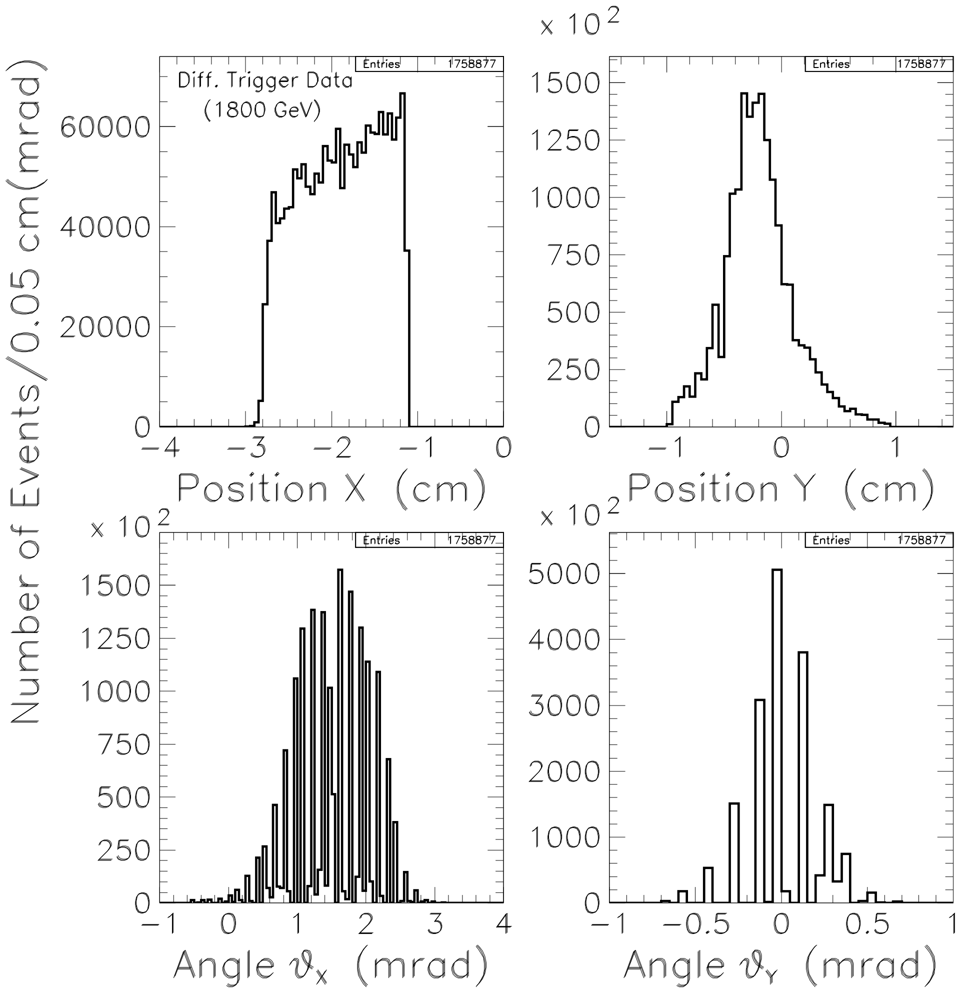

Figure 4.5: X and Y positions (upper), and angles in X-Z and Y-Z planes (lower) of the reconstructed pot tracks in the 1TRK sample.

of the $\bar{p}$. The occupancy is higher near to the beams but not by a large factor. The Y distribution would be nominally symmetric around $Y = 0$ because the track is not deflected by the dipole magnetic field in the vertical plane, and the quadrapoles are symmetric. However there is a shifted peak at $Y = -0.2 \sim -0.3\,\mathrm{cm}$. This could be due to the displacement of the Roman Pots from the nominal position. The dip near $Y = -0.5\,\mathrm{cm}$ (although not significant) is known to be due to a dead channel, and 2/3 times the hits in the dead channel are relocated to one of the neighbor bins (this appears as a spike in the next bin), so that this problem gives only a small reconstruction inefficiency.

Diffractive Kinematics

Based on the information of track position at the Roman Pots and interaction vertex measured in CDF, we can calculate the diffractive kinematics given by ξ, azimuth ϕ and t. The ξ is a fractional momentum loss of the reconstructed track to the initial $\bar{p}$ beam, and t is four momentum transfer squared of the pomeron. In addition to the track position and interaction vertex, the beam transportation calculation taking into account the Tevatron accelerator magnets is necessary in ξ and t reconstruction. In this analysis ξ and t reconstruction codes that implement the beam transportation calculation using a higher order transport matrix, Roman Pot position correction and initial beam information at the CDF, developed by Hosai Nakada (University of Tsukuba), are used (see [48] for details).

After rejecting about 2.2 K events with unphysical solutions of ξ and t, we obtain a sample of **1,756,689** events with successfully reconstructed ξ and t. Figure 4.6(a) and 4.6(b) show the distributions of ξ and $|t|$ in this 1TRK sample. The acceptance of the Roman Pot is maximum (actually 100 %, i.e., full azimuth ϕ coverage, for much of this region) for recoil $\bar{p}$ with about $0.05 < \xi < 0.09$ and $|t| \lesssim 1\,\mathrm{GeV}^2$, but there is still some acceptance at smaller ξ $(0.01 < \xi < 0.035)$. The corresponding $|t|$ to this smaller ξ is relatively higher $(> 0.1 - 0.2\,\mathrm{GeV}^2)$ than $|t|$ in the maximum acceptance

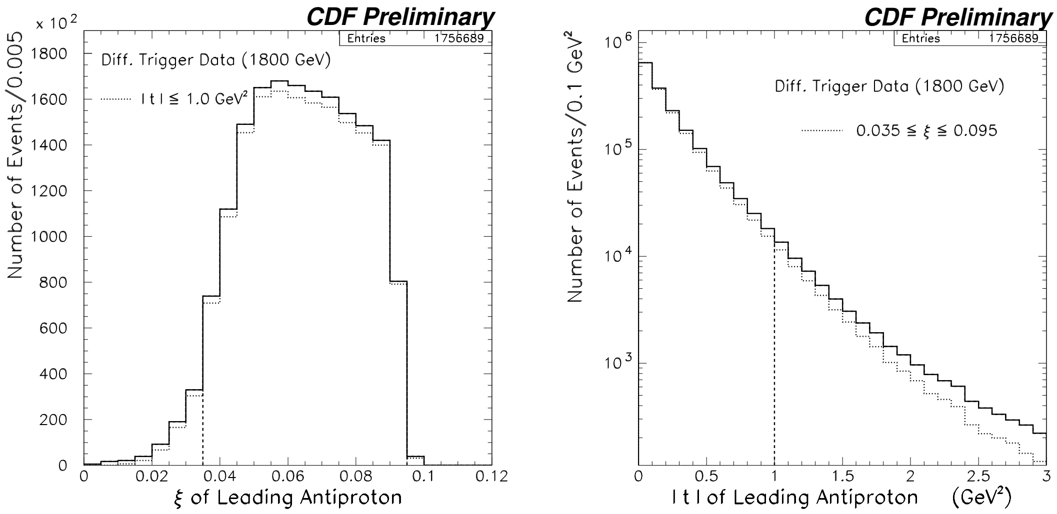

(a) Reconstructed Roman Pot ξ

(b) Reconstructed Roman Pot $|t|$

Figure 4.6: (a) ξ and (b) $|t|$ distributions of the leading antiproton in a sample of events with successfully reconstructed ξ and t. The dashed lines show the Roman Pot acceptance cuts of $0.035 < \xi < 0.095$ and $|t| < 1.0\,\mathrm{GeV}^2$. The dotted histograms show the distributions with the ξ and $|t|$ cuts.

region of $0.05 < \xi < 0.09$, as seen in the correlation between ξ and $|t|$ of Figure 4.7. Consequently the Roman Pot acceptance at smaller ξ is small.

In Figure 4.8 the Roman Pot acceptance $A(\xi, |t|)$ as a function of ξ and $|t|$ is shown. In the following analysis we use, in principle, the data with pot tracks in the full acceptance region and neighboring area satisfying $0.035 < \xi < 0.095$ and $|t| < 1.0\,\mathrm{GeV}^2$ (shown by the dashed area). These Roman Pot acceptance cuts kill 7 % of reconstructed (ξ, t) sample and bring the number of events to **1,638,993**. This data sample consists of events with a single good vertex and a good reconstructed pot track within a reasonable Roman Pot acceptance, so that it is called **RP** (**R**oman **P**ot) data below. A summary of the number of events after pre-selection cuts described in this section is given in Table 4.3.

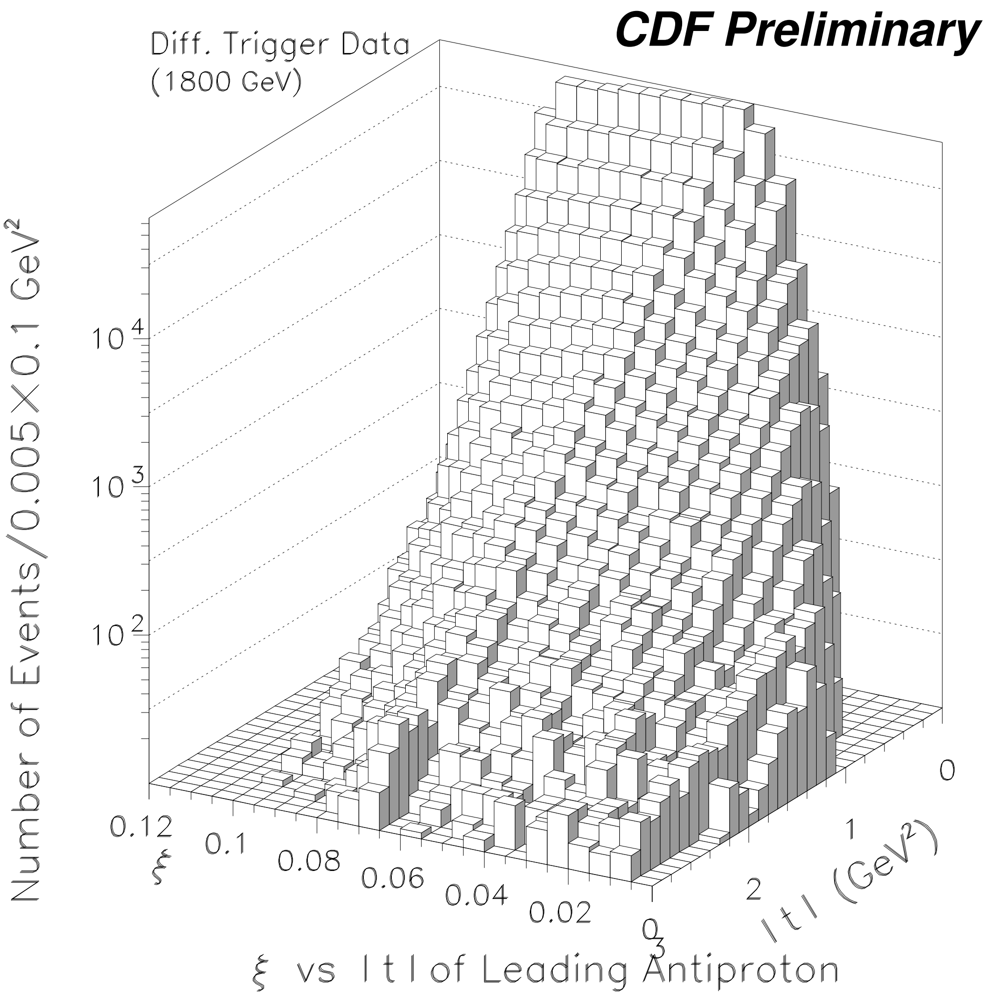

Figure 4.7: Correlation between the ξ and $|t|$ of the leading antiproton, reconstructed with the Roman Pots.

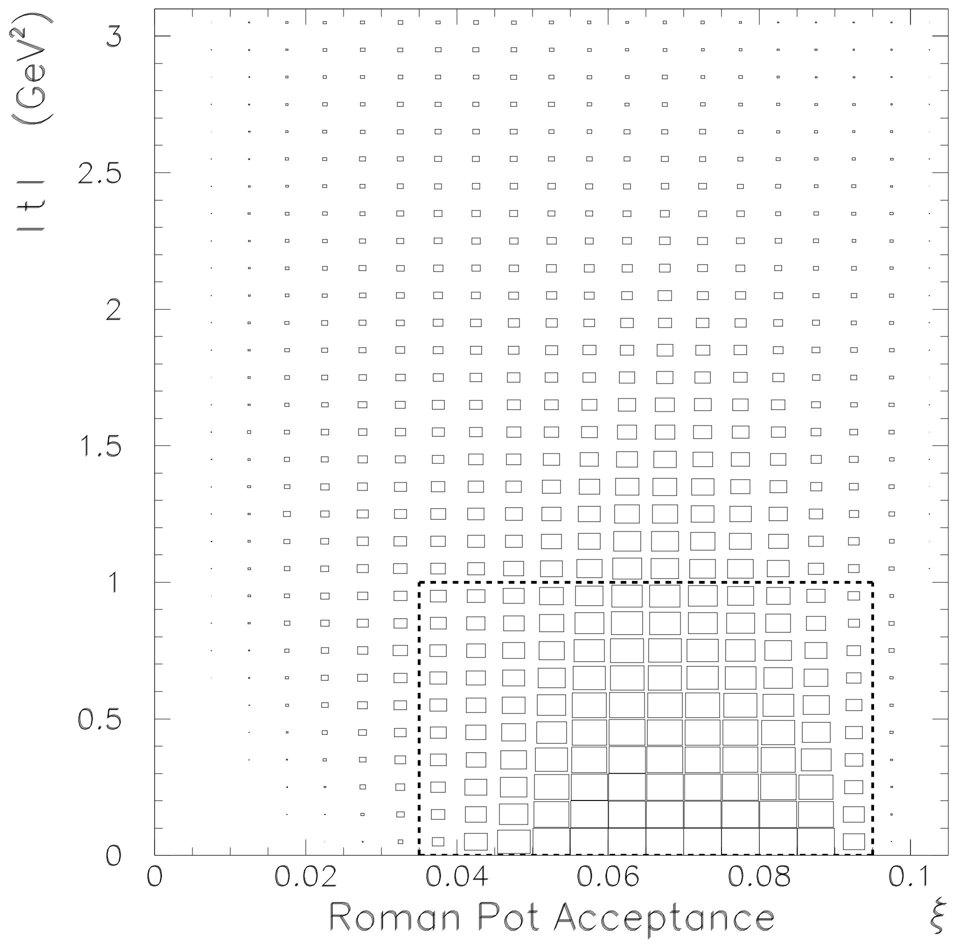

Figure 4.8: Roman Pot acceptance $A(\xi, |t|)$ as a function of ξ and $|t|$. The bin widths of ξ and $|t|$ are 0.005 and $0.1\,\mathrm{GeV}^2$ respectively. The size of rectangle in each bin approximately represents the acceptance, e.g., a bin with a rectangle fully covering the bin size such as $0.060 < \xi < 0.065$ and $0.0 < |t| < 0.1\,\mathrm{GeV}^2$ has about 100 % acceptance. The dashed area corresponds to the acceptance cuts used in the analysis.

Table 4.3: The number of events after the pre-selection cuts used in the analysis. The second column shows the sample names used in the text.

Pre-Selection Cuts	**Sample**	**# Events**
Total Triggers		**3,119,137**
Select Inclusive Trigger		3,114,497
COSFLT Filter		3,114,334
$\not{E}_T \leq 20\,GeV$		3,114,318
Single Vertex (1 Class$\geq$ 5 Vertex)		2,479,062
$\lvert Z_{vertex}\rvert \leq 60\,cm$		2,290,541
For Roman Pot Track		
1 M.I.P. Cuts*	1MIP	2,144,022
1 or 2 Reconstructed Tracks		1,819,549
$3X$+$3Y$ Hits at 3 Roman Pots	1TRK	1,758,877
For Diffractive Kinematics (ξ, t)		
(ξ, t) Reconstructed		**1,756,689**
$0.035 < \xi < 0.095$, $\lvert t\rvert < 1.0\,\mathrm{GeV}^2$	**RP**	**1,638,993**

1 M.I.P. Cuts* =
Trigger $ADC_i \geq 250$, $\sum_i ADC_i \leq 1800$ (i = Pot1,2,3)

4.4.2 Non-Diffractive Data

Using Run 1C minimum-bias trigger data, we obtained a sample of non-diffractive events in inelastic $\bar{p}p$ collisions. As described in Section 4.3.2, now we have 340,698 events after applying the COSFLT filter. As for diffractive data, we next require the missing $E_T \leq 20\,\mathrm{GeV}$, which kills only 13 events. For non-diffractive events we do not use the single vertex cut, but apply the Z_{vertex} cut of $\lvert Z_{vertex}\rvert \leq 60\,\mathrm{cm}$. As a result, **299,959** events remain after these cuts. This sample is called the inclusive non-diffractive sample below.

Chapter 5

Dijet Production by Single Diffractive Excitation

The dijet production in single diffractive excitation (Single Diffractive dijet or SD dijet) is studied using the sample of inclusive Roman Pot data (**RP**) with $0.035 < \xi < 0.095$ and $|t| < 1.0\,\mathrm{GeV}^2$. An observation of jets in diffractive events would confirm the existence of hard scattering process between constituents of the proton and the exchanged object (predominantly, the pomeron). If the structure of the exchanged object is similar to that of the proton, we may expect that the E_T of diffractively produced jets drops faster than that of non-diffractive jets because of the smaller center of mass energy in diffractive events. In the later analysis, a threshold of $E_T > 7\,\mathrm{GeV}$ was primarily applied for the jet selection. If the statistics is enough large for $E_T > 7\,\mathrm{GeV}$, a higher E_T threshold of $E_T > 10\,\mathrm{GeV}$ would be used. Since the center of mass energy in DPE events is even lower, DPE dijets could have even lower E_T than the single diffractive jets. This also supports the low E_T threshold.

First, we briefly discuss the jet reconstruction algorithm. We usually use a "cone algorithm" to reconstruct the jets in CDF [49]. In this algorithm, a jet is defined as an energy-weighted vector of calorimeter towers in a cone of η-ϕ space with a certain radius. A reconstructed jet is then processed through the offline corrections to convert the measured jet E_T to the true parton momentum at the production. These corrections were brought together into an offline analysis package, called "JTC96". It is therefore often referred to as JTC96 corrections.

A certain detector noise due to "hot towers" in the calorimeter mimics the jet. These noise jets were removed from the data. Another source contributing to the jet events is non-diffractive overlay background. This background was also rejected using as a template the shape of BBC and forward calorimeter tower multiplicities of minimum-bias jet events. This is because non-diffractive background fills the gap region covered by the BBC and forward calorimeters with the particles, in contrast to diffractive events showing the zero or low multiplicities for the gap range. Single vertex selection would kill a portion of the jets in single interaction events. The efficiency for this requirement is also discussed.

5.1 Jet Clustering at CDF

In the CDF jet clustering algorithm, a jet is formed from the calorimeter towers. An offline routine called JETCLU [49] is used to reconstruct the jets based on the following three steps:

1. Pre-Clustering

Before clustering the towers in a cone, a pre-clustering is done using the seed towers. The seed towers with E_T above threshold (at default $E_T > 1\,\mathrm{GeV}$) are listed, and then a loop is performed to group the seed towers into a pre-cluster. In the loop over the seed towers a certain radius R_0 is chosen.

2. Cone Clustering

A loop over the towers around the pre-cluster centroid is done, and the tower with $E_T > 100\,\mathrm{MeV}$ is added into a cluster if it is within a cone of R_0 (cone radius) around the pre-cluster centroid. Including the new towers added, a cluster centroid is recalculated, and then a loop is again performed around the new centroid. This procedure is repeated until the lists of towers in the clusters are unchanged. The most common value of R_0 is selected to be 0.4, 0.7 and 1.0, depending on the analysis.

3. Merging and Resolving

There could be some towers assigned to more than one clusters in this cone algorithm. The overlapping energy is calculated from these towers and if it is greater than a certain threshold (usually 75 % of the smallest cluster), the clusters are merged. If the overlapping energy is lower than the threshold, the shaded towers are grouped into the nearest cluster. After merging or resolving the overlap towers, the centroid of each cluster is recalculated.

5.2 Jet Energy Corrections

An offline correction routine JTC96 contains the following corrections to jets and the actual corrections are carried out in this order:

- Relative Correction,
- Absolute Correction,
- Underlying Event (UE) Subtraction,
- Out-of-Cone (OC) Correction.

The relative correction is used to correct for the detector non-uniformity in response to jets. The detector response would be different between the calorimeters and the "cracks" (uninstrumented region) in-between, and even between the central and plug (or forward) calorimeters. Using jet balancing, the response of jets outside the central region are corrected back to that of central jets, which are well understood in calorimeter response.

The absolute correction is then performed, in which the measured jet is transformed to the particles generated in the cluster. Taking into account the ambiguities due to detector non-linearity, fragmentation, cone clustering, the true energy of particles at the parton level is estimated from the jet energy measured in a calorimeter.

We have to consider the energy due to underlying event in a jet. There are in general two possible sources of underlying event in a single hadron-hadron collision: 1) fragmentation of beam remnants and 2) multiple interactions of partons in hadrons. After the relative and absolute corrections are done, the underlying event energy which was measured in minimum-bias events is subtracted from the jet. As discussed later, this correction has been modified for the analysis of diffractive events including DPE because the subtracted energy used in default JTC96 was obtained in quite different condition from that of our diffractive data.

In the fragmentation process some energy (e.g., soft gluon radiation) could leak out of a cone of jet. The energy of jet outside a cone is called out-of-cone energy, and it is finally added to a jet in JTC96. From studies of Monte Carlo simulation, the out-of-cone energies (around $0.5 \sim 2\,\mathrm{GeV}$) for three cone sizes were evaluated as a function of jet P_T.

5.3 Dijet Event Selection

The triggered data of both diffractive and non-diffractive events is passed through the jet clustering algorithm JETCLU. In this process we use the JETCLU with standard CDF settings. We then apply the JTC96 corrections to the reconstructed (raw) jet clusters. The standard relative and absolute corrections are imposed to the jets, which are followed by the underlying event (UE) subtraction and out-of-cone (OC) correction. We use the OC correction contained in the standard JTC96 package, but for UE subtraction we use the UE energy which we measured instead of standard JTC96 UE energy.

We expect that the standard UE energy used by JTC96 would be quite different from our data with tight vertex cut (single vertex with class≥ 5) since it was obtained for events with high particle multiplicity vertex such as class 12. We therefore measured the UE energies for SD dijets at $\sqrt{s} = 1800\,\text{GeV}$ and $630\,\text{GeV}$, and DPE dijets at $\sqrt{s} = 1800\,\text{GeV}$. In addition, the UE energy for ND dijets was also measured. The UE energy of ND sample would basically increase with increasing instantaneous luminosity due to multiple $\bar{p}p$ interactions as shown in Figure 5.1. When requiring a single vertex for every event, the UE energy is almost flat over entire luminosity range. We do not apply the single vertex cut to ND dijet sample, but it is obtained from low luminosity runs so the luminosity dependence of UE energy is negligibly small, as seen in the lower half of the figure.

Using the measured UE energies, in JTC96 corrections we subtract $0.54\,\text{GeV}$ (1.16 GeV) from the E_T of single diffractive (non-diffractive) jets. Due to rapidity gaps most DPE events are expected to have zero multiplicities for both the BBC and forward calorimeter towers on the proton direction. Accordingly, we subtract a lower E_T of $0.37\,\text{GeV}$ from the jets of these events. In the later analysis we apply a conservative uncertainty of 30 % to these UE energies.

Processing the data of about 1,639 K diffractive events and about 300 K non-diffractive events through the JETCLU and applying the JTC96 corrections to the events containing jets, we obtain 40,077 (7,232) diffractive events and 43,379 (14,224) non-diffractive events with at least 2 jets with corrected $E_T > 7$ (10) GeV. In the following, the E_T of jet is JTC96 corrected transverse energy unless explicitly mentioned.

5.3.1 Hot Tower Rejection Filter

Figure 5.2 shows the detector η (η^{jet}_{det}) versus ϕ^{jet} of leading jets in $E_T > 7\,\text{GeV}$ diffractive dijet sample. We observe that a large fraction of jets appeared to emerge at certain η^{jet}_{det} and ϕ^{jet} spots. Particularly it is significantly observed for the plug region. A similar distribution is observed for non-diffractive dijet events. From these we conclude that the clusters reconstructed in these calorimeter spots would contain a large fraction of fake jets causing from *hot towers* of calorimeters. Also, we find that the hot

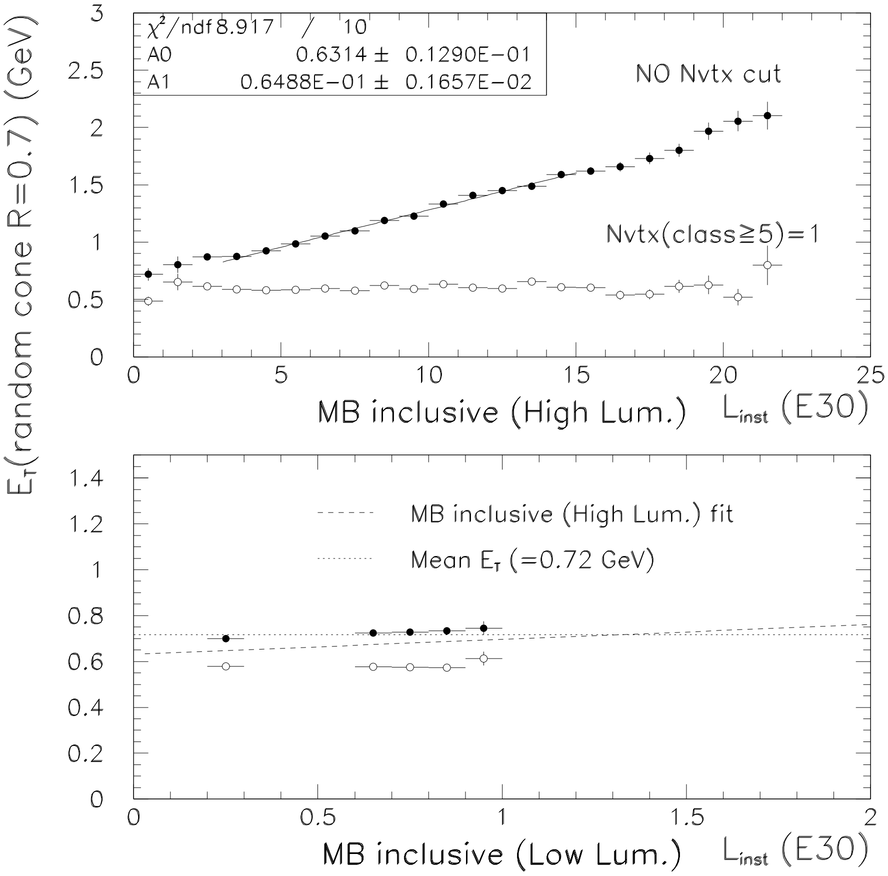

Figure 5.1: E_T within a randomly chosen cone $R = 0.7$ as a function of instantaneous luminosity in inclusive non-diffractive sample. The black points represent the case without any vertex cut, and open points show the case with single vertex cut (1 class$\geq$ 5 vertex). Upper half shows non-diffractive data during high luminosity, while lower shows that during low luminosity which we use in the analysis. The dashed line in the lower plot is an extrapolation of linear fit to upper high luminosity data, and the dotted line is an average E_T of our low luminosity sample. Multiplication of 1.6 to E_T within a random cone gives the underlying event energy to be subtracted from the jets.

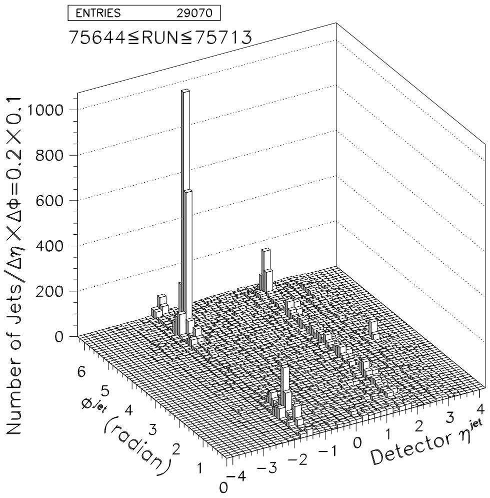

(a) 75644 $\leq$RUN$\leq$ 75713: LEGO

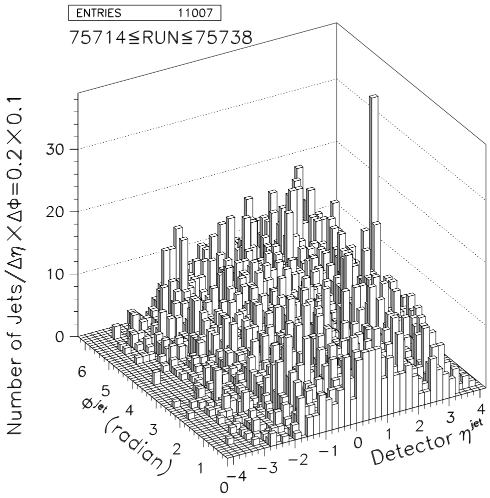

(b) 75714 $\leq$RUN$\leq$ 75738: LEGO

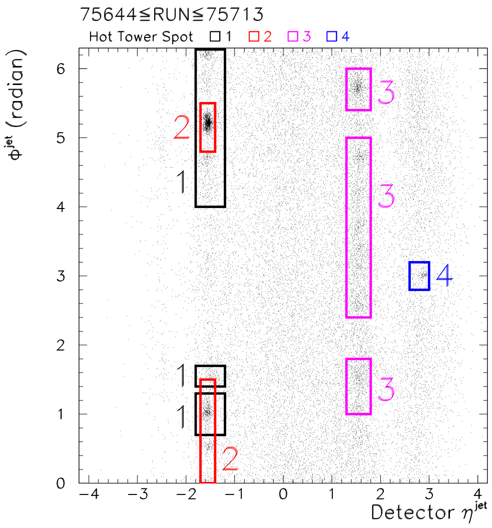

(c) 75644 $\leq$RUN$\leq$ 75713: HT Spot

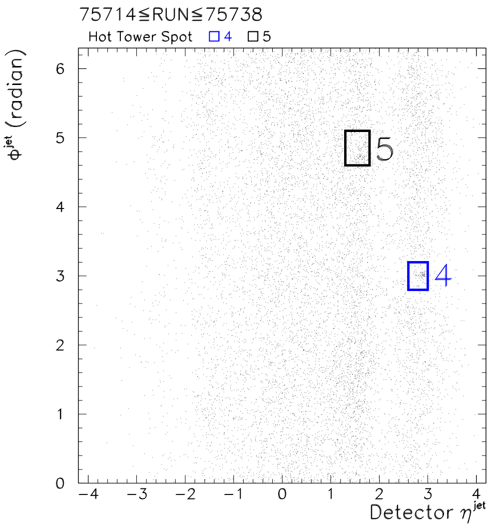

(d) 75714 $\leq$RUN$\leq$ 75738: HT Spot

Figure 5.2: Leading jet distribution on the detector η^{jet} versus ϕ^{jet} plane in a sample of events with at least 2 jets with $E_T > 7\,\mathrm{GeV}$ at (a)(c) 75644 $\leq$RUN$\leq$ 75713 and (b)(d) 75714 $\leq$RUN$\leq$ 75738. Five typical hot tower spots, defined as the rectangle areas shown in (c) and (d), are observed.

tower spots appeared during a certain run period. Figure 5.2(c) shows that many hot tower spots emerged in the plug region during the runs 75644 $\leq$RUN$\leq$ 75713. Also seen in Figure 5.2(d) is that most hot tower spots disappeared at latter half of low luminosity runs 75714 $\leq$RUN$\leq$ 75738.

Therefore, to remove hot tower clusters, we use the "Hot Tower Rejection Filter" (HTFLT). This filter is defined as the cuts on the EM fraction of reconstructed clusters, selected by the following characteristics of hot tower clusters:

- Localized hot tower spots in η–ϕ space,
- Different EM fraction from that of normal jets.

Here the EM fraction of a jet, F_{EM}^{jet}, is defined as the ratio of electromagnetic to total (electromagnetic and hadronic) energy of a jet:

$$F_{EM}^{jet} \equiv \frac{E_{EM}^{jet}}{E_{EM}^{jet} + E_{HAD}^{jet}}. \tag{5.1}$$

Figure 5.3 shows the EM fraction of clusters in typical five hot tower spots selected by looking at jet distributions on η_{det}^{jet} versus ϕ^{jet} plane (Figure 5.2(c) and Figure 5.2(d)). Comparing with the EM fraction of normal jets, we find that the EM fractions of hot tower spots are quite different. So that, we decide to apply a cut on the EM fraction of each hot tower cluster, as shown in Figure 5.3. The EM fraction cuts of HTFLT filter used in the analysis are listed in Table 5.1. We should note that the HTFLT does not reject the events, it just determines if the jet is "hot" or not.

In the analysis the HTFLT filter is applied to all the data independently of run numbers to simplify the analysis and to make the calculation of efficiency easy. Also, this filter is imposed only on the two leading jets in dijet events. When at least one jet of the two leading jets is rejected by the HTFLT, we remove this event. For events that pass the HTFLT, we observe a reasonable η versus ϕ distributions of jets which is shown in Figure 5.4. The efficiency of HTFLT, defined as a probability that good dijet events pass the HTFLT filter, is necessary for the later analysis. We determine this

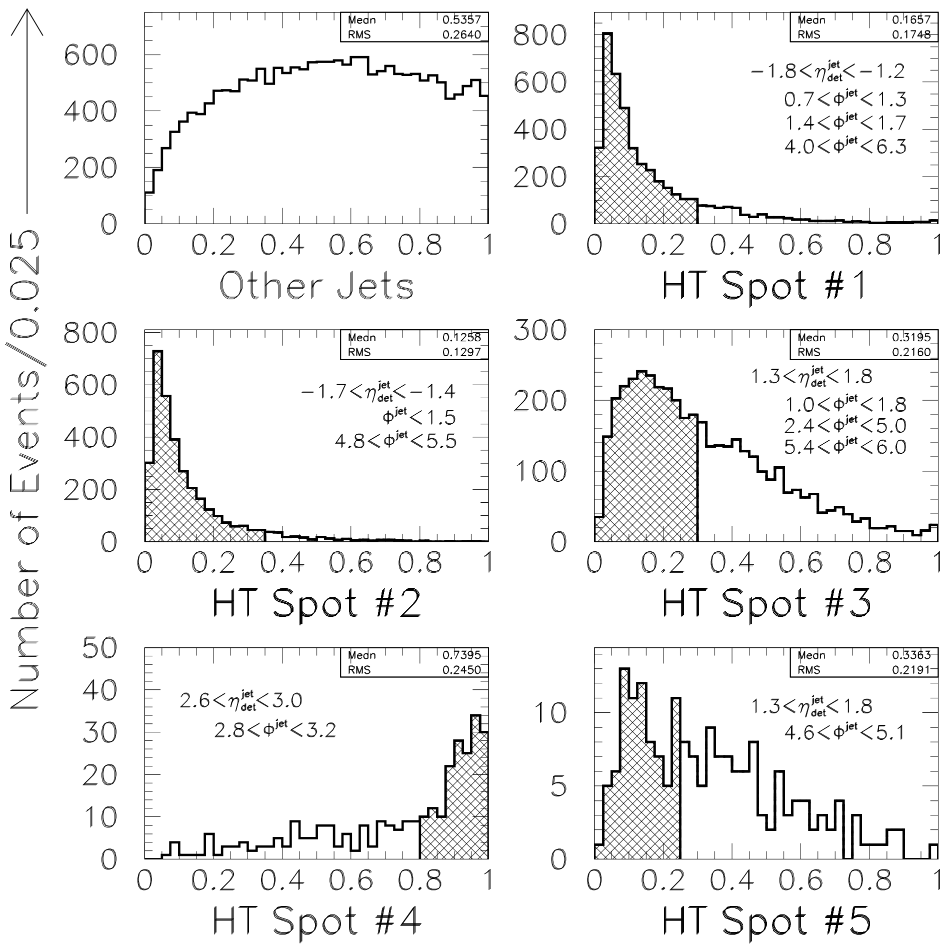

Figure 5.3: EM fraction of jets in five typical hot tower spots. Top left shows the distribution of jets excluding them. The shaded regions show the hot tower clusters rejected by the Hot Tower Rejection Filter.

Table 5.1: Cuts on the EM fraction of reconstructed clusters in five hot tower spots, that form the Hot Tower Rejection Filter.

Hot Tower Spot (Run Range)	**Detector η^{jet}**	**ϕ^{jet} (radian)**	**Cut**
Spot 1 (75644–75713)	$-1.8 < \eta^{jet}_{det} < -1.2$	$0.7 < \phi^{jet} < 1.3$	> 0.3
		$1.4 < \phi^{jet} < 1.7$	
		$4.0 < \phi^{jet} < 6.3$	
Spot 2 (75644–75713)	$-1.7 < \eta^{jet}_{det} < -1.4$	$\phi^{jet} < 1.5$	> 0.35
		$4.8 < \phi^{jet} < 5.5$	
Spot 3 (75644–75713)	$1.3 < \eta^{jet}_{det} < 1.8$	$1.0 < \phi^{jet} < 1.8$	> 0.3
		$2.4 < \phi^{jet} < 5.0$	
		$5.4 < \phi^{jet} < 6.0$	
Spot 4 (75644–75738)	$2.6 < \eta^{jet}_{det} < 3.0$	$2.8 < \phi^{jet} < 3.2$	< 0.8
Spot 5 (75714–75738)	$1.3 < \eta^{jet}_{det} < 1.8$	$4.6 < \phi^{jet} < 5.1$	> 0.25

efficiency by applying the EM fraction cuts of HTFLT to the clean samples of data and Monte Carlo simulation. The data used is Run 1B minimum-bias data where the hot tower noise is very small, and the simulation is the PYTHIA Monte Carlo [51] which generates QCD high p_T processes producing the jets. The procedure is as follows.

(1) Select dijet events with $E_T^{jet} > 7\,\mathrm{GeV}$ for clean samples of the data and simulation. The generated events in the simulation are passed through the full detector simulation and the same analysis chain as the non-diffractive data.

(2) Pick up the leading jets lying in certain areas of detector η_{jet} versus ϕ_{jet}, corresponding to the hot tower spots seen in the diffractive data.

(3) Apply the same EM fraction cuts to the selected clean leading jets, and count the number of rejected jets or remaining jets for each hot spot.

(4) Count the number of good diffractive jets (i.e., not rejected by the HTFLT) for each hot spot in diffractive data.

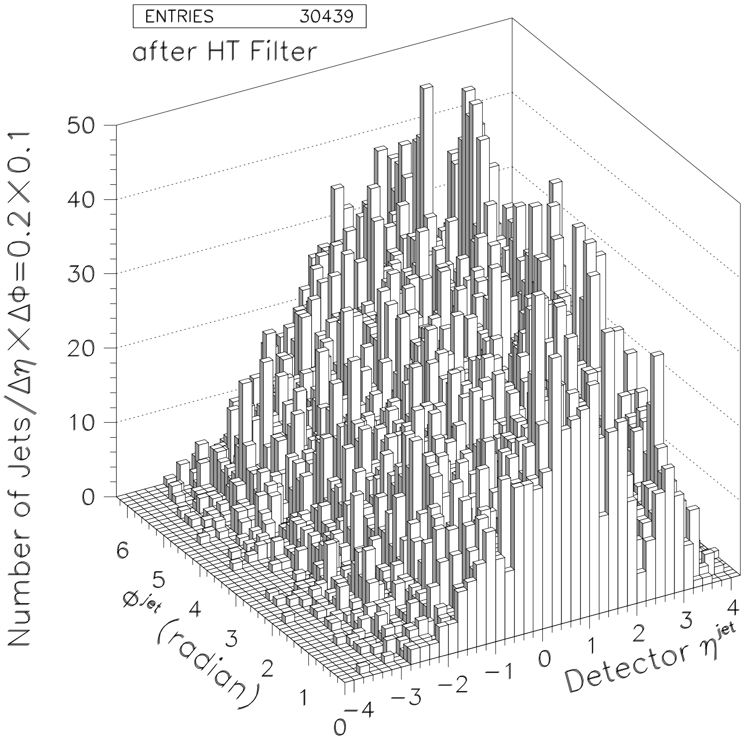

Figure 5.4: Leading jet distribution on detector η^{jet} versus ϕ^{jet} plane after applying the Hot Tower Rejection Filter in a sample of events with at least 2 jets with $E_T > 7\,\mathrm{GeV}$.

(5) Divide the number of rejected jets by that of remaining jets in (3), then multiplying it by (4) for each hot spot.

(6) Sum up the (5) over all the hot spots.

(7) Divide the number of diffractive dijet events after the HTFLT applied by the sum of this number and (6) multiplied by 2. The second jet should be also taken into account, which causes a factor 2.

From the above, we obtain the HTFLT efficiency $\varepsilon_{SDjj}^{HTFLT}$ to be

$$\varepsilon_{SDjj}^{HTFLT} \;=\; 96.9 \;\pm\; 0.2(stat.)\,\%.$$

This is an average of two obtained values: $97.4 \pm 0.1(stat.)\,\%$ for Run 1B data and

Table 5.2: The number of events after the selection cuts used in the analysis. Second column shows the sample names used in the text.

Selection Cuts	**Sample**	**# Events**	
$0.035 < \xi < 0.095$, $\|t\| < 1.0\,\mathrm{GeV}^2$ ⇒ *Diff. Inclusive Events* (= N_{SD}^{incl})	**RP**	1,638,993	
For Jets			
JTC96 Energy Corrections*		$> 7\,\mathrm{GeV}$	$> 10\,\mathrm{GeV}$
≥ 2 jets with $E_T > E_{Tmin}$		40,077	7,232
Hot Tower Rejection Filter	**PJJ**	30,439	5,510
For Low Multiplicity on Pot Side			
West $N_{BBC}(-5.9 < \eta < -3.2) \leq 6$ ⇒ *SD Dijet Events* (= N_{SD}^{jj})	**PJJ**	27,405	4,866
For DPE Selection			
East $N_{BBC}(3.2 < \eta < 5.9) = 0$		257	43
East $N_{CAL}(2.4 < \eta < 4.2) = 0$		132	17
(⇒ *DPE Dijet Candidate Events*)			

* Including the subtraction of UE energy E_T :
0.54 (0.37) GeV for SD (DPE) dijets

$96.4 \pm 0.3(stat)\,\%$ for PYTHIA Monte Carlo simulation. Also, we apply the difference (0.5 %) between the data and simulation results as a systematic uncertainty of the efficiency.

Finally, the HTFLT filter provides 30,439 (5,510) diffractive events and 32,629 (10,514) non-diffractive events with $E_T > 7$ (10) GeV good dijets. The former is called later the **"POT+ DIJET"** or **"PJJ"** event class. It means that it consists of events with a good leading $\bar{p}$ (=**P**) and at least 2 jets (=**JJ**) with $E_T > 7$ or 10 GeV. The numbers of diffractive and non-diffractive dijet events in each selection cut are given in Tables 5.2 and 5.3 respectively.

5.3.2 Overlay Background of ND Events

The main background contribution in the **PJJ** sample could be due to non-diffractive events in a minimum-bias (MB) type interaction, together with a random coincidence

Table 5.3: The number of non-diffractive events after the selection cuts used in the analysis.

Selection Cuts	**# Events**	
Total Triggers	342,150	
BADRUN Filter	342,150	
Select MB Trigger	340,727	
COSFLT Filter	340,698	
$\not{E}_T \leq 20\,\text{GeV}$	340,685	
$\Rightarrow$ *ND Inclusive Events* ($= N_{ND}^{incl}$)		
$\lvert Z_{vertex}\rvert \leq 60\,\text{cm}$	299,959	
For Jets		
JTC96 Energy Corrections*	$> 7\,\text{GeV}$	$> 10\,\text{GeV}$
≥ 2 jets with $E_T > E_{Tmin}$	43,379	14,224
Hot Tower Rejection Filter	32,629	10,514
$\Rightarrow$ *ND Dijet Events* ($= N_{ND}^{jj}$)		

* Including the subtraction of UE energy E_T : 1.16 GeV

of an event containing a Roman Pot track. Since dijets can be produced in either a diffractive or non-diffractive event, this background would consist of two possible compositions: 1) a diffractive dijet event overlapping with a MB inclusive event, and 2) a non-diffractive dijet event overlapping with a diffractive inclusive event. Thus this is in general an “overlay” background and will be proportional to the luminosity. However, we can evaluate this background using the forward detectors because the ND event fills the forward phase space with produced particles, in contrast to diffractive interactions in which the forward region should be void due to rapidity gap (or at least low multiplicity, in the cases where the gap does not cover the detector).

Figure 5.5 and Figure 5.6 show the BBC hit and FCAL tower multiplicities on the Roman Pot side (west) for the **PJJ** samples of $E_T > 7$ and 10 GeV dijet events respectively. The BBC hit multiplicity N_{BBC} is obtained from latched BBC bank using BBLDUN routine. The FCAL tower multiplicity N_{CAL} is obtained by counting the number of towers within $2.4 < \eta < 4.2$ having E_T above η-dependent thresholds

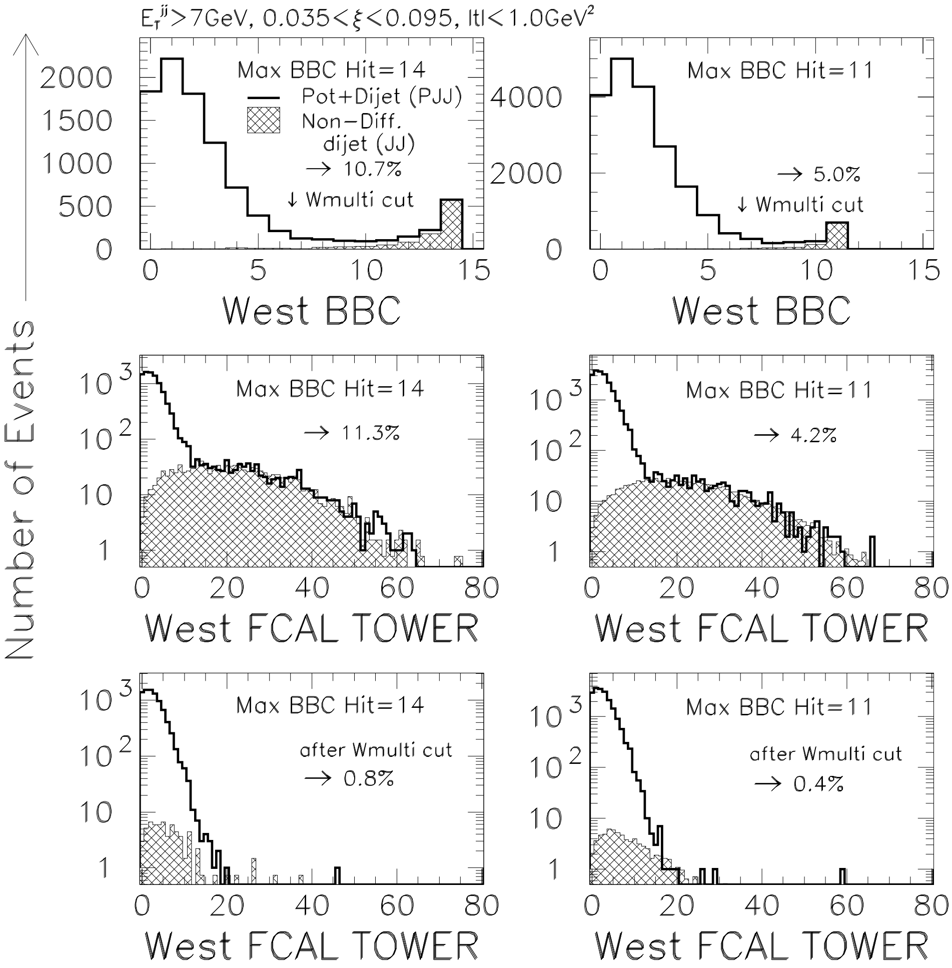

Figure 5.5: West BBC and FCAL tower multiplicity distributions for $E_T > 7\,\text{GeV}$ dijet events. In each plot left (right) side is for runs of maximum BBC hit=14 (11). Top plots show BBC distributions before the low multiplicity cut, and middle (bottom) plots show FCAL tower distributions before (after) the cut. The distributions of non-diffractive sample (shaded histogram) are normalized to the contents of diffractive sample (full line) at the maximum BBC hit bin $N_{BBC} = 14$ or 11, and $N_{CAL} \geq 20$ respectively.

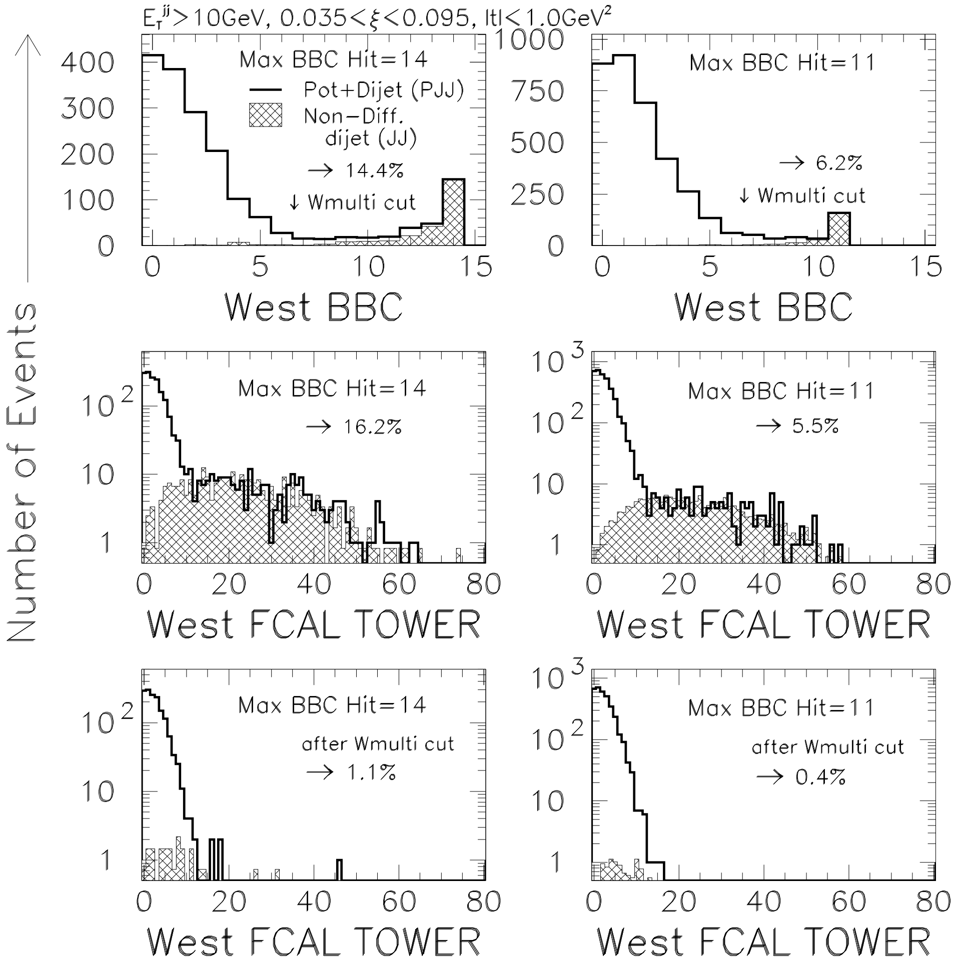

Figure 5.6: West BBC and FCAL tower multiplicity distributions for $E_T > 10\,\mathrm{GeV}$ dijet events. In each plot left (right) side is for runs of maximum BBC hit=14 (11). Top plots show BBC distributions before the low multiplicity cut, and middle (bottom) plots show FCAL tower distributions before (after) the cut. The distributions of non-diffractive sample (shaded histogram) are normalized to the contents of diffractive sample (full line) at the maximum BBC hit bin $N_{BBC} = 14$ or 11, and $N_{CAL} \geq 20$ respectively.

given by

$$E_T\,(\text{GeV}) > \begin{cases} 0.2 & (|\eta| < 1.1), \\ 0.450 \times \sin\left(2\tan^{-1} e^{-\eta}\right) & (1.1 \le |\eta| \le 1.5), \\ 0.2 & (1.5 < |\eta| \le 2.3), \\ -0.143 \times |\eta| + 0.579 & (2.3 < |\eta| \le 3.0), \\ -0.0625 \times |\eta| + 0.3375 & (3.0 < |\eta| \le 4.2). \end{cases} \tag{5.2}$$

This E_T threshold was developed in the diffractive W analysis for Run 1A+1B data [16] (details in [52]). We know that this tower threshold could increase the ability to discriminate more efficiently against non-diffractive "gaps" than a fixed E_T threshold of 200 MeV, as described in [53] and [54], and thereby increase the sensitivity for observing diffractive signals.

These figures show the distributions for non-diffractive dijet events (**JJ**) by the shaded histograms. The **PJJ** and **JJ** samples have completely different shapes, being dominated by low and high BBC counts respectively. We do not expect to see a first bin ($N_{BBC} = 0$) enhancement for **PJJ** sample because $\xi_{min} = 0.035$ corresponds approximately to a rapidity gap lying within the range $\eta_{gap} \le -7.5 + (-\ln \xi_{min}) = -4.1$ for the west side or $\eta_{gap} \ge 7.5 - (-\ln \xi_{min}) = 4.1$ for the east side. So the gap will not fully cover the BBC counters with the coverage $3.2 < |\eta| < 5.9$. Also, we should note that our diffractive data sample contains two types of runs with different maximum BBC hits of 14/15 ($75644 \le \text{RUN} \le 75647$, $75737 \le \text{RUN} \le 75738$), and 11/12 ($75650 \le \text{RUN} \le 75734$) for the west/east BBC. For the latter runs, some BBC counters were not working. So we separately deal with these samples as seen in the figures, and then combined them.

In Figures 5.5 and 5.6, diffractive dijet event distribution (full line) shows there exists some non-diffractive (overlay) background in the high multiplicity region. From top left plots showing the non-diffractive dijet distribution (shaded histogram) normalized to the content in the maximum bin =14, it is indicated that 10.7 % (14.4 %) of **PJJ** sample with $E_T > 7$ (10) GeV dijets can be attributed to non-diffractive overlay background. Top right plots show that the **PJJ** sample with $E_T > 7$ (10) GeV dijets for maximum BBC bin =11 contains 5.0 % (6.2 %) overlay background. Combining the results of two samples of runs, we get 6.9 % (8.9 %) overlay background for $E_T > 7$ (10) GeV dijets. Also, by normalizing the non-diffractive FCAL tower distributions to diffractive distributions at $N_{CAL} \geq 20$, we get 6.5 % (9.0 %) overlay background for $E_T > 7$ (10) GeV dijets. Finally, by averaging over the BBC and FCAL tower results, we obtain $6.7 \pm 0.1(stat.)\,\%$ ($9.0 \pm 0.3(stat.)\,\%$) overlay background for **PJJ** sample of $E_T > 7$ (10) GeV dijets.

Figures 5.5 and 5.6 also show that an overlay background could be removed by using a cut to N_{BBC}. When we select a cut of $N_{BBC} \leq 6$, we estimate a remaining overlay background fraction $F^{ND\,BG}_{SD\,jj}$ to be

$$\begin{aligned} F^{ND\,BG}_{SD\,jj} &= 0.51 \pm 0.04(stat.)\,\% \qquad (E_T > 7\,\mathrm{GeV}) \\ &= 0.65 \pm 0.12(stat.)\,\% \qquad (E_T > 10\,\mathrm{GeV}). \end{aligned}$$

This cut brings the number of **PJJ** events from 30,439 (5,510) to 27,405 (4,866) for $E_T > 7$ (10) GeV **PJJ** sample. The FCAL tower distributions after requiring $N_{BBC} \leq 6$ are shown in bottom plots of these figures. By counting the expected non-diffractive events corresponding to the shaded regions and dividing them by the total number of remaining diffractive events, we evaluate the above fractions. The systematic uncertainty of background fraction is estimated by changing the cut to $N_{BBC} \leq 5$ or $N_{BBC} \leq 7$. The result is a variation of $\pm 0.15\,\%$ ($\pm 0.15\,\%$) for $E_T > 7$ (10) GeV jets. We call this BBC multiplicity requirement the "low multiplicity cut" to the dijet events, and the dijet selected by the low multiplicity cut would be thought of as a single diffractive (SD) dijet. We use this terminology but do not claim that all these events are actually due to pomeron exchange. From now on, the dijet event after the low multiplicity cut will be also called **PJJ** class. The number of diffractive dijet events in each dijet selection is summarized in Table 5.2.

The efficiency of this low multiplicity cut is evaluated by subtracting the estimated non-diffractive overlay background from the **PJJ** sample, and then dividing the number of diffractive dijet events above BBC cut threshold by the total number of diffractive events after overlay background subtraction. As a result, we find the BBC cut efficiency $\varepsilon_{SD\,jj}^{Wmutli}$ to be

$$\begin{aligned}\varepsilon_{SD\,jj}^{Wmutli} &= 96.2 \pm 0.1(stat.)\,\% \qquad (E_T > 7\,\mathrm{GeV}) \\ &= 96.3 \pm 0.3(stat.)\,\% \qquad (E_T > 10\,\mathrm{GeV}).\end{aligned}$$

The systematic errors are estimated in the same way as above, to be 1.7 % (1.4 %) for two E_T thresholds.

5.4 Single Vertex Selection for SD Dijet

The single vertex selection could reject diffractive dijet events with high track multiplicity produced in a single interaction because high particle multiplicity would produce multiple fake vertices due to reconstruction ambiguities. Secondary particles in the interactions between particles and the beam pipe also could make vertices. Figure 5.7 and Figure 5.8 show the BBC and FCAL tower multiplicity distributions on the west side for $E_T > 7\,\mathrm{GeV}$ and $> 10\,\mathrm{GeV}$ SD dijet events with multiple (> 1) vertices.

For $E_T > 7\,\mathrm{GeV}$ SD dijet events, we have 30,439 dijets with a single vertex before the low multiplicity cut. By fitting the single vertex BBC distribution to that of multiple vertices (13,995 events) at $N_{BBC} = 0 - 2$, we estimate that 48.5 % ($6,789.6 \pm 65.4$) of multiple vertices could be produced in single interactions. This means the 1-vertex selection efficiency, defined as a fraction of single interaction events that pass the single vertex cut, for $E_T > 7\,\mathrm{GeV}$ SD dijet events can be estimated as follows,

$$\varepsilon_{SD\,jj}^{1vtx}(\mathrm{BBC}) = \frac{30,439}{30,439 + (6,789.6 \pm 65.4)} = 81.8 \pm 0.6(stat.)\,\%.$$

On the other hand, the FCAL tower distribution shows that 48.5 % ($6,792.0 \pm 58.6$) of events with multiple vertices could be produced in single interactions. We then estimate the 1-vertex efficiency based on west FCAL tower distribution to be

$$\varepsilon_{SD\,jj}^{1vtx}(\mathrm{FCAL}) = \frac{30,439}{30,439 + (6,792.0 \pm 58.6)} = 81.8 \pm 0.6(stat.)\,\%.$$

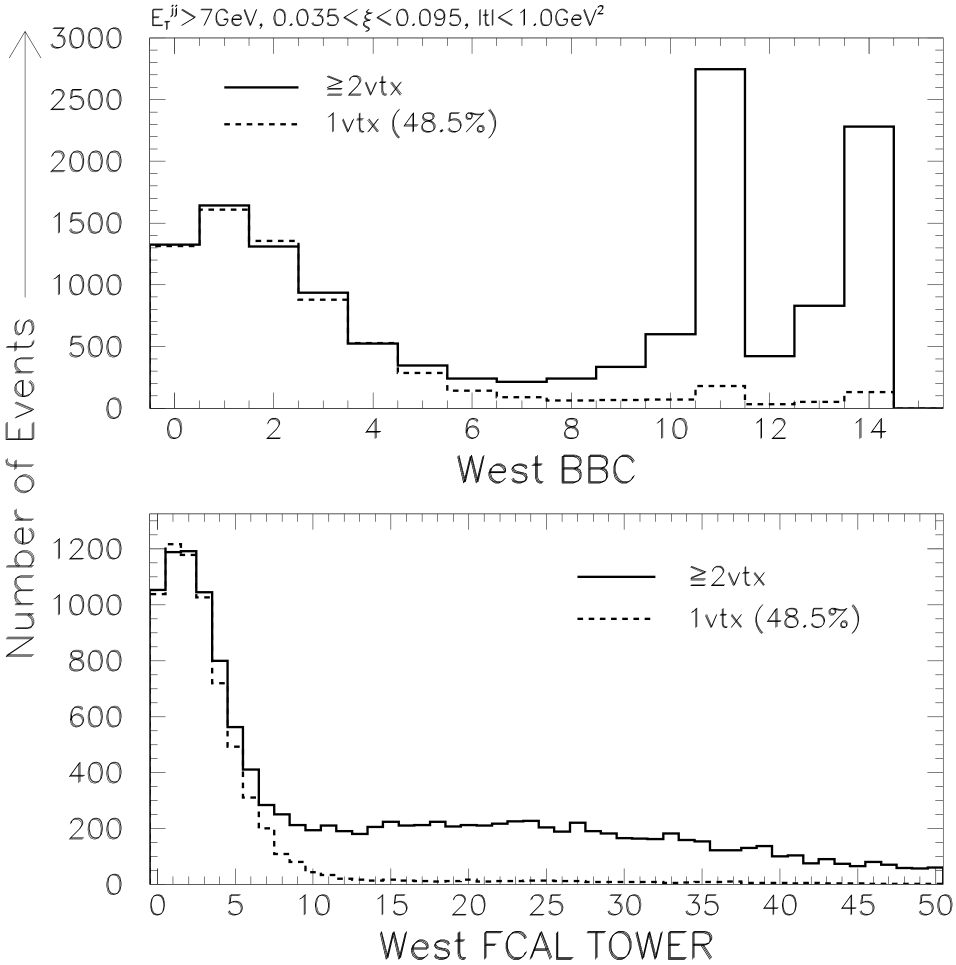

Figure 5.7: West BBC and FCAL tower multiplicity distributions for $E_T > 7\,\mathrm{GeV}$ dijet events with multiple vertices. The BBC is shown in top, and FCAL tower in bottom. The dashed histograms are the distributions of single vertex data, fitted to the low multiplicity region ($N_{BBC} \leq 2$ or $N_{CAL} \leq 2$) of the data with multiple vertices (full lines).

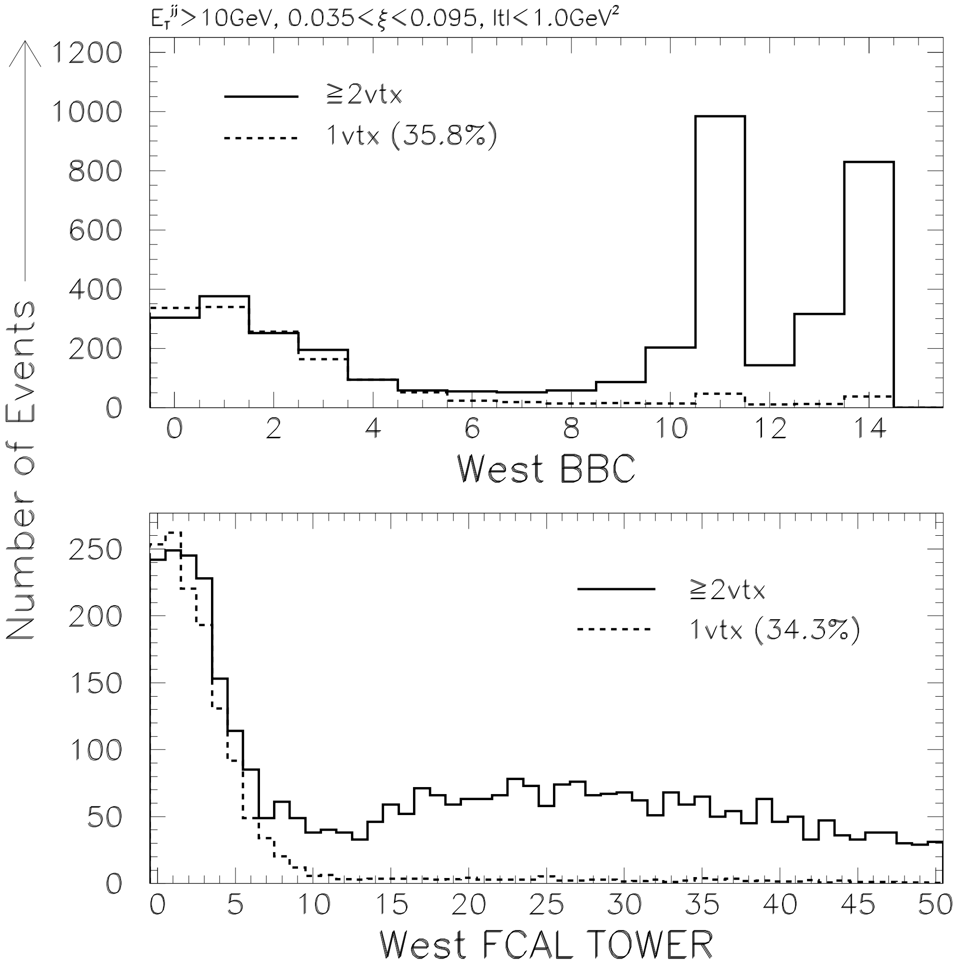

Figure 5.8: West BBC and FCAL tower multiplicity distributions for $E_T > 10\,\mathrm{GeV}$ dijet events with multiple vertices. The BBC is shown in top, and FCAL tower in bottom. The dashed histograms are the distributions of single vertex data, fitted to the low multiplicity region ($N_{BBC} \leq 2$ or $N_{CAL} \leq 2$) of the data with multiple vertices (full lines).

Table 5.4: Efficiencies and background fractions of SD dijets with $E_T > 7\,\mathrm{GeV}$ and $E_T > 10\,\mathrm{GeV}$, and inclusive SD events. All the errors are statistical only.

SD Inclusive Events	N_{SD}^{incl}	$1,638,993 \pm 1,280$	
⇒ after RP acceptance correction	$N_{SD}^{incl,\,RP}$	$2,086,855 \pm 1,727$	
ND Overlay Background	$F_{SD\,incl}^{ND\,BG}$	$3.0 \pm 0.01\,\%$	
BEAM-GAS Background	$F_{SD\,incl}^{GAS}$	$5.2 \pm 0.02\,\%$	
Single Vertex Selection Efficiency	$\varepsilon_{SD\,incl}^{1vtx}$	$88.5 \pm 0.1\,\%$	
Dijet $\boldsymbol{E_{Tmin}}$		$\boldsymbol{E_T > 7\,\mathrm{GeV}}$	$\boldsymbol{E_T > 10\,\mathrm{GeV}}$
SD Dijet Events	N_{SD}^{jj}	$27,405 \pm 166$	$4,866 \pm 70$
⇒ after RP acceptance correction	$N_{SD}^{jj,\,RP}$	$34,413 \pm 219$	$6,049 \pm 91$
ND Overlay Background	$F_{SD\,jj}^{ND\,BG}$	$0.51 \pm 0.04\,\%$	$0.65 \pm 0.12\,\%$
Single Vertex Selection Efficiency	$\varepsilon_{SD\,jj}^{1vtx}$	$81.8 \pm 0.4\,\%$	$79.6 \pm 0.9\,\%$
Wmulti Cut Efficiency	$\varepsilon_{SD\,jj}^{Wmulti}$	$96.2 \pm 0.1\,\%$	$96.3 \pm 0.3\,\%$
HT Filter Efficiency	$\varepsilon_{SD\,jj}^{HTFLT}$	$96.9 \pm 0.2\,\%$	

(Statistical Errors Only)

By taking an average of the two estimated values from BBC and FCAL tower, the single vertex selection efficiencies for SD dijet events are estimated as follows,

$$\begin{aligned} \varepsilon_{SD\,jj}^{1vtx} &= 81.8 \ \pm\ 0.4(stat.)\,\% \qquad (E_T > 7\,\mathrm{GeV}) \\ &= 79.6 \ \pm\ 0.9(stat.)\,\% \qquad (E_T > 10\,\mathrm{GeV}). \end{aligned}$$

The BBC and FCAL tower results give very similar results. So, we conservatively apply a systematic uncertainty of 10 % of $(1 - \varepsilon_{SD\,jj}^{1vtx})$ to the efficiency, according to [64]. So the systematic error is 1.8 % (2.0 %) for dijet events of $E_T > 7$ (10) GeV. It would be worth noting that the efficiency at $E_T > 10\,\mathrm{GeV}$ is lower than 7 GeV because higher E_T jets could make more fake vertices in single interaction events. This is consistent with the result of [64].

The efficiencies and background fractions estimated above are listed in Table 5.4. In the table the numbers of dijet and inclusive events corrected for the Roman Pot acceptance are also given. This correction is done by applying a weight of $1/A(\xi, |t|)$ to every event as a function of ξ and $|t|$, where $A(\xi, |t|)$ is the Roman Pot acceptance that is shown in Figure 4.8. The statistical uncertainty on the number of acceptance corrected events is obtained as $\sqrt{\sum_i (1/A(\xi, |t|)_i)^2}$, where the sum is carried up to the number of events before the acceptance correction is applied.

Chapter 6

Dijet Production by Double Pomeron Exchange

Using SD dijet data with a leading antiproton observed in the Roman Pot (**PJJ**), we search for the signal of dijet production by Double Pomeron Exchange (DPE) process. The method used in DPE search is based on finding a rapidity gap due to the pomeron exchange from the proton because the DPE exchange signal is expected to be observed with zero or low particle multiplicities in the forward detectors on the outgoing proton (east) direction. Note that a rapidity gap means strictly zero particles, however it may not extend fully across the gap search region, in which case we can have low multiplicity.

After discussing the dijet kinematics, we estimate the dijet production cross section in DPE events and compare it with those of single diffractive and non-diffractive events. In the estimation we experimentally measure the ξ of the pomeron from the proton and a corresponding rapidity gap acceptance, defined as the fraction of DPE events with a rapidity gap on the proton side to total DPE events. These measurements will allow us to check the factorization property for the proton and antiproton in diffractive $\bar{p}p$ interactions. Another issue of interest is a measurement of the mass fraction of dijets for DPE events. This quantity will provide the information of the pomeron parton distribution function.

6.1 Search for DPE Dijet Production

We use the gap method in search for DPE signal since we do not have the Roman Pots for the outgoing proton side. The upper half of Figure 6.1 shows the multiplicity distribution of the BBC hits N_{BBC-p} ($3.2 < \eta < 5.9$) versus FCAL towers N_{CAL-p} ($2.4 < \eta < 4.2$) on the proton side in $E_T > 7\,\mathrm{GeV}$ **PJJ** sample of 27,405 SD dijet events with $0.035 < \xi < 0.095$ and $|t| < 1.0\,\mathrm{GeV}^2$. The subscript p means the outgoing proton direction. The η-dependent tower threshold (Eq. (5.2)) is used for tower multiplicity. We have put all the events with $N_{BBC-p} \geq 12$ in an overflow bin because for this analysis we only need to know that there were "many" hits.

We find three major components of **PJJ** dijet sample: 1) large multiplicity around $N_{BBC-p} > 10$ or $N_{CAL-p} > 10$, 2) low multiplicity roughly around $2 < N_{BBC-p} < 5 \sim 6$ or $2 < N_{CAL-p} < 10$, and 3) a clear spike seen in $N_{BBC-p} = N_{CAL-p} = 0$ bin (called (0,0) bin from now on). The former 1) and 2) are SD dijet events, but 3) implies that there is no particle in the BBC and FCAL tower coverage, that is, a rapidity gap extending over $2.4 < \eta < 5.9$ on the proton side.

The POMPOMPYT Monte Carlo simulation, a generator for DPE events (Section 7.2 in Chapter 7) predicts the shape of this multiplicity distribution for DPE dijet events (see Figure 7.2). Details of the Monte Carlo will be described there, but one of the impressive results is that the low multiplicity distribution of DPE Monte Carlo events around $N_{BBC-p} = 0$ and $N_{CAL-p} \leq 3$ is in qualitative agreement with the data distribution. Of course it depends on the pomeron model but we obtain a consistent distribution assuming the most probable parton density function of the pomeron. However, a portion of the simulated DPE events spreads over a wider tower range depending on ξ of the pomeron from the proton. In addition, the multiplicity range $1 \leq N_{BBC-p} \leq 3 \sim 4$ of the data would contain the background from SD dijet events

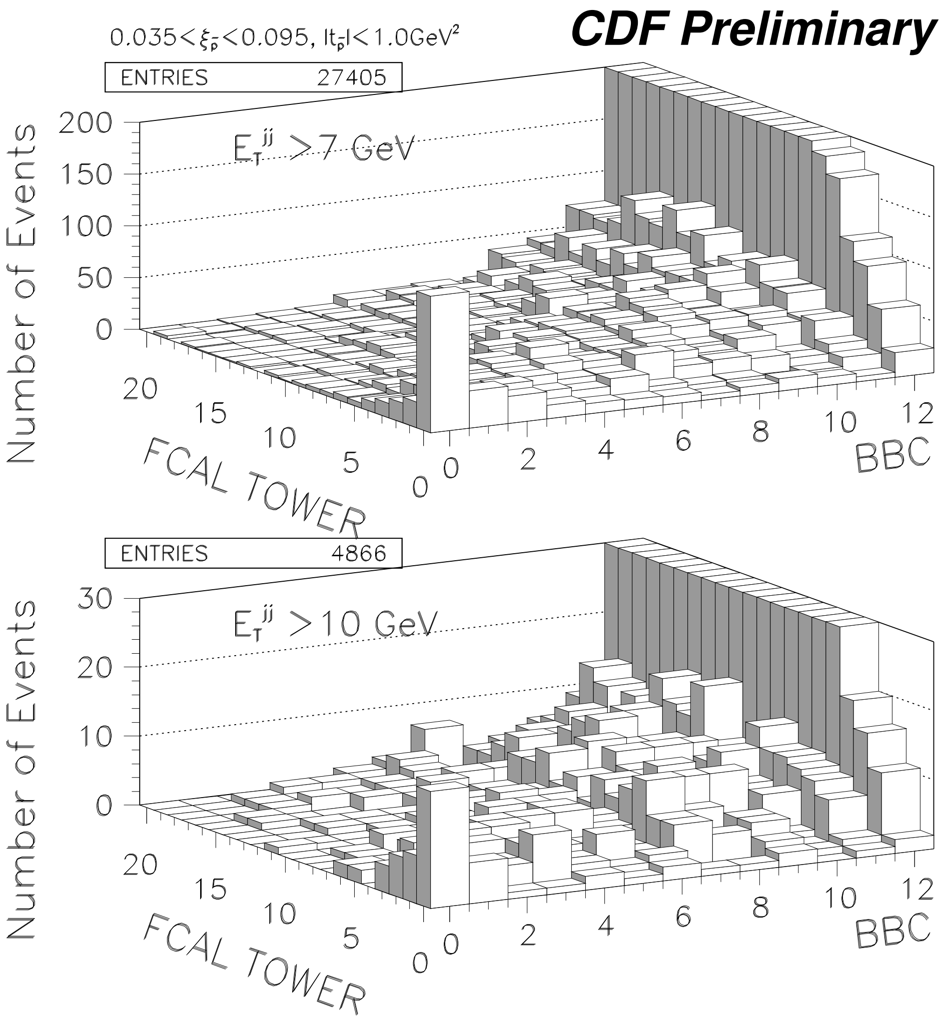

Figure 6.1: Multiplicity distribution of the BBC hits versus FCAL towers on the p side in a sample of diffractive events with dijets of $E_T > 7\,\mathrm{GeV}$ (upper) and $E_T > 10\,\mathrm{GeV}$ (lower). The ξ and t for leading antiproton are referred to as $\xi_{\bar{p}}$ and $t_{\bar{p}}$ respectively, also in the following figures.

with low multiplicity. Therefore we should carefully extract the "pure DPE events" from the "data signal" in the (0,0) bin. In the DPE signal estimation, the POMPOMPYT simulation would help us to understand the background distribution under the peak at the (0,0) bin, and develop a proper estimate of the DPE contribution.

The distribution for $E_T > 10\,\mathrm{GeV}$ dijets is shown in the lower half of Figure 6.1. The Monte Carlo simulation expects more signal concentrating at the (0,0) bin for higher $E_T > 10\,\mathrm{GeV}$ dijets in comparison to lower $7\,\mathrm{GeV}$ case. It is clearly seen that there is a rapidity gap signal due to DPE events in the (0,0) bin for this higher E_T sample, too.

A typical event display of DPE dijet candidates is shown in Figure 6.2. This event contains two jets with $E_T = 19\,\mathrm{GeV}$ and $18\,\mathrm{GeV}$ and a good leading antiproton with $\xi = 0.069$ and $|t| = 0.0078\,\mathrm{GeV}^2$ in the Roman Pots. Both east and west Microplugs are almost empty due to the rapidity gaps. The number of BBC hits and forward calorimeter tower multiplicity on positive η side (proton direction) are also both zero.

6.2 Estimate of the DPE Signal

In order to estimate the DPE contribution in the data signal, we looked at the diagonal multiplicity (N_{DIAG-p}) distribution of the BBC versus FCAL tower. Figure 6.3 shows the number of events in each (N_{BBC-p}, N_{CAL-p}) bin and the diagonal multiplicity distribution for $E_T > 7\,\mathrm{GeV}$ and $> 10\,\mathrm{GeV}$ dijet events. As described above, a fraction of DPE signal events could leak out of the (0,0) bin while some SD background events leak in. We expect that the extrapolation from high multiplicity region into the (0,0) bin is a good scheme to extract the signal, since high multiplicity bins contain only SD background events. Finally, after trying several methods, we have concluded that the extrapolation along the diagonal direction from $N_{DIAG-p} = 2, 3, \ldots$ into the (0,0) bin provides a good estimate of DPE events since 1) the DPE signal extending over

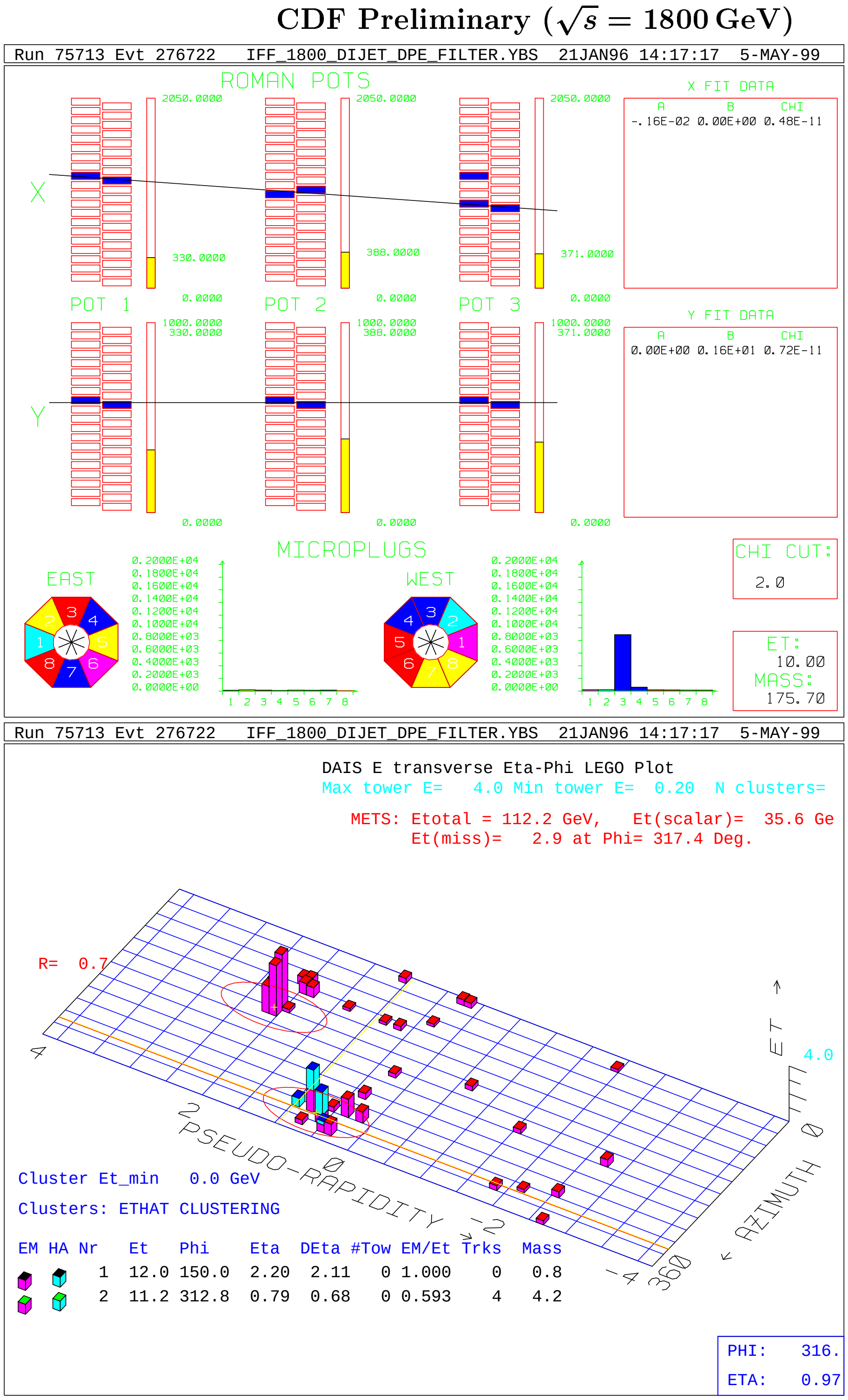

Figure 6.2: A DPE dijet candidate event observed with the Roman Pots.

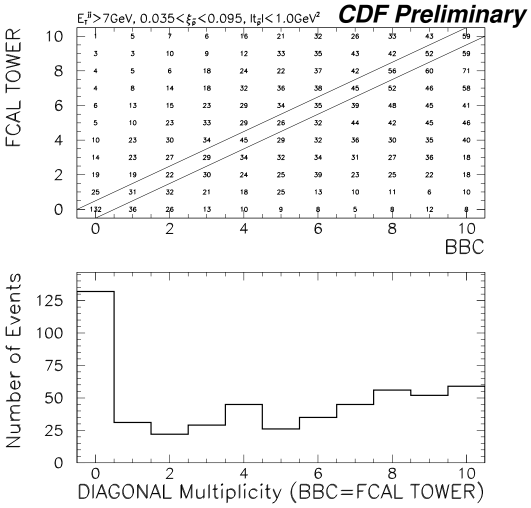

(a) Dijet $E_T > 7\,\mathrm{GeV}$

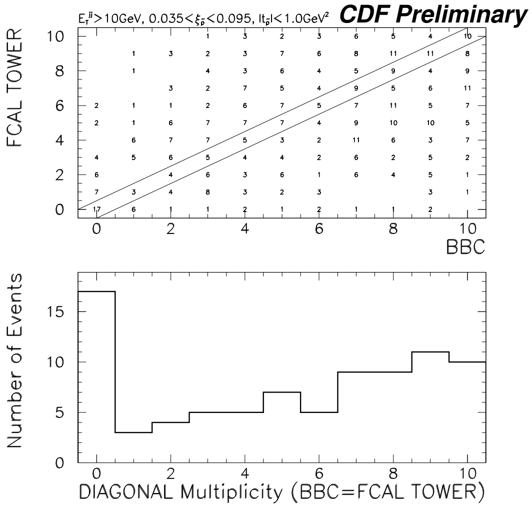

(b) Dijet $E_T > 10\,\mathrm{GeV}$

Figure 6.3: BBC – FCAL diagonal multiplicity distribution on the p side for diffractive events with dijets of (a) $E_T > 7\,\mathrm{GeV}$ and (b) $E_T > 10\,\mathrm{GeV}$. Upper half shows the number of events, and lower half shows the distributions along the diagonal direction.

neighbor bins along the diagonal is very small, but 2) a sizeable fraction ($\sim 10\,\%$) of the DPE events extends to the next (1,1) bin, as seen in the table of POMPOMPYT prediction (Figure 7.2).

As the next step to estimate the signal and background in the (0,0) bin, we perform linear fits to the diagonal distribution. We put a start point of the linear fit at $N_{DIAG-p} = 2$, and then fit the distribution within the ranges up to $N_{DIAG-p} = 4, 5, \ldots, 10$, so that 7 fits are done (this is called Fit 1). The fits from $N_{DIAG-p} = 1$ to $N_{DIAG-p} = 3, 4, \ldots, 10$ (total 8 fits) are also done to estimate the systematic uncertainty in the fits (called Fit 2). Figure 6.4 and Figure 6.5 show the diagonal distributions with the linear fits of Fit 1 and 2 respectively, along with the obtained fit results (P1 is an intercept at $N_{DIAG-p} = 0$, and P2 is a slope of linear function). By taking average of the intercepts and slopes over the fit range, and using the uncer-

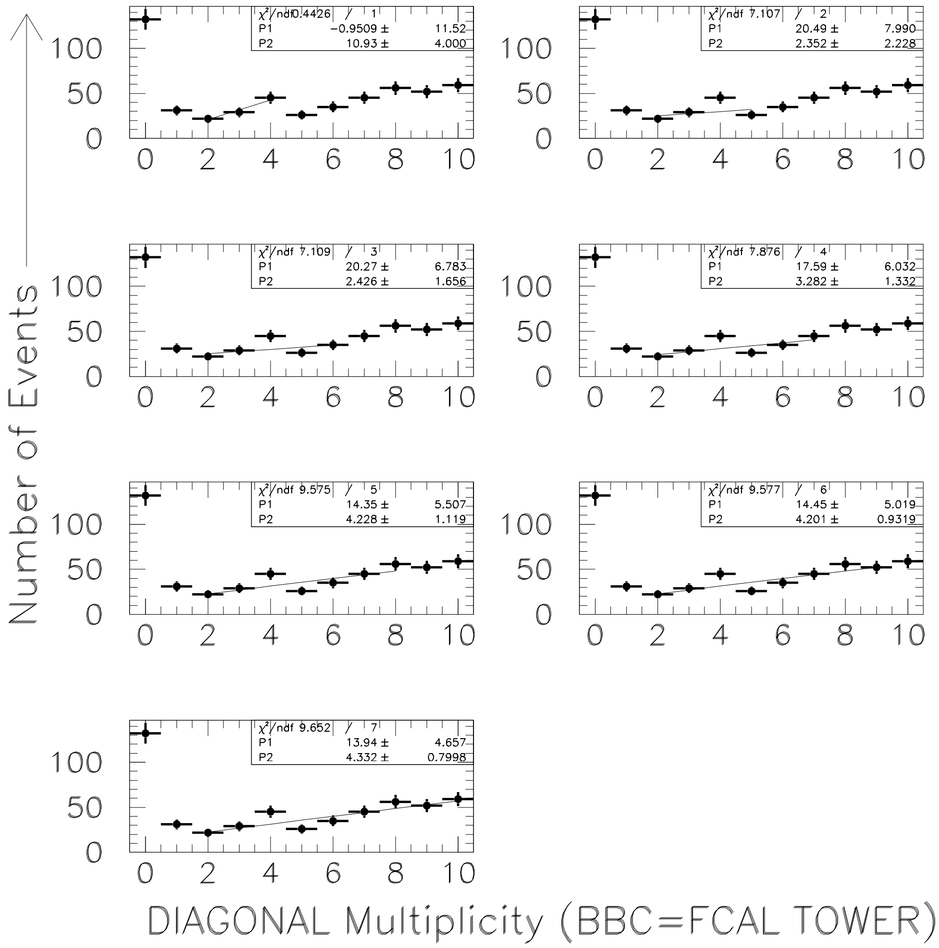

Figure 6.4: Diagonal multiplicity distribution between the BBC hits and FCAL towers on the p side for diffractive events with dijets of $E_T > 7\,\text{GeV}$. Also shown are the linear fits to data within 7 ranges $2 \leq N_{DIAG-p} \leq 4, 5, \ldots, 10$ to estimate the DPE events in the first bin.

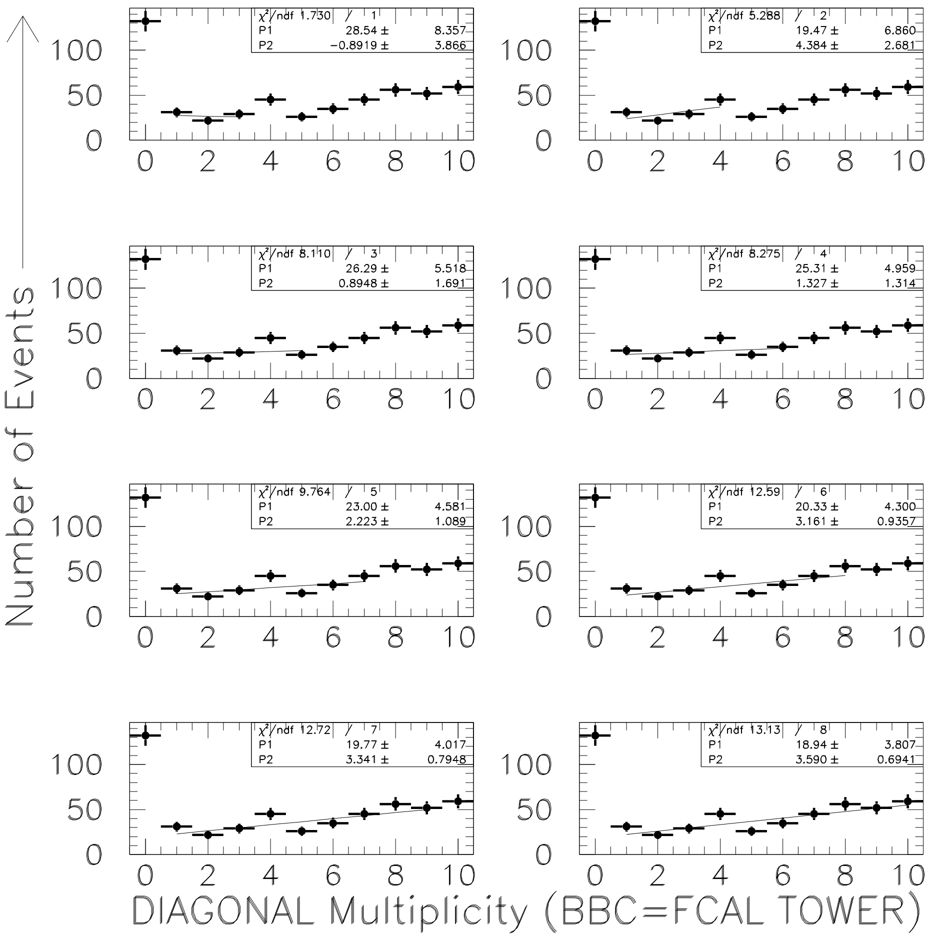

Figure 6.5: Diagonal multiplicity distribution between the BBC hits and FCAL towers on the p side for diffractive events with dijets of $E_T > 7\,\mathrm{GeV}$. Also shown are the linear fits to data within 8 ranges $1 \leq N_{DIAG-p} \leq 3, 4, \ldots, 10$ to estimate the systematic uncertainty of the fits.

tainties in the fit in which the intercept and slope are closest to the mean values of each Fit 1 and 2, we have the final linear fit functions used to estimate the DPE contribution, and their systematic uncertainty from the fit. Figure 6.6 shows the results of the fits for $E_T > 7\,\text{GeV}$ dijet events. As seen in the left side plot, extrapolating Fit 1 linear function into the (0,0) bin, we obtain the number of DPE events to be $N^{jj}_{DPE} = 117.7 \pm 5.5(syst.)_{fit}$. This systematic uncertainty is equivalent to the shaded error band at the (0,0) bin in Figure 6.6, and it arises from the uncertainties of the fit parameters. Finally the number of DPE dijet events in the data signal is estimated to be

$$N^{jj}_{DPE} \;=\; 117.7 \;\pm\; 12.1(stat.) \;\pm\; 11.0(syst.)_{fit} \qquad (E_T > 7\,\text{GeV}).$$

The systematic uncertainty of 11.0 events is derived by adding in quadrature the difference between Fit 1 and Fit 2 results and the uncertainties on the fit parameters. When applying the same extrapolation method to higher $E_T > 10\,\text{GeV}$ dijet events, we obtain

$$N^{jj}_{DPE} \;=\; 14.4 \;\pm\; 4.4(stat.) \;\pm\; 2.5(syst.)_{fit} \qquad (E_T > 10\,\text{GeV}),$$

as seen in Figure 6.7.

We have tried different methods to estimate the DPE signal. The DPE signal region was changed from the (0,0) bin to the 2×2 area on the 2-dimensional (N_{BBC-p}, N_{CAL-p}) plane, i.e., (0,0), (0,1), (1,0) and (1,1) bins (called the range S). Then, to estimate the background, the three expanding bands, 1) ($N_{BBC-p} \leq 2$, $N_{CAL-p} \leq 2$) except the range S (total 5 bins), 2) ($N_{BBC-p} \leq 3$, $N_{CAL-p} \leq 3$) except the S (total 12 bins), and 3) ($N_{BBC-p} \leq 4$, $N_{CAL-p} \leq 4$) except the S (total 21 bins) were taken. By summing up the number of events in the band 1, 2 and 3, and then dividing them by 5, 12 and 21 respectively, we obtained the average number of background in one bin. Under the assumption that the background distribution is flat, we obtained the consistent number of DPE events within the uncertainty by subtracting the evaluated number of background from the events in the (0,0) bin. Another choice of signal area

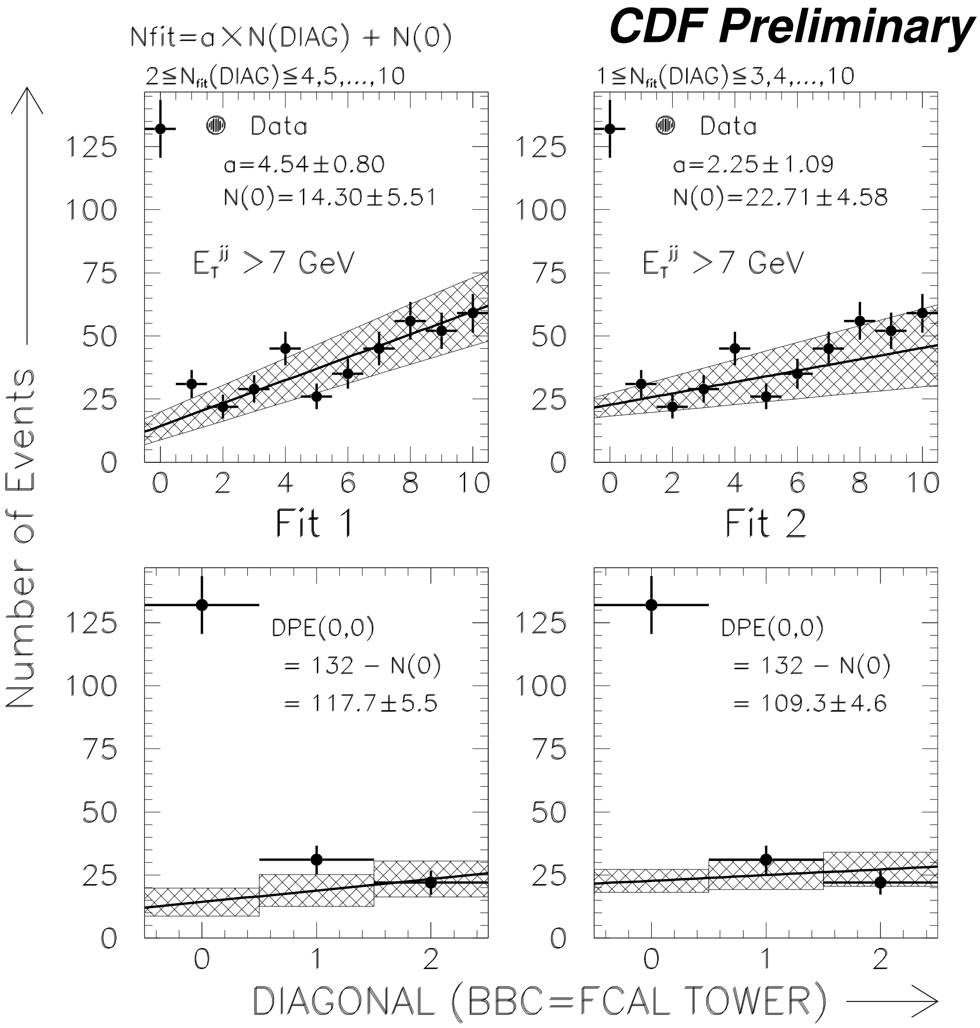

Figure 6.6: Linear fit results to the diagonal multiplicity distribution between the BBC hits and FCAL towers on the p side for diffractive events with dijets of $E_T > 7\,\mathrm{GeV}$. Left plots are for the fits to the ranges $2\leq\ N_{DIAG-p}\ \leq\ 4, 5, \ldots, 10$ to estimate the DPE events (Fit 1), and right for the ranges $1\leq\ N_{DIAG-p}\ \leq\ 3, 4, \ldots, 10$ to estimate the systematic uncertainty of the fits (Fit 2). The shaded bands correspond to the fit functions varying with the $\pm 1\sigma$ uncertainties of intercepts N(0) and slopes a. Lower half shows the region of $N_{DIAG-p} \leq 2$.

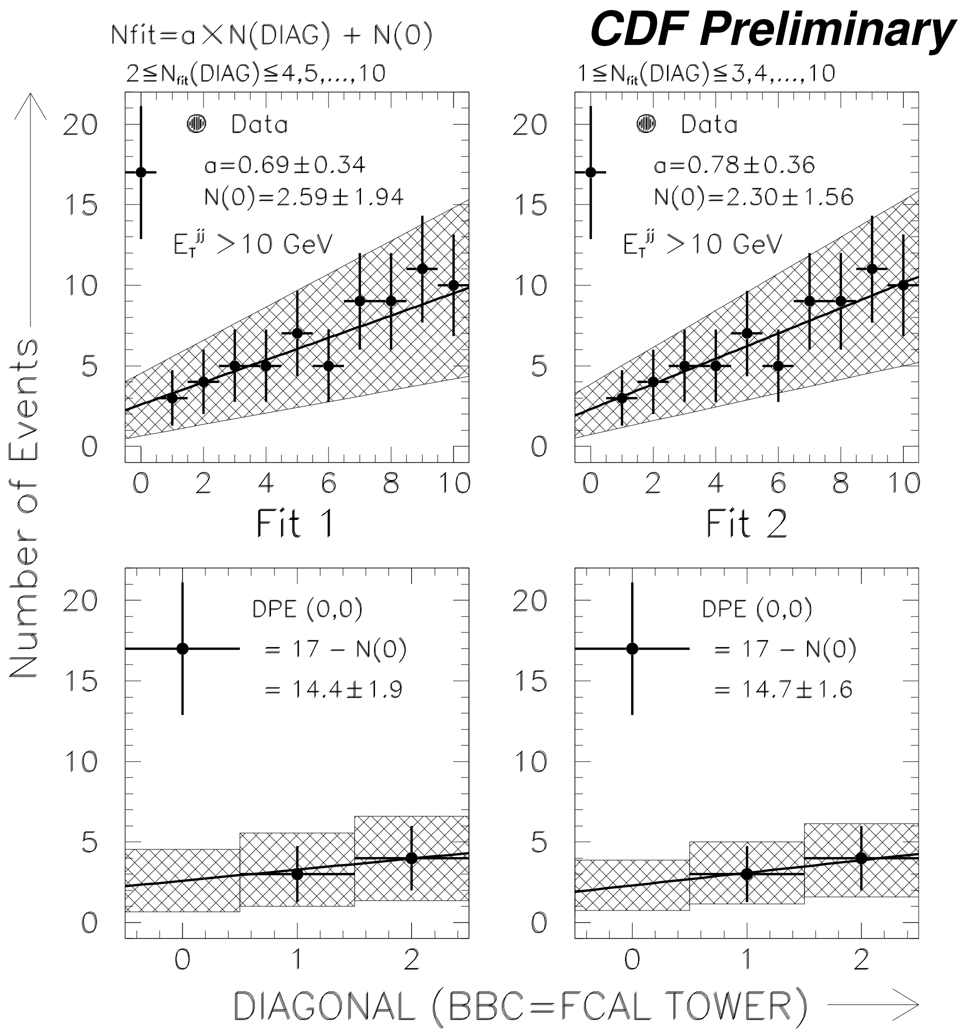

Figure 6.7: Linear fit results to the diagonal multiplicity distribution between BBC hits and FCAL towers on the p side for diffractive events with dijets of $E_T > 10\,\mathrm{GeV}$. Left plots are for the fits to the ranges $2\leq\ N_{DIAG-p}\ \leq\ 4, 5, \ldots, 10$ to estimate the DPE events (Fit 1), and right for the ranges $1\leq\ N_{DIAG-p}\ \leq\ 3, 4, \ldots, 10$ to estimate the systematic uncertainty of the fits (Fit 2). The shaded bands correspond to the fit functions varying with the $\pm 1\sigma$ uncertainties of intercepts N(0) and slopes a. Lower half shows the region of $N_{DIAG-p} \leq 2$.

such as 3×1 also gave the similar results. Consequently we conclude that the diagonal extrapolation method would be optimal.

6.3 Single Vertex Selection for DPE Dijet

In the calculation of dijet cross section for DPE events, we have to know the single vertex selection efficiency for DPE dijet events, as for SD events. For this purpose, the whole data sample including events with multiple vertices is reanalyzed. Using all the same cuts except for the vertex multiplicity requirement, two samples of 33,730 $E_T > 7\,\mathrm{GeV}$ and 6,198 $E_T > 10\,\mathrm{GeV}$ dijet events are obtained.

To see the effect of single vertex selection on the magnitude of DPE signal, the multiplicity correlation between the BBC hits and FCAL towers on the proton side (Figure 6.8 and Figure 6.9) is taken for all the dijet events including multiple vertices, and compared with that for single vertex data. It is seen that the magnitude of the spike in single vertex data is similar to that of events with multiple vertices, indicating that the single vertex selection is efficient. Using the linear extrapolation scheme along the diagonal, the number of DPE events in the (0,0) bin for data including multiple vertices is estimated to be

$$\begin{aligned} N_{DPE}^{jj,\geq 1\,vtx} &= 122.8 \pm 12.5(stat.) \pm 10.4(syst.)_{fit} \qquad (E_T > 7\,\mathrm{GeV}) \\ &= 16.7 \pm 4.6(stat.) \pm 2.5(syst.)_{fit} \qquad (E_T > 10\,\mathrm{GeV}). \end{aligned}$$

We therefore find that the single vertex requirement rejects $N_{DPE}^{jj,\geq 1\,vtx} - N_{DPE}^{jj} \approx 5$ $E_T > 7\,\mathrm{GeV}$ DPE events with single interactions. Because true multiple interactions (not single interactions with fake multiple vertices) would produce some particles in the relevant forward detectors, they are expected to show non-zero multiplicity for BBC or FCAL tower on the proton side. Thus, the single vertex selection efficiency $\varepsilon_{DPE\,jj}^{1vtx}$ for DPE dijets is evaluated to be

$$\varepsilon_{DPE\,jj}^{1vtx} = 95.9 \pm 1.9(stat.)\,\%,$$

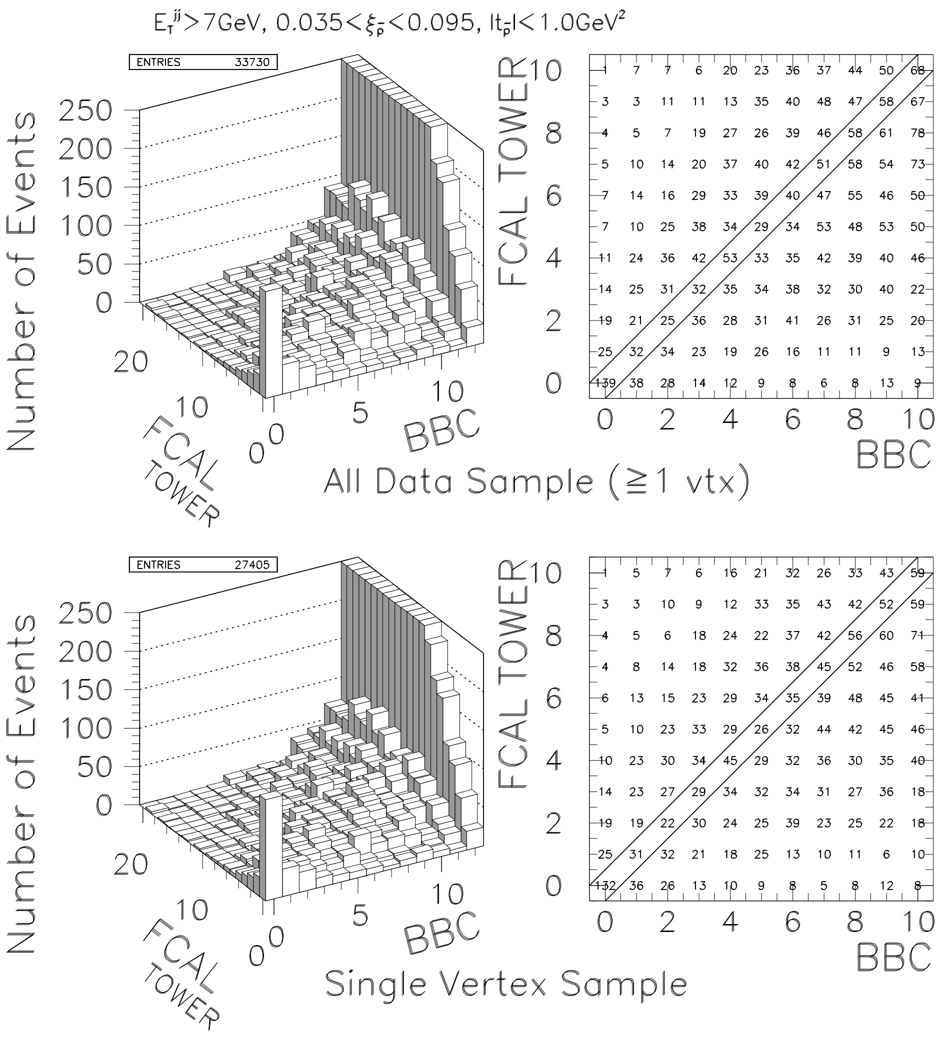

Figure 6.8: Multiplicity distribution of the BBC hits versus FCAL towers on the p side for diffractive events with dijets of $E_T > 7\,\text{GeV}$. A spike at $N_{BBC-p} = N_{CAL-p} = 0$ for the data including multiple vertices (upper) has the similar magnitude to that for single vertex data (lower), which indicates high single vertex selection efficiency.

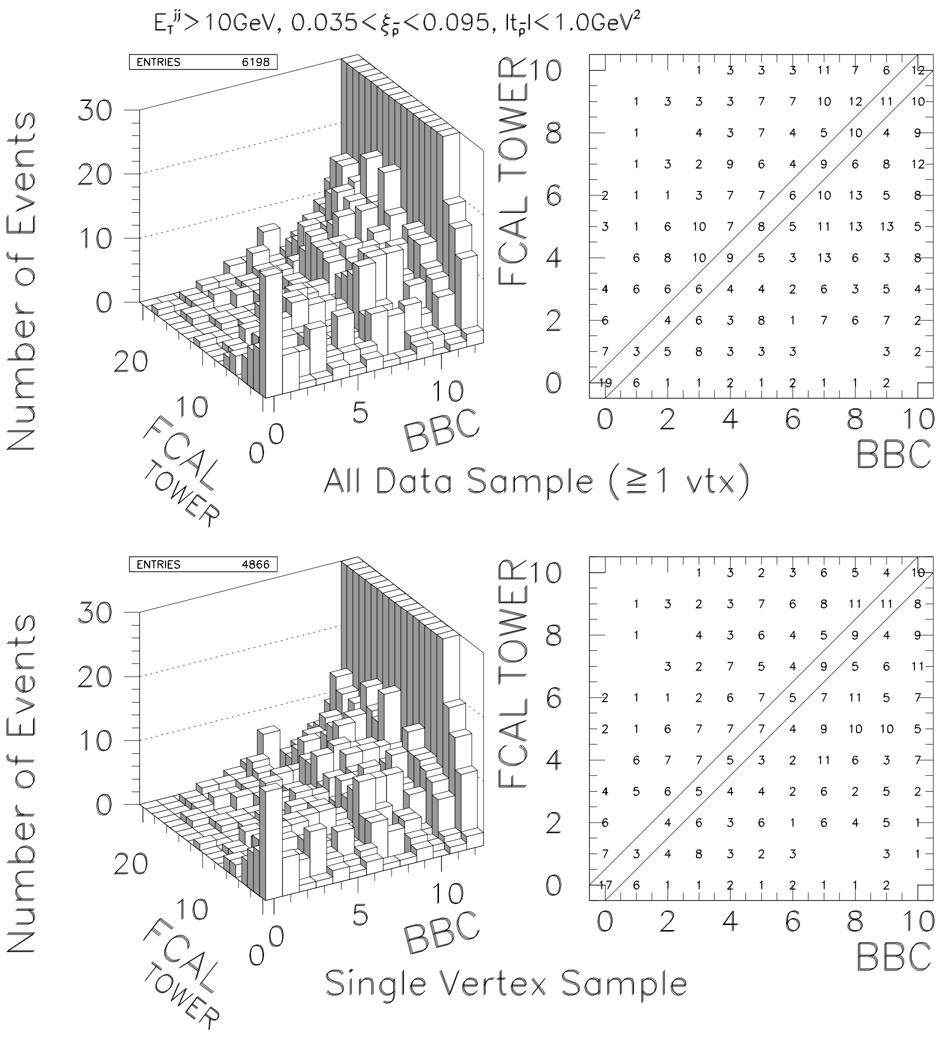

Figure 6.9: Multiplicity distribution of the BBC hits versus FCAL towers on the p side for diffractive events with dijets of $E_T > 10\,\mathrm{GeV}$. A spike at $N_{BBC-p} = N_{CAL-p} = 0$ for the data including multiple vertices (upper) has the similar magnitude to that for single vertex data (lower), which indicates high single vertex selection efficiency.

as $N^{jj}_{DPE}/N^{jj,\geq 1\,vtx}_{DPE} = 117.7/122.8$ for $E_T > 7\,\mathrm{GeV}$. Higher $E_T > 10\,\mathrm{GeV}$ case shows slightly lower efficiency 14.4/16.7=86.5 % with large statistical uncertainty. Recalling the fact that the single vertex efficiency for SD dijet events is approximately constant for both E_T thresholds, we assume this efficiency to be approximately constant at 95.9 % for both thresholds in DPE events. An analogy to SD dijet would give a systematic uncertainty of 0.4 % as 10 % of $(1 - \varepsilon^{1vtx}_{DPE\,jj})$, but we assign conservatively the statistical error of 1.9 % to the systematic uncertainty.

The Hot Tower Rejection filter (Section 5.3.1) has also been applied to DPE dijet events. The filter efficiency for DPE dijets is assumed to be approximately 100 % because the HTFLT filter has the sensitivity mostly around the plug and forward regions (Table 5.1), while DPE jets are more central.

In addition to these, the low west BBC multiplicity cut is used for DPE dijets as in SD dijets (Section. 5.3.2). We obtain the efficiency for this cut by using a similar method as in the single vertex selection efficiency above. Using the same diagonal fit to a sample of dijet events without the low multiplicity cut, the number of DPE events is evaluated as follows,

$$\begin{aligned} N^{jj,Wmulti}_{DPE} &= 126.2 \pm 12.6(stat.) \pm 11.7(syst.)_{fit} \qquad (E_T > 7\,\mathrm{GeV}) \\ &= 17.1 \pm 4.8(stat.) \pm 4.0(syst.)_{fit} \qquad (E_T > 10\,\mathrm{GeV}). \end{aligned}$$

In the same manner the efficiency is determined to be about $117.7/126.2 = 93.3\,\%$ ($14.4/17.1 = 84.2\,\%$) for $E_T > 7$ (10) GeV dijets. But, from the fact that the efficiency for SD dijets is similar at both E_T thresholds, we decide to use

$$\varepsilon^{Wmulti}_{DPE\,jj} = 93.3 \pm 2.5(stat.)\,\%,$$

as the efficiency of the low multiplicity cut for DPE dijets with $E_T > 7$ and 10 GeV. The systematic uncertainty is taken to be 2.5 %, same as the statistical error.

6.4 Event Kinematics of DPE Dijet

As shown in Figure 6.3(a), we observe 132 $E_T > 7\,\mathrm{GeV}$ dijet events in the (0,0) bin. The number of DPE dijet events in the (0,0) bin is about 117.7 events and the SD background is 14.3 (11 %). In the following plots we correct the number of observed DPE or SD events for the Roman Pot acceptance. Figure 4.8 shows the Roman Pot acceptance $A(\xi, |t|)$ as a function of ξ and $|t|$ with the bin width of $\Delta\xi = 0.005$ and $\Delta|t| = 0.1\,\mathrm{GeV}^2$. The Roman Pot acceptance correction is done by weighting each event by a factor $1/A(\xi, |t|)$. The corresponding statistical uncertainty is evaluated as $\sqrt{\sum_i (1/A(\xi, |t|)_i)^2}$ where the sum is carried over the diffractive events. After the correction is done, the number of events in the (0,0) bin becomes 166.2, which consists of 143.2 DPE events and 23.0 SD background (14 %). In this section we study the characteristics of DPE dijet kinematics (corrected for the Roman Pot acceptance) by selecting events in the (0,0) bin.

6.4.1 Comparison with SD Dijet Sample

Figure 6.10(a) shows the ξ and $|t|$ distributions of 132 events in the (0,0) bin, called "DPE signal region" from now on. In these plots "low multiplicity" and "high multiplicity" SD dijet samples are compared with the DPE signal region. Low multiplicity dijet sample is defined as diffractive dijet events with low multiplicity on the proton side, required to be $N_{BBC-p} \leq 5$ and $N_{CAL-p} \leq 5$ except for $N_{BBC-p} \leq 1$ and $N_{CAL-p} \leq 3$. The excluded region is the area of DPE signal concentration predicted from POMPOMPYT prediction ($N_{BBC-p} = 0$ and $N_{CAL-p} = 0, 1, 2$) plus adjacent bins. On the contrary, the high multiplicity dijet sample is defined as dijet events with high BBC or high FCAL tower multiplicity with $N_{BBC-p} > 5$ or $N_{CAL-p} > 5$. This class of events contains most SD dijets. In Figure 6.10(a) it appears that events in the DPE signal region tend to have slightly larger ξ than other SD samples although not so significant. In particular, the difference between DPE candidate events and low multiplicity SD sample is remarkable. One possibility of this observed trend is that the pomeron-pomeron c.m. energy enough to produce dijet in DPE needs higher ξ; another possibility is a contribution from enhanced meson exchange in large ξ. The first kinematic effect is studied with POMPOMPYT Monte Carlo in Section 7.2. In general, it is expected that the meson contribution increases at large ξ and small $|t|$, but $|t|$ distributions in lower half show the similar spectra for all three samples.

The E_T distributions of leading and second jets (Figure 6.10(b)) show similar E_T spectra for all dijet samples. Figure 6.10(c) shows the η distributions of leading and second jets, and the mean η of dijets. We see that DPE dijets are boosted toward the negative η direction (outgoing $\bar{p}$ direction) in contrast to high multiplicity sample showing shift to positive η side, and low multiplicity showing dijets produced almost symmetrically. This feature of DPE events implies that the pomeron from the p (traveling toward positive η) has smaller momentum than the pomeron from the $\bar{p}$ (negative η) because the accepted data has large ξ by a cut of $0.035 < \xi < 0.095$ for the pomeron from $\bar{p}$. The determination of ξ of the pomeron from the proton is discussed in Section 6.5. The difference of azimuthal angle ϕ between the two leading jets is shown in Figure 6.10(d). Good back-to-back dijets are observed in DPE signal region.

6.4.2 Comparison with SD/ND Dijet Sample

Next, DPE dijets in signal region are compared with non-diffractive (ND) dijets from minimum-bias data, and with single diffractive (SD) dijets. As previously mentioned, there is about 14% SD background in events in the (0,0) bin. We subtract these SD background from the distributions of events in DPE signal region, by assuming that the SD background would have the same shape as low multiplicity SD dijet sample which is already presented above. This subtraction would allow us to obtain the kinematics of pure DPE events. Figure 6.11(a) shows E_T distributions of leading and second jets for DPE, SD and ND dijet events. The E_T spectrum of DPE dijets

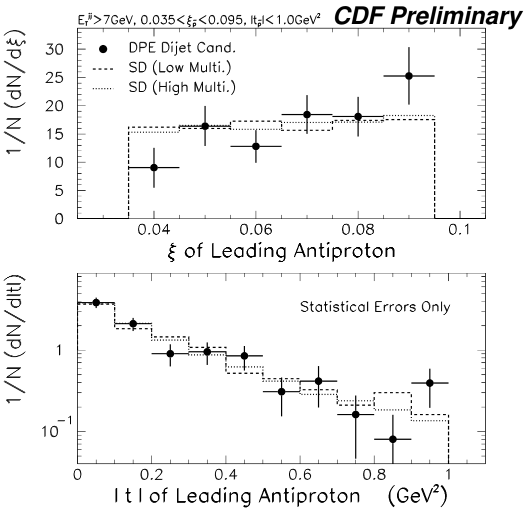

(a) Reconstructed Roman Pot ξ and $|t|$

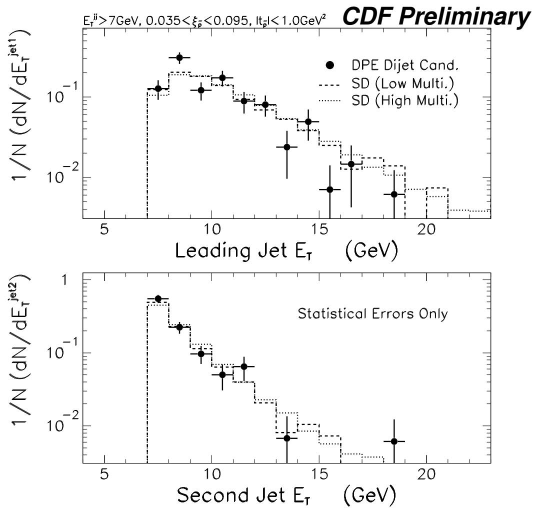

(b) E_T of jets

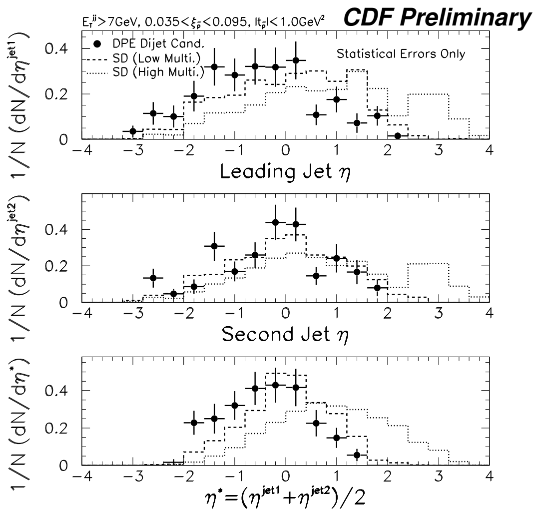

(c) η of jets

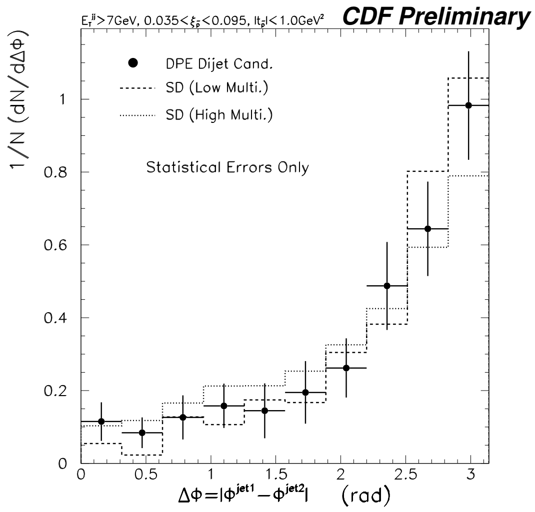

(d) azimuthal opening angle of dijet

Figure 6.10: Comparison of $E_T > 7\,\mathrm{GeV}$ DPE dijet candidate events (black points) with low (dashed histogram) and high (dotted histogram) multiplicity SD dijet samples : (a) ξ (upper) and $|t|$ (lower) of leading antiproton, (b) E_T of leading (upper) and second (lower) jets, (c) η of leading (top) and second (middle) jets, average η of dijets (bottom), (d) azimuthal opening angle between the two leading jets.

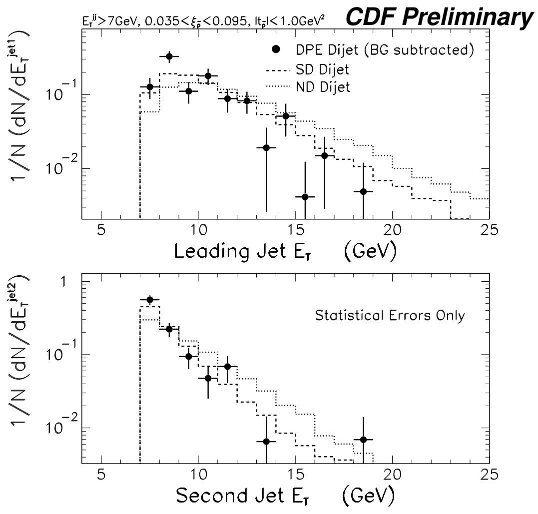

(a) E_T of jets

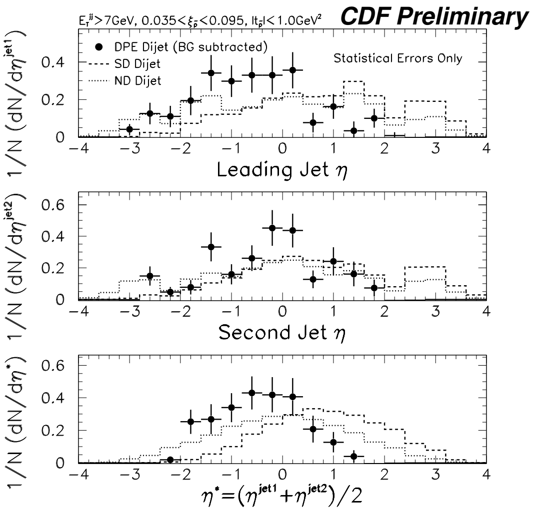

(b) η of jets

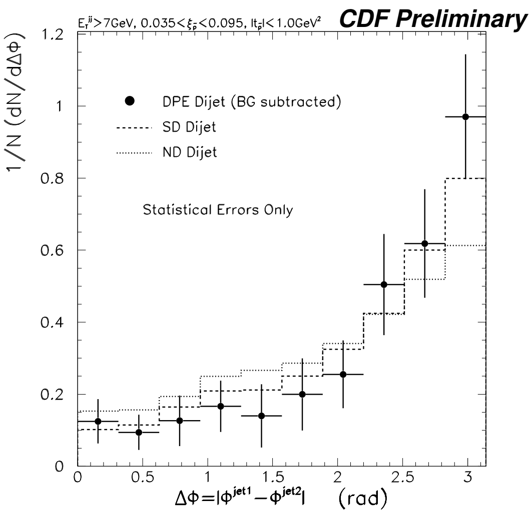

(c) azimuthal opening angle of dijet

Figure 6.11: Comparison of $E_T > 7\,\text{GeV}$ DPE dijet events (black points) with SD (dashed histogram) and ND (dotted histogram) dijet events : (a) E_T of leading (upper) and second (lower) jets, (b) η of leading (top) and second (middle) jets, average η of dijets (bottom), (c) azimuthal opening angle between the two leading jets. The DPE dijet distributions are obtained by subtracting the SD background from the events in the (0,0) bin.

is similar to that of SD dijets, but it seems to fall slightly faster than SD dijets, seen in the second jet E_T shape. Also, these two E_T spectra are clearly softer than ND dijets. As for the η distributions shown in Figure 6.11(b), a clear difference is observed among these three samples. The DPE dijets are produced toward the west (dijet mean $\eta \sim -0.40$) contrary to SD dijet shifted eastward (~ 0.84), and ND dijet produced symmetrically (~ 0). These features are understood, at least qualitatively, by kinematics of interacting objects (predominantly $I\!P$-$I\!P$ for DPE, p-$I\!P$ for SD and p-$\bar{p}$ for ND). The azimuthal angle difference between the two leading jets indicates that the DPE dijet is produced more back-to-back than single diffractive and non-diffractive dijets (Figure 6.11(c)). This can be attributed to less radiation in the interaction of two color singlet objects. Accordingly, these DPE dijet events are generally cleaner with a lower level of underlying activity, than the SD or ND dijet events at the same jet E_T.

6.5 Measurement of ξ for the Proton

A measurement of ξ_p (momentum fraction of the proton carried by the pomeron) is important and essential for a comparison with any theoretical predictions. To determine the ξ_p without measuring the leading proton momentum, we use the formula:

$$M^2_{DPE} = \xi_p \cdot \xi_{\bar{p}} \cdot s, \tag{6.1}$$

where M_{DPE} is the DPE system mass and $\xi_{\bar{p}}$ is the momentum fraction of the antiproton carried by the pomeron.

In general, the square of the mass of the system X in the reaction $\bar{p} + p \rightarrow X$ is given by

$$M^2_X = \left(\sum_i E_i\right)^2 - \left(\sum_i \vec{P}_i\right)^2, \tag{6.2}$$

where E_i and $\vec{P}_i$ are the energy and momentum of the ith produced particle. Assuming that the sum of P_i^X or P_i^Y over all central particles is zero, this formula is written as

$$M_X^2 = \left(\sum E_T e^{+\eta}\right) \cdot \left(\sum E_T e^{-\eta}\right), \tag{6.3}$$

where the subscript i is omitted. This equation is strictly correct when the exponent is true rapidity y, not pseudorapidity η.

This mass formula is valid in non-diffractive (ND), single diffractive (SD), and DPE events. In ND events, this gives the square of the ND system mass, M_{ND}^2, as

$$\begin{aligned} M_{ND}^2 &= \left(\sum E_T e^{+\eta}\right) \cdot \left(\sum E_T e^{-\eta}\right) \\ &= \sqrt{s} \cdot \sqrt{s} \\ &= s. \end{aligned} \tag{6.4}$$

In SD events of our Roman Pot data, a leading antiproton escapes from the system X. However, the relation $\sum E_T e^{+\eta} \sim \sqrt{s}$ still holds in SD events because the η of leading antiproton is very large negative number. So, the square of the SD system mass, M_{SD}^2, is given by

$$M_{SD}^2 = \sqrt{s} \cdot \left(\sum E_T e^{-\eta}\right). \tag{6.5}$$

Compared with using Eq. (6.2) to SD events, this equation would enable us to estimate the SD system mass more accurately because what we need is only a term $\sum E_T e^{-\eta}$ and this term is insensitive to large positive η particles which could dominate our SD data sample. (Of course, the relation $M_{SD}^2 = \xi_{\bar{p}}^{RP} \cdot s$ where $\xi_{\bar{p}}^{RP}$ denotes the $\xi_{\bar{p}}$ measured by the Roman Pots should give the best method to obtain the true SD system mass.). Using Eq. (6.5), we should have another method to obtain $\xi_{\bar{p}}$, independently of the Roman Pot track, as follows,

$$\begin{aligned} \xi_{\bar{p}}^X &\equiv \frac{M_{SD}^2}{s} \\ &= \frac{\sum E_T e^{-\eta}}{\sqrt{s}}. \end{aligned} \tag{6.6}$$

The superscript X means that this quantity is obtained from the SD system.

For DPE events, the DPE system mass M_{DPE} is related to ξ_p by Eq. (6.1). By using Eq. (6.3) and Eq. (6.6), we therefore evaluate the ξ_p as follows,

$$\xi_p^X \equiv \frac{\left(\sum E_T e^{+\eta}\right) \cdot \left(\sum E_T e^{-\eta}\right)}{\xi_{\bar{p}} \cdot s} \tag{6.7}$$

$$= \frac{\left(\sum E_T e^{+\eta}\right) \cdot \left(\sum E_T e^{-\eta}\right)}{\frac{\sum E_T e^{-\eta}}{\sqrt{s}} \cdot s} \tag{6.8}$$

$$= \frac{\sum E_T e^{+\eta}}{\sqrt{s}}, \tag{6.9}$$

where the superscript X means that this quantity is obtained from the DPE system. This derivation does not depend on the Roman Pot measured ξ. The term $\sum E_T e^{+\eta}$ is sensitive to particles with large positive η. However, DPE events contain less particles in positively forward direction due to the rapidity gap, accordingly the use of Eq. (6.9) is expected to be better than the use of Eq. (6.7). In addition, Eq. (6.9) also indicates that large negative η particles from the central system do not almost contribute to the ξ_p. When putting Eq. (6.9) into Eq. (6.1) inversely and using the Roman Pot measured $\xi_{\bar{p}}$, we obtain a formula to get the mass of the DPE system:

$$M_{DPE} = \sqrt{\sum E_T e^{+\eta} \cdot \xi_{\bar{p}}^{RP} \cdot \sqrt{s}}. \tag{6.10}$$

A calculation of the mass using Eq. (6.5) for single diffractive events needs all the E_T and η of particles produced in an event. In the calculation we select firstly events containing at least two jets with $E_T > 7\,\mathrm{GeV}$ as usual, using the standard jet reconstruction algorithm. A primary choice of a cone radius is $R = 0.7$. We apply the JTC96 energy corrections to the jets including the relative and absolute corrections, underlying event energy subtraction, but the out-of-cone correction is not used. Only two highest E_T jets are considered here, and the 3rd or 4th jets, even if they exist, are not taken in account there because they are expected to have enough low energies.

For the particles outside the jets, we use the whole calorimeters in mass reconstruction. By finding the η and ϕ of the jets in the calorimeter, we isolate the towers outside the jet cones ($R = 0.7$) and sum up their $E_T e^{\pm\eta}$. Here we require the E_T of each tower to be greater than the threshold given in Eq. (5.2) used for the counting of the tower multiplicity. Also, applied is a multiplication of 1.6 to the tower detector energy as a canonical absolute energy correction. This correction would be reasonable also for remaining jets other than two highest E_T jets that were not considered above.

In a jet reconstruction we subtract the underlying energy contribution from the jets, but it should be included in the mass of total system. From the fixed E_T subtracted from the jets (0.54 GeV for single diffractive jets and 0.37 GeV for double pomeron jets) and the η of the jets, we could estimate the underlying event energy within the two jet cones. Also, we have to evaluate the particles outside the calorimeter, mostly in the BBC range, since a calorimeter coverage is restricted to $\eta = \pm 4.2$. To estimate the BBC particle, we assume that one BBC hit corresponds to on average $\frac{2}{3}$ particles because a particle within the BBC coverage has about 50 % probability of hitting two BBC counters from the BBC structure (see Figure 3.6). A BBC particle is assumed to have $E_T = 0.5$ GeV and $\eta = \pm 4.5$ (a central value of BBC coverage). The $E_T = 0.5$ GeV is determined from the fact that the average E_T of particles in $\bar{p}p$ collisions is about 0.5 GeV. As discussed later, the definition of the BBC particle is insensitive to the ξ_p measurement. Next, a factor 1.5 is multiplied by the number of BBC hits because neutral particles would be produced on average by a half of charged particles. Finally we subtract the number of forward calorimeter towers above thresholds within $3.2 < |\eta| < 4.2$ from the corrected number of BBC hits with 1.5 multiplication, in order to avoid double counting due to overlap between the BBC and the forward calorimeter.

Figure 6.12 shows the mass (top) and $\xi_{\bar{p}}$ (middle) reconstructed using Eq. (6.5) and Eq. (6.6) for single diffractive events with dijets of $E_T > 7$ GeV. Comparing the $\xi_{\bar{p}}^X$ with the $\xi_{\bar{p}}$ measured by the Roman Pots, $\xi_{\bar{p}}^{RP}$, its ratio:

$$R(\xi) \;=\; \frac{\xi_{\bar{p}}^X}{\xi_{\bar{p}}^{RP}}, \tag{6.11}$$

is shown in the bottom. If the experimental method to derive the $\xi_{\bar{p}}^X$ is correct (and

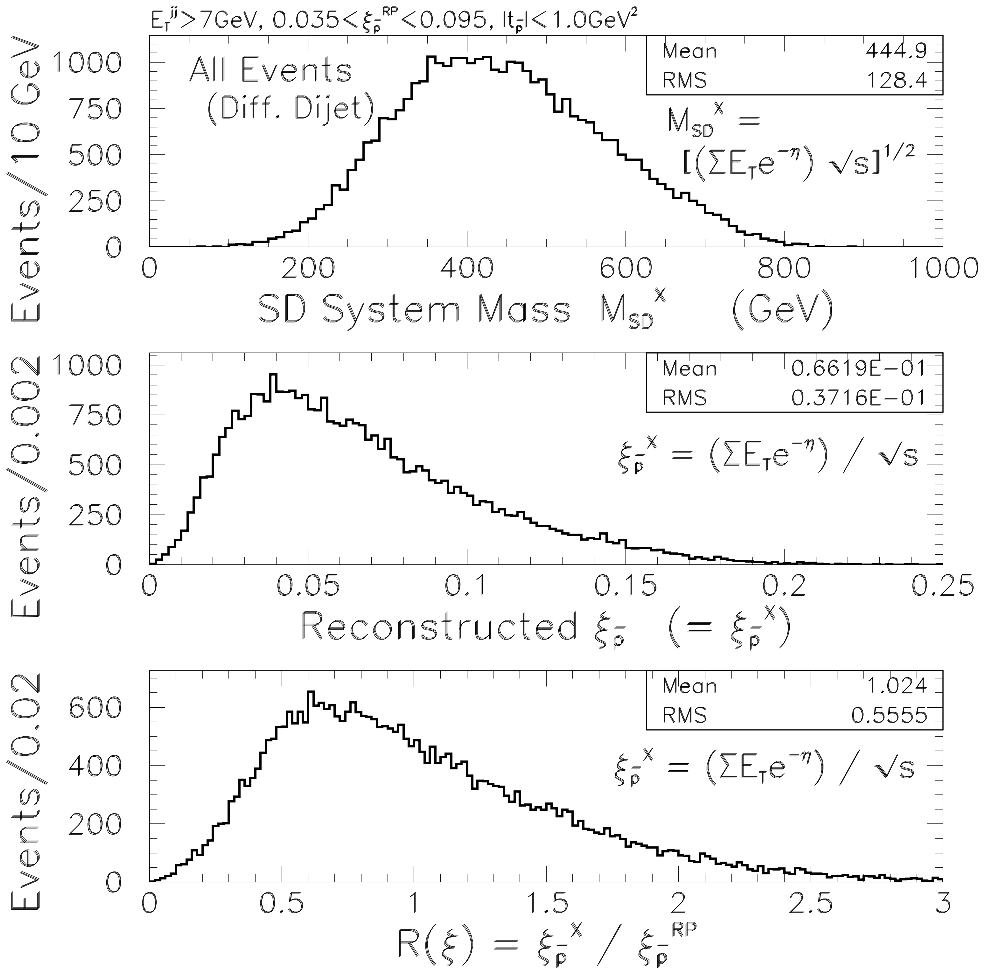

Figure 6.12: Reconstructed mass (top), $\xi_{\bar{p}}^{X}$ (middle) and the ratio of $\xi_{\bar{p}}^{X}$ to $\xi_{\bar{p}}^{RP}$ (bottom) for all single diffractive events with dijets of $E_T > 7\,\mathrm{GeV}$.

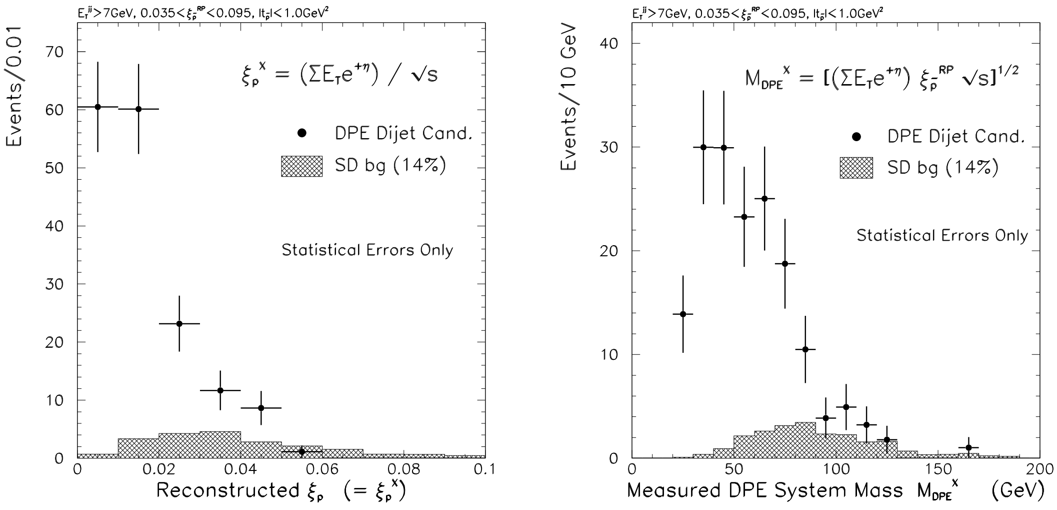

(a) Reconstructed ξ_p

(b) Reconstructed DPE Mass

Figure 6.13: (a) Reconstructed ξ_p^X, and (b) the mass of system for DPE candidate events with dijets of $E_T > 7\,\mathrm{GeV}$ (points). The shaded histograms show the shapes of single diffractive dijet background.

the system X includes any leading forward particles, the $R(\xi)$ should be 1 because we know that $\xi_{\bar{p}}^{RP}$ is a true $\xi_{\bar{p}}$ within the accuracy of $\Delta\xi_{\bar{p}} \sim 10^{-3}$ [48]. If there is an unobserved leading proton as in DPE events, $\xi_{\bar{p}}^X \ll \xi_{\bar{p}}^{RP}$ and the $R(\xi)$ will be much less than 1. Figure 6.12 (bottom) shows that the mean of $R(\xi)$ is about 1, which means both the $\xi_{\bar{p}}$ measurements using the Roman Pots and the final system give approximately the same values on average.

Figure 6.13 shows (a) the ξ_p^X and (b) the mass of DPE system reconstructed using Eq. (6.9) and Eq. (6.10) for DPE dijet candidates ($E_T > 7\,\mathrm{GeV}$) in the (0,0) bin. Both distributions were corrected for the Roman Pot acceptance as done in the kinematics comparison. The shaded histograms are the shapes of 14 % SD dijet background expected assuming that the background has the same distribution as low multiplicity SD events. High ξ_p^X or high mass tail contains a large fraction of the background. The

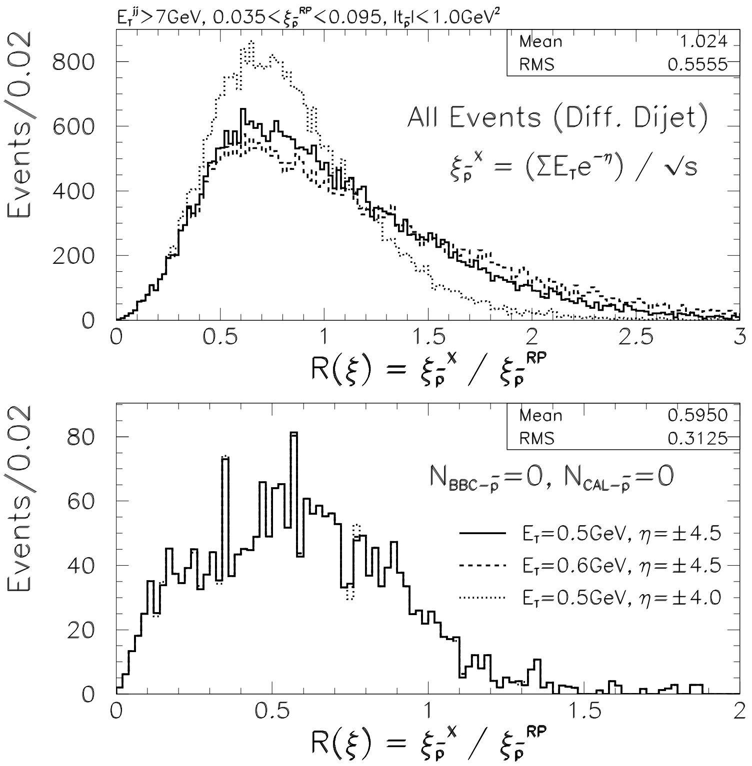

Figure 6.14: Ratio of $\xi_{\bar{p}}^{X}$ to $\xi_{\bar{p}}^{RP}$ for all single diffractive events with dijets of $E_T > 7\,\mathrm{GeV}$ (upper). Lower half shows the distributions for events with $N_{BBC-\bar{p}} = N_{CAL-\bar{p}} = 0$. The full histograms show the case of (0.5 GeV, ±4.5) for BBC particle's (E_T, η), and the dashed histograms show (0.6 GeV, ±4.5), the dotted histograms (0.5 GeV, ±4.0).

shapes after subtraction of the shaded distributions will be real distributions for DPE events. But the calibration of the ξ_p^X for any losses of particles, e.g., particles which are lost below thresholds and due to detector inefficiency such as cracks, has to be done before that.

In order to estimate this correction, we can use the $R(\xi)$ distribution for single diffractive events with zero BBC multiplicity $N_{BBC-\bar{p}} = 0$ and zero FCAL tower multiplicity $N_{CAL-\bar{p}} = 0$ on the $\bar{p}$ direction. Recalling that the $\xi_{\bar{p}}^{X}$ given by Eq. (6.6) strongly depends on large negative η particles, we expect that the reconstruction ambiguity of $\xi_{\bar{p}}^{X}$ should be small by requiring $N_{BBC-\bar{p}} = N_{CAL-\bar{p}} = 0$. In addition,

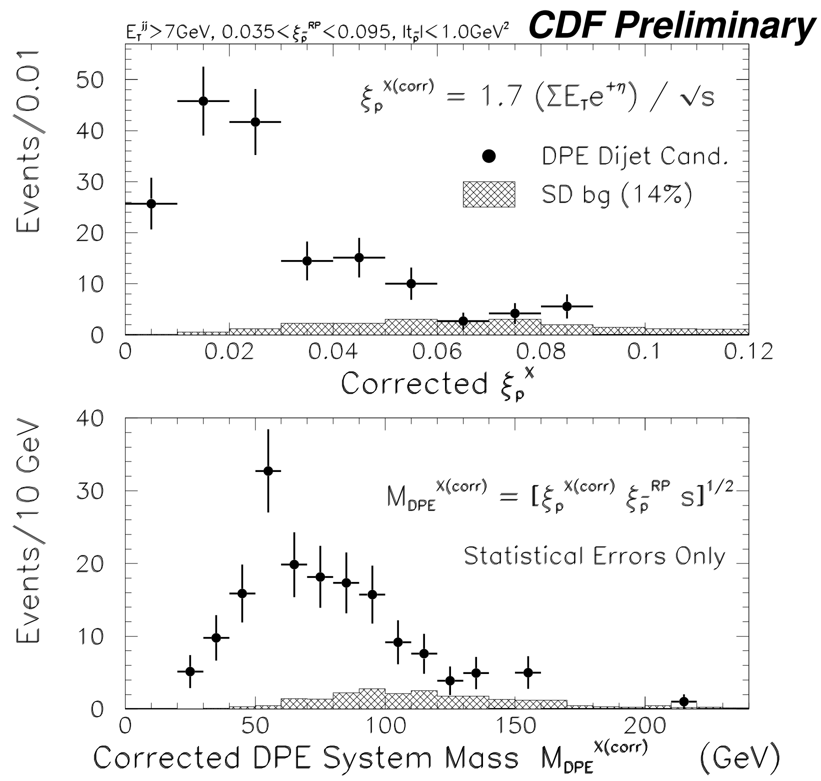

Figure 6.15: Corrected ξ_p^X (upper) and the corrected mass of a central DPE system (lower) for DPE candidate events with dijets of $E_T > 7\,\mathrm{GeV}$ (points). The shaded histograms show the shapes of single diffractive dijet background. A multiplication of a factor 1/0.595=1.7 is used to correct the raw ξ_p^X.

the $\xi_{\bar{p}}^X$ is insensitive to positive η particles and this requirement would lead to a fixed correction being independent of the definition of the BBC particle. When the E_T and η of a BBC particle are changed from ($E_T = 0.5\,\mathrm{GeV}$, $\eta = \pm 4.5$) to ($E_T = 0.6\,\mathrm{GeV}$, $\eta = \pm 4.5$) or ($E_T = 0.5\,\mathrm{GeV}$, $\eta = \pm 4.0$), the $R(\xi)$ distribution of all dijet events changes the shape as shown in Figure 6.14(upper). When requiring $N_{BBC-\bar{p}} = N_{CAL-\bar{p}} = 0$, $R(\xi)$ is fully constant as in lower plot. From the mean of the distribution for $E_T = 0.5\,\mathrm{GeV}$, $\eta = \pm 4.5$ (full line), we obtain an averaged correction factor to the raw ξ_p to be 1/0.595 = 1.7. This factor can be used to correct for the raw ξ_p but we have to note that it is valid only on average, not on an event-by-event basis.

Applying a factor 1.7 multiplication to the raw ξ_p^X distribution, we obtain the calibrated ξ_p^X distribution for DPE dijet events, presented in Figure 6.15 (corrected ξ_p^X is referred to as $\xi_p^{X(corr)}$ in the following text and plots). It is seen that most DPE events in the (0,0) bin have the corrected ξ_p^X within the range $0.01 < \xi_p^{X(corr)} < 0.03$. The $\xi_p^{X(corr)}$ and Roman Pot measured $\xi_{\bar{p}}$ would allow us to estimate the central DPE system mass, $M_{DPE}^{X(corr)}$, given by Eq. (6.1). The corrected mass $M_{DPE}^{X(corr)}$ distribution is shown in Figure 6.15(lower).

6.5.1 Rapidity Gap Acceptance

A separation of single diffractive to non-diffractive events is essential for diffractive analysis. For DPE analysis of our Roman Pot data, a separation of DPE to SD event is important. Particularly if we obtain pure DPE event sample, we can estimate, independently of the Monte Carlo, the rapidity gap acceptance, defined as a fraction of the number of DPE events in the (0,0) bin on the proton direction to that of total DPE events. Our scheme based on the diagonal distribution of the BBC and FCAL tower multiplicities gives a good estimate of the rapidity gap, as seen in Figure 6.3, but even this method contains about 10 % single diffractive background under the peak in the (0,0) bin. However, the calculation of ξ_p^X using Eq. (6.9) indicates that single diffractive events have much larger ξ_p^X than DPE events because most SD events contain much more particles with large positive η. This provides us a possibility of separating the DPE to SD event based on the ξ_p^X.

Figure 6.16 shows the $\xi_p^X = \sum E_T e^{+\eta}/\sqrt{s}$ for all single diffractive dijet events. The mean of distribution, 0.26, is about a factor 16 larger than that of DPE events (0.016), which is shown as a shaded histogram in an expanded view of low ξ_p^X range. Also seen in the figure is that the very low ξ_p^X range $0.0 < \xi_p^X < 0.02$ is almost completely dominated by DPE dijets in the (0,0) bin. As mentioned above, the diagonal distribution clearly shows a rapidity gap signal in the (0,0) bin, so combining the diagonal multiplicity and ξ_p^X would clearly show the separation between DPE and SD dijets at low

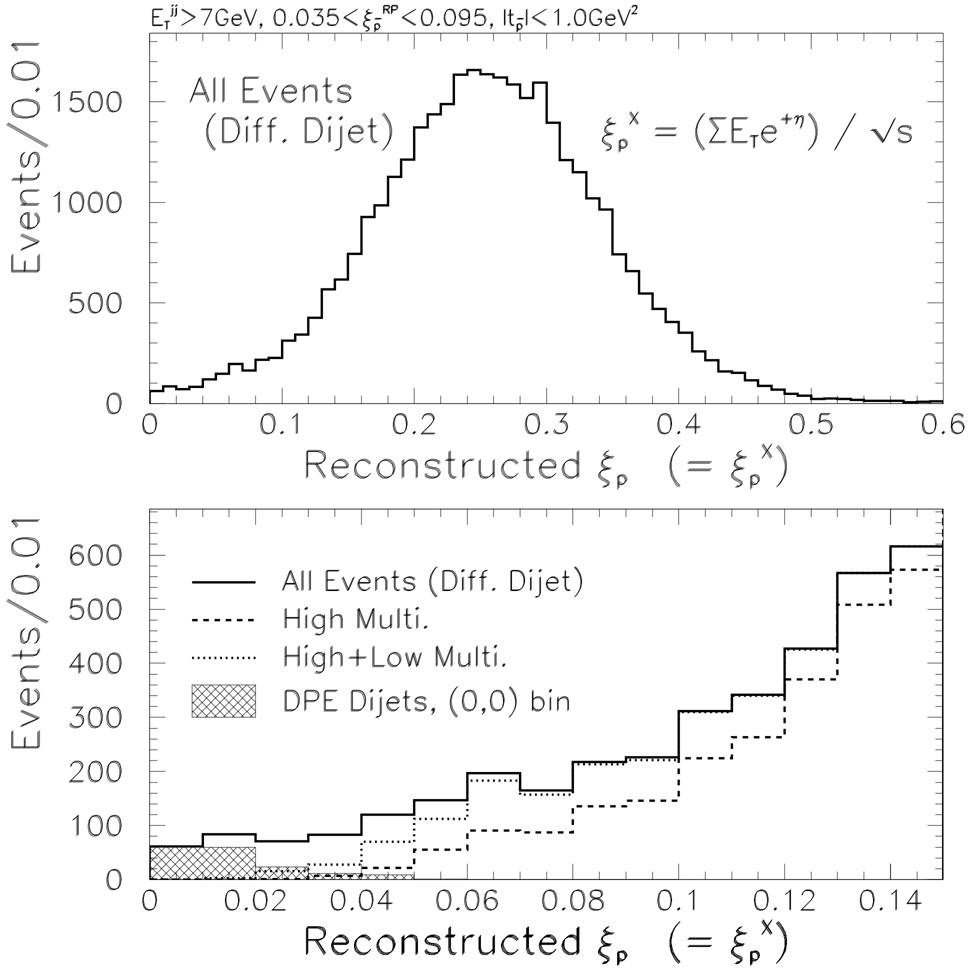

Figure 6.16: ξ_p^X distribution for all diffractive dijet events of $E_T > 7\,\mathrm{GeV}$. Lower half is an expanded view of low ξ_p^X range $\xi_p^X < 0.15$. The dashed (dotted) histogram represents single diffractive events with high (both high and low) N_{BBC-p} and N_{CAL-p} multiplicities. The shaded histogram shows the DPE dijet candidates with $N_{BBC-p} = N_{BBC-p} = 0$. All the ξ_p^X distributions are not corrected for the detector inefficiency.

ξ_p^X range. We display its correlation in Figure 6.17 before applying the correction of factor 1.7 multiplication. As expected, SD dijets have always large $\xi_p \sim 0.25$ and large diagonal multiplicity > 10, while DPE dijets make a clear peak at very low ξ_p^X region $0.0 < \xi_p^X < 0.02$ and zero diagonal multiplicity. The background from SD dijets under the peak is at the level of a few events or less. Consequently we are able to obtain clean DPE sample by selecting events with $0.0 < \xi_p^X < 0.02$ (roughly corresponding to corrected ξ_p^X range $0.01 < \xi_p^{X(corr)} < 0.03$). The SD event background within this range is very small, but it can be estimated using the ξ_p^X distribution for events with $N_{BBC-p} = N_{CAL-p}$ (i.e., 1 dimensional projection of Figure 6.17). Performing the linear fits to ξ_p^X distribution of events dominated by SD and extrapolating the fit into the range $0.0 < \xi_p^X < 0.02$, we estimate the number of SD background events in this range to be 3.0 ± 0.7.

Given that the background with $0.0 < \xi_p^X < 0.02$ is very small, we show in Figure 6.18 the multiplicity distribution, corrected for the Roman Pot acceptance, of the BBC hits versus FCAL towers for dijets with $E_T > 7\,\text{GeV}$ and $0.01 < \xi_p^{X(corr)} < 0.03$. The number of events in the (0,0) bin $N_{(0,0)}$ (all bins N_{total}) is 87.5 (104.5), which gives the rapidity gap acceptance:

$$A_{gap} \;=\; 83.7 \;\pm\; 11.1\,\%,$$

by dividing $N_{(0,0)}$ by N_{total}. We take $\sigma_{(0,0)}^{stat}/N_{total} = 10.5\,\%$ as a statistical uncertainty of A_{gap}, where $\sigma_{(0,0)}^{stat} = \sqrt{\sum_i (1/A(\xi,|t|)_i)^2}$ and here $A(\xi,|t|)$ is the Roman Pot acceptance and the sum is carried over the events in the (0,0) bin up to the number of events before the Roman Pot acceptance correction. For the systematic uncertainty we assign $2.3\,\%$ in analogy to the live time acceptance described in Appendix B. In addition, for the SD background of 3.0 events we apply an additional $2.9\,\%$ (=3.0/104.5) error as the systematics. Adding them in quadrature gives the total error of $11.1\,\%$.

For events with dijets of $E_T > 10\,\text{GeV}$, we evaluate $A_{gap} = 74.4\,\%$ in the same way. Given that a statistical uncertainty is pretty large ($\sim 30\,\%$), it would be natural to regard the acceptance at $E_T > 10\,\text{GeV}$ as being consistent with the result for

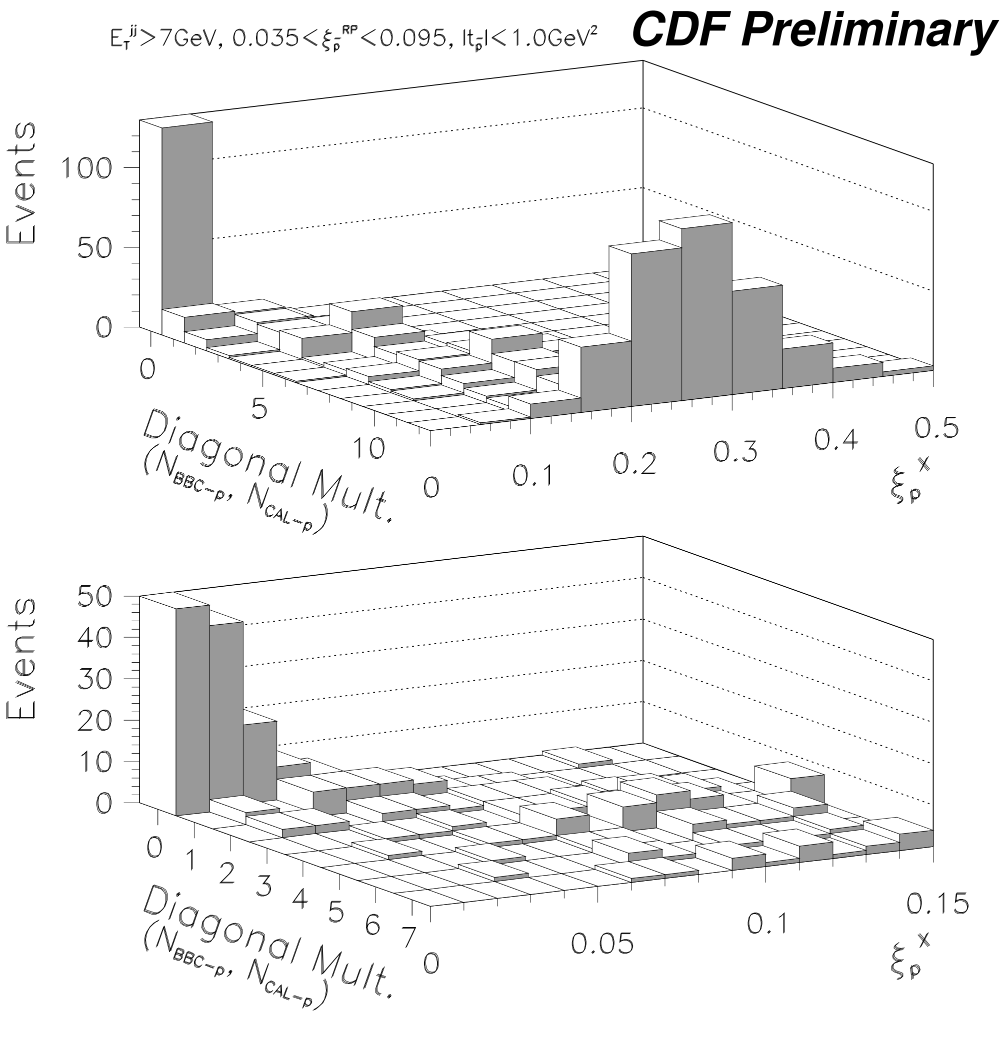

Figure 6.17: Correlation between the diagonal multiplicity of the BBC hits and FCAL towers, and ξ_p^X for all diffractive dijet events of $E_T > 7\,\mathrm{GeV}$. Lower half is an expanded view of low ξ_p^X range $\xi_p^X < 0.15$ and low diagonal multiplicity $N_{DIAG-p} \leq 7$. DPE events make a peak at very low $\xi_p^X < 0.02$ and zero diagonal multiplicity.

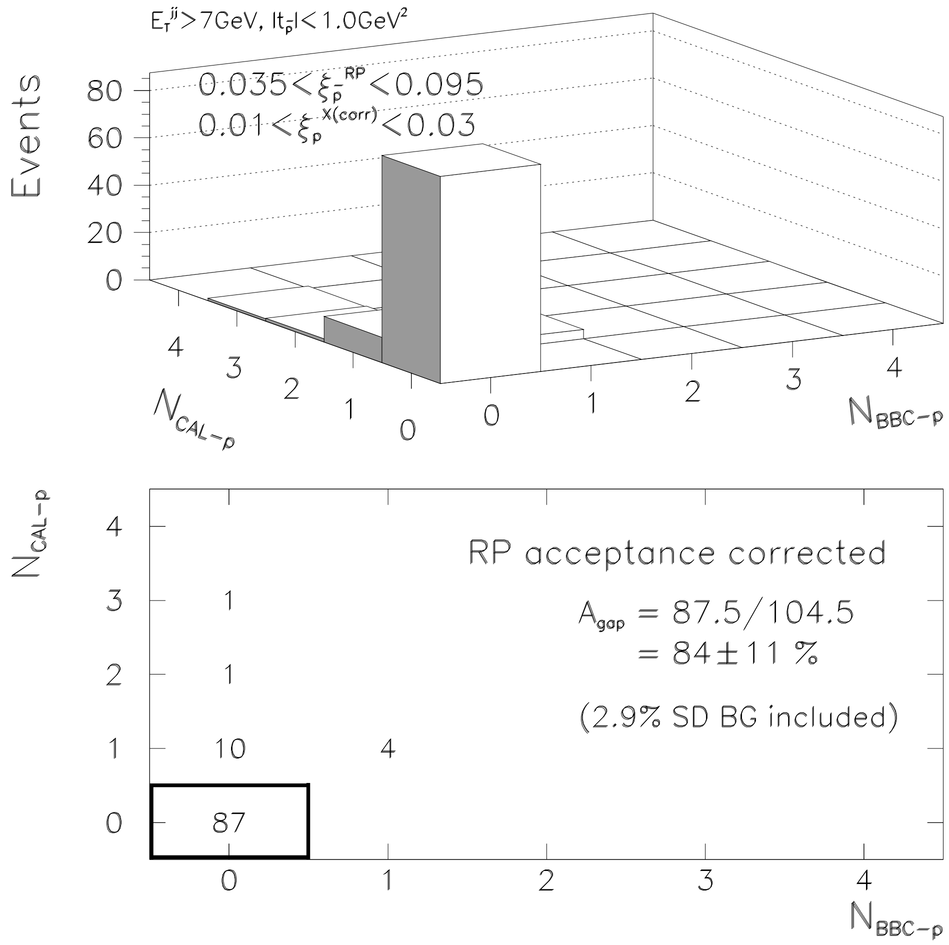

Figure 6.18: Multiplicity distribution of the BBC hits versus FCAL towers for diffractive events with dijets of $E_T > 7\,\mathrm{GeV}$ and $0.035 < \xi_{\bar{p}}^{RP} < 0.095$, $0.01 < \xi_p^{X(corr)} < 0.03$. Lower half shows the number of events in each bin. The Roman Pot acceptance was corrected for events, so the number of events is not an integer.

$E_T > 7\,\mathrm{GeV}$. This is reasonable because we expect that a rapidity gap acceptance depends on primarily the structure of the exchanged object (parton distribution) or the ξ range (rapidity gap width), not the E_T of jets (hard process). The number of events in the (0,0) bin (all bins) with $0.01 < \xi_p^{X(corr)} < 0.03$ for $E_T > 10\,\mathrm{GeV}$ dijets is 6.1 (8.2) and it is quite smaller than what we measured using the diagonal extrapolation, $14.4 \pm 4.4(stat.) \pm 2.5(syst)_{fit}$. This is due to that a requirement of higher E_T dijets for DPE events kinematically makes ξ_p^X larger because the jets dominate DPE system. Figure 6.19 shows the corrected ξ_p^X distribution for events in the (0,0) bin with dijets of $E_T > 7\,\mathrm{GeV}$ (upper) and $E_T > 10\,\mathrm{GeV}$ (lower). Seen in the figure is that the higher E_T data have larger ξ_p^X as expected, hence the range $0.01 < \xi_p^{X(corr)} < 0.03$ covers only a small portion of events in the (0,0) bin. Hereafter we simply refer to the corrected ξ_p^X as ξ_p.

6.6 Measurement of Dijet Cross Sections

6.6.1 Non-Diffractive Dijet Cross Section

In the sample of 340,685 inclusive non-diffractive (ND) events, we observe 32,629 and 10,514 dijet events with $E_T > 7\,\mathrm{GeV}$ and $E_T > 10\,\mathrm{GeV}$ respectively, as listed in Table 5.3. To estimate the ND dijet cross section, the number of dijet events divided by the number of inclusive events is normalized to the measured BBC cross section $\sigma_{BBC} = 51.15 \pm 1.60(syst.)\,\mathrm{mb}$ [39, 40, 41]. Thus the non-diffractive dijet cross section is obtained in the following way:

$$\sigma_{ND}^{jj} = \left[\frac{N_{ND}^{jj}}{\varepsilon_{ND\,jj}^{HTFLT} \cdot \varepsilon_{ND\,jj}^{Zvtx}} \Bigg/ \sum_{i=1}^{N_{ND}^{incl}} N_i \right] \times \sigma_{BBC}, \tag{6.12}$$

where N_{ND}^{jj} (N_{ND}^{incl}) is the number of non-diffractive dijet (inclusive) events, and $\varepsilon_{ND\,jj}^{HTFLT}$ is the HTFLT filter efficiency $96.9 \pm 0.2(stat.)\,\%$ obtained in Section 5.3.1. N_{ND}^{incl} is for inclusive events before the Z_{vertex} cut.

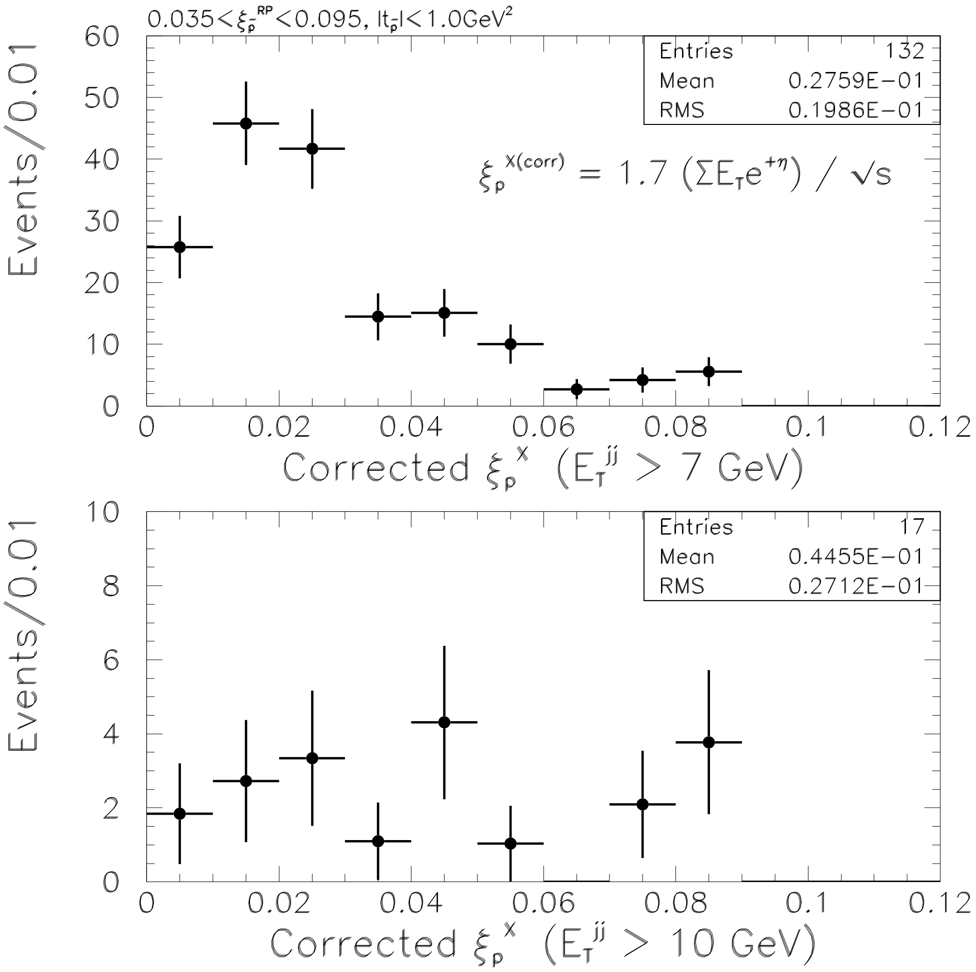

Figure 6.19: Corrected ξ_p^X distributions for DPE candidate events in the (0,0) bin with dijets of $E_T > 7$ GeV (upper) and $E_T > 10\,\mathrm{GeV}$ (lower).

The efficiency of this Z_{vertex} cut to dijet events, $\varepsilon^{Zvtx}_{ND\,jj}$, is obtained as follows. The Z_{vertex} distribution of events can be approximated as

$$\frac{dL}{dz} \propto e^{-\frac{z^2}{2\sigma_z^2}} \Big/ \left[1 + \frac{(z - z_{min})^2}{\beta^{*2}}\right], \tag{6.13}$$

where z_{min} is the mean of the Z_{vertex} distribution, and β^* is the Tevatron low beta quad parameter, σ_z is the longitudinal bunch length [57]. Figure 6.20 shows the Z_{vertex} distributions of inclusive diffractive (upper) and non-diffractive (lower) events along with the fits to the distributions within $|Z_{vertex}| \leq 60\,\mathrm{cm}$. Both the distributions are well parameterized within the fit range. We can evaluate the efficiency to be $\varepsilon^{Zvtx} = \int_{-60\,cm}^{+60\,cm} dL(z) \,/\, \int_{-\infty}^{+\infty} dL(z)$, but we restrict the integration range within $\pm 150\,\mathrm{cm}$ in the calculation. The obtained value for non-diffractive dijet events is

$$\varepsilon^{Zvtx}_{ND\,jj} = 95.9 \pm 2.0(syst.)\,\%,$$

and it is similar to that for inclusive events. An error of 2.0 % is quoted from [57], which was obtained in comparison with various fit results for Run 1B minimum-bias data.

We know that the average number of non-diffractive interactions per bunch crossing for every event is given by

$$\langle n \rangle_i = \frac{\mathcal{L}^i_{inst} \cdot \sigma_{BBC} \cdot (1 - 0.002704 \cdot \mathcal{L}^i_{inst})}{f_0}, \tag{6.14}$$

where $\mathcal{L}^i_{inst}$ is the instantaneous luminosity of the ith event, and $f_0 = 286.278\,\mathrm{kHz}$ is the Tevatron bunch crossing frequency. The term $[1 - 0.002704 \cdot \mathcal{L}^i_{inst}]$ is the accidental correction factor for $\mathcal{L}^i_{inst}$ [58]. The Poisson statistics gives the following correction factor as an event weight for every event:

$$N_i = \frac{\sum_{j=1}^{\infty} P(j) \cdot j}{\sum_{j=1}^{\infty} P(j)} = \frac{\langle n \rangle_i}{1 - e^{-\langle n \rangle_i}}. \tag{6.15}$$

Finally, dividing the number of dijets by the efficiencies and a sum of event weights over all inclusive events, the ND dijet cross sections is estimated as given in Table 6.1.

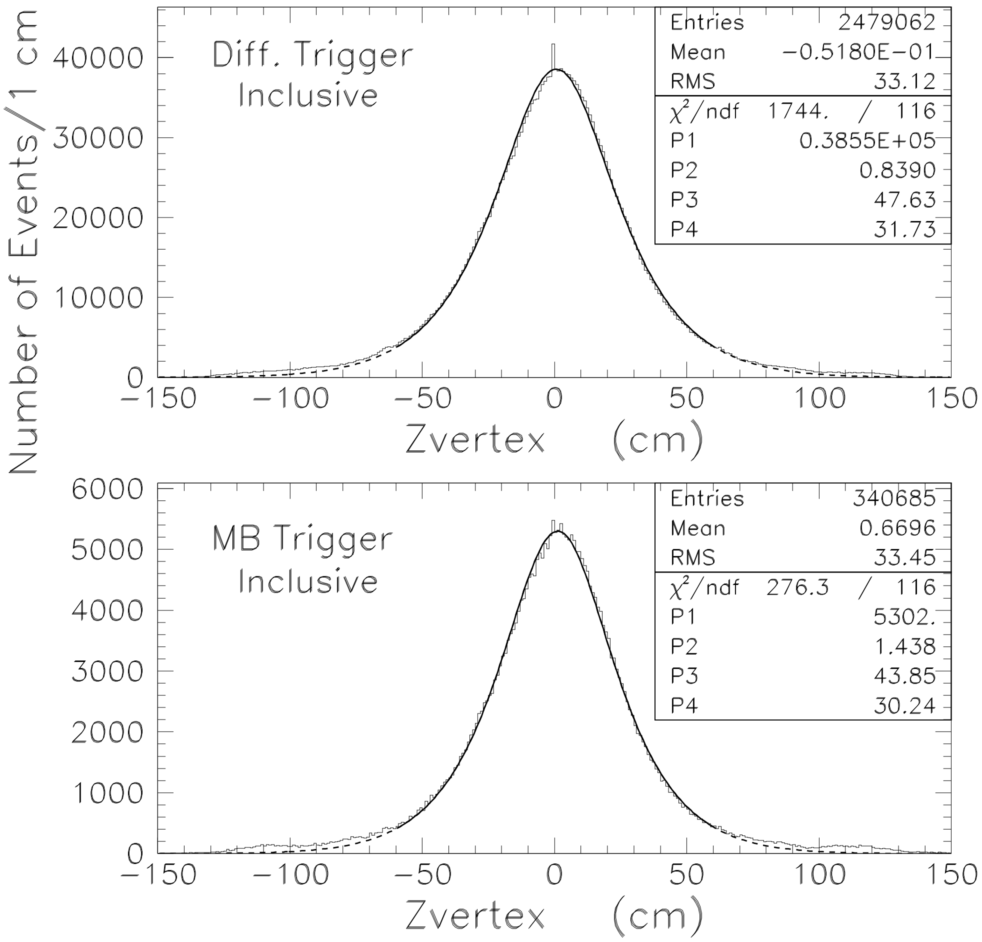

Figure 6.20: Z_{vertex} distributions for diffractive inclusive sample (upper) and non-diffractive minimum-bias sample (lower). Shown as the thick lines are the fit functions with the form $C \cdot e^{-z^2/2\sigma_z^2}/[1+(z-z_{min})^2/\beta^{*2}]$, where $P1$ is a normalization C, $P2 = z_{min}$, $P3 = \sigma_z$ and $P4 = \beta^*$.

Table 6.1: Cross section of non-diffractive events with dijets of $E_T > 7\,\mathrm{GeV}$ and $E_T > 10\,\mathrm{GeV}$. All the errors are statistical only.

Dijet E_{Tmin}	**$E_T > 7$ GeV**	**$E_T > 10$ GeV**
σ_{ND}^{jj}	5.04 ± 0.03 mb	1.62 ± 0.02 mb

(Statistical Errors Only)

6.6.2 Single Diffractive Dijet Cross Section

To estimate the cross section of single diffractive (SD) dijets, the background contributions in the inclusive diffractive sample should be obtained. We expect that the inclusive sample contains 1) non-diffractive overlay background like the dijet events, and 2) background from the beam-gas interactions other than the normal beam-beam interactions. The overlay background of ND events can be determined, in analogy to the dijet case, using the west BBC and FCAL tower distributions. Figure 6.21 shows the multiplicity distributions for the relevant forward detectors in inclusive diffractive events with $0.035 < \xi_{\bar{p}} < 0.095$ and $|t_{\bar{p}}| < 1.0\,\mathrm{GeV}^2$. The high multiplicity range shows an enhancement, which is attributed to the overlaying ND events. Using the same evaluation as in the dijet case, the overlaying ND background is estimated to be $3.0 \pm 0.01(stat.)\,\%$.

$$\begin{aligned} F^{ND\,BG}_{SD\,incl}(\mathrm{BBC}) &= \frac{22,700.5 \;+\; 49273.9}{497,856 \;+\; 1,141,137} \;=\; 4.4\,\%, \\ F^{ND\,BG}_{SD\,incl}(\mathrm{FCAL}) &= \frac{19,512.5 \;+\; 5,815.2}{497,856 \;+\; 1,141,137} \;=\; 1.5\,\%, \end{aligned}$$

$$F^{ND\,BG}_{SD\,incl} \;=\; \frac{F^{ND\,BG}_{SD\,incl}(\mathrm{BBC}) \;+\; F^{ND\,BG}_{SD\,incl}(\mathrm{FCAL})}{2} \;=\; 3.0 \pm 0.01(stat.)\,\%.$$

Comparing with the case of dijets, the BBC and FCAL tower results are slightly different. So that, we use a half of their difference (1.4 %) as a systematic uncertainty.

Second, beam-gas interaction background is expected to have a low multiplicity on the proton side [59]. Figure 6.22 shows the east BBC and FCAL tower distributions in the same inclusive sample as above. Both distributions show the peaks at zero multiplicity bin and their magnitudes are consistent with each other. A straight line fit in the range $2 \leq N_{BBC} \leq 7$ gives a fraction of excess events, $5.2 \pm 0.02(stat.)\,\%$, by extrapolating the fit to zero multiplicity bin. The observed peak is most probably attributed to beam-gas interaction background, so this fraction is taken as the beam-gas background fraction in inclusive diffractive sample.

$$F^{GAS}_{SD\,incl} \;=\; 5.2 \;\pm\; 0.02(stat.)\,\%.$$

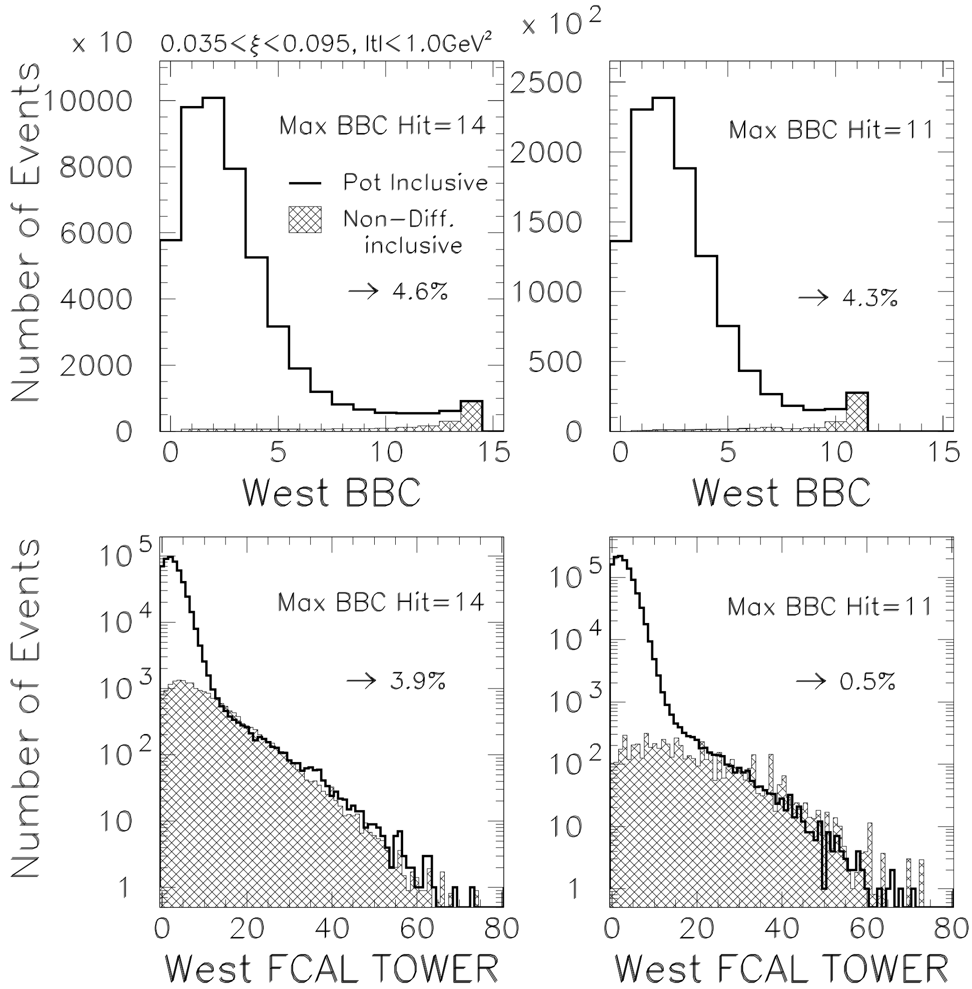

Figure 6.21: BBC hit (upper) and FCAL tower (lower) multiplicity distributions for the $\bar{p}$ side in inclusive diffractive events. Left (right) side shows the distributions for runs of maximum BBC hit=14 (11). The distributions of non-diffractive sample (shaded histograms) are normalized to the contents of diffractive sample (full histogram) at the maximum BBC hit bin $N_{BBC-\bar{p}} = 14$ or 11, and $N_{CAL-\bar{p}} \geq 20$.

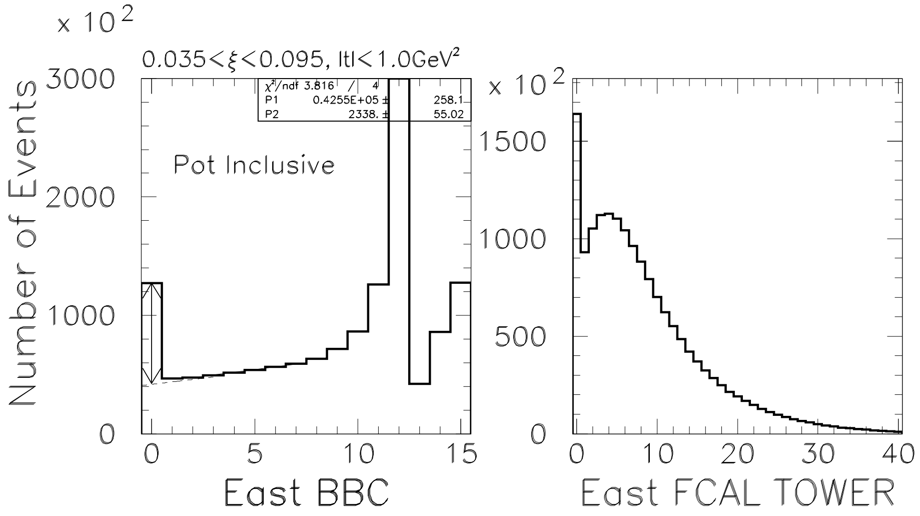

Figure 6.22: BBC hit (left) and FCAL tower (right) multiplicity distributions for the p side in inclusive diffractive events. The peak at zero multiplicity bin is attributed to the beam-gas interaction background.

A straight line fit gives an error of 0.02 % on beam-gas background fraction, so this is included as a systematic uncertainty.

Not only the dijet sample, but also the inclusive one should be corrected for the single vertex requirement. In the inclusive sample we have to take care of two possible cases:

case 1 A single interaction in $\bar{p}p$ collisions may not be reconstructed as a visible vertex due to some possible ambiguities (detector inefficiency, soft collision, etc.). In this case we obtain "zero vertex" events.

case 2 A single interaction event with relatively high particle multiplicity could have multiple fake vertices.

In the dijet case we consider only the case 2 because dijet events have always a reconstructed vertex.

For case 1, we sample the data with no vertex requirement in the trigger. This subsample (110 K events) is identical to that used in a cross check of live time acceptance

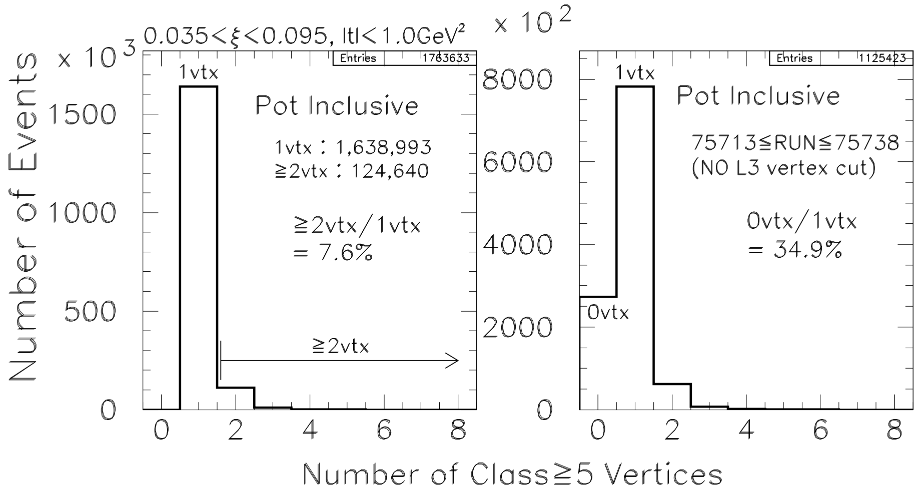

Figure 6.23: Number of class$\geq$ 5 vertices in inclusive diffractive events (left), and the subsample which was triggered without any vertex requirement (right).

in Appendix B. The vertex multiplicity distribution for class $\geq$ 5 in this sample is shown in the right side of Figure 6.23 (right). The distribution with number of vertices $\geq$ 1 is very similar to that of our whole data sample (left) used in main analysis. From this multiplicity distribution without any bias of vertex cut, we know that the ratio of zero vertex to single vertex data is $R_{01} = 34.9 \pm 0.1(stat.)\,\%$. Figure 6.24(top) shows the east BBC multiplicities of zero vertex sample (first bin of Figure 6.23), compared with those of single vertex sample. Left is for the sample with maximum BBC hit =15, and right for =12. Normalization of single vertex to zero vertex data at the maximum hit bin gives the fractions of 18.1 % and 21.5 % for both samples. When we apply these fractions to tower multiplicity distributions of single vertex data, and superimpose them on the zero vertex ones as shown in Figure 6.24 (middle left), the shapes of both distributions are different. Therefore, taking the ratio of these two tower distributions (middle right), then multiplying the single vertex shape by this ratio, we obtain the reasonable distributions normalized to the zero vertex shape. These are shown in the bottom two plots. In the calculation of the ratio, an exponential fit is done to the plot (middle right) in the range $8 \leq N_{CAL} \leq 28$ and then the fit function values are multiplied by the FCAL tower distribution of single vertex data for whole N_{CAL} range. Shown in the figure is only for the sample with maximum BBC hit =15, but it is done for the sample with maximum hit =12 separately. The obtained distributions indicate the fractions of 18.4 % and 23.8 % for two types of samples, which are consistent with the BBC values above. Combining two samples of data and taking the average of obtained numbers for the BBC and FCAL tower, we evaluate a fraction of single interactions in zero vertex events to be $F_{10} = 21.3 \pm 0.1(stat.)\,\%$. These evaluations allow us to obtain the number of single interaction events in the whole zero vertex data to be

$$N_{1/0} \;=\; N_{SD}^{incl} \;\times\; R_{01} \;\times\; F_{10} \;=\; 121,782 \;\pm\; 627(stat.),$$

where $N_{SD}^{incl} = 1,638,993$ is the number of diffractive inclusive events with relevant analysis cuts used in the main analysis. The systematic uncertainty of $N_{1/0}$ is estimated to be $\pm 4,582$ events, which is originated from half of difference between the BBC and FCAL tower results.

For case 2, the method used in dijet case can be used again. Figure 6.25 shows the west BBC and FCAL tower multiplicities in a sample of multiple vertices, compared with those of single vertex. By normalizing the low multiplicity range ($N_{BBC} \leq 2$ or $N_{CAL} \leq 2$) of single vertex shape to that of multiple vertices, the fractions of single interactions in events with multiple vertices are obtained to be 83.2 % (75.1 %) from the BBC (FCAL tower) shape comparison. From the total number of events with multiple vertices $N_{\geq 2} = 124,640$, the average of BBC and FCAL tower values gives

$$N_{1/\geq 2} \;=\; 98,623 \;\pm\; 222(stat.),$$

which is the number of single interaction events in a whole sample of multi-vertices. A half of difference between the BBC and FCAL tower values, $\pm 5,066$, can be used as a systematic uncertainty. Finally, from these two numbers of N_{10} and $N_{1/\geq 2}$, we estimate the single vertex selection efficiency of diffractive inclusive sample as follows,

$$\varepsilon_{SD\,incl}^{1vtx} \;=\; \frac{N_{SD}^{incl}}{N_{SD}^{incl} \;+\; (\varepsilon_{SD\,incl}^{Zvtx} \cdot N_{1/0}) \;+\; N_{1/\geq 2}}$$

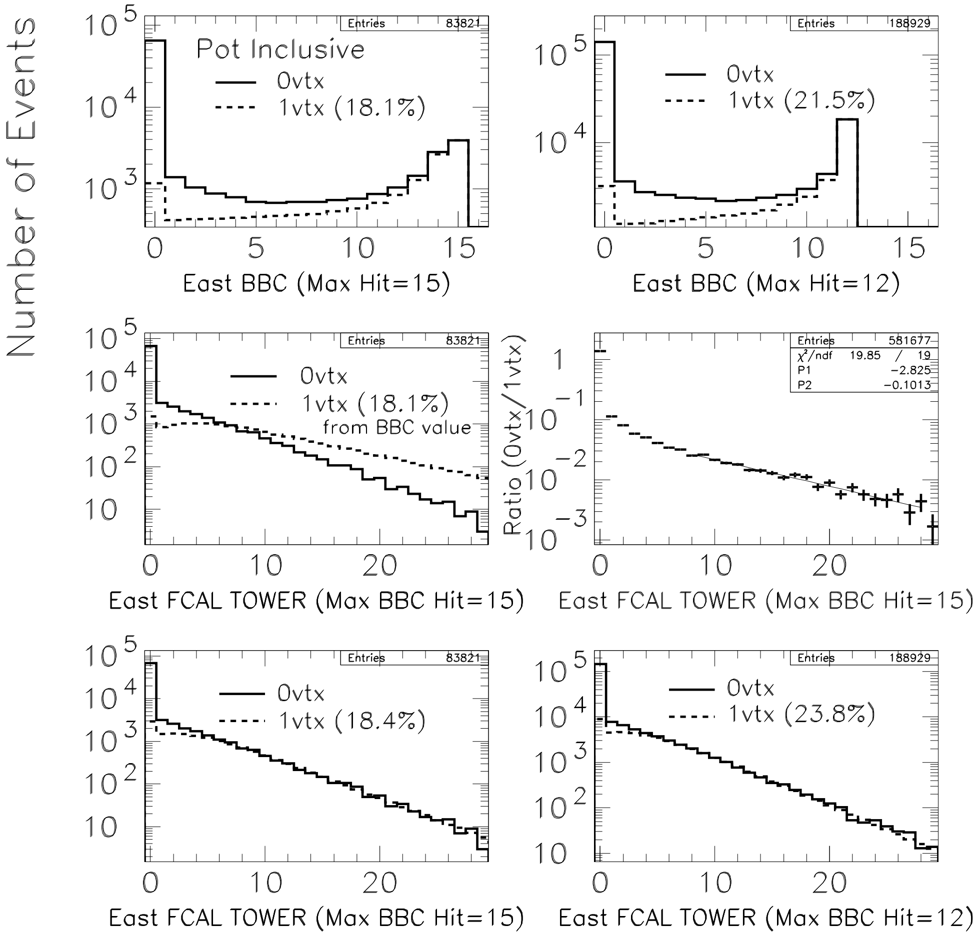

Figure 6.24: BBC hit and FCAL tower multiplicity distributions for the p side in zero vertex sample (full histogram), compared with those of single vertex sample (dashed histogram). Each plot is described in the text.

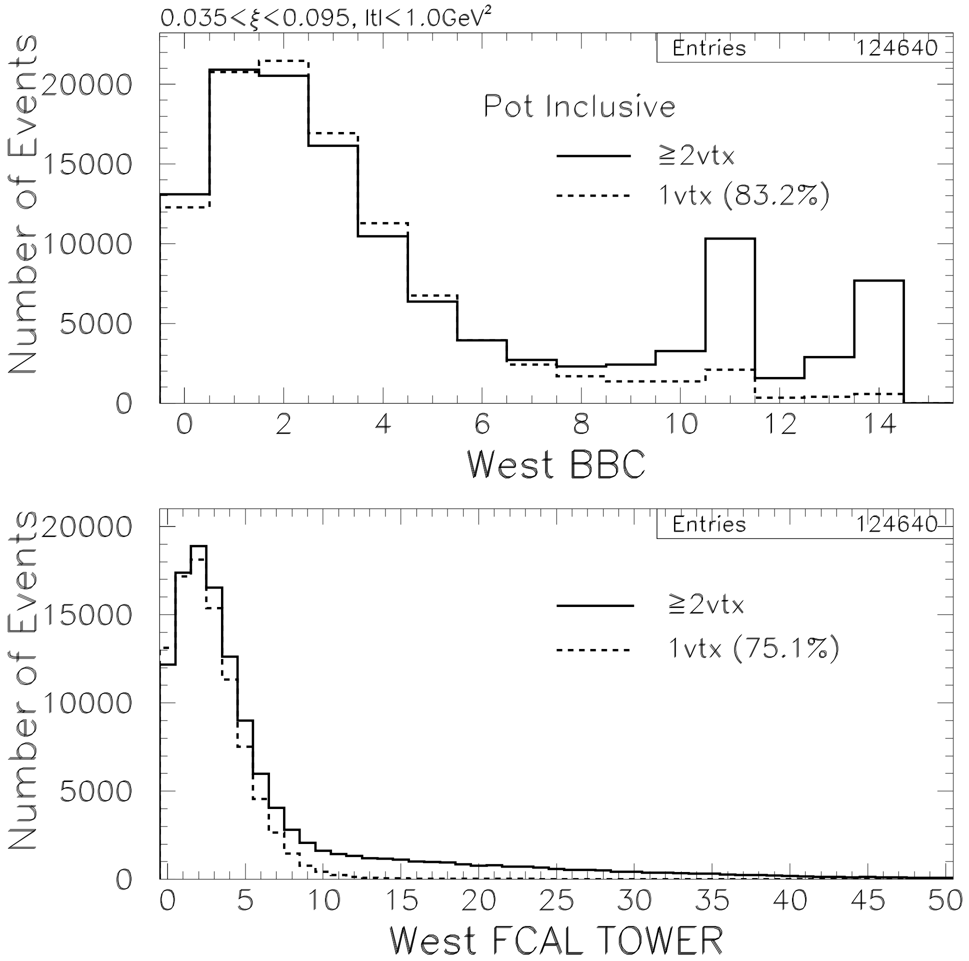

Figure 6.25: BBC hit (upper) and FCAL tower (lower) multiplicity distributions for the $\bar{p}$ side in events with multi-vertices (full histogram), compared with those of single vertex sample (dashed histogram).

Table 6.2: The ratio of dijet to inclusive diffractive events, and cross section of diffractive events with dijets of $E_T > 7\,\mathrm{GeV}$ and $E_T > 10\,\mathrm{GeV}$. The kinematic range of the measurement is given at the top of the table. The data is corrected for the Roman Pot acceptance. All the errors are statistical only.

$0.035 < \xi_{\bar{p}} < 0.095$, $|t_{\bar{p}}| < 1.0\,\mathrm{GeV}^2$

Dijet E_{Tmin}	$E_T > 7\,\mathrm{GeV}$	$E_T > 10\,\mathrm{GeV}$
$R^{jj}_{incl}(SD)$	$2.07 \pm 0.02\,\%$	$0.37 \pm 0.01\,\%$
σ^{jj}_{SD}	$16.2 \pm 0.1\,\mu\mathrm{b}$	$2.9 \pm 0.1\,\mu\mathrm{b}$

(Statistical Errors Only)

$$= \; 88.5 \; \pm \; 0.1(stat.)\,\%,$$

where $\varepsilon^{Zvtx}_{SD\,incl} = 94.4\,\%$ is the efficiency of the cut $|Z_{vertex}| \leq 60\,\mathrm{cm}$ to diffractive inclusive sample, which is measured by using the previously described fit to Z_{vertex} distribution.

The cross section of SD dijets is now calculable by the following equations:

$$\sigma^{jj}_{SD} \;=\; R^{jj}_{incl}(SD) \;\times\; \sigma^{incl}_{SD}, \tag{6.16}$$

$$R^{jj}_{incl}(SD) \;=\; \frac{N^{jj,RP}_{SD} \cdot (1 - F^{ND\,BG}_{SD\,jj})}{\varepsilon^{Wmulti}_{SD\,j} \cdot \varepsilon^{HTFLT}_{SD\,jj} \cdot \varepsilon^{1vtx}_{SD\,jj}} \Bigg/ \frac{N^{incl,RP}_{SD} \cdot (1 - F^{ND\,BG}_{SD\,incl}) \cdot (1 - F^{GAS}_{SD\,incl})}{\varepsilon^{1vtx}_{SD\,incl}}, \tag{6.17}$$

where $R^{jj}_{incl}(SD)$ is the ratio of dijet to inclusive diffractive cross section. The number of diffractive dijet events is normalized to that of diffractive inclusive events after the data is corrected for the Roman Pot acceptance, then it is multiplied by single diffractive cross section σ^{incl}_{SD} integrated over our kinematical range $0.035 < \xi < 0.095$ and $|t| < 1.0\,\mathrm{GeV}^2$. We use

$$\sigma^{incl}_{SD} \;=\; 0.78 \;\pm\; 0.16\,\mathrm{mb},$$

as single diffractive cross section, where an error of 0.16 mb is assigned as an overall 20 % uncertainty of 0.78 mb. This value is obtained in the evaluation of the cross section based on the CDF published results of single diffractive cross section at $\sqrt{s} =$

1800 GeV [37]. Substituting the evaluated efficiencies and background contributions shown in Table 5.4 into the equation, we obtain $R^{jj}_{incl}(SD)$ and σ^{jj}_{SD} as in Table 6.2. It is worth noting that $R^{jj}_{incl}(SD)$ is a factor 5 lower than $\sigma^{jj}_{ND}/\sigma_{ND}$ for $E_T > 7$ GeV; i.e., SD events are less efficient at producing jets.

6.6.3 Double Pomeron Dijet Cross Section

Finally we have estimated the cross section of the dijet produced in Double Pomeron Exchange (DPE) events. The kinematic range of our measurement is $0.035 < \xi_{\bar{p}} < 0.095$, $0.01 < \xi_p < 0.03$ in ξ, and $|t_{\bar{p}}| < 1.0\,\mathrm{GeV}^2$, all $|t_p|$ (integrated) in t. The following equations allow us to derive the DPE dijet cross section.

$$\sigma^{jj}_{DPE} = R_{\frac{DPE}{SD}} \times \sigma^{jj}_{SD}, \tag{6.18}$$

$$R_{\frac{DPE}{SD}} = \frac{N^{jj,RP}_{DPE}}{\varepsilon^{Wmulti}_{DPE\,jj} \cdot \varepsilon^{HTFLT}_{DPE\,jj} \cdot \varepsilon^{1vtx}_{DPE\,jj} \cdot A_{LIVE}} \Bigg/ \frac{N^{jj,RP}_{SD} \cdot (1 - F^{ND\,BG}_{SD\,jj})}{\varepsilon^{Wmulti}_{SD\,jj} \cdot \varepsilon^{HTFLT}_{SD\,jj} \cdot \varepsilon^{1vtx}_{SD\,jj}}, \tag{6.19}$$

where $R_{\frac{DPE}{SD}}$ is the ratio of DPE to SD dijet cross section, and σ^{jj}_{SD} is the SD dijet cross section obtained above. The number of DPE and SD dijet events are corrected for the Roman Pot acceptance. Also, the number of DPE dijet events is corrected for the rapidity gap acceptance $A_{gap} = 83.7 \pm 11.1\,\%$. From the measured values of the efficiencies and background fraction listed in Table 6.3, the DPE dijet cross sections are obtained along with the cross section ratios: DPE relative to SD, SD to ND and DPE to ND dijet for both $E_T > 7$ GeV and $E_T > 10$ GeV thresholds and they are given in Table 6.4. In Eq. (6.19), A_{LIVE} is the "live time acceptance" which is used to correct for the occupancies of the BBC and forward calorimeter by the detector noise or particles from soft interactions which are not reconstructed as the visible vertices. In Appendix B we evaluate this acceptance and obtain it to be

$$A_{LIVE} = 97.0 \pm 2.7(syst.)\,\%.$$

Table 6.3: Efficiencies and background fractions evaluated for DPE and SD dijet events of $E_T > 7\,\mathrm{GeV}$ and $E_T > 10\,\mathrm{GeV}$. All the errors are statistical only unless explicitly mentioned.

Dijet E_{Tmin}		$E_T > 7\,GeV$	$E_T > 10\,GeV$
DPE Dijet Candidates	N^{jj}_{DPE}	117.7 ± 12.1	14.4 ± 4.4
⇒ after RP acceptance correction	$N^{jj,RP}_{DPE}$	143.1 ± 13.8	17.4 ± 5.0
Single Vertex Selection Efficiency	$\varepsilon^{1vtx}_{DPE\,jj}$	$95.9 \pm 1.9\,\%$	
Wmulti Cut Efficiency	$\varepsilon^{Wmulti}_{DPE\,jj}$	$93.3 \pm 2.5\,\%$	
HT Filter Efficiency	$\varepsilon^{HTFLT}_{DPE\,jj}$	100 % assumed.	
SD Dijet Events	N^{jj}_{SD}	$27,405 \pm 166$	$4,866 \pm 70$
⇒ after RP acceptance correction	$N^{jj,RP}_{SD}$	$34,413 \pm 219$	$6,049 \pm 91$
ND Overlay Background	$F^{ND\,BG}_{SD\,jj}$	$0.51 \pm 0.04\,\%$	$0.65 \pm 0.12\,\%$
Single Vertex Selection Efficiency	$\varepsilon^{1vtx}_{SD\,jj}$	$81.8 \pm 0.4\,\%$	$79.6 \pm 0.9\,\%$
Wmulti Cut Efficiency	$\varepsilon^{Wmulti}_{SD\,jj}$	$96.2 \pm 0.1\,\%$	$96.3 \pm 0.3\,\%$
HT Filter Efficiency	$\varepsilon^{HTFLT}_{SD\,jj}$	$96.9 \pm 0.2\,\%$	
Live Time Acceptance	A_{LIVE}	$97.0 \pm 2.7(syst.)\,\%$	

(Statistical Errors Only)

From the table we conclude that the measured cross section ratios of DPE to SD and SD to ND dijet events are all at similar level of 0.2–0.4 %.

6.6.4 Systematic Uncertainty

The most dominant systematic uncertainty on the dijet cross section is expected to be due to the jet energy scale. A jet in CDF is generally defined as the sum of E_T of calorimeter towers within a η-ϕ cone of radius R. The R is typically selected to be 0.4, 0.7 or 1.0. The E_T of jets reconstructed with CDF algorithm is estimated to be correct within the following accuracy:

$$\Delta E_T^{jet} = 3.2 \pm 1.5(stat.) \pm 4.1(syst.)\,\% \qquad \text{(Cone } R = 0.4\text{)},$$

$$\Delta E_T^{jet} = 1.8 \pm 1.3(stat.)\,\% \qquad \text{(Cone } R = 0.7\text{)},$$

for the jet with raw $E_T^{jet} \geq 8\,\mathrm{GeV}$ and $|\eta^{jet}| < 2.4$ (a cone radius of 0.4 or 0.7) [61]. From this, we assign the systematic uncertainty of $R = 0.4$ jet ($\pm 4.1\,\%$) to $R = 0.7$ jet

Table 6.4: The ratios of DPE to SD, SD to ND and DPE to ND dijet production cross section, and the cross section of DPE events with dijets of $E_T > 7\,\text{GeV}$ and $E_T > 10\,\text{GeV}$. The kinematic range of the measurement is given at the top of the table. The DPE and SD data are corrected for the Roman Pot acceptance. In addition, the rapidity gap acceptance correction is applied for DPE data. All the errors are statistical only.

$0.035 < \xi_{\bar{p}} < 0.095$, $0.01 < \xi_p < 0.03$, $|t_{\bar{p}}| < 1.0\,\text{GeV}^2$

Dijet E_{Tmin}	$E_T > 7\,\text{GeV}$	$E_T > 10\,\text{GeV}$
$R_{\frac{DPE}{SD}}$	$0.27 \pm 0.03\,\%$	$0.12 \pm 0.03\,\%$
$R_{\frac{SD}{ND}}$	$0.32 \pm 0.003\,\%$	$0.18 \pm 0.004\,\%$
$R_{\frac{DPE}{ND}}$	$[0.86 \pm 0.09] \times 10^{-5}$	$[0.21 \pm 0.06] \times 10^{-5}$
σ_{DPE}^{jj}	$43.6 \pm 4.4\,\text{nb}$	$3.4 \pm 1.0\,\text{nb}$

(Statistical Errors Only)

that is the case of our jet. Then we add the additional $\pm 3.0\,\%$ in quadrature because our E_T threshold (corrected $E_T > 7\,\text{GeV}$ or $10\,\text{GeV}$) is lower than raw $E_T \geq 8\,\text{GeV}$ so the uncertainty should be larger. For the forward jets with $|\eta^{jet}| \geq 2.4$, we further add the $\pm 2.5\,\%$ uncertainty [60]. Hence we obtain the total jet energy scale uncertainty δE_T^{jet} to be

$$\delta E_T^{jet} = \pm 5.6\,\% \quad (|\eta^{jet}| < 2.4), \tag{6.20}$$

$$\delta E_T^{jet} = \pm 6.1\,\% \quad (|\eta^{jet}| \geq 2.4). \tag{6.21}$$

The uncertainty on the underlying event (UE) energy δE_T^{UE} which we should subtract from the jet will have a large contribution to the total systematic uncertainty. As discussed in the dijet event selection of Section 5.3, we assign the $\pm 30\,\%$ uncertainty to the UE energy subtraction for all the DPE, SD and ND dijets. So that, subtracted from the jets are $1.16 \pm 0.35\,\text{GeV}$, $0.54 \pm 0.16\,\text{GeV}$ and $0.37 \pm 0.11\,\text{GeV}$ for DPE, SD and ND dijets respectively. Here the DPE dijet event is defined as the dijet event with $N_{BBC-p} = N_{CAL-p} = 0$.

Table 6.5: Systematic uncertainties on non-diffractive dijet cross section for dijets with $E_T > 7\,\text{GeV}$ and $E_T > 10\,\text{GeV}$.

For ND Inclusive Events		
BBC Cross Section	3.1 %	
Average Number of ND Interactions	1.0 %	
For ND Dijet Events	$\boldsymbol{E_T > 7\,\text{GeV}}$	$\boldsymbol{E_T > 10\,\text{GeV}}$
Jet Energy Scale	13.9 %	23.4 %
Underlying Event Energy	13.8 %	15.8 %
HT Filter Efficiency	0.5 %	
Z_{vertex} Cut Efficiency	2.0 %	
Total Systematic Uncertainty	20.0 %	28.5 %

Uncertainty on Non-Diffractive Dijet Cross Section

We have evaluated the non-diffractive dijet cross section using Eq. (6.12) and the results are given in Table 6.1. The systematic uncertainties taken into account on the cross section are listed in Table 6.5. The uncertainties from the jet energy scale and UE energy are evaluated by changing their values by $\pm 1\sigma = \delta E_T^{jet}$ or δE_T^{UE} and taking the lager differences in the number of dijet events. The BBC cross section uncertainty is estimated from Eq. (3.5) to be

$$\left.\frac{\delta\sigma_{ND}^{jj}}{\sigma_{ND}^{jj}}\right|_{\sigma_{BBC}} = \frac{\delta\sigma_{BBC}}{\sigma_{BBC}} = 3.1\,\%.$$

In the calculation of the average number of non-diffractive interactions per bunch crossing, we use σ_{BBC}, so σ_{BBC} uncertainty could affect the total number of non-diffractive interactions. This effect causing from σ_{BBC} uncertainty is estimated to be about 0.2 % by changing the σ_{BBC} value by $\pm 1\sigma$. Other possible uncertainties (e.g., instantaneous luminosity) could contribute, and so the total uncertainty on the number of inclusive non-diffractive interactions is assigned to be 1.0 %. The uncertainties from HTFLT filter and Z_{vertex} cut efficiencies are estimated to be

$$\begin{aligned}\left.\frac{\delta\sigma_{ND}^{jj}}{\sigma_{ND}^{jj}}\right|_{\varepsilon} = \frac{\delta\varepsilon}{\varepsilon} &= 0.5\,\% \qquad \text{(HTFLT Filter Efficiency)}\\ &= 2.0\,\% \qquad (Z_{vertex}\ \text{Cut Efficiency}),\end{aligned}$$

Table 6.6: Systematic uncertainties on single diffractive dijet cross section for dijets with $E_T > 7\,\mathrm{GeV}$ and $E_T > 10\,\mathrm{GeV}$.

For SD Inclusive Events		
Inclusive Diffractive Cross Section	20.0 %	
ND Overlay Background	1.5 %	
BEAM-GAS Background	0.02 %	
Single Vertex Selection Efficiency	1.6 %	
For SD Dijet Events	$\boldsymbol{E_T > 7\,\mathrm{GeV}}$	$\boldsymbol{E_T > 10\,\mathrm{GeV}}$
Jet Energy Scale	23.1 %	30.5 %
Underlying Event Energy	11.3 %	9.1 %
ND Overlay Background	0.2 %	0.2 %
Single Vertex Selection Efficiency	2.2 %	2.5 %
Wmulti Cut Efficiency	1.7 %	1.5 %
HT Filter Efficiency	0.5 %	
$(\xi_{\bar{p}}, t_{\bar{p}})$ resolution	1.3 %	1.7 %
Total Systematic Uncertainty	32.8 %	37.8 %

from $\varepsilon_{NDjj}^{HTFLT} = 96.9 \pm 0.5(syst.)\,\%$ and $\varepsilon_{NDjj}^{Zvtx} = 95.9 \pm 2.0(syst.)\,\%$. Including all the uncertainties, we finally obtain the following non-diffractive dijet cross sections σ_{ND}^{jj}:

$\boldsymbol{E_T^{jet} > 7\,\mathrm{GeV}}$	$\boldsymbol{5.04 \pm 0.03(stat.) \pm 1.01(syst.)\,\mathrm{mb}}$
$\boldsymbol{E_T^{jet} > 10\,\mathrm{GeV}}$	$\boldsymbol{1.62 \pm 0.02(stat.) \pm 0.46(syst.)\,\mathrm{mb}}$

For $E_T > 7\,\mathrm{GeV}$ dijets, the jet energy scale and UE energy uncertainties contribute roughly at the same magnitude, but for the higher threshold of $E_T > 10\,\mathrm{GeV}$, the most dominant uncertainty is due to the jet energy scale.

Uncertainty on Single Diffractive Dijet Cross Section

In addition to the jet energy scale and UE energy, the uncertainties on the efficiencies and background contributions, and the resolutions of $\xi_{\bar{p}}$ and $t_{\bar{p}}$ are taken into account. Sources of possible systematic uncertainties are listed in Table 6.6. As described in Section 6.6.2, we assign a 20 % uncertainty (0.16 mb) on single diffractive cross section

$\sigma_{SD}^{incl} = 0.78\,\mathrm{mb}$, which results in the same uncertainty on the dijet cross section.

$$\left.\frac{\delta\sigma_{SD}^{jj}}{\sigma_{SD}^{jj}}\right|_{\sigma_{SD}^{incl}} = \frac{\delta\sigma_{SD}^{incl}}{\sigma_{SD}^{incl}} = 20\,\%.$$

Basically the uncertainties of the efficiencies or non-diffractive overlay background are obtained as the difference between the two independent measurements, as described previously. Their uncertainties on the cross section are given as follows,

$$\begin{aligned}\left.\frac{\delta\sigma_{SD}^{jj}}{\sigma_{SD}^{jj}}\right|_{\varepsilon} = \frac{\delta\varepsilon}{\varepsilon} &= 0.5\,\% \qquad \text{(HTFLT Filter Efficiency)}\\ &= 1.7\,(1.5)\,\% \qquad \text{(Wmulti Cut Efficiency)}\\ &= 2.2\,(2.5)\,\% \qquad \text{(Single Vertex Efficiency for Dijet)}\\ &= 1.6\,\% \qquad \text{(Single Vertex Efficiency for Inclusive)},\end{aligned}$$

for the efficiencies of dijet events of $E_T > 7$ (10) GeV, and

$$\begin{aligned}\left.\frac{\delta\sigma_{SD}^{jj}}{\sigma_{SD}^{jj}}\right|_{F} = \frac{\delta F}{1-F} &= 0.2\,\% \qquad \text{(ND Overlay Background for Dijet)}\\ &= 1.5\,\% \qquad \text{(ND Overlay Background for Inclusive)}\\ &= 0.02\,\% \qquad \text{(BEAM-GAS Background)},\end{aligned}$$

for the background fractions, given in Table 6.6.

The $\xi_{\bar{p}}$ and $t_{\bar{p}}$ reconstructed from the Roman Pot tracks have the typical resolutions of $\delta\xi_{\bar{p}} \approx 10^{-3}$ and $\delta t_{\bar{p}} \approx 0.1\,\mathrm{GeV}^2$. When we select the data within the region $0.035 < \xi_{\bar{p}} < 0.095$ and $|t_{\bar{p}}| < 1.0\,\mathrm{GeV}^2$ in the main analysis, the selected data would have the effect of this finite resolution. For $E_T > 7$ (10) GeV dijet and inclusive events, we find that the number of SD dijet and inclusive events after the Roman Pot acceptance is corrected could change by about $\pm 2.5\,\%$ ($\pm 2.9\,\%$) and $\pm 1.2\,\%$ respectively, under the variations of $\xi_{\bar{p}} \pm \delta\xi_{\bar{p}}$ and $t_{\bar{p}} \pm \delta t_{\bar{p}}$. Therefore, in the calculation of SD dijet cross section, their uncertainties for $E_T > 7$ (10) GeV dijets are partly canceled out and then reduced to $\pm 1.3\,\%$ ($\pm 1.7\,\%$) by taking the ratio of number of dijet to inclusive events.

$$\left.\frac{\delta\sigma_{SD}^{jj}}{\sigma_{SD}^{jj}}\right|_{(\xi_{\bar{p}},\, t_{\bar{p}})} \approx \left[1 + \frac{\delta N_{SD}^{jj,\,RP}}{N_{SD}^{jj,\,RP}}\right] \Bigg/ \left[1 + \frac{\delta N_{SD}^{incl,\,RP}}{N_{SD}^{incl,\,RP}}\right] - 1$$

$$\begin{aligned} &= [1 + 0.025\,(0.029)]/[1 + 0.012] - 1 \\ &= 1.3\,\%\,(1.7\,\%). \end{aligned}$$

The obtained values of SD dijet cross sections σ_{SD}^{jj} including these possible uncertainties are given below:

$0.035 < \xi_{\bar{p}} < 0.095,\ |t_{\bar{p}}| < 1.0\,\mathrm{GeV}^2$

$E_T^{jet} > 7\,\mathrm{GeV}$	$16.2\ \pm\ 0.1(stat.)\ \pm\ 5.3(syst.)\,\mu\mathrm{b}$
$E_T^{jet} > 10\,\mathrm{GeV}$	$2.9\ \pm\ 0.1(stat.)\ \pm\ 1.1(syst.)\,\mu\mathrm{b}$

Uncertainty on Double Pomeron Dijet Cross Section

From Eqs. (6.16) (6.17) and (6.18) (6.19), the cross section of DPE dijet events is given by

$$\begin{aligned} \sigma_{DPE}^{jj} &= R_{\frac{DPE}{SD}} \times \sigma_{SD}^{jj} \\ &= R_{\frac{DPE}{SD}} \times R_{incl}^{jj}(SD) \times \sigma_{SD}^{incl} \\ &= \left[\frac{N_{DPE}^{jj,\,RP}}{\varepsilon_{DPE\,jj}^{Wmulti} \cdot \varepsilon_{DPE\,jj}^{HTFLT} \cdot \varepsilon_{DPE\,jj}^{1vtx} \cdot A_{LIVE}} \Bigg/ \frac{N_{SD}^{incl,\,RP} \cdot (1 - F_{SD\,incl}^{ND\,BG}) \cdot (1 - F_{SD\,incl}^{GAS})}{\varepsilon_{SD\,incl}^{1vtx}} \right] \\ &\quad \times \sigma_{SD}^{incl}. \end{aligned}$$

So the uncertainty on the DPE dijet cross section depends on the ambiguity of the measurements for DPE dijets and inclusive SD events. As in ND and SD events, we estimate the dependence of the number of observed DPE events on the jet energy scale and UE energy. Figure 6.26 shows the diagonal multiplicity of the BBC hits versus FCAL tower on the p side for diffractive dijet events of $E_T > 7\,\mathrm{GeV}$ after the jet energy is scaled up or down by 1σ (=5.6 % for $|\eta^{jet}| < 2.4$, 6.1 % for $|\eta^{jet}| \geq 2.4$). From the observed number of DPE events, 159.4 (81.0) for 1σ up (down), we find that the number of DPE events could change by about 35 % at most due to the jet energy scale uncertainty. Also, by varying the UE energy by $1\sigma = \pm 30\,\%$, there are 101.4 (126.7) events observed for the case of increasing (decreasing) UE energy. This indicates that the uncertainty on the number of observed DPE events is about 14 %

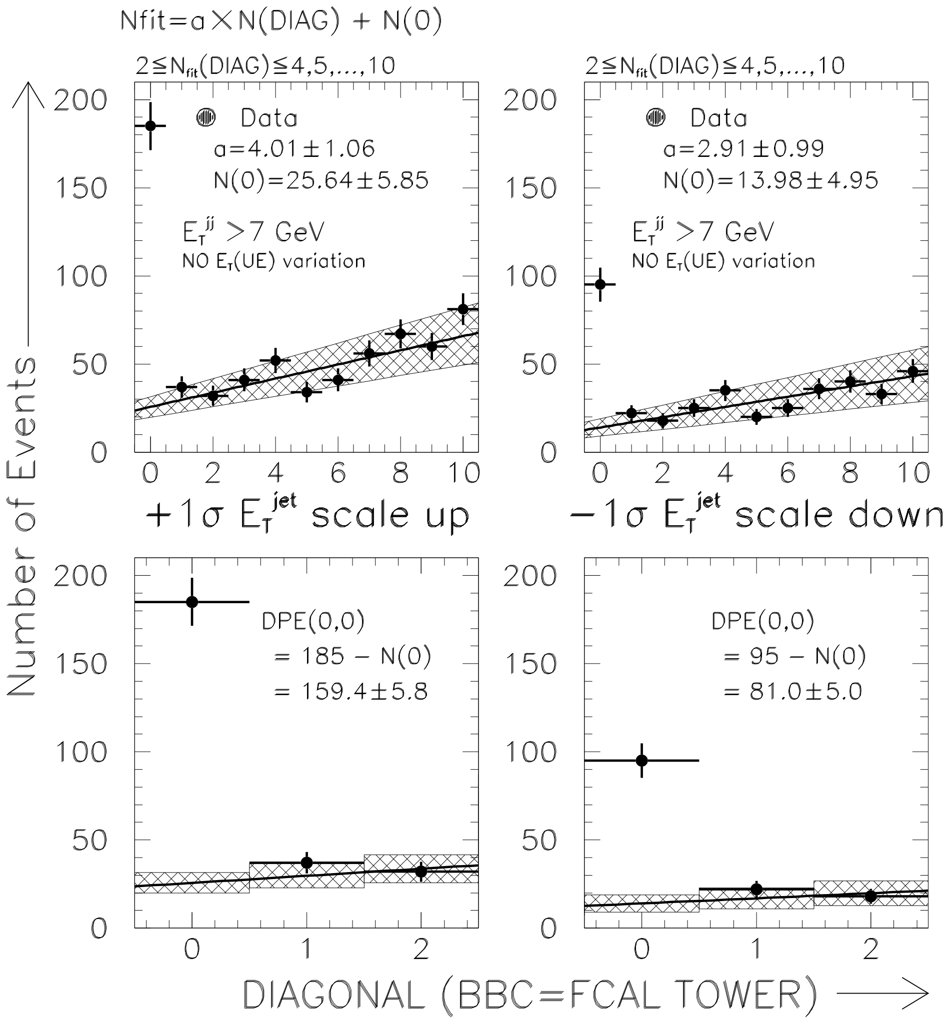

Figure 6.26: Linear fit results to the diagonal multiplicity distribution between the BBC hits and FCAL towers on the p side for diffractive events with dijets of $E_T >$ 7 GeV. Left (right) plots are for jets whose E_T was scaled up (down) by 1σ (=5.6 % for $|\eta^{jet}| < 2.4$, 6.1 % for $|\eta^{jet}| \geq 2.4$). The fits were done for the range 2$\leq N_{DIAG-p} \leq$ $4, 5, \ldots, 10$ to estimate the DPE events. The shaded bands correspond to the fit functions varying with the $\pm 1\sigma$ uncertainties of intercepts N(0) and slopes a. Lower half shows the region of $N_{DIAG-p} \leq 2$.

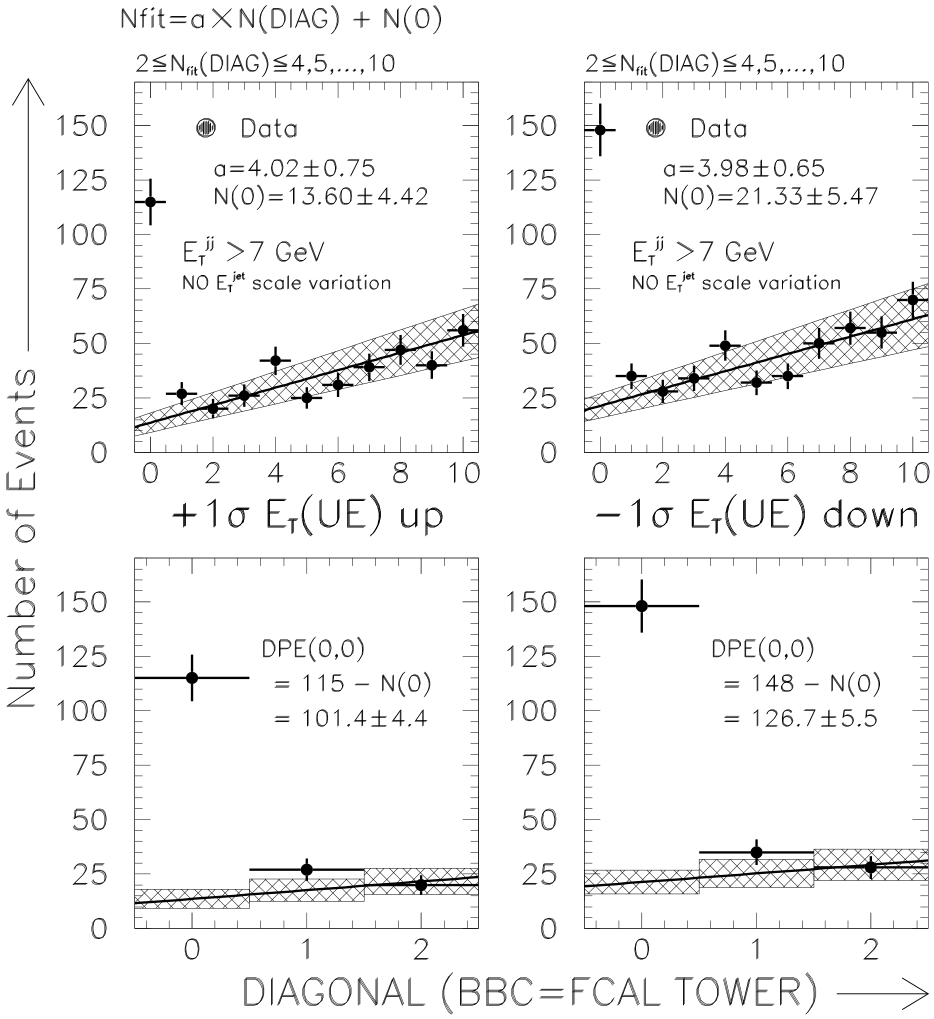

Figure 6.27: Linear fit results to the diagonal multiplicity distribution between the BBC hits and FCAL towers on the p side for diffractive events with dijets of $E_T >$ 7 GeV. Left (right) plots are for jets from which the underlying event energy increased (decreased) by 1σ (=30 %) was subtracted. The fits were done for the range $2\leq$ $N_{DIAG-p} \leq 4, 5, \ldots, 10$ to estimate the DPE events. The shaded bands correspond to the fit functions varying with the $\pm1\sigma$ uncertainties of intercepts N(0) and slopes a. Lower half shows the region of $N_{DIAG-p} \leq 2$.

Table 6.7: Systematic uncertainties on double pomeron dijet cross section for dijets with $E_T > 7\,\mathrm{GeV}$ and $E_T > 10\,\mathrm{GeV}$.

For SD Inclusive Events		
Inclusive Diffractive Cross Section	20.0 %	
ND Overlay Background	1.5 %	
BEAM-GAS Background	0.02 %	
Single Vertex Selection Efficiency	1.6 %	
For DPE Dijet Events	$\boldsymbol{E_T > 7\,\mathrm{GeV}}$	$\boldsymbol{E_T > 10\,\mathrm{GeV}}$
Jet Energy Scale	40.5 %	39.2 %
Underlying Event Energy	16.7 %	25.5 %
Linear Fit for DPE Signal Estimate	9.6 %	25.6 %
Single Vertex Selection Efficiency	2.0 %	
Wmulti Cut Efficiency	2.6 %	
Live Time Acceptance	2.8 %	
Rapidity Gap Acceptance	4.4 %	
$(\xi_{\bar{p}}, t_{\bar{p}})$ resolution	1.3 %	1.7 %
Total Systematic Uncertainty	49.6 %	57.4 %

at most, as shown in Figure 6.27. These variations are relatively large, compared with those of ND or SD dijets, since the DPE events are dominated by events with low E_T dijets.

The uncertainties causing from the acceptances are evaluated as follows,

$$\left.\frac{\delta\sigma^{jj}_{DPE}}{\sigma^{jj}_{DPE}}\right|_A = \frac{\delta A}{A} = 2.8\,\% \quad \text{(Live Time Acceptance)}$$
$$= 4.4\,\% \quad \text{(Rapidity Gap Acceptance)},$$

from $A_{LIVE} = 97.0 \pm 2.7(syst.)\,\%$ and $A_{gap} = 83.7 \pm 3.7(syst.)\,\%$. There could be also the resolution effects of reconstructed $\xi_{\bar{p}}$ and $t_{\bar{p}}$ for DPE events, but it would be difficult to estimate it due to small statistics. We therefore assign the same uncertainty as SD dijet events, $\pm 2.5\,\%$ ($\pm 2.9\,\%$) for dijets with $E_T > 7$ (10) GeV, which results in $\pm 1.3\,\%$ ($\pm 1.7\,\%$) uncertainty on the cross section.

$$\left.\frac{\delta\sigma^{jj}_{DPE}}{\sigma^{jj}_{DPE}}\right|_{(\xi_{\bar{p}},t_{\bar{p}})} \approx \left.\frac{\delta\sigma^{jj}_{SD}}{\sigma^{jj}_{SD}}\right|_{(\xi_{\bar{p}},t_{\bar{p}})} = 1.3\,\%\,(1.7\,\%).$$

Calculating the uncertainties on the cross section as in SD dijet case, we obtain the systematic uncertainties as given in Table 6.7. The measured cross sections σ^{jj}_{DPE} of DPE dijet events including these uncertainties are given as follows,

$0.035 < \xi_{\bar{p}} < 0.095,\ 0.01 < \xi_p < 0.03,\ |t_{\bar{p}}| < 1.0\,\mathrm{GeV}^2$

$E_T^{jet} > 7\,\mathrm{GeV}$	$43.6 \pm 4.4(stat.) \pm 21.6(syst.)\,\mathrm{nb}$
$E_T^{jet} > 10\,\mathrm{GeV}$	$3.4 \pm 1.0(stat.) \pm 2.0(syst.)\,\mathrm{nb}$

The ratios of DPE to SD, SD to ND and DPE to ND dijet production cross sections for $E_T > 7\,\mathrm{GeV}$ and $E_T > 10\,\mathrm{GeV}$ are given below:

$0.035 < \xi_{\bar{p}} < 0.095,\ 0.01 < \xi_p < 0.03,\ |t_{\bar{p}}| < 1.0\,\mathrm{GeV}^2$

$E_T^{jet} > 7\,\mathrm{GeV}$	$R_{\frac{DPE}{SD}}$	$0.27 \pm 0.03(stat.) \pm 0.05(syst.)\,\%$
	$R_{\frac{SD}{ND}}$	$0.32 \pm 0.003(stat.) \pm 0.07(syst.)\,\%$
	$R_{\frac{DPE}{ND}}$	$[0.86 \pm 0.09(stat.) \pm 0.23(syst.)] \times 10^{-5}$
$E_T^{jet} > 10\,\mathrm{GeV}$	$R_{\frac{DPE}{SD}}$	$0.12 \pm 0.03(stat.) \pm 0.05(syst.)\,\%$
	$R_{\frac{SD}{ND}}$	$0.18 \pm 0.004(stat.) \pm 0.04(syst.)\,\%$
	$R_{\frac{DPE}{ND}}$	$[0.21 \pm 0.06(stat.) \pm 0.10(syst.)] \times 10^{-5}$

6.7 Cross Section Ratios $R_{\frac{DPE}{SD}}$ and $R_{\frac{SD}{ND}}$

In terms of the parton density functions of the proton $f_{p_i/p}(x_1,\, Q^2)$, and the antiproton $f_{p_k/\bar{p}}(x_2,\, Q^2)$, the non-diffractive (inclusive) dijet production cross section σ^{jj}_{ND} is given by

$$\frac{d^3\sigma^{jj}_{ND}}{dx_1\, dx_2\, d\hat{t}} = \sum_{i,k} f_{p_i/p}(x_1,\, Q^2) \cdot f_{p_k/\bar{p}}(x_2,\, Q^2) \cdot \frac{d\hat{\sigma}(ik \to jj)}{d\hat{t}}, \tag{6.22}$$

where $d\hat{\sigma}(ik \to jj)/d\hat{t}$ is the cross section for the parton subprocess $ik \to jj$. The x_1 and x_2 are the momentum fractions of the p and $\bar{p}$ carried by the struck partons p_i and p_k, respectively. The diffractive dijet production cross section σ^{jj}_{SD} is given by Eq. (2.18) in terms of $f_{p_i/p}(x_1,\, Q^2)$ and the diffractive structure function $F^D_{p_k/\bar{p}}(\xi,\, t,\, \beta,\, Q^2)$ of the antiproton, where β is the fraction of the pomeron momentum carried by the struck parton p_k. The cross section ratio $R_{\frac{SD}{ND}}$ of diffractive to non-diffractive dijet production is therefore given as

$$R_{\frac{SD}{ND}}(\xi,\, t) \;=\; \frac{\displaystyle\int dx_1 \int d\beta \int d\hat{t}\, \sum_{i,k} f_{p_i/p}(x_1,\, Q^2)\cdot F^D_{p_k/\bar{p}}(\xi,\, t,\, \beta,\, Q^2)\cdot \frac{d\hat{\sigma}(ik\to jj)}{d\hat{t}}}{\displaystyle\int dx_1 \int dx_2 \int d\hat{t}\, \sum_{i,k} f_{p_i/p}(x_1,\, Q^2)\cdot f_{p_k/\bar{p}}(x_2,\, Q^2)\cdot \frac{d\hat{\sigma}(ik\to jj)}{d\hat{t}}}. \tag{6.23}$$

The diffractive structure function $F^D_{p_k/\bar{p}}(\xi,\, t,\, \beta,\, Q^2)$ is defined as

$$F^D_{p_k/\bar{p}}(\xi,\, t,\, \beta,\, Q^2) \;\equiv\; f_{I\!P/\bar{p}}(\xi,\, t)\cdot f_{p_k/I\!P}(\beta,\, Q^2), \tag{6.24}$$

so, if we use a bold assumption that the quark and gluon composition of the pomeron is the same as that of the proton or antiproton, we get the following relation:

$$R_{\frac{SD}{ND}}(\xi,\, t) \;=\; f_{I\!P/\bar{p}}(\xi,\, t). \tag{6.25}$$

Recalling the DPE cross section given by Eq. (2.20), the DPE dijet production cross section σ^{jj}_{DPE} is given by

$$\frac{d^4\sigma^{jj}_{DPE}}{d\xi_{\bar{p}}\, d\xi_p\, dt_{\bar{p}}\, dt_p} \;=\; \frac{1}{\sigma^{jj}_{ND}}\, \frac{d^2\sigma^{jj}_{SD-\bar{p}}}{d\xi_{\bar{p}}\, dt_{\bar{p}}}\, \frac{d^2\sigma^{jj}_{SD-p}}{d\xi_p\, dt_p}, \tag{6.26}$$

where $\sigma^{jj}_{SD-p(\bar{p})}$ is the diffractive dijet production cross section in single diffractive events with a diffracted p ($\bar{p}$). Integrating over the $\xi_{\bar{p}}$ and $t_{\bar{p}}$, the cross section ratio $R_{\frac{DPE}{SD}}$ of DPE to single diffractive dijet production is given as follows,

$$\begin{aligned} R_{\frac{DPE}{SD}}(\xi_p,\, t_p) \;&=\; \frac{d^2\sigma^{jj}_{DPE}}{d\xi_p\, dt_p} \Big/ \sigma^{jj}_{SD-\bar{p}} \\ &=\; \frac{d^2\sigma^{jj}_{SD-p}}{d\xi_p\, dt_p} \Big/ \sigma^{jj}_{ND}. \end{aligned} \tag{6.27}$$

Recalling the above arguments for the $R_{\frac{SD}{ND}}$ ratio, the $R_{\frac{DPE}{SD}}$ ratio is written as

$$R_{\frac{DPE}{SD}}(\xi_p,\, t_p) = \frac{\displaystyle\int dx_2 \int d\beta \int d\hat{t}\, \sum_{i,k} f_{p_k/\bar{p}}(x_2,\, Q^2)\cdot F^D_{p_i/p}(\xi_p,\, t_p,\, \beta,\, Q^2)\cdot \frac{d\hat{\sigma}(ik\to jj)}{d\hat{t}}}{\displaystyle\int dx_2 \int dx_1 \int d\hat{t}\, \sum_{i,k} f_{p_k/\bar{p}}(x_2,\, Q^2)\cdot f_{p_i/p}(x_1,\, Q^2)\cdot \frac{d\hat{\sigma}(ik\to jj)}{d\hat{t}}}, \tag{6.28}$$

where $F^D_{p_i/p}(\xi,\,t,\,\beta,\,Q^2)$ is the diffractive structure function of the proton defined as

$$F^D_{p_i/p}(\xi,\,t,\,\beta,\,Q^2) \;\equiv\; f_{I\!P/p}(\xi,\,t)\cdot f_{p_i/I\!P}(\beta,\,Q^2), \tag{6.29}$$

and the p_i denotes the interacting parton in the pomeron. Under the above bold assumption, we get the following relation:

$$R_{\frac{DPE}{SD}}(\xi,\,t) \;=\; f_{I\!P/p}(\xi,\,t). \tag{6.30}$$

From Eqs. (6.25) and (6.30), if we rely on the bold assumption that the quark and gluon composition of the pomeron is the same as that of the proton or antiproton, we expect that the two ratios $R_{\frac{DPE}{SD}}$ and $R_{\frac{SD}{ND}}$ should be same at the same ξ, t.

The fractional momentum of the antiproton ($x_{\bar{p}}$) and the proton (x_p) carried by the interacting parton can be reconstructed from the E_T and pseudorapidity of the jets in the following way:

$$x_{\bar{p}} \;=\; \frac{1}{\sqrt{s}}\sum_{i=1}^{N_{jet}} E_T^i e^{-\eta_i}, \tag{6.31}$$

$$x_p \;=\; \frac{1}{\sqrt{s}}\sum_{i=1}^{N_{jet}} E_T^i e^{+\eta_i}, \tag{6.32}$$

where N_{jet} is the number of jets. Figure 6.28 shows the $x_{\bar{p}}$ (upper) and x_p (lower) distributions reconstructed from the two leading jets plus the third jet if it has $E_T^{jet3} > 5\,\mathrm{GeV}$, using Eqs. (6.31) and (6.32). Compared in the figure are the distributions for DPE events at the (0,0) bin and SD, ND dijet events. The ND background in SD sample is found to be so small (less than 1 %) that it can be neglected, while the SD background in DPE data, shown as the shaded histograms, is expected to be large (14 %).

To study the cross section ratios, we select events (corrected for the Roman Pot acceptance) with the following kinematical range, and then make the ratio $R_{\frac{DPE}{SD}}$ of DPE to SD dijet production rate as a function of x_p; $7 < E_T^{jet} < 10\,\mathrm{GeV}$ for two leading jets, $0.035 < \xi_{\bar{p}} < 0095$ for SD and DPE, and $0.01 < \xi_p < 0.03$ for DPE events.

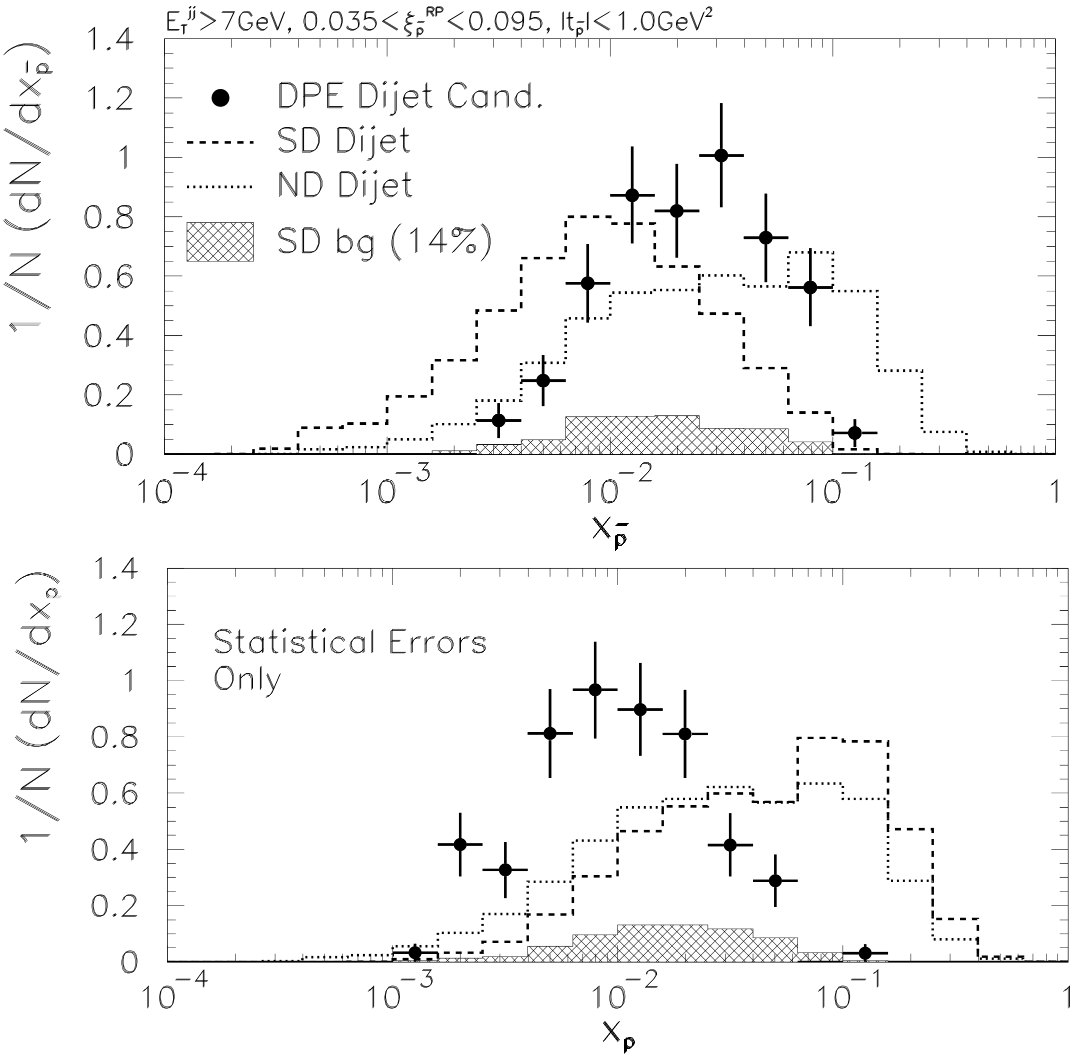

Figure 6.28: $x_{\bar{p}}$ (upper) and x_p (lower) distributions of DPE dijet candidates (black points), SD (dashed histogram) and ND (dotted histogram) dijets with $E_T > 7\,\text{GeV}$. The shaded histograms show the shapes of SD background events in DPE candidates.

The $t_{\bar{p}}$ range $|t_{\bar{p}}| < 1.0\,\mathrm{GeV}^2$ is fixed for both SD and DPE data. The three highest E_T jets are used in the x_p evaluation if the third jet has $E_T^{jet3} > 5\,\mathrm{GeV}$ as above. The E_T^{jet} cut is imposed to select the data with approximately same Q^2 ($\approx \langle (E_T^{jet})^2 \rangle$), justified by that the E_T spectra of two leading jets in DPE events are similar to those in SD events (see Figure 6.11(a)). Also, another reason for this cut is to reduce the influence of E_T dependence of x_p distributions. As discussed previously, the SD background in DPE events at the (0,0) bin is negligibly small by applying the cut of $0.01 < \xi_p < 0.03$. For DPE events, a rapidity gap acceptance (88.0 %) is also corrected. This value is higher than 83.7 % which is obtained in Section 6.5.1, due to the cut of upper E_T^{jet} threshold. The result of $R_{\frac{DPE}{SD}}$ ratio is shown as a function of x_p in Figure 6.29(a). The increasing trend of the ratio with decreasing x_p is observed. To make comparison with $R_{\frac{SD}{ND}}$, ratio of SD to ND dijet rate, the $R_{\frac{DPE}{SD}}$ is divided by the width of ξ_p range $= 0.02$ to get the ratio per unit ξ_p. Therefore, the $R_{\frac{SD}{ND}}$ per unit $\xi_{\bar{p}}$ as a function of $x_{\bar{p}}$ should be compared and it is shown in Figure 6.29(b). The E_T^{jet} and $\xi_{\bar{p}}$ ranges are same as for $R_{\frac{DPE}{SD}}$. Figure 6.29(b) shows that the $R_{\frac{SD}{ND}}$ increases as $x_{\bar{p}}$ decreases.

The best way to study the cross section ratios is to compare them at the same $\xi_{\bar{p}}$ and ξ_p ranges to minimize the ξ dependence of the pomeron flux factors. But, the Roman Pot acceptance is restricted within the range $\xi_{\bar{p}} > 0.03$ and hence only the comparison for different ξ ranges is possible. In studies of diffractive dijets at $\sqrt{s} = 1800\,\mathrm{GeV}$ [64], we observe that the diffractive structure function is dependent of both β and ξ and behaves like $\sim \frac{1}{\beta} \cdot \frac{1}{\xi}$. However, the ratio of diffractive to non-diffractive dijet cross section as a function of $x_{\bar{p}}$ is found to be approximately independent of $\xi_{\bar{p}}$. This indicates that the $R_{\frac{SD}{ND}}$ ratio for $0.01 < \xi_{\bar{p}} < 0.03$ is almost same in both the shape and normalization as that for all the data range $0.035 < \xi_{\bar{p}} < 0.095$, by simply assuming that the observed behavior of approximate ξ independence is adopted even at lower ξ values which we cannot measure.

The effect of including the third or higher jets into the x evaluation is important in the rate and shape comparison. In study of diffractive dijets [64], the ratios of SD

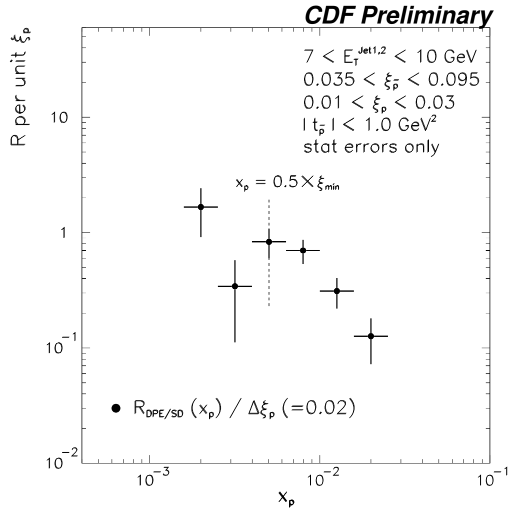

(a) $R_{\frac{DPE}{SD}}$ vs x_p

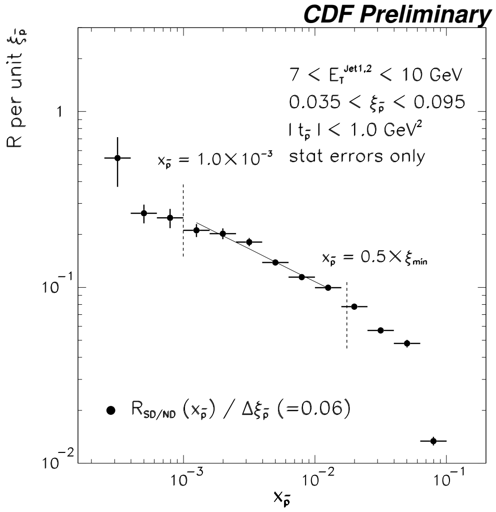

(b) $R_{\frac{SD}{ND}}$ vs $x_{\bar{p}}$

Figure 6.29: (a) Ratio of DPE to SD dijet event rates per unit ξ_p as a function of x for the p. (b) Ratio of SD to ND dijet event rates per unit $\xi_{\bar{p}}$ as a function of x for the $\bar{p}$. The kinematical ranges applied in x evaluation are shown in the figures. The dashed line in (a) shows an upper limit of effective x_p range, selected to be $0.5 \times \xi_{p\,min}$ where $\xi_{p\,min} = 0.01$. A right dashed line in (b) is the same as above but $\xi_{\bar{p}\,min} = 0.035$. A left dashed line shows a lower limit of effective $x_{\bar{p}}$ range, which is applied to avoid the detector end effects.

to ND events for higher jet E_T thresholds of 10 and 15 GeV show a slightly lower rate than that for $E_T > 7$ GeV, and also they show a steeper rise than 7 GeV case at the smallest $x_{\bar{p}}$ range. These observed effects can be understood by taking into account the larger amount of radiation in non-diffractive dijet sample, which causes the large activity of third or higher jets. The cut value (5 GeV) on the third jet E_T^{jet3} used in the main analysis might give some possible uncertainties to the rate and slope of the x_p and $x_{\bar{p}}$ ratios. We investigate the effects of number of jets included in the x evaluation on the x ratios, by changing the number of included jets and the third jet E_T cut. Figure 6.30 shows the $R_{\frac{DPE}{SD}}$ versus x_p for four different cases of jets used in x calculation: (a) the two leading jets plus the third jet with $E_T > 5$ GeV, as in main analysis, (b) only the two leading jets, (c) the two leading jets plus at most three jets (i.e., third, fourth and fifth jets) with $E_T > 5\,\mathrm{GeV}$, and (d) the two leading jets for events with exact two jets, selected by $E_T^{jet3} < 5\,\mathrm{GeV}$. The dashed lines represent $x_p = 0.001$ and $x_p = 0.5 \cdot \xi_{p\,min}$. Inclusion of third or higher jets would increase the x_p range as seen in comparison with (a) or (c) and (b), but it is not so significantly different. All the distributions look similar although the statistical error is relatively large. About 66 % (55 %) of DPE (SD) events with at least two jets of $7 < E_T^{jet} < 10\,\mathrm{GeV}$ for the above kinematical range have only two jets ($E_T^{jet3} < 5\,\mathrm{GeV}$). When we select these events, the ratio overall increases but the shape does not change so much, as shown in (d).

For the above four different cases, the ratio $R_{\frac{SD}{ND}}$ of SD to ND dijet event rates versus the $x_{\bar{p}}$ is also shown in Figure 6.31. The fraction of exact two jet events in ND dijet sample is about 34 % for this E_T^{jet} range, so the ratio $R_{\frac{SD}{ND}}$ goes up in the case of exact two jet events (open circles).

As mentioned previously, we have found [64] that the $R_{\frac{SD}{ND}}$ ratio as a function of $x_{\bar{p}}$ has approximately no $\xi_{\bar{p}}$ dependence in both shape and normalization within the range $0.035 < \xi_{\bar{p}} < 0.095$. It is worth looking again into the $\xi_{\bar{p}}$ dependence of the $R_{\frac{SD}{ND}}(x_{\bar{p}})$ ratio for our measured kinematical range. The $R_{\frac{SD}{ND}}(x_{\bar{p}})$ ratio per unit $\xi_{\bar{p}}$ for 6 different $\xi_{\bar{p}}$ ranges is presented in Figure 6.32. The data below $x_{\bar{p}} = 0.001$ in which the ratio could be affected by the detector end effects is not shown. The full lines represent the fits to the ratio by the form $a \times x_{\bar{p}}^{b}$. The right dashed lines give the values $x_{\bar{p}} = 0.5 \cdot \langle \xi_{\bar{p}} \rangle$ which are the upper edges of the fit ranges. There is again no visible $\xi_{\bar{p}}$ dependence in the $R_{\frac{SD}{ND}}(x_{\bar{p}})$ ratio for $0.035 < \xi_{\bar{p}} < 0.095$. Under the assumption that this $\xi_{\bar{p}}$ independence of the $R_{\frac{SD}{ND}}(x_{\bar{p}})$ ratio still holds at lower $\xi_{\bar{p}}$ range $0.01 < \xi_{\bar{p}} < 0.03$, we compare the $R_{\frac{SD}{ND}}(x_{\bar{p}})$ with the $R_{\frac{DPE}{SD}}(x_p)$.

In Figure 6.33 we present the ratio $R_{\frac{DPE}{SD}}(x_p)$ per unit ξ_p (black points), superimposed on the distribution of the ratio $R_{\frac{SD}{ND}}(x_{\bar{p}})$ per unit $\xi_{\bar{p}}$ (open points). The relevant x ranges which can be used in the rate comparison is expanded from $0.001 < x <$

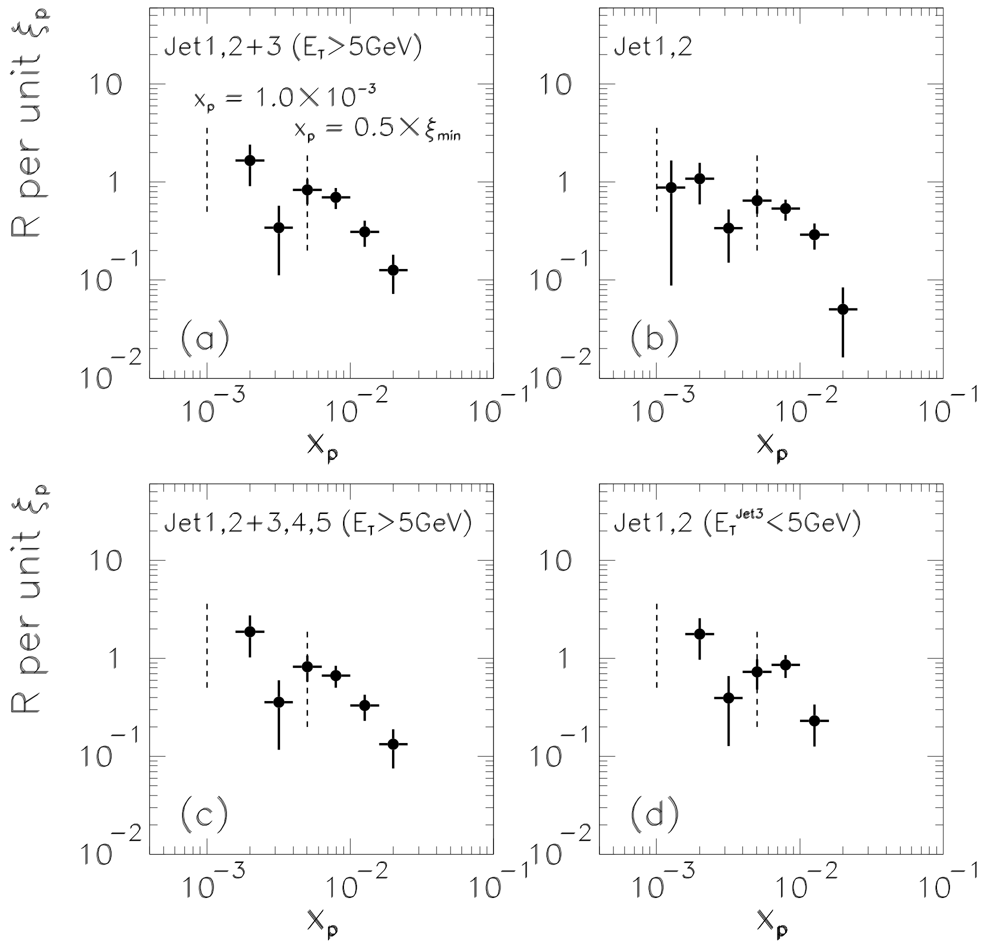

Figure 6.30: Ratio of DPE to SD dijet event rate per unit ξ_p as a function of x for the p. The distributions are shown for four different cases of the jets included in x_p evaluation. (a): the two leading jets plus the third jet with $E_T > 5\,\mathrm{GeV}$, (b): only the two leading jets, (c): the two leading jets plus at most five jets with $E_T > 5\,\mathrm{GeV}$. For these three cases the dijet events are used. For (d), only the two leading jets are used for events with exact two jets, selected by $E_T^{jet3} < 5\,\mathrm{GeV}$.

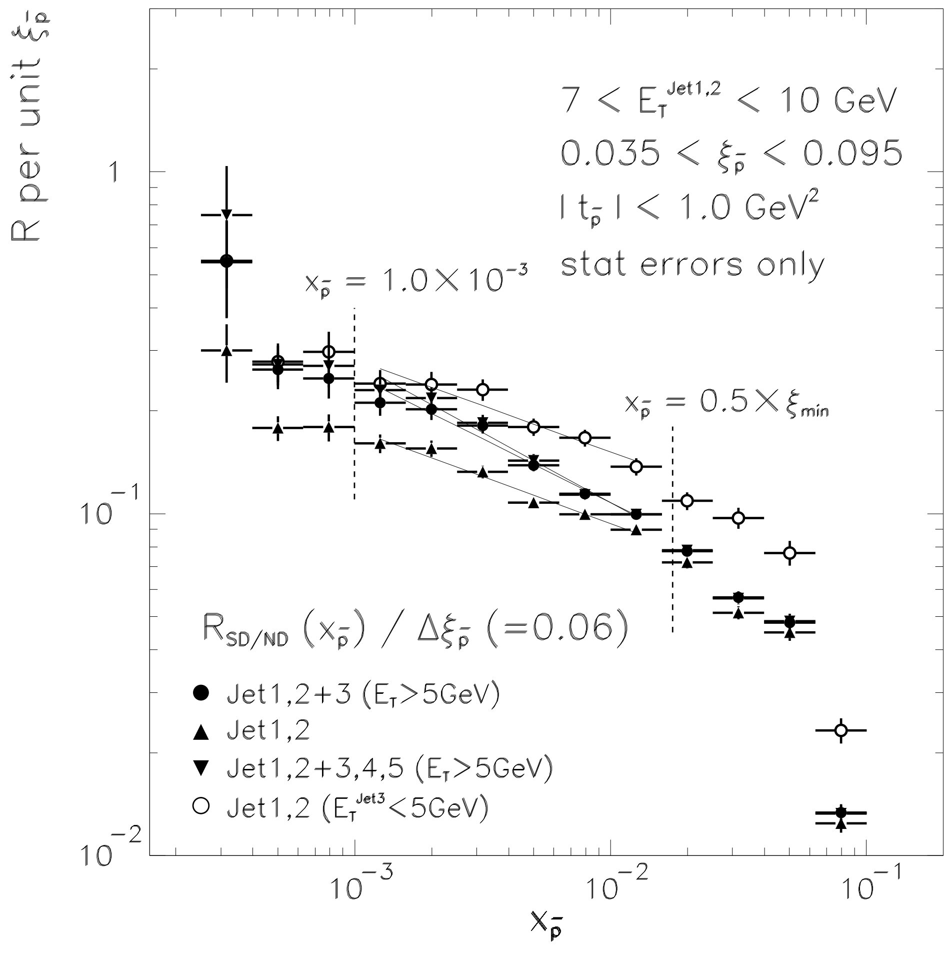

Figure 6.31: Ratio of SD to ND dijet event rate per unit $\xi_{\bar{p}}$ as a function of x for the $\bar{p}$. The distributions are shown for four different cases of the jets included in $x_{\bar{p}}$ evaluation. (black circles): the two leading jets plus the third jet with $E_T > 5\,\text{GeV}$, (triangles): only the two leading jets, (downward triangles): the two leading jets plus at most five jets with $E_T > 5\,\text{GeV}$. For these three cases the dijet events are used. For (open circles), only the two leading jets are used for events with exact two jets, selected by $E_T^{jet3} < 5\,\text{GeV}$.

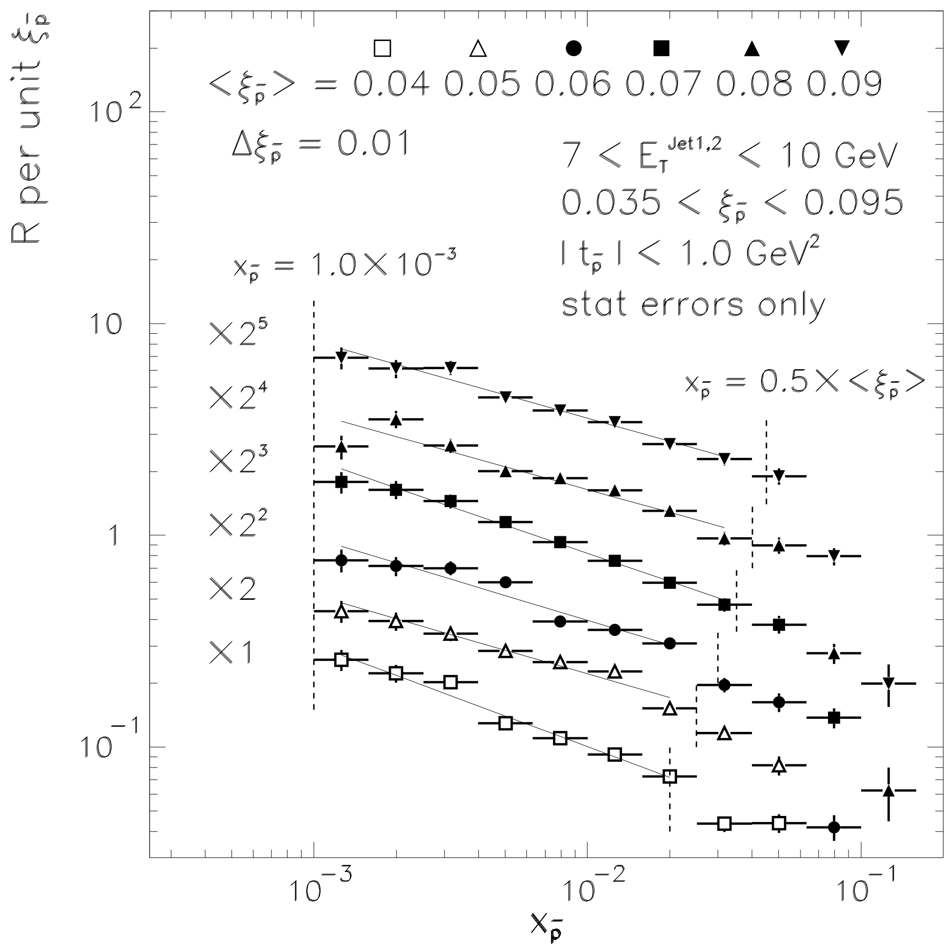

Figure 6.32: Ratio of SD to ND dijet event rate per unit $\xi_{\bar{p}}$ as a function of x for the $\bar{p}$. The distributions are shown for six different $\xi_{\bar{p}}$ ranges with a size of 0.01 between 0.035 and 0.095. Shown are the range $x_{\bar{p}} \geq 0.001$. The right dashed lines represent the upper edges of the fits by the form $P1 \times x_{\bar{p}}^{P2}$ shown by the full lines.

$0.5 \cdot \xi_{p\,min}$ to $0.001 < x < 0.5 \cdot \langle\xi_p\rangle$ ($\langle\xi_p\rangle = 0.02$) because of no $\xi_{\bar{p}}$ dependence of $R_{\frac{SD}{ND}}(x_{\bar{p}})$ within $0.001 < x_{\bar{p}} < 0.5 \cdot \langle\xi_{\bar{p}}\rangle$ shown in Figure 6.32. In Figure 6.33 the errors with the horizontal bars represent the statistical uncertainties. The outer errors of $R_{\frac{DPE}{SD}}$ ratio show the statistical and systematic uncertainties added in quadrature. The systematic uncertainty of $R_{\frac{SD}{ND}}$ is given by the shaded band at $x_{\bar{p}} > 0.001$. Here one should note that an overall normalization uncertainty of 19 % (22 %) for $R_{\frac{DPE}{SD}}$ ($R_{\frac{SD}{ND}}$), evaluated in the previous section, is not included in the systematics. The systematic uncertainties plotted here are estimated by looking at the shape difference in R for three different cases of including jets in the x evaluation: (a) the two leading jets plus the third jet with $E_T > 5\,\mathrm{GeV}$, used in the main analysis, (b) only the two leading jets, and (c) the two leading jets plus at most three jets with $E_T > 5\,\mathrm{GeV}$.

Figure 6.33 shows that the $R_{\frac{DPE}{SD}}$ is higher than $R_{\frac{SD}{ND}}$ within the range $0.001 < x < 0.5 \cdot \langle\xi_p\rangle$. In obtaining the results for the $R_{\frac{DPE}{SD}}$ plotted in Figure 6.33, we use the rapidity gap acceptance of $A_{gap} = 83.7 \pm 11.1\,\%$. However, at $0.001 < x_p < 0.5 \cdot \langle\xi_p\rangle$ the rapidity gap acceptance becomes large (93 %) because the ξ_p would also become small due to a correlation between x_p and ξ_p and hence the rapidity gap size increases. This $x_p - \xi_p$ correlation arises from a similarity of the formulas Eqs. (6.32) and (6.9), and from the fact that a DPE system with small center of mass energy is dominated by jets. Picking up four data points of $R_{\frac{DPE}{SD}}$ and $R_{\frac{SD}{ND}}$ with $-2.8 < \log_{10} x_{p(\bar{p})} < -2.0$ and calculating a weighted average with the errors including the overall normalization uncertainties, we obtain

$$\langle R_{\frac{DPE}{SD}}\rangle = 0.80 \pm 0.26(stat.)\,^{+\,0.16}_{-\,0.25}(syst.)\,\%,$$
$$\langle R_{\frac{SD}{ND}}\rangle = 0.14 \pm 0.01(stat.)\,^{+\,0.03}_{-\,0.04}(syst.)\,\%.$$

Thus, we estimate the ratio between them, D, defined as $\langle R_{\frac{DPE}{SD}}\rangle$ divided by $\langle R_{\frac{SD}{ND}}\rangle$ within the range $-2.8 < \log_{10} x_{p(\bar{p})} < -2.0$, to be

$$D = 5.6\,^{+\,1.3}_{-\,1.6}.$$

Under our above assumption that the quark and gluon composition of the pomeron is

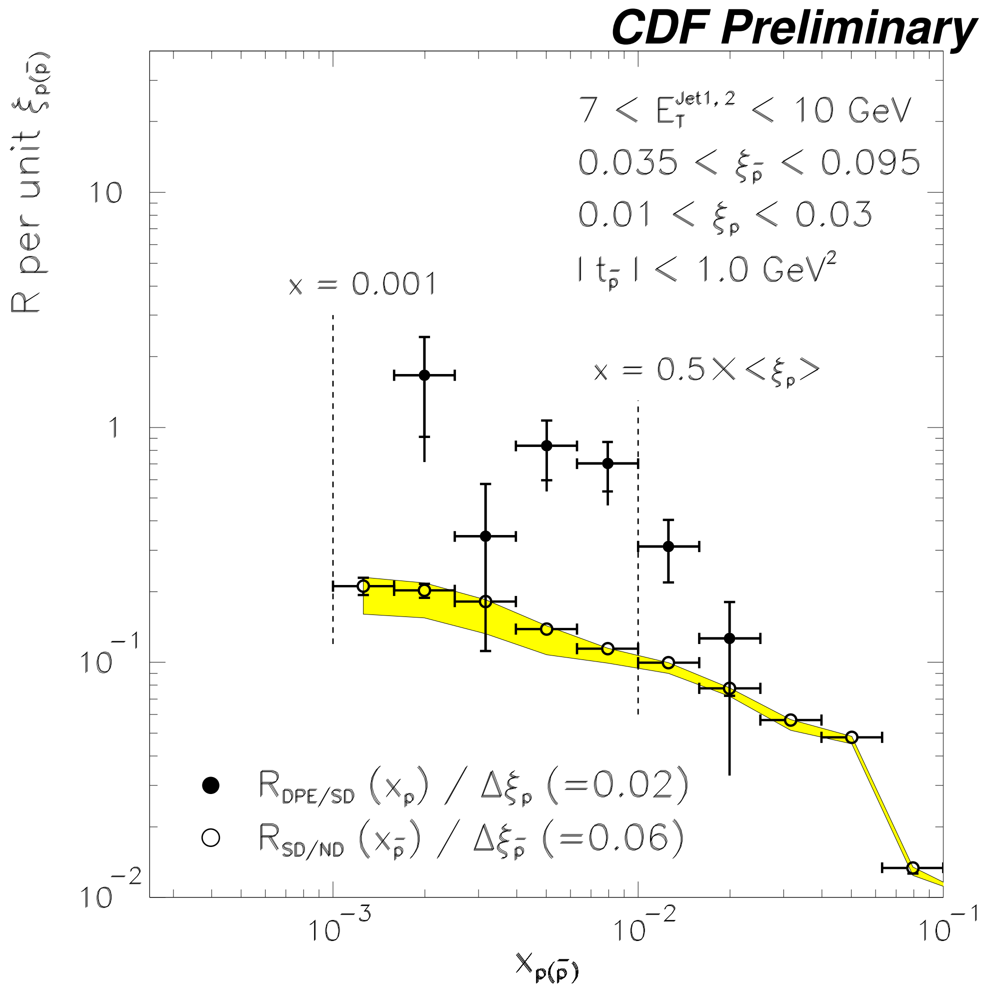

Figure 6.33: Ratio of DPE to SD (SD to ND) dijet event rate per unit ξ_p ($\xi_{\bar{p}}$) as a function of x for the p ($\bar{p}$), shown by the black (open) points. The kinematical ranges are shown in the figures. The dashed lines represent the effective x range used in the rate comparison. The errors with the bars represent the statistical uncertainties. The outer errors of $R_{\frac{DPE}{SD}}$ give the statistical and systematic uncertainties added in quadrature. The shaded band shows the systematic uncertainty in $R_{\frac{SD}{ND}}$ for the range $x_{\bar{p}} > 0.001$.

the same as that of the proton or antiproton, we expect that the two ratios $\langle R_{\frac{DPE}{SD}} \rangle$ and $\langle R_{\frac{SD}{ND}} \rangle$ should be same and hence $D = 1$. Our observed ratio $D = 5.6^{+1.3}_{-1.6}$ seems to indicate the process dependence of the pomeron flux factor, although the experimental errors are large, and we have relied on the another assumption that the $\xi_{\bar{p}}$ independence of the $R_{\frac{SD}{ND}}(x_{\bar{p}})$ ratio sill holds at lower $\xi_{\bar{p}}$ range $0.01 < \xi_{\bar{p}} < 0.03$.

6.8 Dijet Mass Fraction

In dijet events of DPE, a measurement of the mass fraction of dijets will be interesting. If the fractional momentum of the pomeron carried by the interacting parton is β, the dijet mass squared in DPE, M_{jj}^2, is given by

$$M_{jj}^2 \;=\; \xi_1\beta_1 \,\cdot\, \xi_2\beta_2 \,\cdot\, s \;=\; \beta_1\,\beta_2\,M_X^2, \tag{6.33}$$

where $M_X = \sqrt{\xi_1\xi_2 s}$ is the central DPE system mass. The fraction of dijet mass to the central system mass, R_{jj}, defined as

$$R_{jj} \;\equiv\; \frac{M_{jj}}{M_X} \;=\; \sqrt{\beta_1\,\beta_2}, \tag{6.34}$$

would give the information on the parton structure of the pomeron in DPE.

One of the theories for the DPE processes, called "Non-Factorizable DPE (NF-DPE) model" [55] predicts that only two jets are produced in DPE, and nothing else:

$$p \,+\, \bar{p} \,\to\, [p' + I\!P] \,+\, [\bar{p}' + I\!P] \,\to\, p' \,+\, \bar{p}' \,+\, jet \,+\, jet, \tag{6.35}$$

that is, a central system X contains only two jets. If this model is valid, the fraction R_{jj} should be very high (theoretically 1).

The dijet mass of DPE events at the (0,0) bin is shown in Figure 6.34(upper). Here the dijets of DPE events are not processed by the out-of-cone (OC) correction in JTC96, as in Section 6.5. This dijet mass is therefore called M_{jj}(cone) because the OC energy is not taken into account. For the denominator of R_{jj}, we use the corrected DPE system mass M_{DPE} that is the measured mass M_{DPE}^X times the constant factor

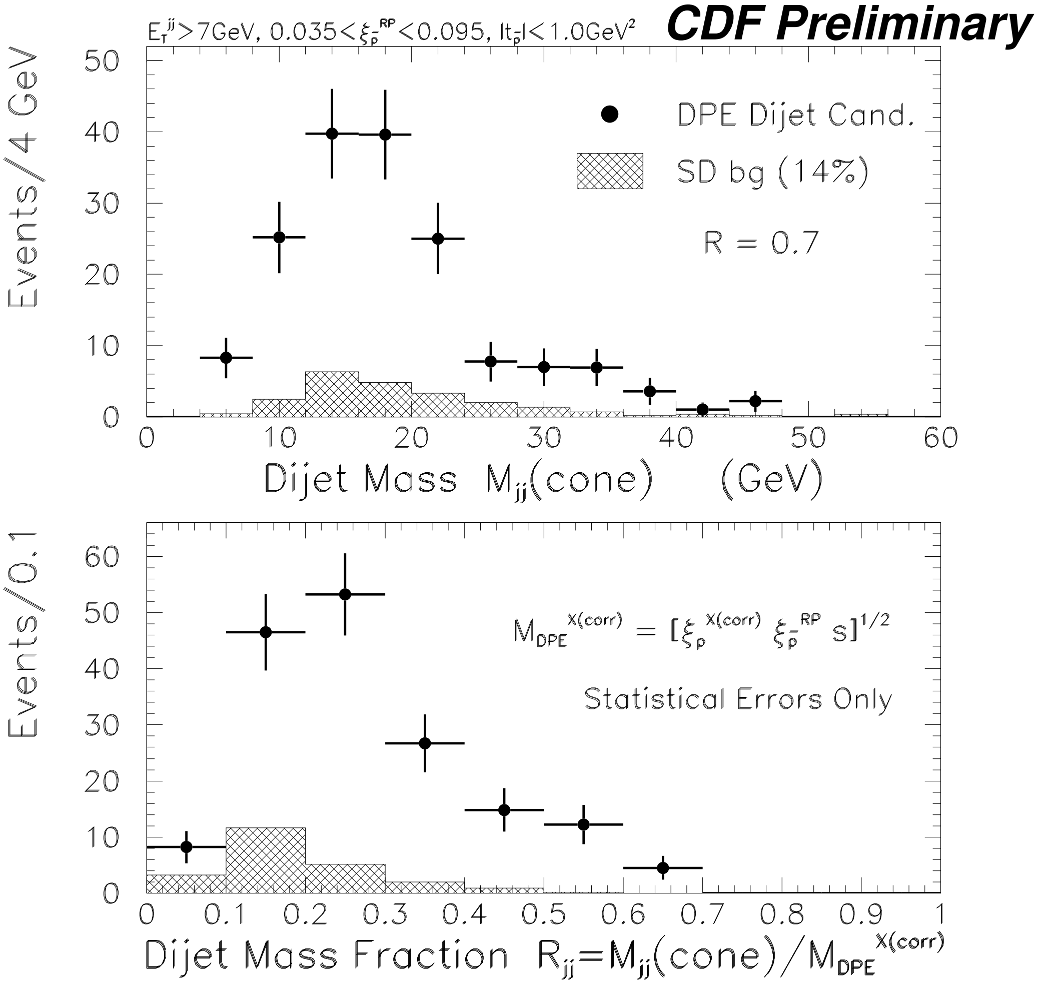

Figure 6.34: Dijet mass M_{jj}(cone) (upper) and dijet mass fraction to central DPE system mass R_{jj} (lower) for DPE events with dijets of $E_T > 7\,\mathrm{GeV}$ (points), and single diffractive background (shaded histograms) in the (0,0) bin.

1.7 (see Section 6.5). We should note that this correction is valid only on average, so that the mass fraction defined as

$$R_{jj} \equiv \frac{M_{jj}(\text{cone})}{M_{DPE}},$$

is not correct on an event-by-event basis. The obtained mass fraction for DPE dijets is shown in Figure 6.34(lower). All the plots are corrected for the Roman Pot acceptance. The dijet mass from SD background has a similar shape, but the R_{jj} of SD background is smaller than that of DPE due to larger system mass of SD than DPE. The mean of R_{jj} for DPE events is around 0.29 ± 0.01 and the tail extends up to about 0.7. We do not observe any events with $R_{jj} > 0.7$. This implies that the contribution from Non-Factorizable DPE to our observed data is small.

6.8.1 Limit on Non-Factorizable DPE

From the dijet mass fraction shown in Figure 6.34, we set a limit on the contribution from Non-Factorizable DPE (NF-DPE) in our kinematical range. For this purpose, we reconstruct the true dijet mass $M_{jj}(\text{total})$ including the OC correction, then estimate the ratio R_{cone}, defined as

$$R_{cone} \equiv \frac{M_{jj}(\text{cone})}{M_{jj}(\text{total})}.$$

The NF-DPE events have only two jets in the final state (excluding the leading proton and antiproton), so that they should have the system mass M_{DPE} being equal to $M_{jj}(\text{total})$. Accordingly, in NF-DPE events we should obtain the following relation:

$$R_{jj} = R_{cone}.$$

Figure 6.35 shows the R_{cone} distributions for (a) $E_T > 7\,\text{GeV}$ and (b) $E_T > 10\,\text{GeV}$ DPE dijet events of (0,0) bin (histograms). The mean R_{cone} is ~ 0.81 (0.84) for $E_T > 7$ (10) GeV dijets, which indicates that the OC particles have about 23 % (19 %) of the energy of the dijets for $E_T > 7$ (10) GeV. Also shown in the figures are the R_{jj} ratios (points). If the NF-DPE model is correct, the R_{jj} distribution should coincide with

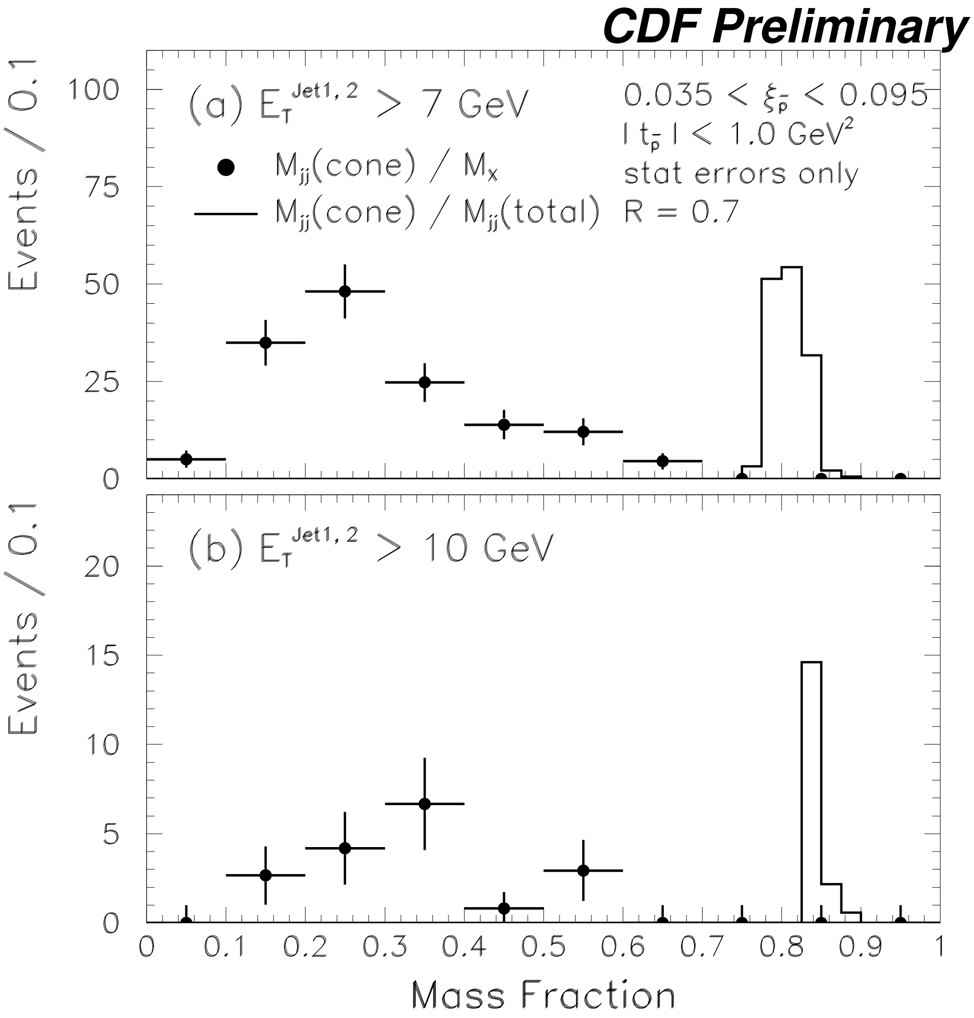

Figure 6.35: Fraction R_{jj} of dijet mass within the cones of $R = 0.7$ to the central system mass for DPE events with (a) $E_T > 7\,\mathrm{GeV}$ and (b) $E_T > 10\,\mathrm{GeV}$ dijets (points). The histograms represent the ratios R_{cone} of dijet mass within the cones to the total dijet mass. All the plots are for DPE events at the (0,0) bin (SD background subtracted), corrected for the Roman Pot acceptance.

the R_{cone} distribution. However, the two distributions are clearly different, as shown in Figure 6.35.

Before setting a limit, it is worth noting that our kinematical range ($0.035 < \xi_{\bar{p}} < 0.095$, $0.01 < \xi_p < 0.03$) should constrain the acceptance of produced jets. In NF-DPE model a parton with 3.5 to 9.5 % of the $\bar{p}$ momentum interacts with the other parton with 1 to 3 % of the p momentum (a pomeron $\approx$ a parton). A simple calculation of kinematics shows that a small fraction of two jets with $E_T \lesssim 6\,\mathrm{GeV}$ could be produced outside a reasonable detector acceptance region $|\eta| < 3$. To be safer, we might have to use higher E_T dijet data of $E_T > 10\,\mathrm{GeV}$. But, as presented below, we expect from recent theoretical calculations that almost all NF-DPE dijets with $E_T > 7\,\mathrm{GeV}$ are produced within the range $|\eta| < 3$. From our observation of zero events with $R_{jj} > 0.7$, we determine the number of NF-DPE events in our DPE data to be less than 3.1 at 95 % confidence level (C.L.) under the assumption of no background with $R_{jj} > 0.7$. For $E_T > 7\,\mathrm{GeV}$ dijets, we therefore evaluate R_{NF}, a fractional NF-DPE contribution to our observed DPE events, to be $R_{NF}^{0.7} < 2.6\,\%$ at 95 % C.L., by dividing 3.1 by the number of our DPE events before the Roman Pot acceptance correction. Here 0.7 of $R_{NF}^{0.7}$ stands for the cone size of jet.

In principle, the shapes of R_{jj} and R_{cone} distributions are not affected by the jet energy scale and underlying event energy uncertainties, and in fact it is seen in the data. But, the total number of observed events could change with these uncertainties. By varying the jet energy scale by $\pm1\sigma$ ($=\pm5.6\,\%$ for $|\eta^{jet}| < 2.4$, $\pm6.1\,\%$ for $|\eta^{jet}| \geq 2.4$), we find that three events have $R_{jj} > 0.7$ in case of energy scale with $+1\sigma$ but in case of -1σ there are still no NF-DPE candidate events. Dividing 3.0 (3.1 at 95 % C.L.) by the total number of events, we obtain $R_{NF}^{0.7} < 1.9\,\%$ (3.8 % at 95 % C.L.) for jet energy scale with $+(-)1\sigma$. Similarly, the changes of $\pm30\,\%$ ($=1\sigma$) of UE energy result in $R_{NF}^{0.7} < 3.0\,\%$ (2.4 %) at 95 % C.L. for $+(-)1\sigma$ variation. We conservatively take a larger variation: 1.2 % for jet energy scale and 0.4 % for UE energy. Adding these variations and statistical uncertainty (1.5 %) in quadrature and conservatively taking the upper end, we obtain

$$R_{NF}^{0.7} \ < \ 4.6\,\% \qquad (95\,\% \text{ C.L.}).$$

When we use a larger cone size $R = 1.0$ to reconstruct the jets, we expect that both the R_{jj} and R_{cone} should become higher due to smaller OC energy. The R_{jj} and R_{cone} distributions for $R = 1.0$ jets are shown in Figure 6.36. Note that the R_{cone} distributions for the two E_T thresholds are narrower than the cases of $R = 0.7$ and localized at $R_{cone} > 0.9$. The NF-DPE signal should appear, if it exists, at $R_{jj} > 0.9$. From 4.5 observed events with $R_{jj} > 0.9$ for $E_T > 7\,\text{GeV}$ dijets (Roman Pot acceptance corrected), $R_{NF}^{1.0} < 1.7\,\%$ is obtained for the cone size $R = 1.0$. The R_{NF} variations resulting from $\pm 1\sigma$ changes of jet energy scale and UE energy are estimated in the same manner to be $^{+0.6}_{-0.4}\,\%$ and $\pm 0.3\,\%$ respectively. Adding the larger errors in quadrature with the statistical uncertainty of $0.8\,\%$ and taking the upper end, the NF-DPE contribution is evaluated to be

$$R_{NF}^{1.0} \ < \ 2.7\,\%,$$

for the cone size $R = 1.0$. The measured R_{NF} limits are consistent for both cone sizes. The limit $R_{NF}^{1.0}$ is covered by the limit $R_{NF}^{0.7}$, so we take the result, $R_{NF}^{0.7} < 4.6\,\%$ (95 % C.L.), as the limit to NF-DPE.

6.8.2 Comparison with Theoretical Predictions

So far a couple of models for Non-Factorizable DPE have been developed. One of them, proposed by A. Berera and J. Collins [66], gives preliminary NF-DPE dijet cross sections at $\sqrt{s} = 1800\,\text{GeV}$ and $630\,\text{GeV}$. They estimated the cross section of events with dijets of $E_T > 5\,\text{GeV}$ and $0 < \xi_1, \xi_2 < 0.05$ where the ξ_1 and ξ_2 are the momentum fractions of incoming protons participating into the hard process. The cross section which they obtained for NF-DPE was about two or more orders of magnitude larger than the conventional Regge Factorized DPE (F-DPE), which applies the Ingelman-Schlein model to DPE.

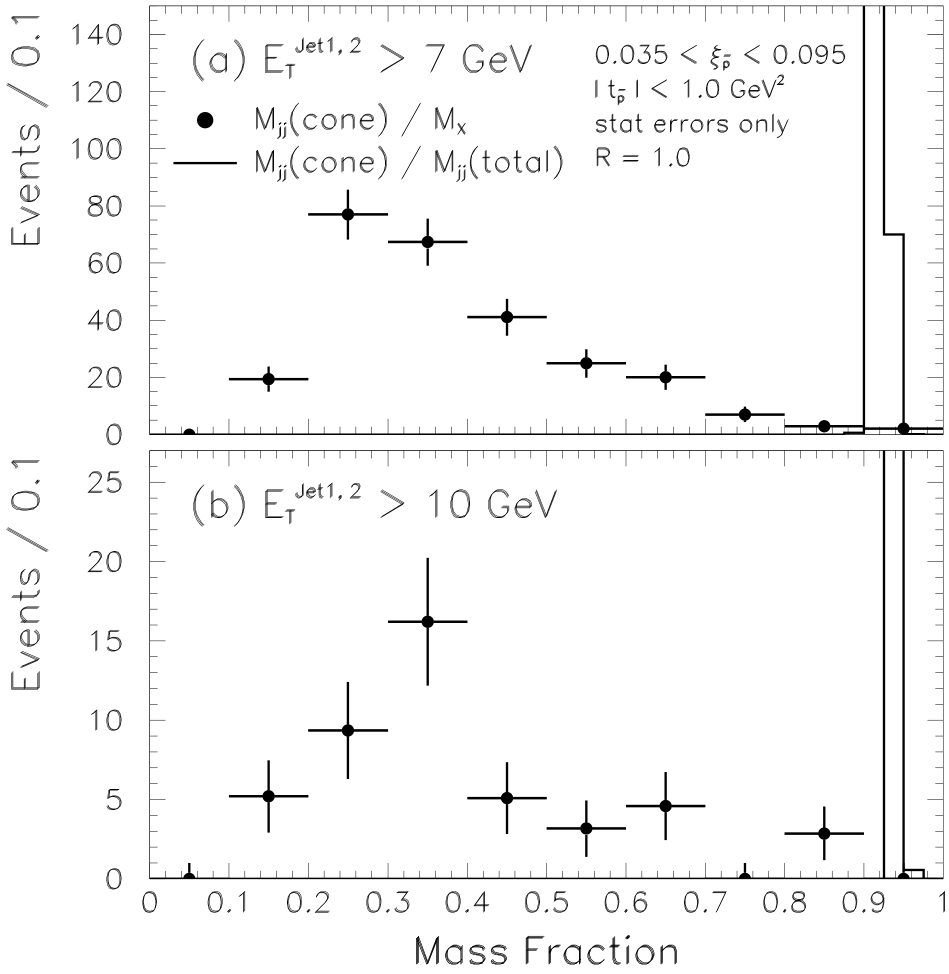

Figure 6.36: Fraction R_{jj} of dijet mass within the cones of $R = 1.0$ to the central system mass for DPE events with (a) $E_T > 7\,\mathrm{GeV}$ and (b) $E_T > 10\,\mathrm{GeV}$ dijets (points). The histograms represent the ratios R_{cone} of dijet mass within the cones to the total dijet mass. All the plots are for DPE events at the (0,0) bin (SD background subtracted), corrected for the Roman Pot acceptance.

Recently new results of DPE dijet cross section which can be directly compared with experimental results were published by A. Berera [67]. In this paper he calculated the E_T and mean η of dijets and compared them for the predictions of F-DPE based on the Ingelman-Schlein model, and NF-DPE of their model. Also, the DPE dijet cross sections were estimated for both models. In these calculations he applied the cuts to compare with the CDF and DØ preliminary results which we and DØ reported in a couple of conferences.

In comparison with CDF data he quoted the analysis cuts which were presented in the Small-x conference [68]: jet $E_T > 7\,\mathrm{GeV}$, $0.04 < \xi_{\bar{p}} < 0.095$ and $0.015 < \xi_p < 0.035$. The rapidity of jets was required to be within the detector region $-4.2 < y_1, y_2 < 2.0$. The upper limit of 2.0 is due to the rapidity gap requirement for the proton direction. The $\xi_{\bar{p}}$ and ξ_p cuts are slightly different from our present ones, but here we don't have to worry about such small differences between the new and old cuts. In this kinematic range he predicted the rapidity and E_T distributions of NF-DPE dijets using his model. One important result is the acceptance of NF-DPE jets versus the jet rapidity. At $E_T = 7\,\mathrm{GeV}$, the NF-DPE jets were produced within the range $-3.3 < y_1 < -2.3$ and $1.4 < y_2 < 2$ (and interchange of y_1 and y_2). As E_T increases, the jet rapidity bands move inwards, i.e., overall rapidity distribution shrinks. This means that the CDF detector acceptance fully covers the NF-DPE signal, and hence supports our above derivation of NF-DPE limit at $E_T > 7\,\mathrm{GeV}$. His calculation of F-DPE and NF-DPE dijet cross sections with CDF cuts is summarized in Table 6.8.

The parton density functions for the Factorized DPE model which he used are quoted from the paper of L. Alvero, J. Collins, J. Terron and J. Whitmore [69], called "ACTW". Five parameterizations of the parton densities used by ACTW are the followings:

Table 6.8: DPE dijet cross sections (in units of μb) with CDF analysis cuts for the (a) Factorizable and (b) Non-Factorizable DPE models, quoted from [67].

(a) σ_{dijet}^{F-DPE} (μb)				
ACTW A	ACTW B	ACTW C	ACTW D	ACTW SG
0.011	1.0	0.011	4.2	0.24

(b) σ_{dijet}^{NF-DPE} (μb)		
No Sudakov	Sudakov $\mu^2 = 1.0$	Sudakov $\mu^2 = 1.3$
5.6	2.5	1.7

A	$\beta f_{q/\boldsymbol{P}}(\beta, Q^2)$	$=$	$a_q \beta(1-\beta)$,
B	$\beta f_{g,q/\boldsymbol{P}}(\beta, Q^2)$	$=$	$a_g \beta(1-\beta) + a_q \beta(1-\beta)$,
C	$\beta f_{q/\boldsymbol{P}}(\beta, Q^2)$	$=$	$a_q[\beta(1-\beta) + \tilde{a}_q(1-\beta)^2]$,
D	$\beta f_{g,q/\boldsymbol{P}}(\beta, Q^2)$	$=$	$a_g \beta(1-\beta) + a_q[\beta(1-\beta) + \tilde{a}_q(1-\beta)^2]$,
SG	$\beta f_{g,q/\boldsymbol{P}}(\beta, Q^2)$	$=$	$a_g \beta^8(1-\beta)^{0.3} + a_q \beta(1-\beta)$,

where β is the momentum fraction of the pomeron carried by the struck quark or gluon (e.g., for B, β in the term $a_g\beta(1-\beta)$ represents the gluon momentum fraction, and β in $a_q\beta(1-\beta)$ the quark momentum fraction.) Therefore, the coefficients a_g, a_q and $\tilde{a}_q$ give the magnitude of the contributions from conventional hard gluon, hard quark and soft quark. For SG, the gluon term is strongly emphasized at large β near 1, so this is called "super-hard gluon". The relative magnitude of gluon and quark contributions were obtained in the fits to experimental data of diffractive deep inelastic scattering and photoproduction at H1 and ZEUS (See details in [69]). The obtained values of coefficients that give the best fits are as follows for the pomeron trajectory $\alpha_{\boldsymbol{P}} = 1.14$.

PDF	a_q	a_g	$\tilde{a}_q$
A	0.240 ± 0.006	0	0
B	0.239 ± 0.006	4.5 ± 0.5	0
C	0.249 ± 0.011	0	-0.031 ± 0.029
D	0.292 ± 0.013	9.7 ± 1.7	-0.159 ± 0.029
SG	0.225 ± 0.008	7.4 ± 2.2	0

Therefore, B, D and SG have much larger contributions from the gluons than the quarks. To provide a good fit to photoproduction data, the parton densities with a large amount of gluon (B, D) were favored. In diffractive $p\bar{p}$ interactions at the Tevatron, it is also found [18] that a large fraction of gluon components is necessary to describe the data. This means that we should compare our data with the predictions obtained using B and D. Seen in Table 6.8 is that the F-DPE dijet cross section of B or D is about 10^2 larger than that of A or C, and it is in the order of μb. Compared with our measured DPE dijet cross section of about 44 nb at $E_T > 7\,\mathrm{GeV}$ (Section 6.6.3), these predictions are higher by an order of two. In addition, as discussed in Section 7.2 of next chapter, we find that the DPE dijet cross section which we measure is about a factor D_{CDF}^2 lower than the predictions of the conventional Regge factorized Monte Carlo (POMPOMPYT) with Donnachie-Landshoff (DL) pomeron flux parameterization. The factor $D_{CDF} = 0.19 \pm 0.04$ is a discrepancy factor from DL flux prediction which we measured in diffractive W, dijet and bottom quark rate analyses [16, 17, 18]. A disagreement with an order of two, which we see between our measured cross section and F-DPE predictions, is consistent with the discrepancy of $D_{CDF}^2 = 0.036$.

What is of great importance in Berera's calculation is that the cross section of NF-DPE dijets is comparable to that of F-DPE (ACTW B or D), and is around a few μb. The suppression from Sudakov corrections to low virtuality gluons taking part in a hard process changes the cross section only by a factor of 2 or 3. On the other hand, as described previously, the fraction of NF-DPE contribution to our total DPE sample is measured to be $R_{NF} < 4.6\,\%$ at $95\,\%$ confidence level. Recalling that our measured DPE cross section is about 44 nb for events with dijets of $E_T^{jet} > 7\,\mathrm{GeV}$, $0.035 < \xi_{\bar{p}} < 0.095$ and $0.01 < \xi_p < 0.03$, we can estimate the NF-DPE dijet cross section in data to be

$$\sigma_{dijet}^{NF-DPE} \lesssim 44\,\mathrm{nb} \times 4.6\,\% = 2.0\,\mathrm{nb}.$$

This concludes that the NF-DPE production rate obtained from the data is an order of 10^{-3} smaller than the theoretical calculation by A. Berera [67].

Chapter 7

Monte Carlo Simulations

The Monte Carlo program to simulate hard scattering processes in diffraction, called "POMPYT" (version 2.6) [56], is used in the analysis. This event generator is based on a generator "PYTHIA" [51] and it consists of the source programs of PYTHIA package with the addition of several components to implement the pomeron exchange process, the pomeron flux factor and parton distribution functions of the pomeron. The hard processes of the partons are executed by the PYTHIA and the fragmentation and hadronization processes are simulated by the JETSET [51]. Basically the POMPYT Monte Carlo can generate single diffractive events in pp, $\bar{p}p$, γp and ep collisions, based on the standard Regge factorization and the Ingelman-Schlein model. Kerstin Borras (The Rockefeller University, CDF) modified the original POMPYT to match with the CDF environment and to simulate the various parton distribution functions of the pomeron which were experimentally measured or theoretically developed [62]. As one of her modifications on POMPYT, the DPE event generation also became possible [63]. This modified POMPYT Monte Carlo which can generate DPE events is called "POMPOMPYT" in this thesis, and described in Section 7.2.

7.1 POMPYT Monte Carlo Simulation

The POMPYT is based on the standard factorization hypothesis as described above. In proton-antiproton collisions with an antiproton diffraction, an incident antiproton emits the pomeron ($I\!P$) characterized by the fractional momentum loss of the antiproton ξ and the four momentum transfer squared t, and then the excited proton with the squared mass $M^2 = s\,\xi$ dissociates. Here s is the center of mass energy squared in proton-antiproton collisions. This algorithm is based on the Ingelman-Schlein model for the hard diffraction (Section 2.2.1).

As discussed in Section 2.2.1, the differential cross section for hard diffractive process is given by

$$\frac{d^4\sigma_{SD}^{jj}}{d\xi\, dt\, dx_i\, dx_2} \;=\; \left[\frac{1}{\sigma(pI\!P \to X)} \cdot \frac{d^2\sigma_{SD}}{d\xi\, dt}\right] \cdot \frac{d^2\sigma(pI\!P \to jj + X)}{dx_1\, dx_2}, \tag{7.1}$$

where $\sigma(pI\!P \to jj+X)$ is the proton-pomeron hard scattering cross section. The term in brackets represents the pomeron flux factor $f_{I\!P/\bar{p}}(\xi,\, t)$. In POMPYT three different parameterizations for the pomeron flux factor can be implemented. The first is a simple form with the exponential t-dependence [6, 9, 70] given by

$$f_{I\!P/\bar{p}}(\xi,\, t) \;=\; \frac{d\sigma^2(\bar{p}p \to \bar{p}X)/d\xi\, dt}{\sigma(pI\!P \to X)} = \frac{1}{\sigma(pI\!P \to X)} \cdot \frac{1}{\xi^{\gamma/2}} \cdot \sum_{i=1}^{3} a_i\, e^{b_i t}, \tag{7.2}$$

where $\sigma(pI\!P \to X)$ is taken to be constant. This form is motivated from the single diffraction cross section measurements. In the case of $\gamma = 2$, the factor $1/\xi^{\gamma/2}$ corresponds to the well-known $1/M^2$ dependence of diffractive scattering.

The second form is given by

$$f_{I\!P/\bar{p}}(\xi,\, t) \;=\; \frac{1}{\sigma(pI\!P \to X)} \cdot \frac{C}{\xi^{\gamma/2}} \cdot \Big[F_1(t)\Big]^2, \tag{7.3}$$

where, for instance, the normalization coefficient C can be chosen so as to obtain the same value as in Eq. (7.2) at $t = 0$, i.e., $C = \sum_i a_i$. The t-dependence in Eq. (7.3) is given by the proton form factor:

$$F_1(t) \;=\; \frac{4m_p^2 - At}{4m_p^2 - t} \cdot \left(\frac{1}{1 - t/B}\right)^2, \tag{7.4}$$

where m_p is the proton mass, and A (=2.8) and B (=0.7) are the parameters obtained by fitting to data.

The last form is the Donnachie-Landshoff flux factor [10] already described in Section 2.2.2 and defined as

$$f_{I\!P/\bar{p}}(\xi,\, t) \;=\; \frac{9\beta_0^2}{4\pi^2} \cdot \Big[F_1(t)\Big]^2 \cdot \left(\frac{1}{\xi}\right)^{2\alpha_{I\!P}(t)-1}, \tag{7.5}$$

where β_0 is the effective pomeron-quark coupling constant and the default value is $\beta_0^2 = 3.24\,\mathrm{GeV}^{-2}$. For the pomeron Regge trajectory $\alpha_{I\!P}(t) = 1 + \varepsilon + \alpha' t$, the default parameter values are $\varepsilon = 0.085$ and $\alpha' = 0.25\,\mathrm{GeV}^{-2}$. This Donnachie-Landshoff flux factor is used in the analysis, along with the CDF measured parameters.

The pomeron-proton hard scattering cross section $\sigma(pI\!P \to jj + X)$ in Eq. (7.1) is rewritten as follows,

$$\frac{d\sigma(pI\!P \to jj + X)}{d\hat{t}} \;=\; \int dx_i \int dx_j \sum_{i,j} f_{p_i/p}(x_i,\, Q^2)\, f_{p_j/I\!P}(x_j,\, Q^2) \frac{d\hat{\sigma}}{d\hat{t}}, \tag{7.6}$$

where $f_{p_i/p}(x_i,\, Q^2)$ and $f_{p_j/I\!P}(x_j,\, Q^2)$ are the parton distribution functions (PDFs) of the proton and the pomeron, respectively. The x_i (x_j) is the momentum fraction of the struck parton p_i (p_j) to the proton (pomeron), and $\hat{\sigma}$ is the cross section for the hard process between two partons. This formula is identical to what Ingelman and Schlein proposed in their model, given by Eq. (2.10).

If the momentum fraction of the pomeron carried by an interacting parton is written as z, the following three functions are often used as the structure functions of the pomeron:

$$z\, f_{g/I\!P}(z) \;=\; 6\,(1-z)^5, \tag{7.7}$$

$$z\, f_{g/I\!P}(z) \;=\; 6\,z(1-z), \tag{7.8}$$

$$z\, f_{q/I\!P}(z) \;=\; \frac{6}{4}\,z(1-z). \tag{7.9}$$

Eq. (7.7) gives the *soft gluon* structure function, where the pomeron is composed of (many) low energy gluons. Eq. (7.8) gives the *hard gluon* structure function, where the

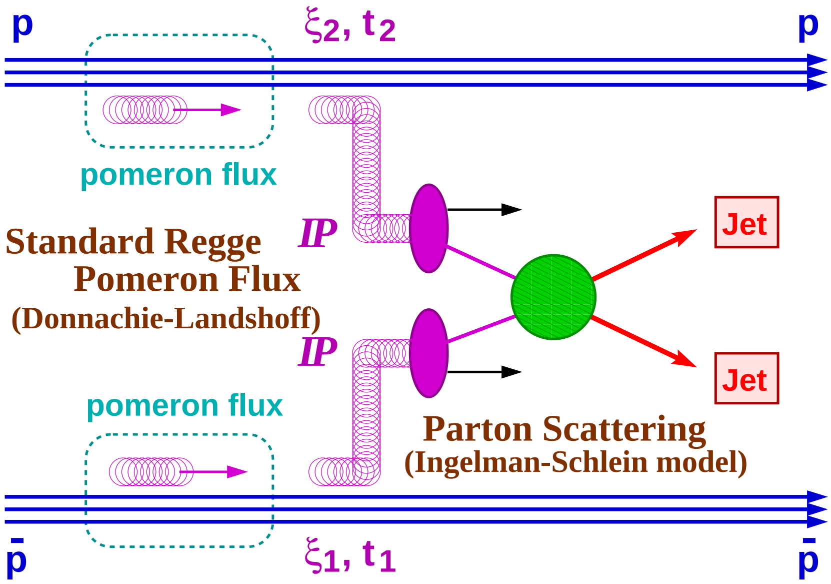

Figure 7.1: The concept of POMPOMPYT Monte Carlo simulation. Dijet production is illustrated as an example of hard scattering of two pomerons.

pomeron is composed of on average two hard gluons. Eq. (7.9) gives the *hard quark* structure function, where the pomeron is composed of on average two hard quarks (u, d, $\bar{u}$, $\bar{d}$). For these structure functions the Q^2 dependence is ignored. Also, it is worth noting that all the distribution functions in POMPYT are normalized to fulfill the momentum sum rule:

$$\int_0^1 dz \sum_i z f_{p_i/I\!P}(z) \;=\; 1. \tag{7.10}$$

7.2 POMPOMPYT Monte Carlo Simulation

The POMPOMPYT for DPE event generation is based on the concept of conventional Regge factorization and the exchanged pomeron with the Ingelman-Schlein type parton model (Figure 7.1).

In the event generation we use the Donnachie-Landshoff flux factor given by Eq. (7.5). For the parameters β_0 and $\alpha_{I\!P}(t)$, we use the following values measured by CDF for

1988–1989 data [36, 37, 38]:

$$\beta_0^2 \;=\; 3.202\,\mathrm{GeV}^{-2}, \quad \alpha_{I\!P}(t) \;=\; 1 + 0.115 + 0.26\,t. \tag{7.11}$$

This is called the *standard pomeron flux factor* in the thesis. In addition, the *renormalized Donnachie-Landshoff pomeron flux factor* is also used. This flux is defined as the standard flux multiplied by a factor D_{CDF} for SD, and D_{CDF}^2 for DPE, where $D_{CDF} = 0.19 \pm 0.04$ is a discrepancy factor obtained from CDF measurements of diffractive W, dijet and bottom quark productions [16, 17, 18]. This is also equivalent to the flux with the Renormalized Pomeron Flux approach [4], being the standard flux divided by the flux factor integral over all available phase space [11, 12, 13]. In actual event generation we multiply the obtained cross section by this factor.

A parton distribution function of the pomeron is a free parameter for both the POMPYT and POMPOMPYT. We have successfully generated DPE events using several distribution functions including the soft gluon, hard gluon and hard quark. Out of them, the following four distribution functions are used to compare with the data:

1. flat gluon $\quad z\,f_{g/I\!P}(z) \;=\; 1,$
2. CDF gluon $\quad z\,f_{g/I\!P}(z) \;=\; \log^{-1}\left(\dfrac{1+a}{a}\right)\cdot\dfrac{1}{z+a} \qquad (a \ll 1),$
3. CDF quark+gluon $\quad z\,f_{g,q/I\!P}(z) \;=\; f_g^{CDF}\cdot 6\,z(1-z) + (1-f_g^{CDF})\cdot\dfrac{1}{4}\displaystyle\sum_{u,\bar{u},d,\bar{d}} 6\,z(1-z),$
4. soft gluon $\quad z\,f_{g/I\!P}(z) \;=\; 6\,(1-z)^5.$

The first distribution function is called *flat gluon* because it is 100 % gluonic and flat in all z range. This is useful in studying the detector acceptance effects on the structure of the pomeron. Another motivation is that the H1 collaboration reports a pomeron structure being consistent with 80–90 % gluon contributions with approximately flat momentum distribution from a measurement of diffractive structure function of the proton F_2^{D3} in diffractive DIS [21]. The second is *CDF gluon*, an approximation of our measured β dependence of diffractive structure function of the antiproton F_{jj}^D [64]. As discussed in CDF results of Section 2.2.4, our measured β dependence is approximately expressed as $\sim \frac{1}{\beta}$ and it should be same as the β dependence of parton density function of the pomeron if the pomeron exchange contribution is dominant in our data. However, the form $zf_{g/I\!P}(z) = 1/z$ violates the momentum sum rule, so $zf(z) = 1/(z+a)$ is used by adding a constant a being much less than 1 to the denominator. In this case the normalization constant is given by $\log^{-1}[(1+a)/a]$. In actual event generation a is chosen to be $a = 10^{-5}$. In addition, $a = 10^{-6}$ is also used to see the difference on generated events. We do not consider here the quark contribution because our particular interest is on a comparison of dijet kinematics and it is expected to be similar for both the quark and gluon dominant models. The third distribution function is a mixture of hard gluon and hard quark. In combined analysis of CDF diffractive W, dijets and bottom quark productions [16, 17, 18], we obtain the gluon fraction of the pomeron to be $f_g^{CDF} = 0.54^{+0.16}_{-0.14}$ by using the POMPYT with the standard flux and assuming a hard structure of the pomeron (Section 2.2.4). So the pomeron model with the mixture of 54 % hard gluon and 46 % hard quark should be consistent with CDF published results. This is called later *CDF quark+gluon*. Comparison of our DPE data with the POMPOMPYT predictions based on these distribution functions would enable us to confirm that our observation of an excess of rapidity gap events is really attributed to DPE. The last structure, *soft gluon*, is unlikely to describe the CDF results which have been reported so far. Therefore, it would be worth illustrating that the disfavored structure function of the pomeron actually give the different behavior from our data. It should be noted that all the distribution functions are formulated to fulfill the momentum sum rule $\int_0^1 dz \sum_i zf_i(z) = 1$.

7.2.1 Event Generation

The generated events of POMPYT and POMPOMPYT are all processed through the CDF detector simulation (QFL version 3.59) to compare with the data, and then the analysis chain is applied as done in data. Our kinematical range of POMPOMPYT event generation is $0.02 < \xi_{\bar{p}} < 0.11$, $0.0001 < \xi_p < 0.11$ in ξ and $|t_{\bar{p}}| < 5.0\,\mathrm{GeV}^2$, $|t_p| < 5.0\,\mathrm{GeV}^2$ in t. In POMPYT the range $0.001 < \xi_{\bar{p}} < 0.11$ and $|t_{\bar{p}}| < 5.0\,\mathrm{GeV}^2$ is used. In the following analysis the $\xi_{\bar{p}}$ and $t_{\bar{p}}$ are required to be $0.035 < \xi_{\bar{p}} < 0.095$ and $|t_{\bar{p}}| < 1.0\,\mathrm{GeV}^2$ which is the data range. If the generated events contain the jets reconstructed by the JETCLU clustering, the JTC96 corrections are applied to them. However, for this correction the underlying event (UE) energy in both simulations has to be measured and then subtracted from the jets. The UE energy can be estimated using the methods used in data, but we have to take care of possible dependence of the UE energy on the center of mass energy at which the event is generated. As illustrated in the figure of [50], the center of mass energy dependence of UE energy is examined for above four distribution functions in both SD and DPE event simulations. The observed behavior of mass dependence is parameterized using the fit. For POMPYT SD event simulation, we find no mass dependence in cases of flat gluon and CDF quark+gluon, but in rest two we observe a linearly increasing UE energy with increasing mass due to their softer structures. For POMPOMPYT DPE event simulation, the observed behavior of UE energy is similar to SD case but all four distribution functions show that the UE energy rapidly increases with increasing mass up to $\sqrt{s_{DPE}} = 40\,\mathrm{GeV}$. In flat gluon and CDF quark+gluon the UE energy becomes almost flat over $\sqrt{s_{DPE}} = 40\,\mathrm{GeV}$, in contrast to other two functions showing still linear increase over the entire generated range.

Figure 7.2 shows the POMPOMPYT multiplicity correlation between the BBC hits and FCAL towers on the proton side, after requiring the two jets with $E_T > 7\,\mathrm{GeV}$ after subtraction of measured UE energy. A BBC hit is defined as a charged particle produced within the BBC coverage $3.2 < \eta < 5.9$. The FCAL tower multiplicity is obtained by counting the *towers* above E_T thresholds used for the data (Eq. (5.2)), where a tower is defined as a charged or neutral particle whose energy corresponds to the detector energy using the η dependent corrections. This conversion method has been

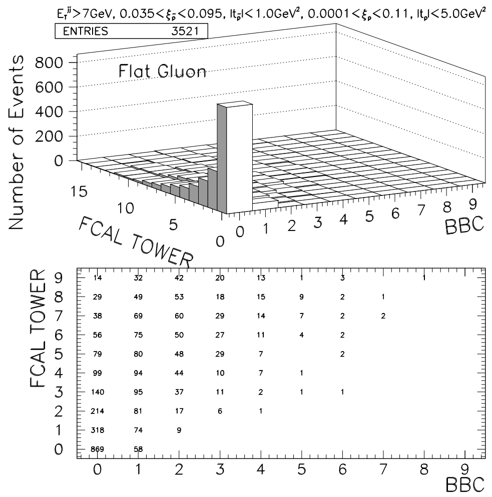

(a) flat gluon

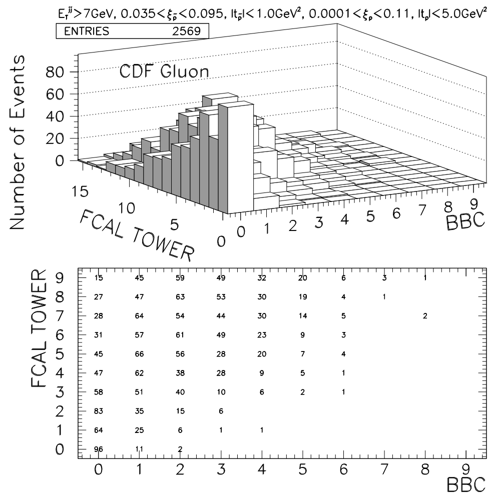

(b) CDF gluon

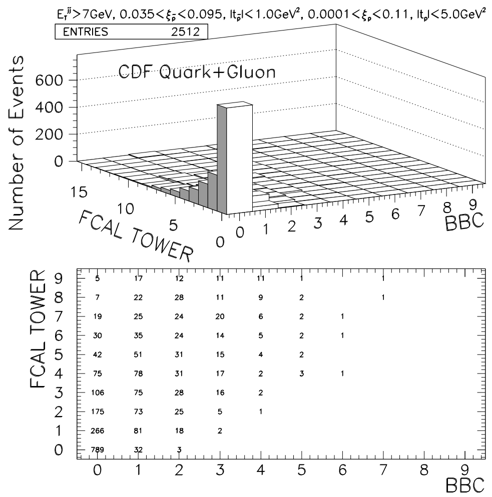

(c) CDF quark+gluon

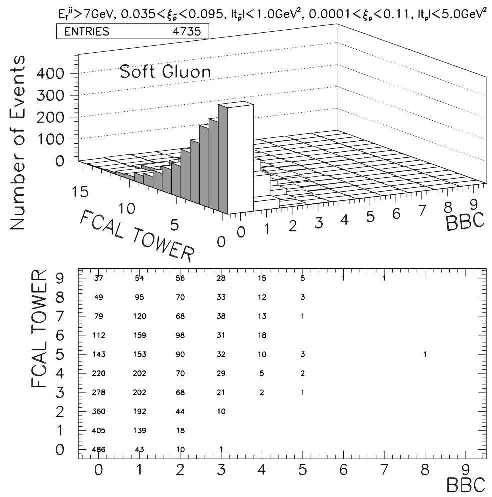

(d) soft gluon

Figure 7.2: Multiplicity correlation between the BBC hits and forward calorimeter towers for $E_T > 7\,\mathrm{GeV}$ dijet events in POMPOMPYT based on the (a) flat gluon, (b) CDF gluon, (c) CDF quark+gluon and (d) soft gluon distribution functions of the pomeron. The definitions of the BBC hit and forward calorimeter tower are described in the text.

developed in diffractive W analysis [16] (details in [54]). In the flat gluon and CDF quark+gluon simulations, we find that the shape of low multiplicity region is in qualitative agreement with that of the data signal (Figure 6.1). However, the CDF gluon case shows the distinctly different shape. We could attribute this apparent difference to an insufficient knowledge of simulating the forward particles mainly originating from the beam fragmentation. This ambiguity is therefore more strongly enhanced in simulation of soft parton distribution functions. The soft gluon also shows larger forward multiplicities and hence the magnitude of the peak of (0,0) bin is reduced.

Figure 7.3 shows the simulated ξ and $|t|$ distributions for DPE events with $E_T >$ 7 GeV dijets. The $\xi_{\bar{p}}$ and $|t_{\bar{p}}|$ are required to be $0.035 < \xi_{\bar{p}} < 0.095$ and $|t_{\bar{p}}| < 1.0\,\mathrm{GeV}^2$. Due to softer distribution functions, both the CDF gluon and soft gluon simulations have ξ_p distributions with a strong enhancement at large ξ_p. It is also seen for all distribution functions that the range $0.005 \lesssim \xi_p \lesssim 0.03$ is dominant for events of (0,0) bin on the proton side. This is roughly consistent with our evaluation of dominant ξ_p range in data $0.01 < \xi_p < 0.03$.

Combining the simulations of POMPOMPYT and POMPYT, the cross section ratios of DPE to SD dijet events can be compared with the data. In studies of PYTHIA Monte Carlo it turns out that the PYTHIA does not well reproduce the data with low E_T jets, in particular for the absolute normalization. We therefore do not expect the POMPYT or POMPOMPYT with a certain pomeron structure to describe the data in normalization since both Monte Carlos are based on PYTHIA. However, a ratio of normalizations in DPE to SD Monte Carlo would be somewhat free from possible ambiguities. We give in Table 7.1 the obtained cross section ratios of DPE to SD dijet events for data range : $0.035 < \xi_{\bar{p}} < 0.095$, $0.01 < \xi_p < 0.03$ in ξ and $|t_{\bar{p}}| < 1.0\,\mathrm{GeV}^2$, $|t_p| < 5.0\,\mathrm{GeV}^2$ in t. We have no information on t_p in data so we do not apply any cut on the generated t_p. Comparing with the data results:

$$\begin{aligned} R_{\frac{DPE}{SD}} &= 0.27 \pm 0.03(stat.) \pm 0.05(syst.)\,\% \qquad (E_T^{jet} > 7\,\mathrm{GeV}) \\ &= 0.12 \pm 0.03(stat.) \pm 0.05(syst.)\,\% \qquad (E_T^{jet} > 10\,\mathrm{GeV}), \end{aligned}$$

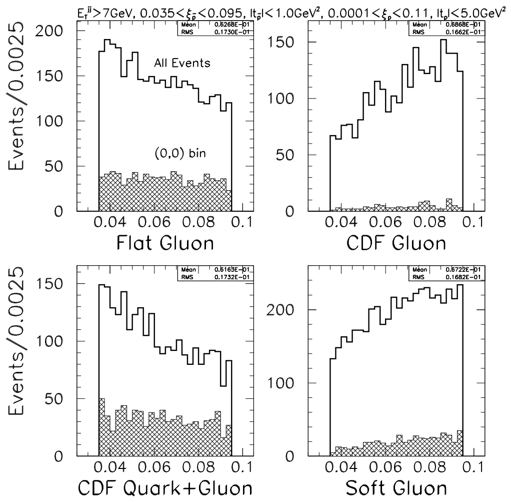

(a) $\xi_{\bar{P}}$

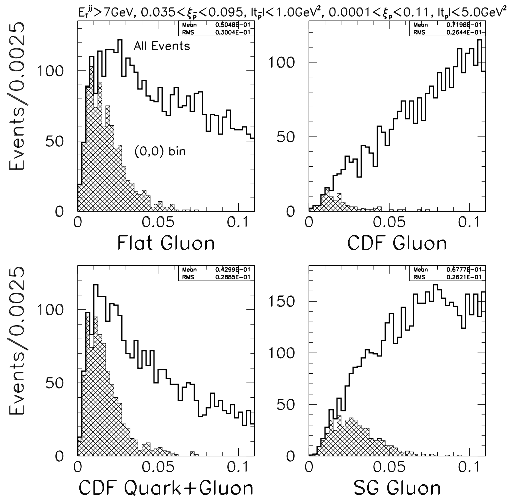

(b) ξ_p

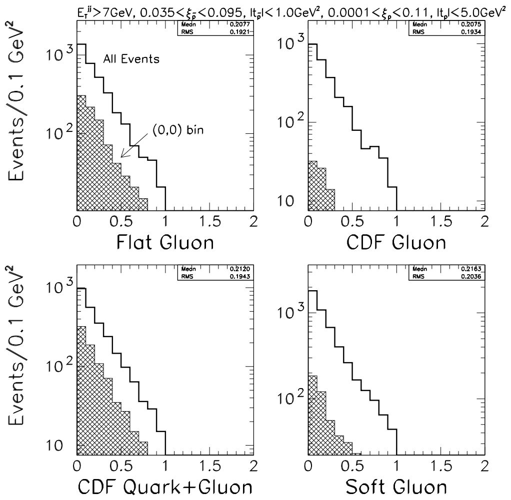

(c) $|t_{\bar{p}}|$

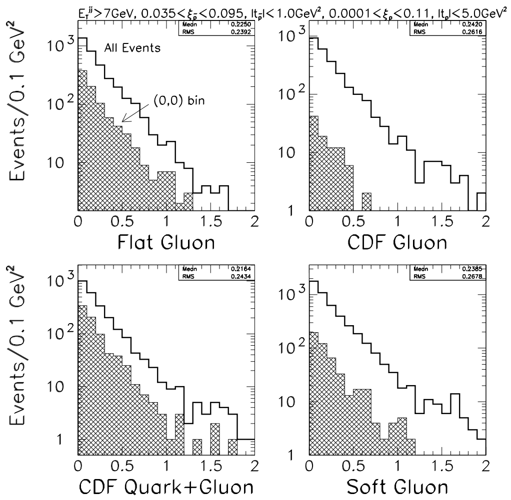

(d) $|t_p|$

Figure 7.3: (a) $\xi_{\bar{p}}$, (b) ξ_p, (c) $|t_{\bar{p}}|$ and (d) $|t_p|$ distributions for DPE events with $E_T > 7\,\mathrm{GeV}$ dijets in POMPOMPYT simulation. In each plot from (a) to (d), a flat gluon is top left, CDF gluon is top right, and CDF quark+gluon is bottom left, soft gluon is bottom right. The ranges of $\xi_{\bar{p}}$ and $|t_{\bar{p}}|$ are required to be the same as for our data. The shaded histograms show the distributions of events with $N_{BBC} = N_{CAL} = 0$ on the proton side.

Table 7.1: The cross section ratios of DPE to SD dijet events for the simulations of flat gluon, CDF gluon, CDF quark+gluon and soft gluon distribution functions of the pomeron. The kinematical range is given at the top of the table. For CDF gluon, ratios of simulations with $a = 10^{-5}$ ($a = 10^{-6}$) are given.

$0.035 < \xi_{\bar{p}} < 0.095$, $0.01 < \xi_p < 0.03$, $|t_{\bar{p}}| < 1.0\,\mathrm{GeV}^2$, $|t_p| < 5.0\,\mathrm{GeV}^2$

Pomeron Structure	**FLAT *g***	**CDF *g***	**CDF *q*+*g***	**SOFT *g***
$E_T^{jet} > 7\,\mathrm{GeV}$				
Standard Flux	1.52 %	0.05(0.04) %	1.87 %	1.98 %
Renormalized Flux	0.29 %	0.01(0.01) %	0.36 %	0.38 %
$E_T^{jet} > 10\,\mathrm{GeV}$				
Standard Flux	0.87 %	0.04(0.03) %	1.19 %	0.64 %
Renormalized Flux	0.17 %	0.008(0.006) %	0.23 %	0.12 %

we obtain about a factor of 5–7 (7–10) larger ratios than the data at $E_T > 7$ (10) GeV for the standard pomeron flux factor, for all distribution functions except for CDF gluon. The renormalized flux predictions are in much better agreements with the data for both E_T thresholds. In case of $a = 10^{-6}$ for CDF gluon we see no significant difference on ratios. This significant small ratio of CDF gluon simulation would be attributed to unlikely large forward particle multiplicities. A discrepancy of data from standard flux factor predictions is observed also in comparison with other parton density functions of the pomeron : the ratios with standard (renormalized) flux factor are evaluated to be 2.05 % (0.39 %) for *hard gluon*, 1.32 % (0.25 %) for *hard quark*, and 1.21 % (0.23 %) for *CDF flat quark+gluon* with $z\, f_{g,q/I\!P}(z) = f_g^{CDF} \cdot 1 + (1 - f_g^{CDF}) \cdot \frac{1}{4} \sum_{u,\bar{u},d,\bar{d}} 1$ at $E_T > 7$ GeV dijet threshold.

The observed rate discrepancy between the data and the standard flux predictions (a factor 5–7) is consistent with the measured discrepancy $D_{CDF} = 0.19 \pm 0.04$ [18] and hence the Renormalized Pomeron Flux model predictions [11, 12, 13]. This discrepancy would be attributed to a breakdown of the factorization in the Ingelman-Schlein model with the Donnachie-Landshoff pomeron flux factor.

7.2.2 Dijet Kinematics

In comparison with the simulation predictions, the dijet kinematics observed in data is shown for the leading and second jet E_T (Figures 7.4(a) and 7.4(b)), mean η of dijet system, $\eta^* = (\eta^{jet1} + \eta^{jet2})/2$ (Figure 7.4(c)), and azimuthal angle difference between the two leading jets, $\Delta\phi = |\phi^{jet1} - \phi^{jet2}|$ (Figure 7.4(d)). We select events of (0,0) bin in data and correct them for the Roman Pot acceptance as done in Section 6.4. The shapes of 14 % single diffractive background are subtracted from the data points. All the following comparison are made by selecting the simulated events of (0,0) bin and then normalizing the distributions of data and simulations to a unit area.

The observed jet E_T distributions are roughly consistent with any Monte Carlo shapes but the E_T slope of soft gluon simulation looks slightly steeper than the data. The Monte Carlo η^* distributions are all similar to the data but again the soft gluon case seems to have sharper peak at $\eta^* \sim -0.5$. The data is almost consistent with Monte Carlo shapes also in $\Delta\phi$ distributions. An increase of events around $\Delta\phi$ near π radian is well reproduced in particular by the simulations with softer parton density functions such as CDF gluon and soft gluon.

7.2.3 Pomeron ξ for the Proton Side

We have evaluated the ξ_p, a fractional momentum loss of the proton, for observed DPE events using the calorimeter tower and BBC hit information (Section 6.5). In Figure 7.5(a), comparison of ξ_p distributions with the POMPOMPYT shapes is presented. As above, the SD background is subtracted from the data and then the Roman Pot acceptance is corrected. The Monte Carlo distributions shown in the figures are the ξ_p at the generated level. The obtained ξ_p distributions of all Monte Carlos except for soft gluon are similar to the data. A soft gluon case shows larger ξ_p and it could be most likely attributed to that the requirement of dijet kinematically enhances large ξ_p due to its soft parton density function.

7.2.4 Dijet Mass Fraction

The shapes of the dijet mass and the mass fraction of dijet to total DPE system are shown for the POMPOMPYT simulations in Figures 7.5(b) and 7.5(c). As above, the Roman Pot acceptance is corrected, then the SD background is removed for the data. For both data and Monte Carlos, the dijet mass is reconstructed from only the towers within the cones so it is M_{jj}(cone). The system mass in simulations is a generated mass (center of mass energy in pomeron-pomeron interactions, $\sqrt{s_{DPE}} = \sqrt{\xi_{\bar{p}} \cdot \xi_p \cdot s}$). We see in comparison with data that the dijet mass is in good agreement with the Monte Carlo shapes of flat gluon, CDF gluon and CDF quark+gluon. In dijet mass fraction R_{jj} we find that the flat gluon and CDF quark+gluon show the similar shapes but it appears that they have slightly larger R_{jj} than data. Contrary to them, the soft gluon Monte Carlo shows much smaller R_{jj} because of its soft z structure. The CDF gluon prediction is somewhat intermediate between the hard (or flat) and soft Monte Carlo shapes and the agreement with the data is obtained.

In these comparisons of dijet events in DPE, we see that three parton density functions which we assume, flat gluon, CDF gluon and CDF quark+gluon, relatively well describe the data shape for the jet E_T, η^*, $\Delta\phi$. The ξ_p and M_{jj}(cone) are also well reproduced. It is unlikely that the soft gluon describes the data distributions. These features are consistent with expectations from our published single diffraction results [16, 17, 18]. Particularly the agreement of our DPE events with CDF gluon or CDF quark+gluon simulation would attribute our observation of gap excess events to real DPE process with two pomerons for both p and $\bar{p}$ sides.

To interpret the similarity among the flat gluon, CDF gluon and CDF quark+gluon, it is worth noting that the low β partons with $\beta \lesssim 0.2$ do not kinematically contribute to the dijet production in DPE for our kinematical range. The flat and hard momentum distributions are therefore indistinguishable so the Monte Carlos with flat gluon and CDF quark+gluon should have similar shapes for all the distributions and actually

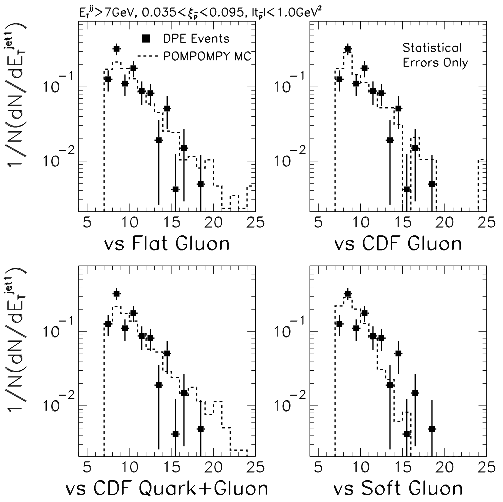

(a) E_T of leading jets

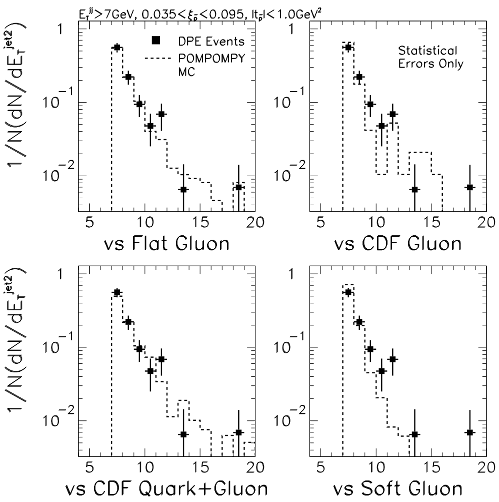

(b) E_T of second jets

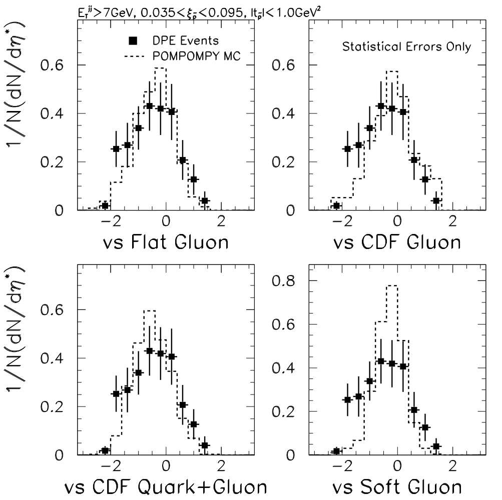

(c) mean η of dijets

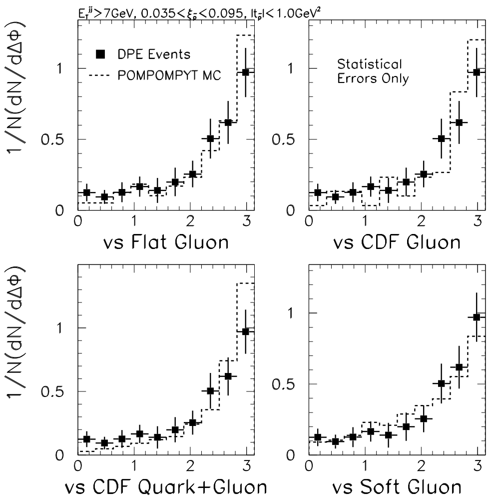

(d) azimuthal opening angle of dijet

Figure 7.4: Comparison of $E_T > 7\,\mathrm{GeV}$ DPE dijet events (black points) with the POMPOMPYT Monte Carlo predictions (dashed histograms) : (a) E_T of the highest E_T jets, (b) E_T of the second highest E_T jets, (c) mean η of dijets, and (d) azimuthal opening angle between the two leading jets. The SD background is subtracted from the data. In each plot from (a) to (d), a flat gluon is top left, CDF gluon is top right, and CDF quark+gluon is bottom left, soft gluon is bottom right.

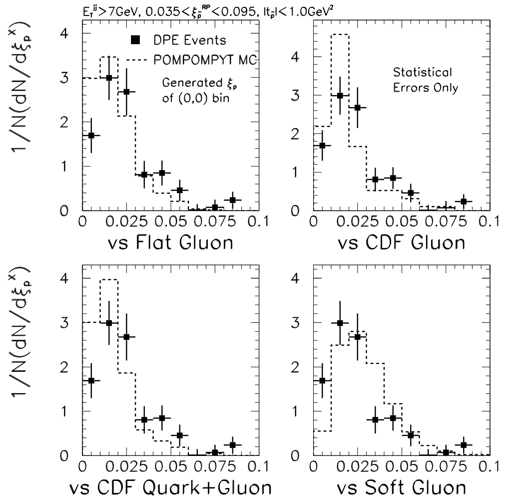

(a) ξ_p

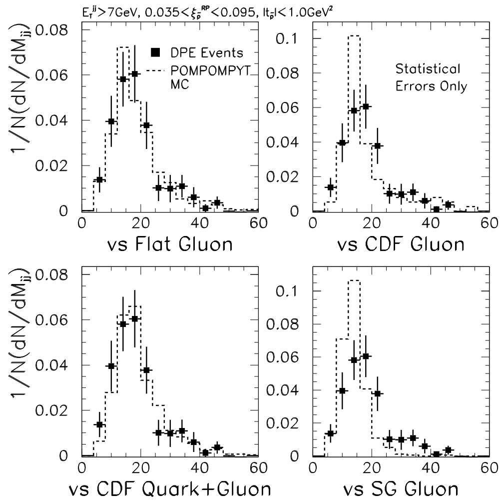

(b) Dijet mass M_{jj}(cone)

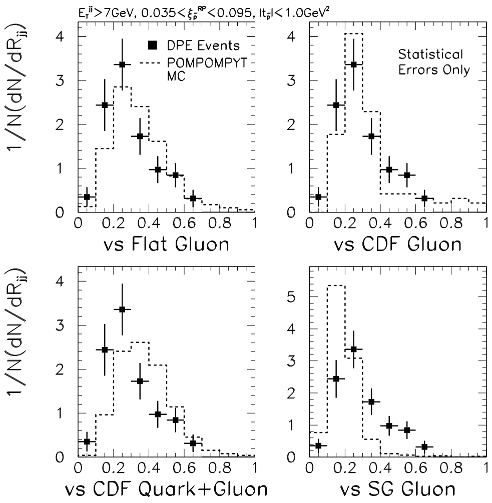

(c) Dijet mass fraction R_{jj}

Figure 7.5: Comparison of $E_T > 7\,\mathrm{GeV}$ DPE dijet events (black points) with the POMPOMPYT Monte Carlo predictions (dashed histograms) : (a) ξ_p, (b) dijet mass within the cones, (c) dijet mass fraction to total DPE system mass. The SD background is subtracted from the data. In each plot from (a) to (c), a flat gluon is top left, CDF gluon is top right, and CDF quark+gluon is bottom left, soft gluon is bottom right.

they have (although the quark component in CDF quark+gluon may cause small difference). The $1/\beta$ behavior of CDF gluon is regarded as soft structure, but due to this kinematical effect only the gluons with $\beta \gtrsim 0.2$, in which the distribution function is approximated by rather flat distribution, contribute. Accordingly we expect that the Monte Carlos with these three distribution functions basically have the similar shapes and they are in good agreement with data distributions. Actually this is seen in comparison of dijet kinematics. However, the data R_{jj} distribution is similar to CDF gluon prediction but looks slightly different from flat gluon and CDF quark+gluon Monte Carlo shapes. Recalling the arguments in Section 6.8, the R_{jj} provides the direct information on the overall β distribution of the exchanged objects. Therefore, a small disagreement of R_{jj} which we see between data and flat gluon prediction could be due to that this quantity more strongly depends on the β structure than the dijet kinematics. This also indicates that at $\beta \gtrsim 0.2$ the data favors the β structure such as CDF gluon, being no more flat but falling with β.

Chapter 8

Conclusions

Using a sample of events containing a diffractively scattered antiproton in $\bar{p}p$ collisions at $\sqrt{s} = 1.8\,\mathrm{TeV}$, we have studied dijet production by Double Pomeron Exchange (DPE) process. A leading antiproton in diffractive $\bar{p}p$ interactions is observed by the Forward Antiproton Spectrometers mounted in the Roman Pots. In the analysis, a leading $\bar{p}$ track with $0.035 < \xi_{\bar{p}} < 0.095$ and $|t_{\bar{p}}| < 1.0\,\mathrm{GeV}^2$ is required, and then we select events containing at least 2 jets with corrected transverse energy $E_T > 7\,\mathrm{GeV}$ and $> 10\,\mathrm{GeV}$ after processing events with JTC96 corrections. The underlying event energy which we measured is subtracted from the jets.

In this sample of dijet events with a leading $\bar{p}$ after non-diffractive (ND) overlay background is subtracted (single diffractive or SD dijet events), we search for the signal of dijets produced by DPE. We observe an excess of dijet events with a rapidity gap in the BBC ($3.2 < \eta < 5.9$) and forward calorimeter tower ($2.4 < \eta < 4.2$) on the outgoing proton side. This excess is qualitatively consistent with the prediction of the DPE Monte Carlo simulation POMPOMPYT [63] that assumes the exchange of the pomeron with the CDF measured parton density function. The ξ_p for the outgoing proton direction is evaluated for these excess events. In our measured kinematical range, we have estimated the cross sections σ^{jj} of DPE, SD and ND dijet events and their relative production rates R as follows,

$\mathbf{0.035 < \xi_{\bar{p}} < 0.095,\ 0.01 < \xi_p < 0.035,\ \lvert t_{\bar{p}}\rvert < 1.0\,GeV^2}$		
$E_T^{jet} > 7\,\mathrm{GeV}$	σ^{jj}_{DPE}	$43.6 \pm 4.4(stat.) \pm 21.6(syst.)$ nb
	σ^{jj}_{SD}	$16.2 \pm 0.1(stat.) \pm 5.3(syst.)$ μb
	σ^{jj}_{ND}	$5.04 \pm 0.03(stat.) \pm 1.01(syst.)$ mb
$E_T^{jet} > 10\,\mathrm{GeV}$	σ^{jj}_{DPE}	$3.4 \pm 1.0(stat.) \pm 2.0(syst.)$ nb
	σ^{jj}_{SD}	$2.9 \pm 0.1(stat.) \pm 1.1(syst.)$ μb
	σ^{jj}_{ND}	$1.62 \pm 0.02(stat.) \pm 0.46(syst.)$ mb

$\mathbf{0.035 < \xi_{\bar{p}} < 0.095,\ 0.01 < \xi_p < 0.035,\ \lvert t_{\bar{p}}\rvert < 1.0\,GeV^2}$		
$E_T^{jet} > 7\,\mathrm{GeV}$	$R_{\frac{DPE}{SD}}$	$0.27 \pm 0.03(stat.) \pm 0.05(syst.)$ %
	$R_{\frac{SD}{ND}}$	$0.32 \pm 0.003(stat.) \pm 0.07(syst.)$ %
	$R_{\frac{DPE}{ND}}$	$[0.86 \pm 0.09(stat.) \pm 0.23(syst.)] \times 10^{-5}$
$E_T^{jet} > 10\,\mathrm{GeV}$	$R_{\frac{DPE}{SD}}$	$0.12 \pm 0.03(stat.) \pm 0.05(syst.)$ %
	$R_{\frac{SD}{ND}}$	$0.18 \pm 0.004(stat.) \pm 0.04(syst.)$ %
	$R_{\frac{DPE}{ND}}$	$[0.21 \pm 0.06(stat.) \pm 0.10(syst.)] \times 10^{-5}$

In comparison of $E_T > 7\,\mathrm{GeV}$ DPE dijets with SD and ND dijets, we find that the jet E_T spectrum of DPE dijets is similar to that of SD dijets, but looks slightly softer than that of ND dijets. The DPE dijet is produced toward the $\bar{p}$ direction due to that the momentum loss of the p is smaller than that of the $\bar{p}$, and this feature is in contrast to SD dijets boosted toward the p direction and ND dijet produced symmetrically. It is seen that the dijets produced in DPE are more back-to-back than SD and ND dijets.

The cross section ratio $R_{\frac{DPE}{SD}}$ of DPE to SD dijet production is compared between the data and the predictions of the Monte Carlo simulations based on the Ingelman-Schlein model with the Donnachie-Landshoff pomeron flux factor. We find the presence of a disagreement of $R_{\frac{DPE}{SD}}$ ratio between the data and the simulations. Incorporating into the simulations the discrepancy from the standard pomeron flux predictions measured in diffractive W, dijet and bottom quark productions at CDF [16, 17, 18], we find that the simulation predictions are in good agreement with the data. These observed rate discrepancies are generally well predicted by the Renormalized Pomeron Flux model [4, 12, 13].

We have evaluated the mass fraction R_{jj} of dijet to central DPE system. For our kinematical range $E_T^{jet} > 7\,\mathrm{GeV}$, $0.035 < \xi_{\bar{p}} < 0.095$, $|t_{\bar{p}}| < 1.0\,\mathrm{GeV}^2$, we estimate a fractional Non-Factorizable DPE [55] contribution in our observed DPE events to be

$$R_{NF}^{0.7} \; < \; 4.6\,\%,$$

at 95 % confidence level for jets with cone size $R = 0.7$. For $R = 1.0$ jets, we obtain $R_{NF}^{1.0} < 2.7\,\%$ which is consistent with $R_{NF}^{0.7}$. Combining the limit $R_{NF}^{0.7}$ and the measured DPE dijet cross section, we estimate the contribution from the Non-Factorizable DPE cross section to be an order of 10^{-3} of the theoretical calculation by A. Berera [67].

Appendix A

Roman Pot : Multi-Reconstructed Tracks

In the Roman Pot trigger data after requiring the missing $E_T < 20\,\mathrm{GeV}$, vertex cuts and 1 M.I.P. selection cuts, we find that a relatively large fraction (17 %) of events contains the two reconstructed tracks in the Roman Pots (See Figure 4.4 in Section 4.4.1). We use the data with two tracks in the main analysis. Therefore, the analysis of the data with two tracks, in particular the reason why it is used, should be discussed (the case with three or more tracks is not described because the fraction of those events is negligibly small and we reject them in the main analysis).

In order to look at the data with two tracks in detail, we use a subset of diffractive trigger data used in the main analysis. The total number of events in the subset is about 438 K, and the same selection cuts as in the main analysis are required. Applying the 1 M.I.P. selection cuts, the number of events is about 343 K. Their reconstructed Roman Pot track multiplicity distribution for these 343 K events is shown in Figure A.1. As seen in Figure 4.4 in Section 4.4.1, the subset used here shows the same multiplicity distribution (only one track $\sim 69\,\%$ and two tracks $\sim 17\,\%$). Hereafter we refer to the data with two tracks (one track) as the NTRK2 (NTRK1) sample.

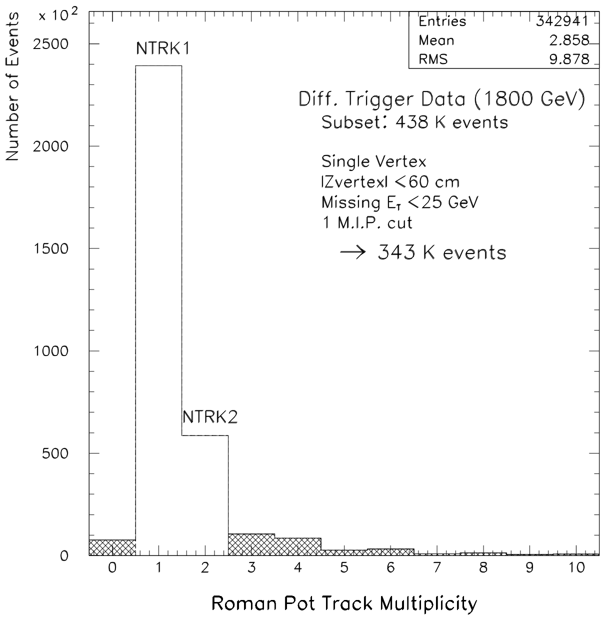

Figure A.1: Multiplicity distribution of reconstructed Roman Pot tracks in the subset after requiring several selection cuts.

Figure A.2 shows the positions and angles of reconstructed tracks at Pot 1 in the NTRK1 and NTRK2 samples. A track with the best reconstruction χ^2 (called T1) is taken for the NTRK2 sample. We see the similar shapes for all the distributions except the X position, in which NTRK2 shows a peak at the edge of the pot acceptance close to the beam. Therefore, a possible concern is a contamination from the beam particles (e.g., $\bar{p}$ beam halo).

To see the beam "halo" particles, we use the "empty events" that have no vertex with class $\geq$ 5, and no BBC hits on both the east and west sides. This sample of events is expected to contain more beam halo contribution. Figure A.3 shows the distributions of the best χ^2 and the next to best χ^2 track (called T2) for both the NTRK2 and empty samples. It is seen that the ϑ_X distribution of empty events shows a different behavior (decreasing with increasing ϑ_X) from that of NTRK2 data. Therefore, to estimate the beam contribution, all the shaded distributions of empty

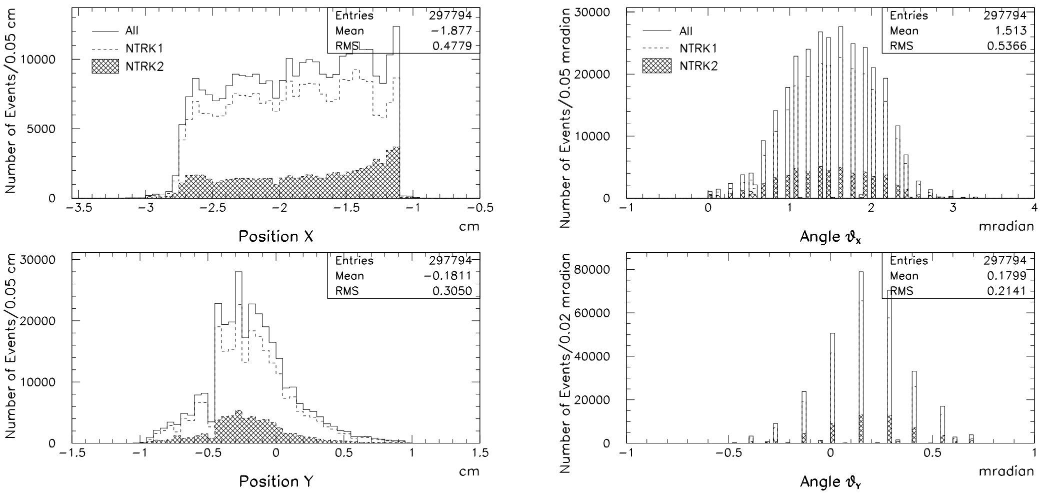

(a) Positions

(b) Angles

Figure A.2: (a) X and Y positions, and (b) angles in the X-Z and Y-Z planes for the events with one or two Roman Pot tracks. The dashed histograms are the distributions for a track in NTRK1 sample. The shaded histograms are those for the best reconstruction χ^2 track in NTRK2 sample. The full histograms show the distributions of all events for both the NTRK1 and NTRK2.

events are normalized by the ratio obtained by fitting ϑ_X distributions of empty events to those of NTRK2 data at $\vartheta_X = 0$. These overlaying distributions indicate that there is a beam particle background in NTRK2 data, but it does not completely account for the low X peak, in particular for T2.

So far there is no proof that two reconstructed tracks are two real particles. In Figure A.4(a) we show the correlation between the difference of two track X positions in Pot 1 ($\Delta X_{12} = |X_1 - X_2|$) and the difference of two track ϑ_X angles in Pot 1 ($\Delta\vartheta_{X12} = |\vartheta_{X1} - \vartheta_{X2}|$) for the NTRK2 data. It is found that most of tracks could be classified into four classes, each of which has a clear dependence between the ΔX_{12} and $\Delta\vartheta_{X12}$. When requiring more accurate reconstruction in the Roman Pots by applying the reconstruction $\chi^2 < 3$ for both the two tracks, the four classes (A–D) can be visibly

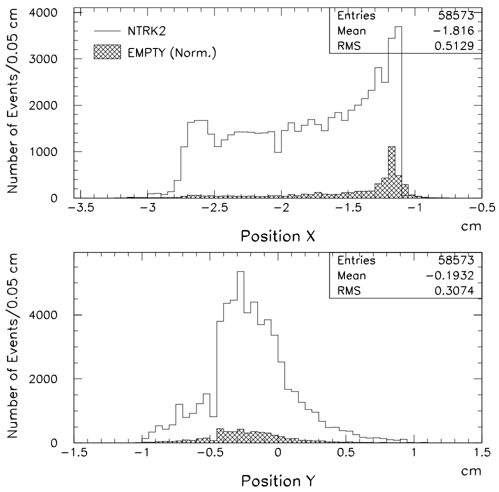

(a) Positions (for T1)

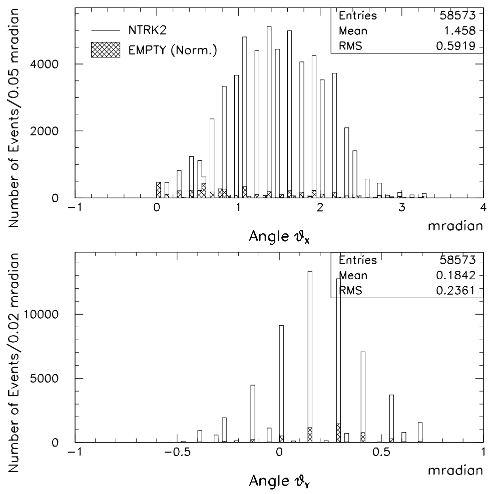

(b) Angles (for T1)

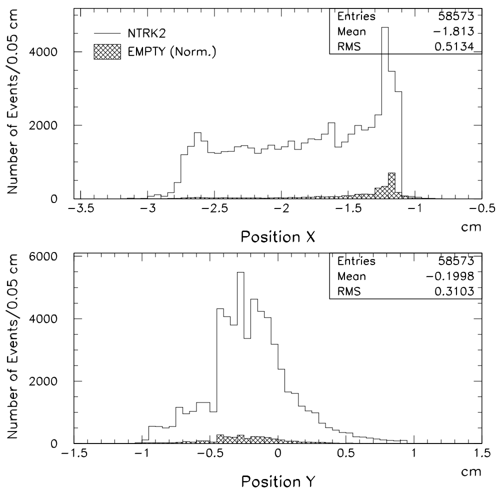

(c) Positions (for T2)

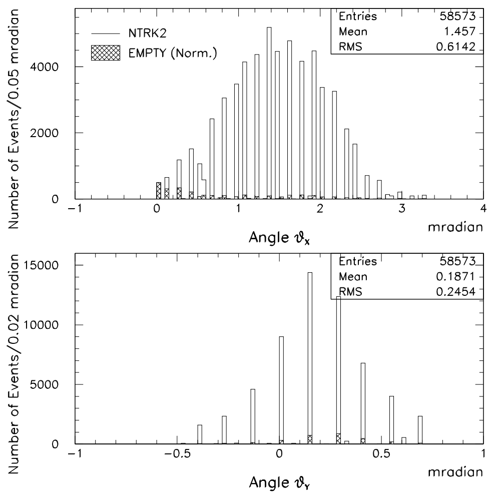

(d) Angles (for T2)

Figure A.3: X and Y positions for (a) T1 and (c) T2, and angles in the X-Z and Y-Z planes for (b) T1 and (d) T2. The definitions of T1 and T2 are described in the text. The plotted data are the NTRK2 (full histograms) and the empty events (shaded histograms). All the distributions of empty events were multiplied by the normalization ratio of ϑ_X distribution.

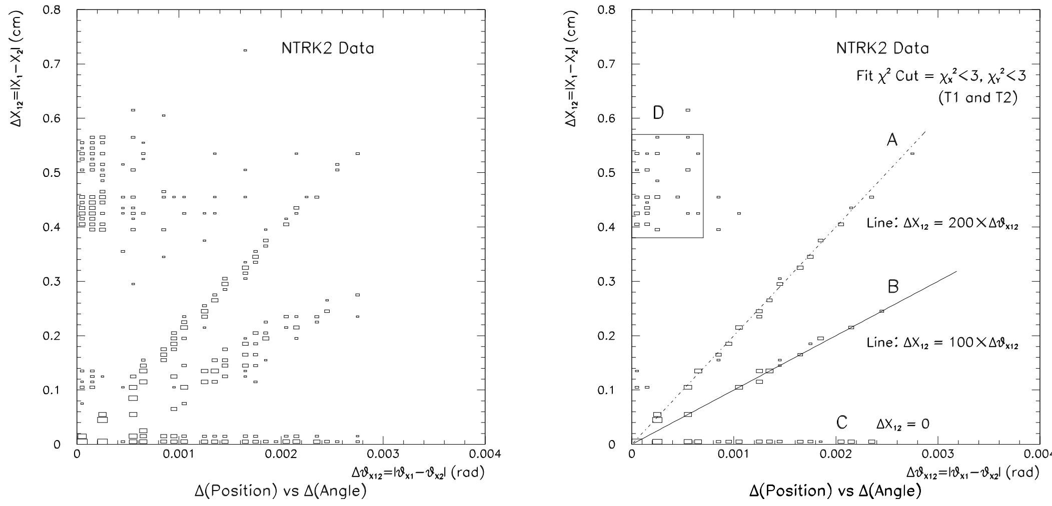

(a) NTRK2 Data (b) NTRK2 Data (χ^2 cut)

Figure A.4: Correlation between the difference of two track X positions (ΔX_{12}) and that of two track ϑ_X angles ($\Delta\vartheta_{X12}$) for (a) the raw NTRK2 data, and (b) for the NTRK2 data after requiring the reconstruction $\chi^2 < 3$.

separated, as shown in Figure A.4(b). The $\Delta\vartheta_{X12}$ dependence of ΔX_{12} for each class is obtained from the figure as follows,

A	:	$\Delta X_{12} = 200\,(\text{cm}) \times \Delta\vartheta_{X12}\,(\text{rad})$,
B	:	$\Delta X_{12} = 100\,(\text{cm}) \times \Delta\vartheta_{X12}\,(\text{rad})$,
C	:	$\Delta X_{12} = 0$,
D	:	$0.38\,(\text{cm}) < \Delta X_{12} < 0.57\,(\text{cm})$, $\Delta\vartheta_{X12} < 0.7\,(\text{mrad})$.

By recalling the dimension of the Roman Pot (the distance between the two pots is about 100 cm, so total length is 200 cm), it turns out that above three classes from A to C could be due to that two paths of reconstructed tracks cross each other at the pot from Pot 3 to 1 respectively, because a track position X is measured at Pot 1 (See Figure 3.8 in Section 3.3.2). Therefore, it is reasonable that one of the two tracks belonging to the classes A to C could be attributed to a fake track resulting from the

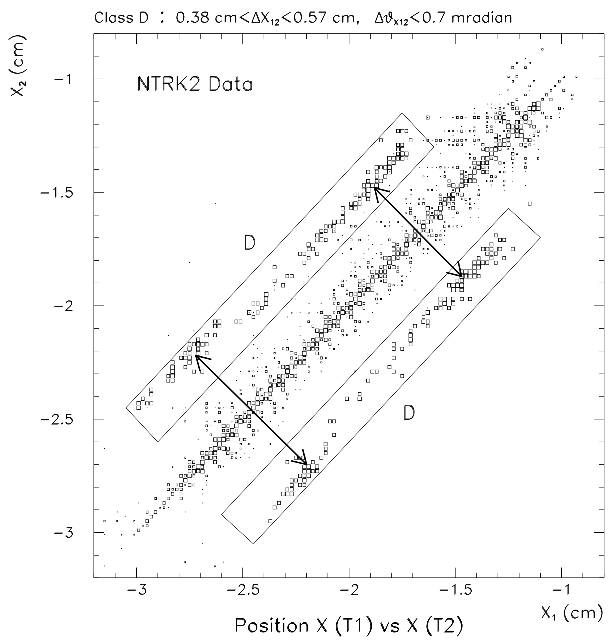

Figure A.5: Correlation between the X positions of two tracks fro the NTRK2 data. Two tracks in the rectangles belong to the class D. The class C is on the line of $X_1 = X_2$. Other two classes A and B make the fine structure near the line, but they are not on the line (except $\Delta X_{12} = \Delta\vartheta_{X12} = 0$).

hit points being shared in the reconstruction. So, in the main analysis we use only the track with the best χ^2 for NTRK2 data.

On the other hand, most tracks in the class D have $\Delta\vartheta_X < 0.3\,\mathrm{mrad}$ and are considered to be two separated tracks in X direction coming from the interaction region almost parallel to each other. However, as seen in Figure A.5, both the two tracks in the class D always hit the fibers at the same position. This plot shows the correlation between the X positions of the two tracks of NTRK2 data. Two tracks in the class D could be grouped into two sub-categories, one of which consists of tracks around $-1.6 < X < -1.3\,\mathrm{cm}$ and $-2 < X < -1.75\,\mathrm{cm}$, and the other around $X = -2.2\,\mathrm{cm}$ and $-2.75\,\mathrm{cm}$. These two sub-categories make almost constant distances between the two tracks, which are seen in Figure A.4(a) as two visible different sub-groups in the class D. Therefore, this study indicates that the class D probably could be due to an accidental coincidence of cross talks in certain channels of the MCPMTs of three Roman Pots, that can make a fake track parallel to original track. This probability is expected to be very small, and it seems to be consistent with about 1 % (0.2 %) of the fraction of the class D in NTRK2 data (all NTRK1 and NTRK2 data).

Appendix B

Live Time Acceptance

In the search for the DPE dijets, we use a rapidity gap method for the proton side. This is based on finding an excess of events at the zero multiplicities for both the BBC and forward calorimeter. This indicates that we need a correction for the occupancies of the calorimeter and BBC by the detector noise or the particles from the interactions which were not reconstructed as the visible vertices. This is called the live time acceptance in the thesis, and it was originally studied in diffractive W analysis [16]. The live time acceptance for the DPE analysis is described below.

First of all, we need events with no visible reconstructed vertices. Therefore, we use a sample of 14 K events in Run 1A, a portion of events triggered by the detector on beam-beam crossing only (RUN > 46146). From this sample we select events with no vertex with class ≥ 5. Then, we estimate the fraction of events with the zero BBC hits and the zero FCAL towers, which corresponds to the BBC and FCAL live time acceptance. This fraction depends on the instantaneous luminosity as shown in Figure B.1. By fitting the luminosity dependence by the linear function, and extrapolating it to the average luminosity of our diffractive data ($\sim 2.08 \times 10^{29}\,\mathrm{cm}^{-2}\mathrm{s}^{-1}$), we obtain the live time acceptance to be $97.0 \pm 2.7(syst.)\,\%$ for the east hemisphere (we are only interested in the east side because it is a correction for the gap signal on the proton side).

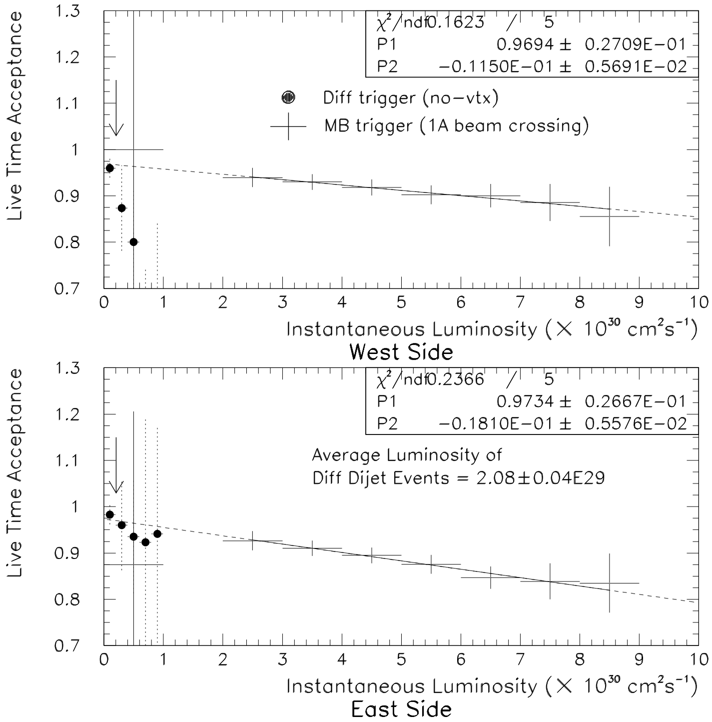

Figure B.1: Live time acceptance (probability of finding exact zero multiplicity in both the BBC and FCAL tower in events with no visible vertex) as a function of instantaneous luminosity. Upper (lower) half is for the west (east) side. The black points represent the subset of the diffractive data, and the crosses the beam-beam crossing data of Run1A. The arrow shows the average instantaneous luminosity of our diffractive data used in the main analysis.

As a check, we evaluate the acceptance using a part of our diffractive data. This subset is collected during the low luminosity runs without any vertex requirement in Level 3 trigger, in contrast to the normal diffractive trigger (See Section 4.1). By selecting events with no class ≥ 5 vertex in this sample, we obtain 411 K events during $75713 \leq \text{RUN} \leq 75738$. Evaluating the fraction of events with the zero BBC and zero FCAL tower multiplicities as above, the consistent live time acceptance is obtained as seen in Figure B.1 although the statistical errors are large. Here a cut to the Roman Pot trigger (total ADC counts < 800) is applied to reduce the bias from the Roman Pot trigger, that enhances the tower multiplicity of the west calorimeter.

Bibliography

[1] P.D.B. Collins, "An Introduction to Regge Theory & High Energy Physics", Cambridge University Press (1977)

[2] K. Goulianos, Physics Reports 101, 169 (1983)

[3] D. Joyce *et al.*, Phys. Rev. D **48**, 1943 (1993)

[4] K. Goulianos, Phys. Lett. B **358**, 379 (1995); B **363**, 268 (1995)

[5] K. Goulianos and J. Montanha, Phys. Rev. D **59**, 114017 (1999), hep-ph/9805496

[6] G. Ingelman, P.E. Schlein, Phys. Lett. B **152**, 256 (1985)

[7] M.G. Albrow *et al.*, Published Proceedings of 1996 DPF/DPB Summer Study on New Directions for High Energy Physics (Snowmass '96), Snowmass, Colorado, June 25-July 12, 1996, FERMILAB-CONF-96/377-E

[8] * M.G. Albrow, G. Bellettini, M. Deninno, D. Goulianos, S. Hasegawa, J. Iwai, P. Melese, C. Pagliarone : "A Search for Disoriented Chiral Condensate in Double Pomeron Exchange",
CDF/DOC/JET/CDFR/**2560**, (April 1994)

[9] P. Bruni, G. Ingelman, Phys. Lett. B **311**, 317 (1993)

[10] A. Donnachie, P.V. Landshoff, Nucl. Phys. B **303**, 634 (1988)

[11] Konstantin Goulianos, "Factorization and Scaling in Hard Diffraction", Published Proceedings of 5th International Workshop on Deep Inelastic Scattering and QCD (DIS97), Chicago, Illinois, April 14-18, 1997, hep-ph/9708217

[12] Konstantin Goulianos, "Pomeron Flux Renormalization: A scaling Law in Diffraction", Published Proceedings of Diffractive Physics, LAFEX International School on High Energy Physics (LISHEP98), Rio de Janeiro, Brazil, February 10-20 1998, hep-ph/9806363

[13] Konstantin Goulianos, "Diffraction: Results and Conclusions", Published Proceedings of Diffractive Physics, LAFEX International School on High Energy Physics (LISHEP98), Rio de Janeiro, Brazil, February 10-20 1998, hep-ph/9806384

[14] R. Bonino *et al.*, Phys. Lett. B **211**, 239 (1988)

[15] A. Brandt *et al.*, Phys. Lett. B **297**, 417 (1992)

[16] F. Abe *et al.*, (CDF Collaboration), Phys. Rev. Lett. **78**, 2698 (1997)

[17] F. Abe *et al.*, (CDF Collaboration), Phys. Rev. Lett. **79**, 2636 (1997)

[18] T. Affolder *et al.*, (CDF Collaboration), Phys. Rev. Lett. **84**, 232 (2000)

[19] Hirofumi IKEDA : Ph. D Thesis, "Observation of Diffractive Bottom Quark Production in 1.8-TeV Proton-Antiproton Collisions"

[20] M. Derrick *et al.*, (ZEUS Collaboration), Phys. Lett. B **356**, 129 (1995), DESY 95-115 (June 1995)

[21] T. Ahmed *et al.*, (H1 Collaboration), Phys. Lett. B **348**, 681 (1995); C. Adloff *et al.*, (H1 Collaboration), Z. Phys. C **76**, 613 (1997)

[22] K. Mauritz, Pub. Proc. of the 7th International Workshop on Deep Inelastic Scattering and QCD, Zeuthen, Germany, April 19-23, 1999, Nucl. Phys. B (Proc. Suppl.) Vol. **79**, (1999)

[23] L. Baksay *et al.*, Phys. Lett. B **61**, 89 (1976); H. DeKerret *et al.*, Phys. Lett. B **68**, 385 (1977); J.C.M. Armitage *et al.*, Phys. Lett. B **82**, 149 (1979)

[24] The AFS Collaboration, T. Akkeson *et al.*, Nucl. Phys. B **264**, 154 (1986)

[25] A. Brandt *et al.*, in *Proceedings of the 25th International Conference on High Energy Physics*, Singapore, (1990), edited by K.K. Phua and Y. Yamaguchi (World Scientific, Singapore, 1991)

[26] THE COLLIDER DETECTOR AT FERMILAB,
A compilation of articles reprinted from Nucl. Instrum. Methods Phys. Res., Sect. A, North-Holland Phys. Pub. - AMSTERDAM

[27] F. Abe *et al.*, (CDF Collaboration), Nucl. Instrum. Methods Phys. Res., Sect. A **271**, 387 (1988)

[28] J. Thompson, "Introduction to Colliding Beams at Fermilab", FERMILAB-TM-1909 (1994)

[29] F. Snider *et al.*, Nucl. Instrum. Methods Phys. Res. A **268**, 75 (1988)

[30] L. Balka *et al.*, Nucl. Instrum. Methods Phys. Res. A **267**, 272 (1988)

[31] S. Bertolucci *et al.*, Nucl. Instrum. Methods Phys. Res. A **267**, 301 (1988)

[32] Y. Fukui *et al.*, Nucl. Instrum. Methods Phys. Res. A **267**, 280 (1988)

[33] C. Haber *et al.* : "Performance and Calibration Studies of the CDF Endplug Hadronic Calorimeter", Published Proceedings of 1985 Gas Sampling Calorimetry, Batavia, 1985

[34] G. Brandenburg *et al.*, Nucl. Instrum. Methods Phys. Res. A **267**, 257 (1988)

[35] S. Cihangir *et al.*, Nucl. Instrum. Methods Phys. Res. A **267**, 249 (1988)

[36] F. Abe *et al.*, (CDF Collaboration), Phys. Rev. D **50**, 5518 (1994)

[37] F. Abe *et al.*, (CDF Collaboration), Phys. Rev. D **50**, 5535 (1994)

[38] F. Abe *et al.*, (CDF Collaboration), Phys. Rev. D **50**, 5550 (1994)

[39] * Stefano Belforte, Paul Derwent, John Marriner, Carla Pilcher : "σ_{BBC} Derivation and Results",
CDF/PHYS/CDF/CDFR/**2361**, (March 1994)

[40] * Stefano Belforte, Paul Derwent, John Marriner, Carla Grosso-Pilcher : "σ_{BBC} Updates",
CDF/PHYS/CDF/CDFR/**2535**, (April 1994)

[41] F. Abe *et al.*, (CDF Collaboration), Phys. Rev. Lett. **76**, 3070 (April 1996)

[42] M. Deninno, M.G. Albrow, C. Moore,J. Huston, G. Bellettini, A. Akopian, G. Apollinari, S. Bagdasarov, A. Bhatti, L. Demortier, N. Giokaris, K. Goulianos, D. Khazins, A. Maghakian, P. Melese, A. Titov, Q. Wang, H. Ikeda, S.H. Kim, K. Kondo, Miyamoto, H. Akimoto, T. Arisawa, Y. Fujimoto, S. Hasegawa, J. Iwai (The Hard Diffraction Group of CDF) : "PROPOSAL FOR HARD DIFFRACTION STUDIES IN CDF",
CDF/DOC/CDF/CDFR/**2940**, (Feb. 1995)

[43] R. Blair *et al.*, (CDF II Collaboration), "The CDF II Detector Technical Design Report", FERMILAB-PUB-96/390-E (1996)

[44] * G. Apollinari, N. Giokaris, K. Goulianos, A. Titov, Z. Wu, E. Hayashi, T. Kaneko, S.H. Kim, K. Kondo, S. Miyashita, K. Takikawa, K. Yasuoka, T. Kamon, V. Barnes : "Microplug Test-Beam Results",
CDF/DOC/CALORIMETRY/PUBLIC/**1736**, (Jan 1992)

[45] D. Amidei *et al.*, Nucl. Instrum. Methods Phys. Res., A **269**, 51 (1988)

[46] * Philip Mélèse : "Diffractive Trigger Level-1/2 Studies",
CDF/ANAL/JET/CDFR/**3344**, (Sept. 1995)

[47] C$DOC:VTVZ.MEM (CDF Internal Memo)

[48] * Hosai Hakada, Michael G. Albrow : “Kinematic Study of Diffractive Dijet Events in $\bar{p}p$ Collisions at $\sqrt{s} = 1.8$ TeV”,
CDF/ANAL/JET/CDFR/**4403**, (Feb. 1998)

[49] F. Abe *et al.*, (CDF Collaboration), Phys. Rev. D **45**, 1448 (1992)

[50] * Hosai Hakada, Koji Terashi, Ken Hatakeyama : “Study of Underlying Events in Diffractive Dijets”,
CDF/ANAL/JET/CDFR/**4716**, (Dec. 1998)

[51] T. Sjöstrand : “PYTHIA 5.7 and JETSET 7.4 — Physics and Manual —”, CERN-TH.7112/93 (Dec. 1993)

[52] * S. Bagdasarov and K. Goulianos : ”Diffractive W analysis: Runs 1A+1B (new cut)”,
CDF/ANAL/JET/CDFR/**3753**, (Aug. 1996)

[53] * S. Bagdasarov and K. Goulianos : ”Diffractive W analysis: Runs 1A+1B”,
CDF/ANAL/JET/CDFR/**3698**, (July 1996)

[54] * S. Bagdasarov and K. Goulianos : ”Search for Diffractive W Production at the Tevatron”,
CDF/ANAL/JET/CDFR/**3708**, (July 1996)

[55] F. E. Low, Phys. Rev. D **12**, 163 (1975); S. Nussinov, Phys. Rev. Lett. **34**, 1286 (1975); Phys. Rev. D **14**, 246 (1976); J. F. Gunion and D. E. Soper, Phys. Rev. D **15**, 2617, (1977) CDF/ANAL/JET/CDFR/**4711**, (May 1999)

[56] P. Bruni, A. Edin, G. Ingelman : “POMPYT version 2.6 — A Monte Carlo to Simulate Diffractive Hard Scattering Processes”, DRAFT (Sept. 1996)

[57] * Brenna Flaugher : “Efficiency of the 60 cm Z-vertex cut”, CDF/ANAL/JET/CDFR/**5094**, (July 1998)

[58] * D. Cronin-Hennessy, A. Beretvas, S. Segler : “Getting Your Luminosity”,// CDF/DOC/CDFR/**4317**, (Sept. 1997)

[59] * Philip Mélèse : “Dijet with Roman-Pot Rate”, CDF/ANAL/JET/CDFR/**3877**, (Sept. 1996)

[60] * Hosai Hakada : “Single Diffractive Dijets in $\bar{p}p$ Collisions at $\sqrt{s} = 1.8$ TeV”, CDF/ANAL/JET/CDFR/**4553**, (Sept. 1998)

[61] * L. Galtieri, J. Lys : “How well do we understand jets in Run I? Study of the Jet Energy Scale for Raw Jet $E_T \geq 8\,\mathrm{GeV}$.” CDF/ANAL/TOP/CDFR/**3983**, Revised Version 1.0 (March 1997)

[62] * Kerstin Borras : “The Generator POMPYT – Experiences and Modifications”, CDF/ANAL/JET/CDFR/**4602** (in preparation)

[63] * Kerstin Borras : “POMPOMPYT – A Generator for Double Pomeron Exchange”, CDF/ANAL/JET/CDFR/**4606** (in preparation)

[64] * Kerstin Borras, Konstantin Goulianos, Ken Hatakeyama : “Update of the Studies of the Structure of the Pomeron with Roman Pot Dijet Events”, CDF/ANAL/JET/CDFR/**4920**, (March 1999)

[65] * K. Borras, K. Goulianos, K. Hatakeyama : “Diffractive Dijet Production at $\sqrt{s} = 630\,\mathrm{GeV}$”, CDF/ANAL/JET/CDFR/**4895**, (March 1999)

[66] A. Berera, J. Collins, Nucl. Phys. B **474**, 183 (1996), A. Berera : “Jet Production Cross Section with Double Pomeron Exchange”, hep-ph/9705283, (1997)

[67] A. Berera : "A Tale of Two Hard Pomerons", hep-ph/9910405, (1999)

[68] K. Terashi, Published Proceedings of 4-th Workshop on Small-x and Diffractive Physics, Fermilab, September 17-20, 1998

[69] L. Alvero, J. Collins, J. Terron, J. Whitmore, Phys. Rev. D **59**, 074022, (1999) CDF/ANAL/JET/CDFR/**4524**, (July 1998)

[70] G. Ingelman, K. Prytz : Z. Phys. C **58**, 285 (1993)